2006

Sediment biogeochemistry of northern Cascadia margin shallow gas hydrate systems

John W. Pohlman
College of William and Mary - Virginia Institute of Marine Science

SEDIMENT BIOGEOCHEMISTRY OF NORTHERN CASCADIA MARGIN
SHALLOW GAS HYDRATE SYSTEMS

_____

A Dissertation

Presented to

The Faculty of the School of Marine Science

The College of William and Mary in Virginia

In Partial Fulfillment

of the Requirements for the Degree of

Doctor of Philosophy

_____

by
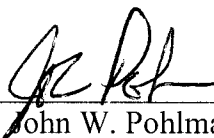
John W. Pohlman

2006
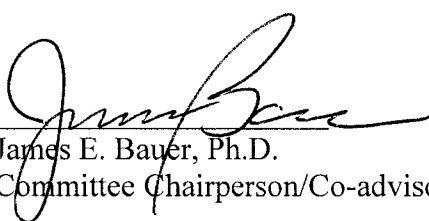
APPROVAL SHEET
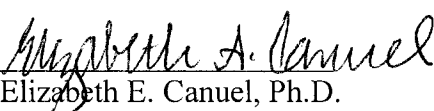
This dissertation is submitted in partial fulfillment of
The requirements for the degree of
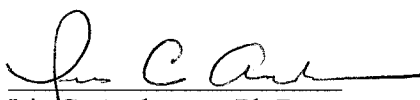
Doctor of Philosophy

John W. Pohlman
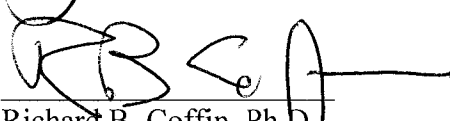
Approved, November 2006

James E. Bauer, Ph.D.
Committee Chairperson/Co-advisor

Elizabeth E. Canuel, Ph.D.
Co-advisor

Iris C. Anderson, Ph.D.

Steve Kuehl, Ph.D.

Richard B. Coffin, Ph.D.
Marine Biogeochemistry, Naval Research Laboratory
Washington D.C.

Charles K. Paull, Ph.D.
Monterrey Bay Aquarium Research Institute
Monterrey, CA

ii

DEDICATION

This dissertation is dedicated to Alyssa,
for your love, support and patience

TABLE OF CONTENTS

ACKNOWLEDGEMENTS

Numerous individuals and organizations had a role in making this dissertation possible. While I am unable to encapsulate my appreciation for the vast support and encouragement I have received, I can say the interactions and discourse have both transformed and humbled me. Bill Green, Rick Coffin and Barry Spargo crafted and supported the program that allowed me to enter the program at VIMS while maintaining employment at NRL. Jim Fye, Doug Rau and Rachael Owlett of Geo-Centers/SAIC helped maintain that program. Jim Bauer and Liz Canuel accepted me as their student and agreed to mentor me during my studies. Anna Miller, Terry DeBatti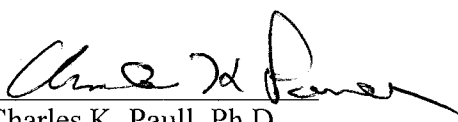sta and Carol Hopkins from Geo-Centers/SAIC and Sue Presson and Fonda Powell from VIMS provided administrative support and guidance to keep my program on track. Clark Mitchell and Rebecca Plummer worked tirelessly with (and without) me in the lab to develop analytical techniques and process samples collected during expeditions on the northern Cascadia margin. The captain and crew of the *CCGS John P. Tully* and ROPOS provided precise and friendly shipboard support during those expeditions. George Spence and Ross Chapman invited me to participate in those expeditions. At sea, Roswald Z. Downer, Ivana Novosel, Bob MacDonald, Courtney Schupp and Andrew Biersmith relentlessly recovered cores, squeezed sediment and processed pore water until the freezers were full. Charlie Paull, Michael Whiticar, Paul Eby, Jeff Chanton, Laura Lapham, Tom Boyd, Ed Kessee, Bill Ussler, Jack McGeehin, Ann McNichol and George Burr shared technical expertise and analytical support for extracting data from those samples. Labmates Beth Waterson and Amanda Spivak kindly guided me through the organic geochemistry lab at VIMS. Warren Wood, Michael Riedel and Carolyn Ruppel patiently and valiantly attempted to relay their geophysical knowledge to me. Rick Coffin, Clark Mitchell, Ken Grabowski, David Knies and Brett Renfru envisioned and realized the dream of developing the NRL Radiocarbon Facility.

Special appreciation is given to my committee members for their interest, support and guidance. They are Jim Bauer, Liz Canuel, Iris Anderson, Steve Kuehl, Rick Coffin and Charlie Paull. I learned immensely from each of them in uncountable ways.

I also have great appreciation for my friends and family who kept me grounded and entertained through the years; in particular those met during my time at VIMS. John Walter and Dave Kerstetter welcomed me into the fraternity of Crow Point. Andrij Horodysky, Paul Burt-Bradley and Frank Parker transported and housed me during my periodic and unannounced visits to VIMS.

Above all, my daughters, Cora and Anna, and wife, Alyssa, have been incredible. Cora and Anna have given me a fresh outlook on and a greater purpose in life. My beautiful wife has shown infinite patience, support and resolve. Without them, none of this would have happened.

LIST OF TABLES

vi

LIST OF FIGURES

ABSTRACT

Methane contained in gas hydrate is a significant component of the global organic carbon inventory. Describing the methane sources supporting these systems and the mechanisms that control the distribution of methane in marine sediments are critical elements in evaluating the resource potential, climate change implications and geologic hazards associated with gas hydrate. Expulsion of methane-charged fluid from accretionary systems concentrates gas hydrate along convergent plate boundaries. The northern Cascadia margin (offshore Vancouver Island, Canada) is a convergent margin with gas hydrate-bearing cold seeps composed of both thermogenic and microbial gas sources. Gas hydrate and sediment cores were collected from each of these settings to examine the sources that sustain the gas hydrate and the biogeochemical processes that control the flux and cycling of methane carbon within the cold seep system.

The isotopic and hydrocarbon composition of gas from the thermogenic gas hydrate site, Barkley Canyon, indicated this cold seep is connected to the landward Tofino Basin petroleum system. Barkley Canyon is the only known accretionary margin setting where thermogenic gas hydrate is exposed at the seafloor. The pore water and sediment geochemistry from distinct seafloor environments (e.g., clam colonies and bacterial mats) were evaluated to identify the fluid flux regimes and metabolic pathways that control how methane carbon was cycled by the microbial consortium. Evidence for coupling between anaerobic oxidation of methane (AOM) and methanogenesis was inferred from the stable carbon isotope composition of the dissolved inorganic carbon (DIC) and methane. Lipid biomarker analysis indicated sulfate reducing bacteria also consumed other sources of organic matter. Coupling between AOM and methanogenesis was also inferred at the microbial gas hydrate cold seep, Bullseye vent. AOM operating within both of these seep systems displayed a remarkable capacity to quantitatively consume methane within the sedimentary system; thus limiting methane emissions to the water column.

The radiocarbon content from gas-hydrate bound methane from six distant oceanic locations was almost entirely of fossil origin. Recognizing that the global gas hydrate reservoir is comprised of fossil carbon may alter our understanding of how gas hydrate methane influences the radiocarbon content of other ocean carbon pools (e.g., dissolved organic carbon). Radiocarbon analysis of sedimentary carbon pools was utilized to reconstruct the depositional history around the Bullseye vent site, which appears to have been subjected to tectonic uplift and erosion since the termination of the last glacial maximum.

This study demonstrates the value of integrating geochemical, chronological and geophysical data to understand the sources and cycling of globally significant reservoirs of methane in cold seep systems. The unique isotopic (^{13}C and ^{14}C) signature of methane is conveyed to and recorded within the pore water and sediment systems. By coupling those patterns with temporal (i.e., radiocarbon) and spatial (i.e., seismic) records, a more comprehensive model for how the northern Cascadia margin is interconnected and how the gas hydrate system has evolved was developed.

ix

SEDIMENT BIOGEOCHEMISTRY OF NORTHERN CASCADIA MARGIN
SHALLOW GAS HYDRATE SYSTEMS

CHAPTER 1

INTRODUCTION

2

Description and Significance of Gas Hydrate

Gas hydrate is an ice-like, crystalline structure that traps gas within a latticed framework of hydrogen-bonded water molecules (Kvenvolden, 1995). Gas hydrate occurs along continental margins and within the arctic permafrost wherever conditions for gas hydrate stability (high pressure and/or low temperature) exist and gas concentrations (primarily methane) are sufficient to saturate the pore water (Kvenvolden, 1999). The depth and thickness of the gas hydrate stability zone is primarily a function of the water depth (minimum depth ~300m), bottom water temperature, sediment geothermal gradient and the gas composition (Kvenvolden 1999).

Estimates of the global quantity of methane sequestered in gas hydrate are highly variable. Until recently, a consensus value of 10,000 Gt C (a quantity equivalent to twice that of all other fossil fuels combined) was considered a reasonable estimate (Kvenvolden, 2000). Direct measurements of gas hydrate concentrations from drilling sites on Blake Ridge and Hydrate Ridge (Dickens et al., 1997; Dickens et al., 2000; Milkov et al., 2003a) have, however, led to an improved understanding of the distribution and abundance of gas hydrate in marine sediments. As a result, more recent estimates of the global gas hydrate inventory have been downsized to 500-2,500 Gt C (Milkov, 2004). While this reduction is substantial and requires a reevaluation of the resource potential of gas hydrate, concentrated reserves may still contain profitable concentrations of methane (Milkov and Sassen, 2001; Milkov and Sassen, 2002; Milkov and Sassen, 2003).

Gas hydrate also plays an important role in climate change and controlling slope stability (Kennett et al., 2000; Paull et al., 2000). Using current estimates, the quantity of methane sequestered in hydrates is 80-4,000 times greater than the amount in the

3

atmosphere (Paull et al., 1991). Transfer of a small fraction of the submarine methane reservoir to the atmosphere could have profound and rapid effects on the present climate (Kastner, 2001). Although current estimates suggest that less than 2% of the annual atmospheric flux of methane originates from gas hydrate destabilization and permafrost melting (Crutzen and Lelieveld, 2001), there are numerous examples of rapid warming events that could have been triggered by massive gas hydrate dissociation during Earth's history (Dickens et al., 1995; Max et al., 1999; Kennett et al., 2000; Beerling et al., 2002; Kennett et al., 2002). Kennett et al. (2002) proposed the "Clathrate Gun Hypothesis" to describe how massive dissociation of marine gas hydrate induced rapid climate change events during the late Quaternary (last 400 kyr). Rapid warming of upper intermediate-water masses may have destabilized the gas hydrate reservoir of upper continental margins "loaded" with gas hydrate during the preceding glacial interval. In addition to releasing massive quantities of methane (a greenhouse gas) into the atmosphere, the sediment disruption resulting from hydrate dissociation may have led to major slope failures along the continental margins.

Sources, Cycling and Fate of Methane in Gas Hydrate-Bearing Sediments

Despite the immensity of the gas hydrate reservoir in ocean sediments, only about 2% of the annual global methane flux to the atmosphere is emitted from the ocean (Cicerone and Oremland, 1988). Ninety percent of methane generated in anoxic marine sediments is removed by the anaerobic oxidation of methane (AOM) within the sediments (Reeburgh, 1996), and high rates of aerobic methane oxidation in the water column (Valentine et al., 2001) remove as much as 98% of methane escaping from

4

seafloor vents (Mienert et al., 1998; Tsunogai et al., 2000). Nevertheless, an increased flux of methane into the water column will likely result in an increased contribution from the ocean to the atmosphere. The mechanisms and agents responsible for these processes are crucial to understanding the role marine systems play in balancing atmospheric greenhouse gas concentrations.

As noted above, AOM removes a substantial fraction of methane generated in anoxic, marine sediments. AOM is mediated by a syntrophic consortium of methanogenic archaea and sulfate reducing bacteria (SRB) (Boetius et al., 2000; Orphan et al., 2001) that facilitates the following reaction (Eq. 1).

$$CH_4 + SO_4^{-2} \rightarrow HCO_3^- + HS^- + H_2O \qquad (Eq. 1)$$
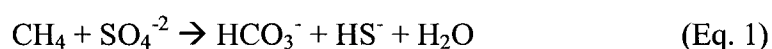
This process occurs in sediments at the sulfate-methane interface (SMI). The SMI is a zone where downward diffusing seawater sulfate encounters dissolved methane diffusing or advecting upward (Fig. 1) (Borowski et al., 1997). Above this interface, sulfate concentrations increase to seawater concentrations at the sediment-water interface (~29 mM), while below, methane concentrations increase due to methanogenesis or migration from deeper microbial and/or thermogenic sources. This process is prevalent in gas hydrate-bearing marine sediments with elevated pore water methane concentrations.

At gas vents (e.g., Tryon et al., 1999; Suess et al., 1999; Tsunogai et al., 2002; Gorman et al., 2002), mud volcanoes (e.g., Abdullaev et al., 1998; Milkov, 2000;

5

MacDonald et al., 2000; Milkov et al., 2003b) and cold seeps (e.g., Abdullaev et al., 1998; von Rad et al., 2000; Huchon and Tokuyama, 2002), the upward flux of methane exceeds the downward flux of sulfate, and methane is diffused or advected directly to the water column where it may be oxidized aerobically (Mienert et al. 1998; Valentine et al. 2001) or transferred to the atmosphere. Gas hydrate is often associated with the aforementioned features; therefore, studying the biogeochemical controls of AOM at these locations is critical to predicting how the gas hydrate reservoir will respond to ocean warming. For example, gas hydrate has been reported to undergo disassociation with as little as a 1.5 °C increase in bottom water temperature (MacDonald et al., 1994). If ocean warming continues, greater gas hydrate dissociation is hypothesized to occur (Kennett et al. 2002), and the number and/or activity of vents, seeps and mud volcanoes may increase. Understanding the role of AOM in intercepting the transfer of methane from sediments to the water column is, therefore, central to understanding how increasing bottom water temperature will affect climate change via a positive feedback loop or other mechanism.

Carbon sinks from AOM in marine sediments include dissolved inorganic carbon (DIC) (Borowski et al., 2000), dissolved organic carbon (DOC) (Bauer et al., 1990; Bauer et al., 1995), total organic carbon (TOC) (Joye et al., 2004), authigenic carbonate (Aloisi et al., 2002), and methanogenic archaeal and SRB biomass (Hinrichs et al., 2000) (Fig. 2). Oxidation and assimilation of ^{13}C-depleted methane (–85 to –55‰ for microbial methane and –60 to –35‰ for thermogenic methane; Whiticar, 1999) result in ^{13}C-depleted oxidation products. Borowski et al. (2000) reported δ^{13}C-DIC values as light as ~ –38‰ from pore water collected at Blake Ridge, and, using a stable carbon isotope

6

mass-balance model, determined that 24% of the DIC was from AOM. Elvert et al. (1999) measured $\delta^{13}C$ values as light as –123‰ for irregular isoprenoids from methanogenic archaea and values ranging between –55‰ to –35‰ for authigenic carbonates from sediments collected at Hydrate Ridge. Zhang et al. (2002) report $\delta^{13}C$ values ranging between –47‰ and –70‰ for lipid biomarkers from SRB. These examples exhibit the utility of stable carbon isotopes as tracers for tracking the fate of methane in anoxic marine sediments.

This study utilized stable carbon (^{13}C), radiocarbon (^{14}C) and deuterium (D) isotope signatures from methane and other carbon pools to characterize the sources and fate of methane at two sites with distinct gas sources (thermogenic and microbial) located on the Northern Cascadia Margin off Vancouver Island (British Columbia, Canada). Additional data from the sites is provided from geophysical surveys in the area.

Northern Cascadia Margin Site Description

The Cascadia Margin extends from Vancouver Island to Northern California. The continental slope of the margin is largely an accretionary prism formed by the subduction of the Juan de Fuca plate beneath the North American plate. Currently, it is subducting at a rate of ~45 mm yr^{-1}(Riddihough, 1984). Sediment scraping and consolidation form a series of anticlinal ridges underlain by thrust faults (Davis and Hyndman, 1989). These faults serve as conduits for gas and fluid migration from deep within the prism and may support gas hydrate formation (Hyndman and Davis, 1992). The presence of gas hydrate on the northern Cascadia Margin has been inferred from seismic reflection profiles (Hyndman and Spence, 1992) and confirmed by coring (Riedel et al., 2002). This study

focuses on two hydrate-bearing cold seep sites: Bullseye Vent and Barkley Canyon (Fig. 3).

Bullseye Vent. Bullseye vent is located within a slope-basin at a water depth of ~1250 m that is filled with modern laminated sediments. The basin is bounded by 200 m high anticlinal ridges formed by thrust faults or folding within the accretionary prism. Seismic reflection profiles from the slope basin contain numerous blank zones indicating the presence of gas hydrate, free gas or carbonate accumulations that appear as vertical shafts (Wood et al., 2002; Riedel et al., 2002). Gas hydrate of microbial origin was first discovered from this location in July 2000 (Riedel et al., 2002).

Barkley Canyon. Barkley Canyon is a headless canyon located on the upper continental slope at ~860 m water depth. In November 2001, a commercial fishing vessel inadvertently "caught" 1-2 tons of gas hydrate while trawling along the canyon wall (Spence and Chapman, 2001). Following this observation, ocean bottom surveys with the remotely-operated submersible ROPOS (August 2002 and July 2003) and piston-coring operations (October 2002) recovered gas hydrate from this region. These field programs provided data and samples for this study. Barkley Canyon is located on an anticlinal ridge, which may be the focus of hydrocarbon rich fluids migrating from the landward Tofino Basin hydrocarbon province (Bustin, 1995). Massive outcrops of gas hydrate at Barkley Canyon are exposed as blocks up to 8 m long and thinly sedimented mounds 2-3 m high (Chapman et al., 2004). Oil seepage observed during ROPOS dives strongly suggests Barkley Canyon may is connected to a petrogenic system.

8

Hypotheses

This study was designed to identify the sources of gas that support the gas hydrate accumulations and processes that control the fate of methane carbon at the Bullseye vent and Barkley Canyon cold seeps. The following hypotheses are addressed:

1. **Microbial and thermogenic hydrate gas from the Northern Cascadia Margin (NCM) are formed from a "deep" fossil (> 50,000 year BP) carbon source.** Radiocarbon analysis of gas hydrate-bound and core gas methane from the NCM was compared to radiocarbon measurements of gas hydrate-bound methane from the Haakon Mosby Mud Volcano, Gulf of Mexico, Blake Ridge and central Chilean margin to examine to what extent gas hydrate methane (regardless of source or production mechanism) is composed of fossil carbon. Support for this hypothesis could influence current paradigms explaining the radiocarbon content of oceanic carbon reservoirs (i.e., DOC).

2. **The source of gas for the thermogenic gas hydrate in Barkley Canyon is the landward Tofino Basin hydrocarbon province.** The stable carbon isotope composition of the C_1-C_4 gases from gas hydrate collected from Barkley Canyon were used to determine if the gases originated from Tofino Basin source rocks. Interpretation of these results includes comparisons of measured and literature data from Gulf of Mexico and Caspian Sea thermogenic hydrate gases to infer the source rock origins.

3. **The flux and anaerobic oxidation of methane from both sites will be greatest near gas hydrate occurrences and will decrease with distance from the gas hydrate.** Concentration gradients and carbon stable isotope composition of

9

dissolved methane, sulfate and DIC were used to describe the flux and anaerobic oxidation of the methane. Fluxes and SMI depths were determined from gradients of pore water constituents along a transect that encompassed the gas hydrate-bearing cold seep and adjacent regions.

4. **"Fossil" methane carbon constitutes a significant fraction of the total organic carbon (TOC), dissolved inorganic carbon (DIC), and authigenic carbonate sediment carbon pools in gas hydrate-bearing sediments.** Radiocarbon based mass balance models were utilized to quantify the fraction of methane carbon present in carbon pools. Endmembers in the model were "fossil" methane and water-column derived particulate organic carbon (POC). The radiocarbon content of methane was measured directly, while buried pelagic foraminifera represented the POC endmember at the equivalent core depth. It was originally assumed that buried pelagic foraminifera were unaffected by fossil methane contributions, and, therefore, would be a suitable proxy for the radiocarbon content of the water-column derived carbon. The model outputs were compared to the concentration gradients and $\delta^{13}C$ signatures of pore water constituents to determine if the contributions of methane carbon were higher where the pore water chemistry indicated AOM was active. Complications related to incorrect assumptions in the stated hypothesis are discussed in the text.

5. **Sulfate-reducing bacterial (SRB) fatty acid composition, concentration and $\delta^{13}C$ will be related to the predominant source (i.e., microbial vs. thermogenic) and flux of the methane.** Fatty acids from Barkley Canyon (thermogenic source) were compared to those from Bullseye Vent (microbial

10

source). Variations in the composition and $\delta^{13}C$ signatures of the SRB fatty acids related to the different gas sources and fluxes were expected. The Bullseye Vent SRB fatty acids were predicted to be similar to those from Hydrate Ridge, where monounsaturated and cyclopropane fatty acids are most abundant and most highly ^{13}C-depleted (Elvert et al. 2003). Conversely, Barkley Canyon fatty acids were expected to be comprised of a greater relative abundance of ^{13}C-depleted methyl-branched fatty acids; as was observed in the northern Gulf of Mexico (Zhang et al. 2002). Concentrations and $\delta^{13}C$ of SRB fatty acids will be greatest and most ^{13}C-depleted, respectively, at the SMI. Sites with greater methane fluxes will have higher concentrations of ^{13}C-depleted SRB fatty acids.

The following chapters address the hypotheses listed above. To date, this is the most detailed biogeochemical study of cold seeps in the northern Cascadia margin accretionary system. Data acquired from sediment, pore water and gas samples collected from the near-surface sediments were used to interpret the complex processes that regulate the flux and control the cycling of methane carbon from gas hydrate-bearing cold seeps. Furthermore, because cold seeps are focal points for fluid and gas discharge from the larger continental slope and shelf system, the data are expected to provide evidence for processes occurring at greater depth, distance and time than the limited spatial and temporal sampling protocol might imply. These objectives will be accomplished through the integrated analysis of source indicators (carbon isotope signatures), temporal indicators (radiocarbon ages) and seismic profiles acquired from the study region.

References

Abdullaev, T.; Falt, L. M.; Akhundov, A.; van Graas, G. W.; Kvamme, T.; Flolo, L. H.; Mehmandarov, K.; Narimanov, A. A.; Olsen, T. S.; Seljeskog, G.; Skontorp, O.; Sultanzade, T.; Tank, N.; Valieva, E. A reservoir model for the main Pliocene reservoirs of the Bahar Field in the Caspian Sea, Azerbaijan. Petroleum Geoscience. 4: 259-270; 1998.

Aloisi, G.; Pierre, C.; Rouchy, J. M.; Faugeres, J. C. Isotopic evidence of methane-related diagenesis in the mud volcanic sediments of the Barbados Accretionary Prism. Continental Shelf Research. 22: 2355-2372; 2002.

Bauer, J. E.; Reimers, C. E.; Druffel, E. R. M.; Williams, P. M. Isotopic constraints on carbon exchange between deep ocean sediments and sea water. Nature. 373: 686-689; 1995.

Bauer, J. E.; Spies, R. B.; Vogel, J. S.; Nelson, D. E.; Southon, J. R. Radiocarbon evidence of fossil-carbon cycling in sediments of a nearshore hydrocarbon seep. Nature. 348: 230-232; 1990.

Beerling, D. J.; Lomas, M. R.; Grocke, D. R. On the nature of methane gas-hydrate dissociation during the Toarcian and Aptian oceanic anoxic events. American Journal of Science. 302: 28-49; 2002.

Boetius, A.; Ravenschlag, K.; Schubert, C. J.; Rickert, D.; Widdel, F.; Gieseke, A.; Amann, R.; Jorgensen, B. B.; Witte, U.; Pfannkuche, O. A marine microbial consortium apparently mediating anaerobic oxidation of methane. Nature. 407: 623-626; 2000.

Borowski, W. S.; Hoehler, T. M.; Alperin, M. J.; Rodriguez, N. M.; Paull, C. K. Significance of anaerobic methane oxidation in methane-rich sediments overlying the Blake Ridge gas hydrates. In: Paull, C. K.; Matsumoto, R.; Wallace, P. J.; Dillon, W. P., ed. Proceeding of the Ocean Drilling Program, Scientific Results: Ocean Drilling Program. 87-99; 2000.

Borowski, W. S.; Paull, C. K.; Ussler, W. Carbon cycling within the upper methanogenic zone of continental rise sediments: An example from the methane-rich sediments overlying the Blake Ridge gas hydrate deposits. Mar. Chem. 57: 299-311; 1997.

Bustin, R. M. Organic maturation and petroleum source-rock potential of Tofino Basin, Southwestern British-Columbia. Bulletin of Canadian Petroleum Geology. 43: 177-186; 1995.

Chapman, N. R.; Pohlman, J. W.; Coffin, R. B.; Chanton, J. P.; Lapham L. Thermogenic gas hydrates in the northern Cascadia Margin. EOS. 85: 361-365; 2004.

Cicerone, R. J.; Oremland, R. S. Biochemical aspects of atmospheric methane. Glob. Biogeochem. Cycle. 2: 299-327; 1988.

Crutzen, P. J.; Lelieveld, J. Human impacts on atmospheric chemistry. Annual Review of Earth and Planetary Sciences. 29: 17-45; 2001.

Davis, E. E.; Hyndman, R. D. Accretion and recent deformation of sediments along the northern Cascadia subduction zone. Geol. Soc. Am. Bull. 101: 1465-1480; 1989.

Dickens, G. R.; O'Neil, J. R.; Rea, D. K.; Owen, R. M. Dissociation of oceanic methane hydrate as a cause of the carbon-isotope excursion at the end of the Paleocene. Paleoceanography. 10: 965-971; 1995.

Dickens, G. R.; Paull, C. K.; Wallace, P. Direct measurement of in situ methane quantities in a large gas-hydrate reservoir. Nature. 385: 426-428; 1997.

Dickens, G. R.; Wallace, P. J.; Paull, C. K.; Borowski, W. S. Detection of methane gas hydrate in the pressure core sampler (PCS): volume-pressure-time relations during controlled degassing experiments. In: Paull, C. K.; Matsumoto, R.; Wallace, P. J.; Dillon, W. P., ed. Proceedings of the Ocean Drilling Program, Scientific Results: Ocean Drilling Program. 113-126; 2000.

Elvert, M.; Suess, E.; Whiticar, M. J. Anaerobic methane oxidation associated with marine gas hydrates: Superlight C-isotopes from saturated and unsaturated C-20 and C-25 irregular isoprenoids. Naturwissenschaften. 86: 295-300; 1999.

Gorman, A. R.; Holbrook, W. S.; Hornbach, M. J.; Hackwith, K. L.; Lizarralde, D.; Pecher, I. Migration of methane gas through the hydrate stability zone in a low-flux hydrate province. Geology. 30: 327-330; 2002.

Hinrichs, K. U.; Summons, R. E.; Orphan, V.; Sylva, S. P.; Hayes, J. M. Molecular and isotopic analysis of anaerobic methane-oxidizing communities in marine sediments. Org. Geochem. 31: 1685-1701; 2000.

Huchon, P.; Tokuyama, H. Japan-france KAIKO-TOKAI project - Tectonics of subduction in the Nankai trough - Preface. Marine Geology. 187: 1-2; 2002.

Hyndman, R. D.; Davis, E. E. A mechanism for the formation of methane hydrate and sea-floor bottom-simulating reflectors by vertical fluid expulsion. J. Geophys. Res. -Solid Earth. 97: 7025-7041; 1992.

Hyndman, R. D.; Spence, G. D. A seismic study of methane hydrate marine bottom simulating reflectors. J. Geophys. Res. -Solid Earth. 97: 6683-6698; 1992.

Joye, S. B.; Boetius, A.; Orcutt, B. N.; Montoya, J. P.; Schulz, H. N.; Erickson, M. J.; Lugo, S. K. The anaerobic oxidation of methane and sulfate reduction in sediments from Gulf of Mexico cold seeps. Chem. Geol. 205: 219-238; 2004.

Kastner, M. Gas hydrates in convergent margins: Formation, occurrence, geochemistry and global significance. Geophysical Monograph. 67-86; 2001.

Kennett, J. P.; Cannariato, K. G.; Hendy, I. L.; Behl, R. J. Carbon isotopic evidence for methane hydrate instability during quaternary interstadials. Science; 288: 128-133; 2000.

Kennett, J. P.; Cannariato, K. G.; Hendy, I. L.; Behl, R. J. Methane Hydrates in Quaternary Climate Change. Washington D.C.: American Geophysical Union; 2002.

Kvenvolden, K. A. A review of the geochemistry of methane in natural gas hydrate. Org. Geochem. 23: 997-1008; 1995.

Kvenvolden, K. A. Potential effects of gas hydrate on human welfare. Proc. Natl. Acad. Sci. U. S. A. 96: 3420-3426; 1999.

Kvenvolden, K. A. Gas hydrate and humans. Annals of the New York Academy of Sciences. 912: 17-22; 2000.

MacDonald, I. R.; Buthman, D. B.; Sager, W. W.; Peccini, M. B.; Guinasso, N. L. Pulsed oil discharge from a mud volcano. Geology. 28: 907-910; 2000.

MacDonald, I. R.; Guinasso, N. L.; Sassen, R.; Brooks, J. M.; Lee, L.; Scott, K. T. Gas Hydrate That Breaches the Sea-Floor on the Continental-Slope of the Gulf-Of-Mexico. Geology. 22: 699-702; 1994.

Max, M. D.; Dillon, W. P.; Nishimura, C.; Hurdle, B. G. Sea-floor methane blow-out and global firestorm at the K-T boundary. Geo-Marine Letters. 18: 285-291; 1999.

Mienert, J.; Posewang, J.; Baumann, M. Gas hydrates along the northeastern Atlantic margin: possible hydrate-bound margin instabilities and possible release of methane. Geological Society of London. 275-292; 1998.

Milkov, A. V. Worldwide distribution of submarine mud volcanoes and associated gas hydrates. Mar. Geol. 167: 29-42; 2000.

Milkov, A. V. Global estimates of hydrate-bound gas in marine sediments: How much is really out there? Earth-Science Reviews. 66: 183-197; 2004.

Milkov, A. V.; Sassen, R. Estimate of gas hydrate resource, northwestern Gulf of Mexico continental slope. Marine Geology. 179: 71-83; 2001.

Milkov, A. V.; Sassen, R. Economic geology of offshore gas hydrate accumulations and provinces. Marine and Petroleum Geology. 19: 1-11; 2002.

Milkov, A. V.; Sassen, R. Preliminary assessment of resources and economic potential of individual gas hydrate accumulations in the Gulf of Mexico continental slope. Marine and Petroleum Geology. 20: 111-128; 2003.

Milkov, A. V.; Claypool, G. E.; Lee, Y. J.; Xu, W. Y.; Dickens, G. R.; Borowski, W. S. In situ methane concentrations, at Hydrate Ridge, offshore Oregon: New constraints on the global gas hydrate inventory from an active margin. Geology. 31: 833-836; 2003a.

Milkov, A. V.; Sassen, R.; Apanasovich, T. V.; Dadashev, F. G. Global gas flux from mud volcanoes: A significant source of fossil methane in the atmosphere and the ocean. Geophysical Research Letters. 30: 1037; 2003b.

Orphan, V. J.; House, C. H.; Hinrichs, K. U.; McKeegan, K. D.; Delong, E. F. Methane-consuming archaea revealed by directly coupled isotopic and phylogenetic analysis. Science. 293: 484-487; 2001.

Paull, C. K.; Ussler, W.; Dillon, W. P. Is the extent of glaciation limited by marine gas-hydrates. Geophysical Research Letters. 18: 432-434; 1991.

Paull, C. K.; Ussler, W.; Dillon, W. P. Potential role of gas hydrate decomposition in generating slope failures. In: Max, M. D., ed. Natural Gas Hydrate in Oceanic and Permafrost Environments: Klewar Academic Publishers. 149-156; 2000.

Reeburgh, W. S. "Soft spots" in the global methane budget. In: Lidstrom, M. E.; Tabita, F. R., ed. Microbial Growth on C_1 Compounds: Kluwer Academic Publishers. 334-342; 1996.

Riddihough, R. Recent movements of the Juan-De-Fuca Plate system. Journal of Geophysical Research. 89: 6980-6994; 1984.

Riedel, M.; Spence, G. D.; Chapman, N. R.; Hyndman, R. D. Seismic investigations of a vent field associated with gas hydrates, offshore Vancouver Island. Journal of Geophysical Research-Solid Earth. 107: doi:10.1029/2001JB000269; 2002.

Spence, G. D.; Hyndman, R. D.; Chapman, N. R.; Walia, R.; Gettrust, J.; Edwards, R. N. North Cascadia deep sea gas hydrates. Ann. NY Acad. Sci. 912: 65-75; 2000.

Spence, G. D.; Chapman, N. R. Fishing trawler nets massive "catch" of methane hydrates. EOS. 82: 621-627; 2001.

Suess, E.; Torres, M. E.; Bohrmann, G.; Collier, R. W.; Greinert, J.; Linke, P.; Rehder, G.; Trehu, A.; Wallmann, K.; Winckler, G.; Zuleger, E. Gas hydrate destabilization: enhanced dewatering, benthic material turnover and large methane plumes at the Cascadia convergent margin. Earth and Planetary Science Letters. 170: 1-15; 1999.

Tryon, M. D.; Brown, K. M.; Torres, M. E.; Trehu, A. M.; McManus, J.; Collier, R. W. Measurements of transience and downward fluid flow near episodic methane gas vents, Hydrate Ridge, Cascadia. Geology. 27: 1075-1078; 1999.

Tsunogai, U.; Yoshida, N.; Ishibashi, J.; Gamo, T. Carbon isotopic distribution of methane in deep-sea hydrothermal plume, Myojin Knoll Caldera, Izu-Bonin arc: Implications for microbial methane oxidation in the oceans and applications to heat flux estimation. Geochimica et Cosmochimica Acta. 64: 2439-2452; 2000.

Tsunogai, U.; Yoshida, N.; Gamo, T. Carbon isotopic evidence of methane oxidation through sulfate reduction in sediment beneath cold seep vents on the seafloor at Nankai Trough. Marine Geology. 187: 145-160; 2002.

Valentine, D. L.; Blanton, D. C.; Reeburgh, W. S.; Kastner, M. Water column methane oxidation adjacent to an area of active hydrate dissociation, Eel River Basin. Geochimica et Cosmochimica Acta. 65: 2633-2640; 2001.

Von Rad, U.; Berner, U.; Delisle, G.; Doose-Rolinski, H.; Fechner, N.; Linke, P.; Luckge, A.; Roeser, H. A.; Schmaljohann, R.; Wiedicke, M. Gas and fluid venting at the Makran accretionary wedge off Pakistan. Geo-Marine Letters. 20: 10-19; 2000.

Whiticar, M. J. Carbon and hydrogen isotope systematics of bacterial formation and oxidation of methane. Chem. Geol. 161: 291-314; 1999.

Zhang, C. L. L.; Li, Y. L.; Wall, J. D.; Larsen, L.; Sassen, R.; Huang, Y. S.; Wang, Y.; Peacock, A.; White, D. C.; Horita, J.; Cole, D. R. Lipid and carbon isotopic evidence of methane-oxidizing and sulfate-reducing bacteria in association with gas hydrates from the Gulf of Mexico. Geology. 30: 239-242; 2002.
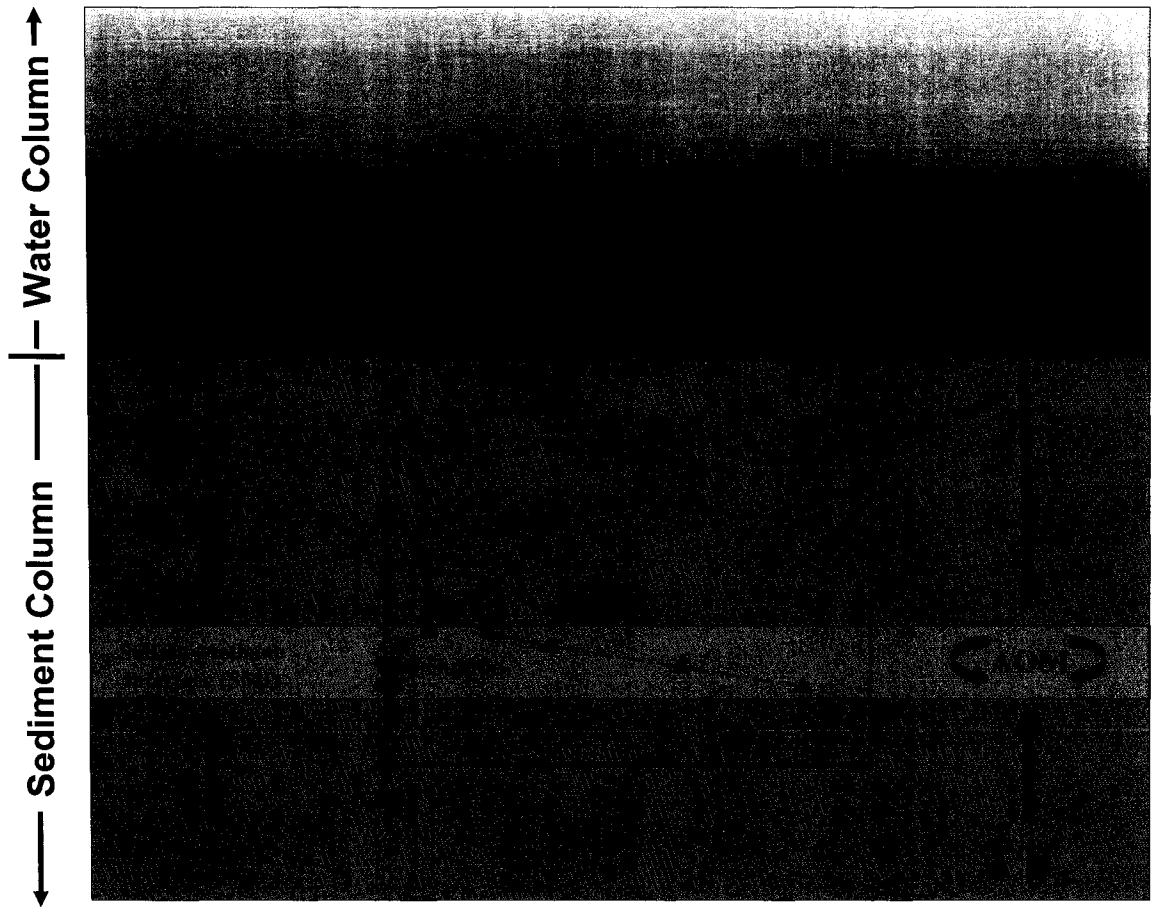
Figure 1. Schematic diagram showing sulfate (red squares), methane (blue triangles) and sulfide (dark yellow shaded area) pore water profiles resulting from anaerobic oxidation of methane (AOM; Eq. 1). Seawater sulfate (~29 mM) diffuses downward and methane migrates upward to the sulfate methane interface (SMI). The SMI is a reactive sedimentary zone where sulfate and methane are cometabolized to sulfide and HCO_3^- (latter not shown) by the AOM consortium.
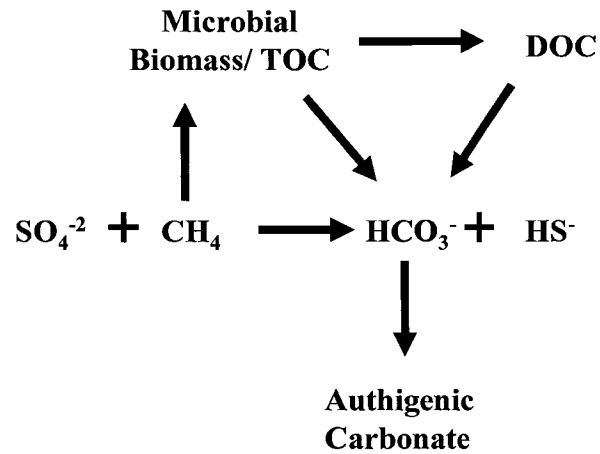
Figure 2. Simple conceptual model for the biogeochemical cycling of carbon in an AOM dominated sediment system. Methane oxidized by anaerobic oxidation of methane (AOM) is mineralized to HCO_3^- (i.e., dissolved inorganic carbon, DIC) where it may remain as part of the DIC pool or precipitate as authigenic carbonate. Some methane is converted to microbial biomass, where it resides as a component of the total organic carbon (TOC) pool matrix. Additional diagenetic processing of the biomass may transfer the methane carbon to the DOC or DIC pools.
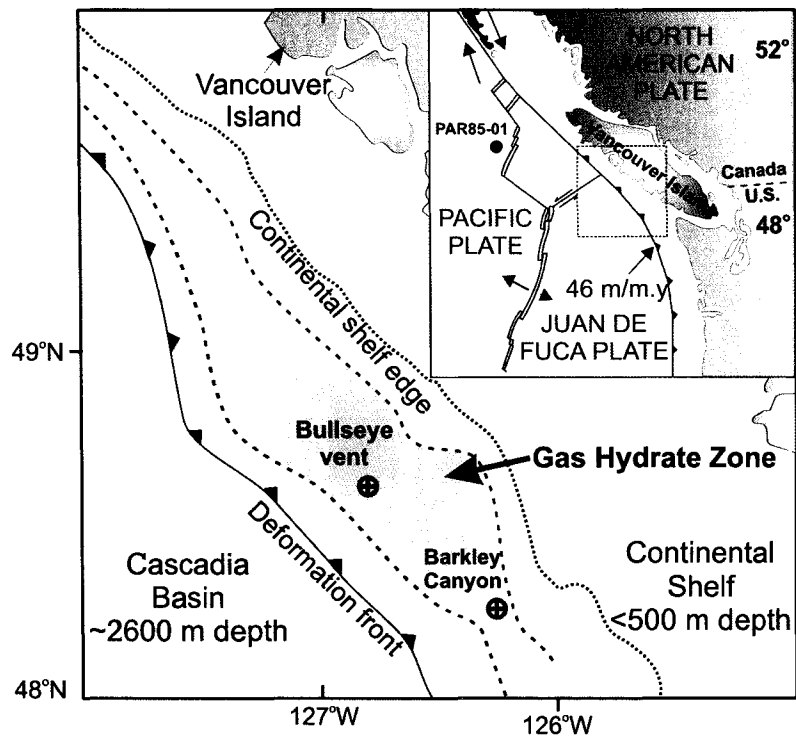
Figure 3. Geographic setting of the northern Cascadia margin. The Bullseye vent and Barkley Canyon sites investigated in this study are located within a 20-30 km wide band of gas hydrate between 50 and 250 meters below the seafloor of the continental slope offshore Vancouver Island, Canada. The existence of gas hydrate (shaded area) is inferred from a bottom simulating reflector (BSR) that covers ~50% of the mid-continental slope (Spence et al., 2000).

CHAPTER 2

EVIDENCE FOR FOSSIL MARINE GAS HYDRATE METHANE: IMPLICATIONS
AND SIGNIFICANCE FOR OCEANIC AND GLOBAL CARBON RESERVOIRS

This chapter follows the format of Geophysical Research Letters

Abstract. Fossil methane from the large and dynamic global marine gas hydrate reservoir has the potential to influence the quantities and isotopic compositions of oceanic and atmospheric carbon pools. However, a fossil signature (i.e., devoid of radiocarbon) for gas hydrate bound methane has not been adequately demonstrated for a representative set of gas hydrate systems. In this study, the radiocarbon (^{14}C) composition of 15 hydrate-bound gas samples and 8 core gas samples recovered from the seafloor or shallow sediment depths (<5 mbsf) from 6 distinct continental margin locations was measured. The systems investigated represent about one-third of the oceanic regions where gas hydrate supported by high gas flux (HGF) regimes have been collected, and thus provide a reasonable global characterization of methane from gas hydrate systems. Radiocarbon composition of the methane indicated that gas hydrate and core gas samples were derived from 99.5% (n=15) and 99% (n=8) fossil sources, respectively. These results suggest methane associated with gas hydrate systems is almost entirely fossil and validates previous atmospheric budget calculations that have assumed a fossil methane source from gas hydrate and seafloor seeps.

1.   Introduction

Natural gas hydrate is recognized as a significant component of the global organic carbon inventory (Kvenvolden, 1999; Milkov, 2004) and global carbon cycle (Dickens, 2003a). A recent estimate of the global gas hydrate inventory ranges from 250-2,500 Gt C ($\sim$1-5 x 10^{15} m^3 at STP) (Milkov, 2004). Although this estimate is a downward revision of the traditionally held "consensus" value of 10,000 Gt C ($\sim$21 x 10^{15} m^3) (Kvenvolden, 1999), it still represents between 5 and 22% of the total organic carbon on Earth, excluding dispersed kerogen and bitumen (Milkov, 2004). In addition, episodic release of gas hydrate-bound methane from sediments has been reported to be associated with rapid global warming events in Earth's history (e.g., Dickens et al., 1995; Hesselbo et al., 2000; Kennett et al., 2002), although recent studies from ice core records suggest the gas hydrate reservoir was relatively stable during warming events of the Late Quaternary (Sowers, 2006, Schaefer et al., 2006).

Methane is routinely classified according to its generation processes. For example, microbial methane is produced by low temperature (<60 °C) diagenetic alterations of organic matter and has $\delta^{13}C$ values typically in the range of -60 to -90‰ (Whiticar, 1999), although certain environmental conditions may lead to values as high as -41‰ (Claypool et al., 1985) and as low as -110‰ (Whiticar et al., 1986). In contrast, thermogenic gases generated by high-temperature (70 to 200 °C) thermal cracking of deeply buried kerogen are characterized by methane with $\delta^{13}C$ values in the range of -20‰ to -50‰ and may contain significant concentrations (> 1%) of higher hydrocarbons depending upon the thermal maturity of the source rock (Claypool and Kaplan, 1974). The known $\delta^{13}C$ range of methane recovered from marine sedimentary gas hydrate is

however more constrained, with reported values from all known sources (microbial and thermogenic) ranging between -42.2‰ to -74.7‰ (Milkov, 2005). The relative thermogenic contribution to a gas sample is frequently indicated by the "Bernard parameter", $C_1/(C_2 + C_3)$ (Bernard et al., 1978). In the absence of significant methane oxidation effects, values less than 50 are typically associated with a thermogenic contribution (Whiticar, 1999). Thus, in most circumstances, the $\delta^{13}C$ of methane and the hydrocarbon composition of the gas are sufficient for discerning the origin of marine gas hydrate (Milkov, 2005).

Differentiating thermogenic and microbial gas in gas hydrate systems on the basis of the methane radiocarbon signature is not as straightforward. Thermogenic methane generated from deeply buried kerogen is unequivocally fossil (i.e., devoid of ^{14}C). Conversely, microbial methane was assumed to be completely modern (^{14}C age near zero) until Cicerone and Oremland (1988) differentiated "old biogenic methane" from "modern biogenic methane". That is, the ^{14}C content of the methane is dictated by the age of the organic matter supporting methane production. Only methane produced from organic matter < 50 kyrs in age will contain measurable amounts of ^{14}C. With a continuous sedimentation rate of 20 cm ka^{-1}, which is representative of continental margins during the Late Pleistocene (G. Spence, pers. comm.), organic carbon would be fossil below depths > ~10 meters below the seafloor (mbsf). Local and regional variations in sediment deposition rates will alter the depth where organic carbon is completely fossil, but the effect of such variations on the average radiocarbon age of methane in the sediment column would be minor considering the methanogenic zone extends to about 1000 mbsf (Clayton, 1992). Recent studies have widely accepted the

concept that modern organic matter is only available to methanogens over a relatively shallow interval of surface sediments (Lelieveld et al., 1998; Milkov et al., 2003; Judd, 2004; Etiope, 2004; Kvenvolden and Rogers, 2005) and have assumed that the radiocarbon signature of the entire gas hydrate methane reservoir and associated seepage is fossil in systems where gas hydrate occurs. Although the conceptual framework for this assumption is sound, the only supporting data for it is a single report of fossil hydrate-bound methane from Hydrate Ridge, offshore of Oregon (Winckler et al., 2002). A more comprehensive study constraining the radiocarbon signatures of the marine methane reservoir from multiple locations is lacking (Reeburgh, 2004).

This study provides the first extensive dataset of shallow seafloor hydrate-bound and hydrate-associated sedimentary methane radiocarbon data and addresses the hypothesis that the global reservoir of methane carbon trapped in and associated with gas hydrate is fossil in origin (Cicerone and Oremland, 1988). The radiocarbon composition of fifteen gas hydrate-bound gas samples and eight core gas samples recovered from six distinct continental margin locations was measured (Table 1). The locations are all high gas flux (HGF) settings where gas migrating to the seafloor supports structural gas hydrate accumulations (Milkov, 2005). Among the samples we analyzed is the first gas hydrate recovered from the Chilean Margin. Results of this study conclusively establish the methane radiocarbon signature of near-seafloor accumulations of hydrate-bound and free gas and, thus, provide important evidence that may influence our understanding of how the dynamic gas hydrate reservoir affects carbon budgets in the atmosphere and ocean on different geological time scales.

2. Sampling and Methods

Gas hydrate and sediment core gas samples were collected during six expeditions that took place between June 2000 and October 2004. The gas hydrate samples were collected by piston coring from depths less than ~5 mbsf from the research vessels *CCGS John P Tully* (northern Cascadia margin: NCM), *R/V Cape Hatteras* (Blake Ridge: BR) and *Vidal Gormaz* (central Chilean margin: CCM) or in pressure cylinders using the research submersibles *ROPOS* (NCM), *Johnson Sealink* (Gulf of Mexico: GoM) and *MIR-1* (Norwegian Sea: NS) (Table 1). Gas hydrate samples were either stored in liquid nitrogen and dissociated back in the home laboratory or immediately transferred to plastic syringes and dissociated shipboard. Sediment gas samples were obtained by puncturing gas expansion cracks in the core liner and withdrawing the gas with a plastic syringe. Samples collected from dissociated gas hydrate are referred to as "hydrate bound gas", and samples extracted from core liners are referred to as "core gas". The core gas represents gas that was dissolved in the *in situ* sediment pore waters, but came out of solution and was trapped in the core liner as the core was depressurized during recovery. The gas hydrate and sediment gas samples were transferred into 50 ml glass serum vials by displacing water from an inverted vial and sealing the vials with 1 cm thick butyl septa, which maintain an intact seal when frozen. The serum vials were frozen at -20 °C until analysis.

The hydrocarbon gas composition was determined with a Shimadzu 14-A gas chromatograph (GC). Gas samples were introduced into the GC through a manual gas-sampling valve. The hydrocarbons were separated on a Porapak-Q column (8', 1/8" OD) with a 270 kPa nitrogen carrier gas pressure. The initial oven temperature of 50 °C was

held for two minutes, during which time methane and ethane eluted. The temperature was then increased at a rate of 20 °C min^{-1} to a final temperature of 150 °C until the C$_3$ - C$_5$ compounds eluted. Compound peak areas were measured with a flame ionization detector (FID) and quantified relative to certified gas standards (Scott Gas, Plumbsteadville, PA).

Stable carbon isotope ratios (^{13}C/^{12}C) of methane were measured with a Finnigan Delta Plus XP isotope ratio mass spectrometer (IRMS) at the Naval Research Lab (NRL) or the University of Victoria (UVic). Methane was separated from the gas matrix with a GSQ PLOT column (30 m, 0.32 mm ID; initial temperature 30 °C, held isothermal for 2 minutes and ramped to 180 °C at 20 °C/min) in a Thermo Finnigan Trace GC (NRL) or a Varian 3400 GC (UVic). The methane was oxidized to CO$_2$ and interfaced to the IRMS through a Thermo Finnigan GCC-III unit. The ^{13}C/^{12}C ratios are reported in the standard δ-notation relative to VPDB with a precision of ± 0.2‰.

Gas samples for radiocarbon analysis were injected into an oxygen enriched He carrier stream and cryogenically separated from carbon dioxide and C$_{2+}$ hydrocarbons with a series of stainless steel loops immersed in dry-ice/ethanol and liquid nitrogen. Following separation, methane was oxidized on-line to CO$_2$ over 1/8" alumina (0.5%) pellets (Acros Organics) at 650°C, purified by cryogenic distillation and converted to graphite by iron catalyzed reduction with hydrogen (Vogel et al., 1987; Pohlman et al., 2000). The graphite was pressed into aluminum targets and analyzed with a 3 MV Pelletron tandem accelerator mass spectrometer (AMS) with an MC-SNICS ion source (Grabowski et al., 2000). Radiocarbon values are reported as percent modern carbon

(pmC) relative to the NIST oxalic acid II standard according to Stuiver and Polach (1977).

3.   Results and Discussion

3.1 Core and Hydrate Bound Gas Composition and $\delta^{13}CH_4$

Methane from hydrate bound and core gas samples from all locations accounted for 62.3 to 99.98% of the C_1-C_5 hydrocarbon composition (Table 2) and had $\delta^{13}C$ values that ranged from -42.9‰ to -79.3‰ (Table 3). Barkley Canyon and Green Canyon - sites associated with petroleum systems (Sassen et al., 2000; Pohlman et al., 2005) - contained methane with $\delta^{13}C$ values that ranged from -42.9‰ to -49.5‰ and ΣC_2-C_5 gases with a relative concentration range from 2.7 to 37.7% of the total hydrocarbon gas content. In contrast, the other locations (Bullseye vent, Concepción methane seep, Blake Ridge diapir and Haakon Mosby mud volcano) had distinctly lower $\delta^{13}C$ values (-61.4‰ to -79.3‰; Table 3) and lower concentrations of ΣC_2-C_5 gases (0.02 to 0.3%; Table 2). When the hydrocarbon composition is expressed as the "Bernard parameter", C1/[C2+C3] (Bernard et al., 1978), and plotted against the $\delta^{13}C$ of methane, the distinction between thermogenic and microbial gas sources for the sites is unequivocal.

Hydrate bound gases from Bullseye vent and Barkley Canyon contained a lower percentage of methane than the core gas samples collected from the same areas (Table 2). For example, Barkley Canyon hydrate bound gas contained 80.3 ± 6.9% (n=5) methane, while the core gas contained 97.2 ± 0.2% (n=2) methane (Table 2). The difference was not as extreme for the Bullseye vent samples - the hydrate bound gas contained 99.79 ± 0.12% (n=3) methane and the core gas contained 99.95 ± 0.02% (n=3) methane - but the

pattern of a lower percent composition of methane in the hydrate bound phase was similar. A lower percentage of methane in the hydrate phase is consistent with previous studies comparing the hydrocarbon and carbon isotope composition of gas hydrate bound and vent gas (Sassen et al., 2000; Pohlman et al., 2005) that suggested C_2-C_5 hydrocarbons are preferentially assimilated (i.e., molecular fractionation) during gas hydrate formation.

Studies suggesting that molecular fractionation occurs during gas hydrate formation also suggested isotopic fractionation does not occur (Sassen et al., 1999; Pohlman et al., 2005). However, the $\delta^{13}C$ values of methane from the hydrate bound phase were greater than those from the core gas samples from Bullseye vent and Barkley Canyon (Table 3). These differences may be attributed to the addition of a ^{13}C-depleted source in the core gas, oxidation of methane in the hydrate bound gas, or a combination of both. Sassen et al. (1999) suggested ^{13}C-enrichment of the hydrate bound methane by as much as 3.9‰ was due to oxidation of methane within the gas hydrate structure; although they did not provide a mechanism for how electron acceptors (e.g. O_2 or SO_4^{-2}) required for methane oxidation might penetrate the gas hydrate structure. The more extreme ~11‰ $\delta^{13}C$ difference between the core gas (-74.9‰ ± 6.3) and gas hydrate bound (-63.9 ± 0.7) methane from Bullseye vent suggests a contribution from a source more ^{13}C-depleted than the gas that supported gas hydrate formation. Temporal variations in the source of methane fluxing into the shallow cold seep system or production of microbial methane in the near surface are both potential explanations for the observation of distinct hydrate bound and core gas methane $\delta^{13}C$ signatures.

3.2 Methane Radiocarbon Signatures

Across all sites, the radiocarbon composition for the hydrate-bound and core gas methane ranged from 0.00 to 2.15 pmC (Table 3). Relative to modern atmospheric CO_2, which has a pmC of ~110 (Duffy et al., 1995), the pmC of the core gas and hydrate bound methane was almost entirely fossil. Core gas and hydrate bound gases were available for comparison only from the northern Cascadia margin (Barkley Canyon and Bullseye vent) and central Chilean margin (CCM) sites. The pmC from all the CCM samples (core and hydrate bound) were consistently low (0.06% ± 0.05) (Table 3). In contrast, the Barkley Canyon and Bullseye vent samples varied with respect to the site and sample type. The pmC from all the Bullseye vent samples (1.58 ± 0.53; n=6) was greater than that of Barkley Canyon samples (0.35 ± 0.39; n=12) (Table 3). Given that Bullseye vent is supported primarily by microbial methane (Fig. 1), the greater pmC for Bullseye vent may be explained as a microbial contribution from diagenesis of non-fossil organic matter in the near-surface sediments; a conclusion consistent with the stable carbon isotope data. Similarly, the pmC of every core gas methane sample was greater than every hydrate bound sample from the same sites (Table 3). The presence of ^{14}C-enriched methane in the core gas strongly supports the carbon isotope based conclusion that the variation between the core gas and hydrate bound gas is related to variations in contributions of microbial methane generated in the near-surface sediment; not oxidation of methane within the gas hydrate. If a ^{14}C fractionation effect related to oxidation of methane in gas hydrate had occurred, we should have found enrichment of ^{14}C in the gas hydrate phase; not a depletion, as was observed.

The predominance of fossil methane supports the hypothesis that contributions from cold seep systems to the atmosphere are a component of the 110 Tg fossil methane balance in the 600 Tg global atmospheric methane burden (Lelieveld et al., 1998). The estimated contribution of gas hydrate methane to the atmosphere ranges from 5-10 Tg yr^{-1} (Cicerone and Oremland, 1988; IPCC, 2001). Estimates of methane emissions from seafloor seeps range from 8 to 70 Tg C yr^{-1} (Hovland et al., 1993; Kvenvolden and Lorenson, 2001; Judd et al., 2002). Milkov et al. (2003) suggested that these values may actually be much greater because they do not adequately represent potential contributions from deep water mud volcanoes, where gas hydrate likely functions as a reservoir for gas migrating to the seafloor (Kvenvolden and Rogers, 2005). The significance of our finding (which includes non-hydrate methane) is, therefore, not limited to gas hydrate specifically, but may be more broadly applicable to deep water seep systems and mud volcanoes where gas hydrate occurs.

A conceptual model illustrates where fossil and/or modern carbon from microbial and thermogenic sources are generated and how they migrate toward the seafloor in a high gas flux setting (Fig. 2). Thermogenic methane is generated from fossil organic matter and migrates from depth to accumulate near the seafloor. Microbial methane is generated throughout the sediment column, but only methane synthesized from shallow ($\leq \sim 10$ mbsf) sediment with modern carbon will contain a modern signature. The age of the organic matter and the relative contribution from the non-fossil sources determine the age of the microbial methane.

3.3 Potential implications for oceanic carbon reservoirs

The sheer size (Kvenvolden, 1999; Mikov, 2005) and dynamic nature of the global gas hydrate reservoir (Dickens, 2003a) present the possibility that fossil methane carbon may also influence the radiocarbon age of carbon reservoirs in the oceans (Fig. 2). Kessler et al. (2005) identified methane in the water column of the Cariaco Basin as 98% fossil and attributed this input to discharge of an unidentified seep. Soloviev (2002) estimates that gas hydrate may underlie approximately 10% of the ocean surface area. Discharge of methane from gas hydrate systems (Dickens, 2003b) has the potential to support a considerable flux of methane across the sediment-water interface to the ocean water column where it may be consumed by methanotrophic bacteria in the water column (Fig. 2) (Reeburgh et al., 1993; Judd et al., 2002). Bacterial biomass in the water column of the northern Gulf of Mexico with $\delta^{13}C$ values as low as -33‰ (less than the algal and terrigenous sources) indicates oxidation of methane escaping from seafloor seeps or other chemoautotrophic processes may support the pelagic bacterial assemblage (Kelley et al., 1998).

The flux of methane-derived metabolic products across the sediment water interface is an additional pathway that can influence the radiocarbon composition of water column carbon pools (Fig. 2). The anaerobic oxidation of methane (AOM) converts methane to dissolved inorganic carbon (DIC) and water soluble metabolites (i.e., dissolved organic carbon (DOC) (Valentine and Reeburgh, 2000). About 30% of the DOC in bottom water above a Gulf of Mexico cold seep was determined to be derived from a fossil carbon source (Wang et al., 2001). The flux of DOC and DIC into the water

column has the potential to influence the radiocarbon age of the water column DIC and

DOC (Bauer et al., 1995); though to an unknown extent.

4. Conclusions

The radiocarbon (^{14}C) content of methane from gas hydrate and gas hydrate

associated sediments from six sites representing all of the major high gas flux seepage

regimes and gas sources for worldwide gas hydrate occurrences that have been thus far

studied was found to be between 97.9% and 100% fossil. The data support a widely

accepted, but previously largely unsupported, assumption that contributions of gas

hydrate methane to the atmosphere are fossil. Definitive recognition of the enormous,

dynamic and reactive gas hydrate reservoir as fossil constrains our understanding of how

methane from gas hydrate systems influences the radiocarbon ages of other ocean carbon

reservoirs (i.e., DOC and DIC). Future studies focusing on the influence of fossil carbon

in targeted pools (e.g., pore water and bottom water DOC) are required to constrain these

potential contributions.

References

Bauer, J. E.; Reimers, C. E.; Druffel, E. R. M.; Williams, P. M. Isotopic constraints on carbon exchange between deep ocean sediments and sea water. Nature. 373: 686-689; 1995.

Bernard, B. B.; Brooks, J. M.; Sackett, W. M. Light-hydrocarbons in recent Texas continental-shelf and slope sediments. Journal of Geophysical Research-Oceans and Atmospheres. 83: 4053-4061; 1978.

Cicerone, R. J.; Oremland, R. S. Biochemical aspects of atmospheric methane. Glob. Biogeochem. Cycle. 2: 299-327; 1988.

Claypool, G. E.; Kaplan, I. R. The origin and distribution of methane in marine sediments. In: Kaplan, I. R., ed. Natural Gases in Marine Sediments: Plenum Press. 99-139; 1974.

Claypool, G. E.; Threlkeld, C. N.; Mankiewicz, P. N.; Arthur, M. A.; Anderson, T. F. Isotopic composition of interstitial fluids and origin of methane in slope sediment of the Middle America Trench, Deep-Sea Drilling Project Leg-84. Initial Reports of the Deep Sea Drilling Project. 84: 683-691; 1985.

Clayton, C. Source volumetric of biogenic gas generation. In: Vially, R., ed. Bacterial Gas: Editions Technip. 191-204; 1992.

Dickens, G. R. Rethinking the global carbon cycle with a large, dynamic and microbially mediated gas hydrate capacitor. Earth and Planetary Science Letters. 213: 169-183; 2003a.

Dickens, G. R. A methane trigger for rapid warming? Science. 299: 1017-1017; 2003b.

Dickens, G. R.; O'Neil, J. R.; Rea, D. K.; Owen, R. M. Dissociation of oceanic methane hydrate as a cause of the carbon-isotope excursion at the end of the Paleocene. Paleoceanography. 10: 965-971; 1995.

Duffy, P. B.; Eliason, D. E.; Bourgeois, A. J.; Covey, C. C. Simulation of bomb radiocarbon in 2 global ocean general-circulation models. Journal of Geophysical Research-Oceans. 100: 22545-22563; 1995.

Etiope, G. New directions: GEM - Geologic emissions of methane, the missing source in the atmospheric methane budget. Atmospheric Environment. 38: 3099-3100; 2004.

Grabowski, K. S.; Knies, D. L.; DeTurck, T. M.; Treacy, D. J.; Pohlman, J. W.; Coffin, R. B.; Hubler, G. K. A report on the Naval Research Laboratory AMS facility. Nucl. Instrum. Methods Phys. Res. Sect. B-Beam Interact. Mater. Atoms. 172: 34-39; 2000.

Hesselbo, S. P.; Grocke, D. R.; Jenkyns, H. C.; Bjerrum, C. J.; Farrimond, P.; Bell, H. S. M.; Green, O. R. Massive dissociation of gas hydrate during a Jurassic oceanic anoxic event. Nature. 406: 392-395; 2000.

Hovland, M.; Judd, A. G.; Burke, R. A. The global flux of methane from shallow submarine sediments. Chemosphere. 26: 559-578; 1993.

IPCC (Intergovernmental Panel on Climate Change) Climate Change 2001 - The Scientific Basis. Cambridge, UK: Cambridge University Press; 2001.

Judd, A. G. Natural seabed gas seeps as sources of atmospheric methane. Environmental Geology. 46: 988-996; 2004.

Judd, A. G.; Hovland, M.; Dimitrov, L. I.; Gil, S. G.; Jukes, V. The geological methane budget at continental margins and its influence on climate change. Geofluids. 2: 109-126; 2002.

Kelley, C. A.; Coffin, R. B.; Cifuentes, L. A. Stable isotope evidence for alternative bacterial carbon sources in the Gulf of Mexico. Limnology and Oceanography. 43: 1962-1969; 1998.

Kennett, J. P.; Cannariato, K. G.; Hendy, I. L.; Behl, R. J. Methane Hydrates in Quaternary Climate Change. Washington D.C.: American Geophysical Union; 2002.

Kessler, J. D.; Reeburgh, W. S.; Southon, J.; Varela, R. Fossil methane source dominates Cariaco Basin water column methane geochemistry. Geophysical Research Letters. 32: L12609; 2005.

Kvenvolden, K. A. Potential effects of gas hydrate on human welfare. Proc. Natl. Acad. Sci. U. S. A. 96: 3420-3426; 1999.

Kvenvolden, K. A.; Lorenson, T. D. The global occurrence of natural gas hydrate. In: Paull, C. K.; Dillon, W. P., ed. Natural Gas Hydrates: Occurrence, Distribution and Detection: American Geophysical Union. 3-18; 2001.

Kvenvolden, K. A.; Rogers, B. W. Gaia's breath - global methane exhalations. Marine and Petroleum Geology. 22: 579-590; 2005.

Lelieveld, J.; Crutzen, P. J.; Dentener, F. J. Changing concentration, lifetime and climate forcing of atmospheric methane. Tellus Series B-Chemical and Physical Meteorology. 50: 128-150; 1998.

Milkov, A. V. Global estimates of hydrate-bound gas in marine sediments: how much is really out there? Earth-Science Reviews. 66: 183-197; 2004.

Milkov, A. V. Molecular and stable isotope compositions of natural gas hydrates: A revised global dataset and basic interpretations in the context of geological settings. Org. Geochem. 36: 681-702; 2005.

Milkov, A. V.; Sassen, R.; Apanasovich, T. V.; Dadashev, F. G. Global gas flux from mud volcanoes: A significant source of fossil methane in the atmosphere and the ocean. Geophysical Research Letters. 30: 1037; 2003.

Pohlman, J. W.; Canuel, E. A.; Chapman, N. R.; Spence, G. D.; Whiticar, M. J.; Coffin, R. B. The origin of thermogenic gas hydrates on the northern Cascadia Margin as inferred from isotopic ($^{13}C/^{12}C$ and D/H) and molecular composition of hydrate and vent gas. Org. Geochem. 36: 703-716; 2005.

Pohlman, J. W.; Knies, D. L.; Grabowski, K. S.; DeTurck, T. M.; Treacy, D. J.; Coffin, R. B. Sample distillation/graphitization system for carbon pool analysis by accelerator mass spectrometry (AMS). Nucl. Instrum. Methods Phys. Res. Sect. B-Beam Interact. Mater. Atoms. 172: 428-433; 2000.

Reeburgh, W. S. Global methane biogeochemistry. In: Keeling, R, ed. The Atmosphere: Elsevier. 65-89; 2004.

Reeburgh, W. S.; Whalen, K. A.; Alperin, M. J. The role of methylotrophy in the global methane budget. In: Murrell, J. C.; Kelley, D. P., ed. Microbial Growth on C-1 Compounds: Interceprt Ltd. 1-14; 1993.

Sassen, R.; Joye, S.; Sweet, S. T.; DeFreitas, D. A.; Milkov, A. V.; MacDonald, I. R. Thermogenic gas hydrates and hydrocarbon gases in complex chemosynthetic communities, Gulf of Mexico continental slope. Org. Geochem. 30: 485-497; 1999.

Sassen, R.; Sweet, S. T.; DeFreitas, D. A.; Milkov, A. V. Exclusion of 2-methylbutane (isopentane) during crystallization of structure II gas hydrate in sea-floor sediment, Gulf of Mexico. Org. Geochem. 31: 1257-1262; 2000.

Schaefer, H.; Whiticar, M. J.; Brook, E. J.; Petrenko, V. V.; Ferretti, D. F.; Severinghaus, J. P. Ice record of delta C-13 for atmospheric CH_4 across the Younger Dryas-Preboreal transition. Science. 313: 1109-1112; 2006.

Soloviev, V. A. Global estimation of gas content in submarine gas hydrate accumulations. Russian Geol. & Geophys. 43: 648-661; 2002.

Sowers, T. Late quaternary atmospheric CH_4 isotope record suggests marine clathrates are stable. Science. 311: 838-840; 2006.

Stuiver, M.; Polach, H. A. Discussion: Reporting ^{14}C data. Radiocarbon. 19: 355-363; 1977.

Valentine, D. L.; Reeburgh, W. S. New perspectives on anaerobic methane oxidation. Environmental Microbiology. 2: 477-484; 2000.

Vogel, J. S.; Southon, J. R.; Nelson, D. E. Catalyst and binder effects in the use of filamentous graphite for ams. Nucl. Instrum. Methods Phys. Res. Sect. B-Beam Interact. Mater. Atoms. 29: 50-56; 1987.

Wang, X. C.; Chen, R. F.; Whelan, J.; Eglinton, L. Contribution of "old" carbon from natural marine hydrocarbon seeps to sedimentary and dissolved organic carbon pools in the Gulf of Mexico. Geophysical Research Letters. 28: 3313-3316; 2001.

Whiticar, M. J. Carbon and hydrogen isotope systematics of bacterial formation and oxidation of methane. Chem. Geol. 161: 291-314; 1999.

Whiticar, M. J.; Faber, E.; Schoell, M. Biogenic methane formation in marine and fresh-water environments – CO_2 reduction vs acetate fermentation isotope evidence. Geochimica et Cosmochimica Acta. 50: 693-709; 1986.

Winckler, G.; Aeschbach-Hertig, W.; Holocher, J.; Kipfer, R.; Levin, I.; Poss, C.; Rehder, G.; Suess, E.; Schlosser, P. Noble gases and radiocarbon in natural gas hydrates. Geophysical Research Letters. 29: 1423; 2002.

Table 1. Gas hydrate sample Locations

Region	Location	Geologic Setting	Site	Latitude	Longitude	Water Depth
North Pacific Ocean	Northern Cascadia Margin (NCM)	Accretionary Prism	Bullseye Vent	N 48° 40.07	W 126° 50.00	1282
		Slope Canyon	Barkley Canyon	N 48° 18.66	W 126° 04.00	857
Southeast Pacific Ocean	Central Chilean Margin (CCM)	Slope Basin	Concepción Methane Seep	S 36° 21.87	W 73° 43.26	850
Northern Gulf of Mexico	Green Canyon (GC)	Fault Related	GC 185 (Bush Hill)	N 27° 46.96	W 91° 30.46	590
		Mud Volcano	GC 234	N 27° 44.76	W 91° 13.32	590
Mid-Atlantic Bight	Blake Ridge (BR)	Passive Margin Contourite	Blake Ridge Diapir	N 32° 29.63	W 76° 11.52	2177
North Atlantic Ocean	Norwegian Sea (NS)	Mud Volcano	Haakon Mosby Mud Volcano	N 72° 00.07	E 14° 43.27	1261

Table 2. Hydrocarbon (C_1-C_5) composition (v/v) of gas hydrate and core gas

Location	Source	Sample ID	C_1	C_2	C_3	i-C_4	n-C_4	[a]neo-C_5	i-C_5	n-C_5
Bullseye Vent, Northern Cascadia Margin (NCM)										
	Gas Hydrate	PGC02-08:Hyd01	99.79	0.21	b.d.	b.d.	b.d.	b.d.	b.d.	b.d.
		PGC00-03:Hyd01	99.90	0.13	<0.01	b.d.	b.d.	b.d.	b.d.	b.d.
		PGC02-08:Hyd02	99.67	0.24	0.04	0.02	0.03	b.d.	b.d.	b.d.
		Average	99.79	0.19	0.01	<0.01	0.01	-	-	-
	Core Gas	PGC02-08:CG02	99.98	0.01	<0.01	b.d.	b.d.	b.d.	b.d.	b.d.
		PGC02-08:CG03	99.94	0.06	<0.01	b.d.	b.d.	b.d.	b.d.	b.d.
		PGC02-08:CG06	99.94	0.06	<0.01	b.d.	b.d.	b.d.	b.d.	b.d.
		Average	99.95	0.04	<0.01	-	-	-	-	-
Barkley Canyon, Northern Cascadia Margin (NCM)										
	Gas Hydrate	PGC02-08:Hyd03	81.9	7.8	5.9	2.0	1.8	0.02	0.30	0.13
		R694:Hyd01	85.1	7.7	3.3	1.1	1.7	0.01	0.46	0.20
		R694:YellowHyd	81.9	10.4	3.8	1.2	2.0	0.02	0.30	0.18
		R694:WhiteHyd	84.3	9.1	3.3	1.0	1.7	0.01	0.35	0.19
		R695:Hyd02	68.1	10.8	12.5	4.2	2.2	0.03	0.95	0.53
		Average	80.3	9.2	5.7	1.9	1.9	0.02	0.47	0.25
	Core Gas	PGC02-08:CG01	97.32	1.63	0.60	0.31	0.14	<0.01	<0.01	<0.01
		PGC02-08:CG05	97.01	1.87	0.63	0.30	0.15	0.01	0.02	b.d.
		Average	97.2	1.75	0.62	0.31	0.15	<0.01	0.01	<0.01
Concepción Methane Seep, Central Chilean Margin (CCM)										
	Gas Hydrate	CHL1004-Hyd01	99.97	0.03	<0.01	b.d.	b.d.	b.d.	b.d.	b.d.
	Core Gas	CHL1004:CG04	99.98	0.02	<0.01	b.d.	b.d.	b.d.	b.d.	b.d.
		CHL1004:CG05	99.95	0.05	<0.01	b.d.	b.d.	b.d.	b.d.	b.d.
		CHL1004:CG06	99.96	0.04	b.d.	b.d.	b.d.	b.d.	b.d.	b.d.
		Average	99.96	0.04	<0.01	-	-	-	-	-
Green Canyon, Northern Gulf of Mexico (GoM)										
	Gas Hydrate	GC234:4220	62.3	8.7	19.4	6.3	1.4	0.03	0.17	1.48
		GC234:4216	68.3	12.6	12.2	3.4	2.1	0.23	0.22	0.21
		GC185:4211	67.8	11.4	14.2	3.4	2.5	0.07	0.45	<0.01
		Average	66.1	10.9	15.3	4.4	2.0	0.11	0.28	0.56
Blake Ridge Diapir, Blake Ridge (BR)										
	Gas Hydrate	BR2002:Hyd01	99.91	0.09	<0.01	b.d.	b.d.	b.d.	b.d.	b.d.
		BR2002:Hyd02	99.92	0.08	<0.01	b.d.	b.d.	b.d.	b.d.	b.d.
		Average	99.92	0.09	<0.01	-	-	-	-	-
Haakon Mosby Mud Volcano, Norwegian Sea (NS)										
	Gas Hydrate	HMMV00:Hyd01	99.96	0.04	<0.01	b.d.	b.d.	b.d.	b.d.	b.d.

[a]neo-C_5: neopentane or 2,2-dimethylbutane
b.d.: below detection

Table 3. Carbon isotope (^{13}C and ^{14}C) composition of hydrate-bound and free gas

Location	Source	Sample ID	AMS ID	^{14}C [pmc]	^{13}C-CH$_4$ [‰ vs PDB]
Bullseye Vent, Northern Cascadia Margin (NCM)					
	Gas Hydrate	PGC02-08:Hyd01[a]	NRL-456	1.43 ± 0.32	-64.6 ± 0.1
		PGC00-03:Hyd01[a]	NRL-458	1.42 ± 0.22	-63.2 ± 0.1
		PGC02-08:Hyd02[a]	NRL-467	0.72 ± 0.14	-63.8 ± 0.1
			Average	1.19 ± 0.41	-63.9 ± 0.7
	Core Gas	PGC02-08:CG02	NRL-454	2.15 ± 0.26	-79.3 ± 0.1
		PGC02-08:CG03	NRL-455	2.11 ± 0.34	-77.9 ± 0.1
		PGC02-08:CG06	NRL-460	1.62 ± 0.25	-67.7 ± 0.1
			Average	1.96 ± 0.30	-74.9 ± 6.3
Barkley Canyon, Northern Cascadia Margin (NCM)					
	Gas Hydrate	PGC02-08:Hyd03[a]	NRL-433	0.05 ± 0.23	-44.7 ± 0.1
			NRL-527	0.00 ± 0.13	
			NRL-834	0.17 ± 0.09	
		R694:Hyd01[b]	NRL-431	0.01 ± 0.21	-43.4 ± 0.1
			NRL-432	0.55 ± 0.17	
		R694:YellowHyd[b]	NRL-472	0.63 ± 0.17	-42.6 ± 0.1
		R694:WhiteHyd[b]	NRL-473	0.03 ± 0.16	-42.9 ± 0.1
		R695:Hyd02[b]	NRL-439	0.16 ± 0.25	-42.7 ± 0.1
			NRL-525	0.65 ± 0.12	
			NRL-883	0.00 ± 0.09	
			Average	0.22 ± 0.27	-43.3 ± 0.9
	Core Gas	PGC02-08:CG01	NRL-442	0.76 ± 0.20	-45.1 ± 0.1
		PGC02-08:CG05	NRL-459	1.16 ± 0.20	-44.9 ± 0.1
			Average	0.96	-45.0
Concepción Methane Seep, Central Chilean Margin (CCM)					
	Gas Hydrate	CHL1004-Hyd01[a]	NRL-1152	0.06 ± 0.18	-61.4 ± 0.1
	Core Gas	CHL1004:CG04	NRL-1147	0.10 ± 0.22	-61.7 ± 0.1
		CHL1004:CG05	NRL-1150	0.08 ± 0.21	-62.5 ± 0.1
		CHL1004:CG06	NRL-1151	0.00 ± 0.18	-63.1 ± 0.1
			Average	0.06 ± 0.05	-62.4 ± 0.7
Green Canyon, Northern Gulf of Mexico (GoM)					
	Gas Hydrate	GC234:4220[b]	NRL-468	0.48 ± 0.28	-49.5 ± 0.1
		GC234:4216[b]	NRL-477	0.62 ± 0.23	-48.8 ± 0.1
		GC185:4211[b]	NRL-478	0.00 ± 0.15	-44.7 ± 0.1
			Average	0.37 ± 0.33	-47.7 ± 2.6
Blake Ridge Diapir, Blake Ridge (BR)					
	Gas Hydrate	BR2002:Hyd01[a]	NRL-470	0.48 ± 0.22	-66.5 ± 0.1
		BR2002:Hyd02[a]	NRL-471	0.54 ± 0.17	-65.3 ± 0.1
			Average	0.51	-65.9
Haakon Mosby Mud Volcano, Norwegian Sea (NS)					
	Gas Hydrate	HMMV00:Hyd01[b]	NRL-469	0.40 ± 0.23	-63.2 ± 0.1

[a]Retrieved with piston core
[b]Retrieved with submersible
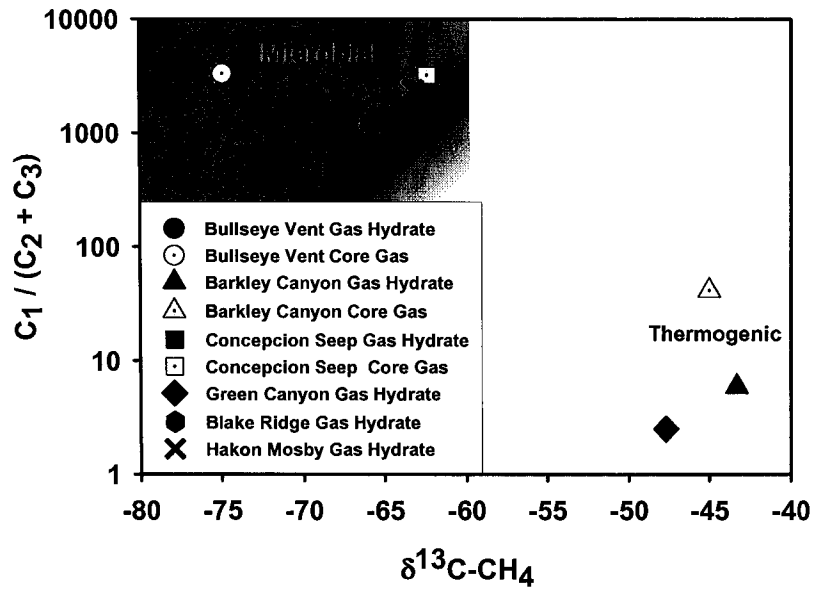
Figure 1. Relationship between the hydrocarbon composition $[C_1/(C_2+C_3)]$ and $\delta^{13}C$ values of methane from the samples evaluated in this study. The thermogenic and microbial fields are defined by Whiticar (1999). Black symbols represent gas hydrate samples and shaded symbols represent core gas samples.

to atmosphere

$CH_4 + O_2 \rightarrow CO_2 + CHO$

0

$CH_4 + SO_4^{-2} \rightarrow CO_2 + CHO$

Gas Hydrate

10^1

^{14}C

Gas Hydrate

Sediment Depth (mbsf)

Microbial Methane

10^2

10^3

Thermogenic Gas

Modern Carbon

Fossil Carbon
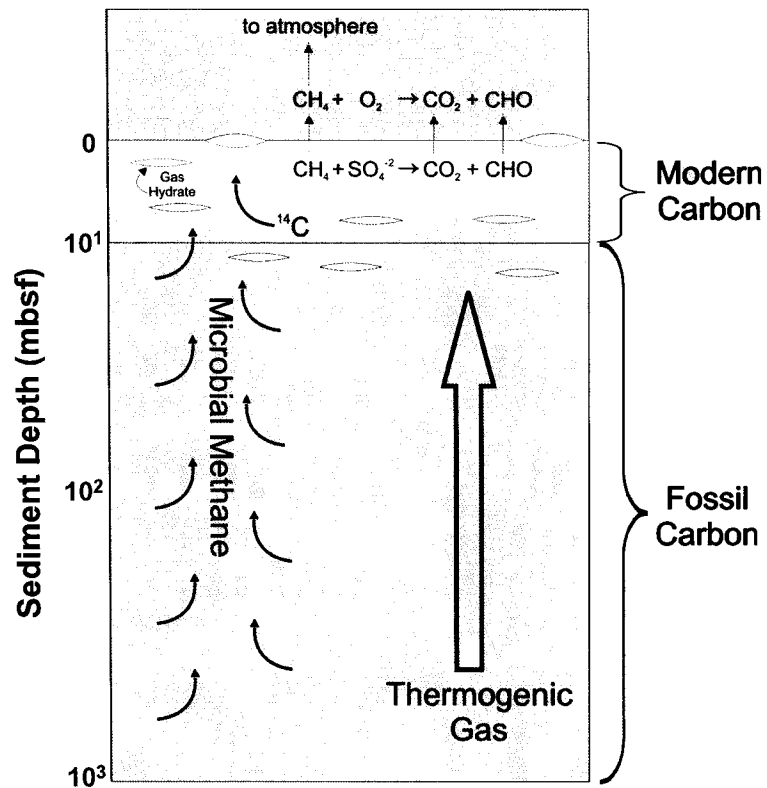
Figure 2. Conceptual model illustrating the radiocarbon signatures and sources of methane supporting gas hydrate accumulations in high gas flux settings. Modern carbon contributions are limited to microbial inputs from a relatively thin interval near the seafloor. Oxidation of fossil methane in the sediments (anaerobic) and the water column (aerobic) has the potential to generate significant quantities of fossil metabolites (e.g., DIC and DOC) that may alter the radiocarbon signatures of ocean carbon pools.

CHAPTER 3

THE ORIGIN OF THERMOGENIC GAS HYDRATES ON THE NORTHERN
CASCADIA MARGIN INFERRED FROM ISOTOPIC (^{13}C/^{12}C AND D/H) AND
MOLECULAR COMPOSITION OF HYDRATE AND VENT GAS

This chapter was published in Organic Geochemistry

Abstract

The isotopic ($\delta^{13}C$ and δD) and hydrocarbon composition of hydrate-bound and vent gas collected from the seafloor of Barkley Canyon (northern Cascadia Margin, offshore Vancouver Island, Canada) were evaluated to characterize the gas and infer the type and maturity of the source rock kerogen. The hydrate gas contained methane having $\delta^{13}C$ values of –43.4 to -42.6 ‰, δD values of –143 to –138 ‰ and a large percentage (14.9 to 31.9 %) of C_2 to C_{5+} hydrocarbons. These data are consistent with a thermogenic gas source. The data from Barkley Canyon are interpreted within the context of similar data from the Gulf of Mexico and Caspian Sea thermogenic hydrates, which occur in regions where the petroleum systems supporting gas and oil generation are better understood. A stable carbon-isotope based natural gas plot model and D/H data from the hydrate gas indicate that the source rock for the Barkley Canyon hydrate and vent gas was primarily Type III kerogen mixed with a small fraction of Type II kerogen. Oil from a seep having a pristane / phytane ratio of 3.2 was identified as a gas condensate, which supports the conclusions drawn from the gas data. A mechanism for explaining how fluids are conducted from the deep petroleum reservoir to the seafloor of Barkley Canyon is proposed.

1. Introduction

Gas hydrates are ice-like structures that contain gas within cages of water molecules. They are distributed worldwide along continental margins where temperature and pressure are within the hydrate stability region and gas concentrations are sufficient to saturate the pore water (Sloan, 1998). The geometry of the hydrate lattice is determined by the size of the gas molecules present during hydrate crystallization. Structure I, the most prevalent form, contains greater than 99% methane and trace amounts of ethane (Sloan, 1998). Structure II and structure H hydrates, which are commonly referred to as thermogenic gas hydrates, contain methane and significant quantities (>1%) of C_2-C_5 hydrocarbons formed by thermal pyrolysis of fossil organic matter (i.e., kerogen) or oil (Brooks et al., 1984; Sassen and MacDonald, 1994).

Thermogenic gas hydrate has been reported from the Gulf of Mexico (Brooks et al., 1984), Caspian Sea (Ginsburg and Soloviev, 1998) and more recently, from the southern summit of Hydrate Ridge offshore Oregon (Milkov et al., 2005) and the northern Cascadia Margin offshore Vancouver Island (British Columbia, Canada) (Fig. 1) (Chapman et al., 2004). At all locations, large accumulations of gas hydrate are found near the seafloor and are supported by a high flux of allochthonous gas. Thermogenic gas hydrate in the Gulf of Mexico is concentrated near structural features, such as salt-related faults and the margins of salt withdrawal basins, which serve as conduits for the migration of fluids from the deep subsurface petroleum reservoir (Sassen et al., 1999a). The oil-stained yellow-orange color and methane stable carbon-isotope composition of the northern Cascadia Margin hydrates is similar to thermogenic hydrates in the Gulf of

Mexico (Chapman et al., 2004; Sassen et al., 1999b) and implies that it is also connected to a deep petroleum reservoir. There are, however, no known salt-related features on the northern Cascadia Margin. Thus, an alternative hydrological process for conducting hydrocarbon-rich fluids from the petroleum reservoir to the seafloor where the gas hydrate occurs is needed. Hydrate Ridge is also located on the Cascadia accretionary complex, but it has a small contribution from thermogenic gas and, therefore, has a limited connection to a deep petroleum reservoir. Of 55 hydrate gas samples analyzed from the Ocean Drilling Program (ODP) Leg 204, the greatest thermogenic contribution to the total gas content was less than 20% - the remainder being microbial (Milkov et al., 2005). To our knowledge, the northern Cascadia Margin is the first location found on a convergent continental margin where the primary source of hydrate gas is thermogenic. Understanding the petroleum system supporting gas hydrate in this type of setting is critical for evaluating the resource, climate change and geohazard potential of gas hydrate.

In this paper, we provide the first complete description of the molecular and stable isotope (δ^{13}C and δD) composition of hydrate-bound gas collected on the northern Cascadia Margin. We determined the relative hydrocarbon distribution and the stable carbon (^{13}C/^{12}C) and hydrogen (D/H) isotope ratios of hydrate gases from both the northern Cascadia Margin and the Gulf of Mexico. The molecular and stable carbon-isotope data from the two study sites are compared to similar literature data from the Caspian Sea (Ginsburg and Soloviev, 1998). By comparing data from Barkley Canyon (where petrologic studies and petroleum exploration have been limited), the Gulf of Mexico and the Caspian Sea (two well studied hydrocarbon-producing basins), we hope

to gain insight into the nature of the petroleum system off Vancouver Island. To that end,

we utilized hydrate gas isotope data, complemented with analysis of vent gas and oil

from seafloor seeps, to establish a hydrate gas-source rock correlation.

1.1 Geologic Setting

1.1.1 Barkley Canyon, Northern Cascadia Margin

Barkley Canyon is located offshore Vancouver Island on the upper slope of the

northern Cascadia Margin accretionary prism where the Juan De Fuca plate converges

with the North American plate (Hyndman et al., 1990). In November 2000, a commercial

fishing vessel trawling across Barkley Canyon recovered greater than 1-ton of gas

hydrate (Spence et al., 2001) (Fig. 1). Although no hydrate samples were preserved on

the fishing vessel, observers at the site noted "a strong, pungent, petroleum-like smell".

Surveys in Barkley Canyon by the remotely operated vehicle *ROPOS* revealed massive

deposits of seafloor gas hydrate (Fig. 2), gas venting and oil seepage (Chapman et al.,

2004). The gas hydrate was located on an anticlinal ridge at ~850 m water depth and

appeared as slabs (up to 7 m long) and thinly sedimented mounds (up to 3 m high). The

gas hydrate field covered an area of approximately 0.5 km^2. Thick, white bacterial mats

and dense clusters of vesicomyid clams were found among the hydrate outcroppings,

though tube worms, which are commonly observed in the Gulf of Mexico (MacDonald et

al., 1990), were conspicuously absent. In many areas light, yellow oil emerged from the

sediments when disturbed by the submersible.

The discovery of thermogenic gas hydrate and oil seepage off the coast of

Vancouver Island is unusual because there are no known petroleum reserves in the

region. In contrast, thermogenic gas hydrate in the Gulf of Mexico and the Caspian Sea occur above significant oil and gas fields. While the geologic and tectonic evolution of the northern Cascadia Margin is well understood (Hyndman et al., 1990; Spence et al., 1991), sedimentological and source rock studies required to evaluate the hydrocarbon potential of this region have been limited by political and environmental factors (Bustin and Mastalerz, 1995). The most detailed source rock study performed in the region utilized cuttings from six exploratory wells drilled in the 1960's by Shell Canada Resources Ltd. in the nearby 7500 km^2 Tofino Basin (Bustin, 1995). Source rocks contain diagenetically altered organic matter, known as kerogen, that is converted to oil or thermogenic gas when heated above 60 °C. Kerogen is classified according to its C, H and O content (Hunt, 1996). Oil-prone Types I and II kerogen are enriched with hydrogen (H/C > 0.9) and are the source of most of the world's oil. Types III and IV kerogen are hydrogen deficient, oxygen enriched (O/C > 0.1) and produce primarily gas. Type III kerogen also produces some gas condensate. Bustin (1995) determined that sediments in Tofino Basin were organically lean (avg. = 0.8 %) and contained Type III kerogen with a low hydrogen index (avg. = 80 mg HC/g TOC). The richest source rocks were found in Miocene and Oligocene strata, but were, nevertheless, determined to be "poor source rocks as traditionally defined". One well contained material with an elevated hydrogen index, indicating a contribution from Type II kerogen. This kerogen mixture was, however, located in immature Pleistocene and Pliocene strata above the oil window (< 60 °C). Clearly, thermogenic gas hydrate and hydrocarbon seepage observed on the seafloor in Barkley Canyon must be supported by petroleum-generating source rock.

1.1.2 Green Canyon (GC 234), Gulf of Mexico

Green Canyon (GC 234), located on the continental slope of the northern Gulf of Mexico, is a fault-related seep area connected to Mesozoic source rocks in a deep salt withdrawal basin (Sassen et al., 2004). The source rocks are organic-rich carbonate and siliclastic shales of marine origin (Hood et al., 2002), and the kerogen is either Type II or Type II-S (McBride et al., 1998). Gas hydrate is present at the seafloor and is typically associated with complex chemosynthetic biological communities (MacDonald et al., 1990). Previous investigations have established links between the northern Gulf of Mexico petroleum system and gas hydrate found along the Texas-Louisiana margin (Brooks et al, 1984; Sassen and MacDonald, 1994; Sassen et al., 1994, 1998, 1999b, 2001a, 2001b, 2003, 2004). Our data from Green Canyon will serve as a benchmark for establishing a hydrate gas-source rock correlation for the northern Cascadia Margin petroleum system.

2. Samples

Gas hydrate samples were dislodged from the hydrate mounds by the research submersibles *ROPOS* (Barkley Canyon) and *Johnson-Sea-Link* (Green Canyon), placed into a pressure cylinder, transported to the surface and transferred into 60-ml plastic syringes. Following complete hydrate dissociation, the gases were transferred into glass serum vials. Vent gas samples from Barkley Canyon were collected in a steel cylinder with a ball valve on each end. Water was flushed from the cylinder by opening both valves and placing the cylinder above the gas stream. The back valve was closed, gas

was collected, and the cylinder was transported to the surface with both valves closed. A check valve, with a cracking pressure of 100 psi, prevented overpressure in the cylinder. At the surface, vent gas samples were transferred into glass serum vials. Oil from Barkley Canyon was skimmed from water overlying push cores and transferred into glass serum vials. Hydrate gas, vent gas and oil samples were stored at -20 °C until analysis.

3. Analytical Methods

Gas samples for analysis of relative hydrocarbon concentrations were transferred from the serum vial into a 10-ml plastic syringe and diluted 1:10 with nitrogen. The gas was introduced through a manual gas-sampling valve into a Shimadzu 14-A gas chromatograph (GC) equipped with a flame ionization detector (FID). The gas samples were analyzed using a Porapak-Q column (8', 1/8" OD) and a 270 kPa nitrogen carrier gas pressure. An oven profile that progressively ramped to 150 °C, but was isothermal during peak elution, was utilized. Concentrations were determined against certified gas standards (Scott Gas, Plumbsteadville PA).

The whole oil sample was extracted from the oil-water matrix with n-hexane and re-concentrated. Due to this treatment, some of the volatile lower molecular compounds may have been lost from the oil. The major components in the oil extract were separated using a Hewlett Packard 6890 Gas Chromatograph (GC) (injection temperature 30 °C, held isothermal for 2 minutes, ramped to 180 °C at 20 °C/min) equipped with a manual on-column injector and a DB-5 MS capillary column (30 m, 0.32 mm ID). The component peaks were identified using a Hewlett Packard 5973 mass selective detector interfaced to the GC. Compounds were identified using the NIST mass spectral library

and were only accepted if the goodness of fit exceeded 80%. High purity pristane and phytane standards and the oil samples were also analyzed using a Hewlett Packard 5890 GC (injection temperature 30 °C, held isothermal for 2 minutes, ramped to 180 °C at 20 °C/min) equipped with a manual on-column injector, an apolar DB-5 capillary column (30 m, 0.32 mm ID) and an FID to confirm the identification and relative concentrations of pristane and phytane in the oil sample.

D/H and $^{13}C/^{12}C$ isotope ratios were measured using a Finnigan Delta Plus XL isotope ratio mass spectrometer (IRMS). The gas samples were introduced via a Valco 6-port valve onto a GSQ PLOT column (30 m, 0.32 mm ID) in a Varian 3400 GC (injection temperature 30 °C, held isothermal for 2 minutes, ramped to 180 °C at 20 °C/min). For the $^{13}C/^{12}C$ ratios, the GC was interfaced to the IRMS through a combustion line, and for the D/H ratios the GC was interfaced through a 1440 °C pyrolysis unit. Whole oil samples were placed in pre-combusted (450 °C) tin cups and oxidized in a Fisons EA-1108 Elemental Analyzer interfaced to the IRMS through a Conflo-3. Isotope data are reported in the conventional δ-notation relative to the international standards Vienna Peedee Belemnite (VPDB) for $\delta^{13}C$ (precision ± 0.2 ‰) and Vienna Standard Mean Ocean Water (VSMOW) for δD (precision ± 0.2 ‰). The oil sample was normalized to the NBS-22 standard.

4. Results and Discussion

4.1 Hydrate gas hydrocarbon composition and hydrate structure

The molecular composition of the Barkley Canyon hydrate gas was primarily methane (68.1 to 85.1%) with significant quantities of thermogenic C_2-C_{5+} hydrocarbons

(Table 1; Fig 3a). The abundances of methane, ethane, propane and *iso*-butane are

diagnostic of structure II gas hydrate (Brooks et al., 1984), though the inclusion of small

quantities of *n*-butane and C_{5+} hydrocarbons (0.8 to 2.2%) suggests structure H gas

hydrate was a minor constituent of the lattice (Sassen and MacDonald, 1994). The

distribution of the gases from the seafloor hydrates was similar to structure II gas hydrate

collected at the Buzdag site in the Caspian Sea (Ginsburg and Soloviev, 1998) with the

exception that Caspian Sea gas hydrate contained higher quantities of ethane. Structure II

hydrate from Green Canyon in the Gulf of Mexico displayed a somewhat different

molecular composition with less methane and more propane and *iso*-butane. Despite the

noted differences in molecular composition of the hydrate gases, the overall similarity

between the Barkley Canyon hydrate gas and that from Green Canyon and Buzdag

supports the conclusion that Barkley Canyon hydrates are primarily structure II and the

gas is primarily thermogenic.

4.2 Vent gas hydrocarbon composition

Vent gas provides the most realistic indicator of the molecular and isotopic composition of gas generated at the source rock (Sassen et al., 2004). Gas hydrate crystallization concentrates higher hydrocarbons (C_2-C_{5+}) relative to the source gas (Sassen et al., 2000). Accordingly, higher hydrocarbons are enriched in the hydrate gas relative to the vent gas. Methane accounts for 97.3 % (n=1) and 83.3 % (n=4) of the total hydrocarbons in the Barkley Canyon vent gas and hydrate gas, respectively (Table 1). In contrast, vent gas and hydrate gas from Green Canyon contained, on average, 93 % (Sassen et al., 2004) and 65.6 % (n=3, this study) methane, respectively. Type II kerogen, the dominant source rock kerogen in the Gulf of Mexico, generates "wet" gas containing less methane and a higher proportion of C_{2+} hydrocarbons than Type III kerogen, which is reported to produce gas with < 1 % ethane (Whiticar, 1996). The concentration of ethane in the Barkley Canyon vent gas averaged 1.2 %, compared to 3.5 % observed for Green Canyon vent gas (Sassen et al., 2004). The depletion of ethane in Barkley Canyon vent gas relative to Green Canyon vent gas (Type II kerogen source rock) and enrichment relative to that expected for pure Type III kerogen source rock suggests a mixture of Type II and Type III kerogen in the source rocks that generated the vent gas recovered in Barkley Canyon.

4.3 Hydrate gas stable carbon-isotope composition

The stable carbon-isotope signature of methane from gas hydrate is commonly used to determine if the methane was microbially or thermally produced. Pure microbial methane typically has $\delta^{13}C$ values in the range of -90 to -60 ‰, while pure thermogenic methane has $\delta^{13}C$ values in the range of -50 to -20 ‰ (Whiticar, 1999). Gases containing

mixtures of microbial and thermogenic methane, however, are characterized by a broad range of values determined by the relative contributions and $\delta^{13}C$ values of the microbial and thermogenic endmembers. In addition, microbial methane oxidation (Whiticar, 1999) and methanogenesis (Claypool et al., 1985) may enrich microbial methane with ^{13}C to the extent that it appears to be a mixture of thermogenic and microbial methane. Methanogenesis, as a mechanism for generating ^{13}C-enriched methane, has been reported to occur in organic-rich sediments where rapid and prolonged methanogenesis (which preferentially utilizes ^{12}C) enriched the dissolved inorganic carbon (DIC) pool with ^{13}C. Subsequent reduction of the ^{13}C-enriched DIC by methanogens resulted in ^{13}C-enriched microbial methane (Claypool et al., 1985). Complementary carbon isotope analysis of C_{2+} hydrocarbons is useful for differentiating source effects from mixing and microbial alterations (Chung et al., 1988; Rooney et al., 1995; Katz et al., 2002; Sassen et al., 2003).

The stable carbon-isotope compositions of C_1-C_4 hydrate gases from Barkley Canyon are also consistent with a thermogenic origin (Table 1). More interesting, however, were the substantial differences observed among the Barkley Canyon, Caspian Sea and Green Canyon hydrate gases. The Green Canyon gases were consistently more ^{13}C-depleted than those from Barkley Canyon and the Caspian Sea (Fig. 3b). The $\delta^{13}C$ of C_2, C_3 and i-C_4 thermogenic hydrocarbons reported for Barkley Canyon and the Buzdag site in the Caspian Sea (Ginsburg and Soloviev, 1998) are more ^{13}C-enriched than any value identified from thermogenic sites in the Gulf of Mexico (Sassen et al., 1998, 1999b, 2003), and $\delta^{13}C$ values of ethane (-24.8 ‰) and propane (-24.5 ‰) from Barkley Canyon

hydrate gases are the most ^{13}C-enriched values for hydrate gas reported in the literature (Milkov, 2005).

The range and distribution of the stable carbon-isotope signatures of the hydrocarbon gases are a function of the origin and maturity of the source rock (James, 1983; Rooney et al., 1995; Whiticar, 1996) as well as post-generational alterations such as source mixing (Chung et al., 1988), accumulation history (Rooney et al., 1995) and biodegradation (Chung et al., 1988; Katz et al., 2002). These prior studies delineated these effects using free gas samples recovered from gas reservoirs. Because gas hydrate crystallization does not cause significant isotopic fractionation (Table 1; Brooks et al., 1986; Sassen et al., 1999b), the isotopic information recorded in gas hydrate (Table 1) may be suitable for establishing hydrate gas-source rock correlations by evaluating how source and post-depositional effects may have contributed to the measured isotopic composition of the gas.

4.4 Natural gas plot model

We employed the Chung et al (1988) natural gas plot model to elucidate the sources and processes affecting the isotopic composition of the gases (Fig. 4). The stable carbon-isotope ratios of the hydrocarbons (C_{1-4}) are plotted against the reciprocal of the hydrocarbon chain length (1/n). The enrichment of ^{13}C in gases with increasing carbon number (decreasing 1/n) is a result of kinetic isotope fractionation during gas formation. Because the bond strength of a ^{12}C-^{12}C bond is less than a ^{13}C-^{12}C bond, it is more likely to break during thermal cracking of the source rock kerogen. As a result, the hydrocarbon fragments are depleted in ^{12}C relative to the source kerogen. This process -

the kinetic isotope effect (KIE) - is most pronounced in methane. Larger gas fragments (n>1) contain carbon atoms with C-C bonds that were not subjected to the KIE. Assuming the isotopic composition of these carbon atoms represents the isotopic signature of the kerogen, increasing the number of carbon atoms in the gas product dilutes the KIE experienced by the terminal alkyl carbon that previously connected the fragment to the kerogen. Because methane contains no C-C bonds, an "undiluted" KIE is reflected in its stable carbon-isotope signature.

Following the principles outlined above, large thermally cleaved molecules, for which the KIE is "infinitely" diluted, should theoretically have the same $\delta^{13}C$ as the precursor molecule. This value is determined by extrapolating the isotope line to the y-intercept (1/n = 0) (Fig. 4; Table 2). Based on these results alone, it appears as though the Barkley Canyon and Green Canyon gases originated from isotopically similar source rocks (~ -20 ‰), while the Caspian Sea source rocks are somewhat ^{13}C-enriched (~ -16 ‰). A similar value was calculated from Green Canyon hydrate gas data reported by Sassen et al. (2003). The intercept values calculated from the natural gas plot model, however, may not represent the actual values of the source rock organic matter from which the gas components originated. The $\delta^{13}C$ values from two bulk oil samples from Barkley Canyon (a better indicator of the source rock isotopic composition (Chung et al., 1994)) were each -24.1 ‰, which is 4.1 ‰ more ^{13}C-depleted than the intercept result. A greater offset (~ 7 ‰) was observed between the model results and Gulf of Mexico oils (Chung et al., 1994; Sassen et al., 2001b). The difference between the modeled and observed values is most likely due to heterogeneities in the precursor kerogen, hydrocarbon formation mechanisms or maturity effects (Chung et al., 1988; Rooney et

al., 1995). Given the potential variability in the chemical content of the kerogen types and the relative maturities of the source rocks in Barkley Canyon and Green Canyon, the application of the natural gas plot model may not be suitable for extrapolating the exact isotopic composition of the source rock. Laboratory studies should be conducted to test this aspect of the model.

Extrapolation of the C_2-C_4 isotope line to the y-axis where $1/n = 1$ predicts the $\delta^{13}C$ the thermogenic methane endmember (Fig. 4). The predicted value for Barkley Canyon hydrate gas (-30.6‰) was ^{13}C-enriched relative to the Green Canyon and Caspian Sea estimates (-37.9‰ and –35.5‰, respectively) (Table 2). The differences among the gases are most likely due to the gas from Barkley Canyon being generated at higher maturity than gas in Green Canyon or the Caspian Sea. With increasing maturation and prolonged exposure to kinetic isotope fractionation, the source rock becomes progressively ^{13}C-enriched. Thermogenic gases accumulating during the course of thermal maturation also become ^{13}C-enriched as predicted by the Rayleigh distillation model (Rooney et al., 1995). The relative maturation is graphically represented in Fig. 4 as the slope of the C_2-C_4 isotope line. The steeper slopes calculated from the Green Canyon and Caspian Sea data represent a lower maturity gas than the moderate slope calculated from the Barkley Canyon data (Table 2). Furthermore, the linearity of the C_2-C_4 isotope line ($r^2 \geq 0.99$) (Fig. 4; Table 2) indicates these gases originated from a single reservoir (no mixing) and have not been subjected to biodegradation (Chung et al., 1988; George et al., 2002).

In higher maturity gases, the isotope separation between the hydrocarbons (e.g., $\delta^{13}C_{propane}$ - $\delta^{13}C_{butane}$) is less than that of the lower maturity gases. For example, the

separation between propane and butane for the more mature Barkley Canyon gases is 0.9 ‰ and the separation for both Green Canyon and the Caspian Sea gases is 1.6 ‰. The relationship between the isotopic separation of gases and gas maturity is based upon the same principle - the KIE - as the natural gas plot model (Chung et al. 1988). James (1983) correlated isotope separations with source rock vitrinite reflectance ($\%R_o$), a common metric for expressing source rock maturity. The James (1983) model predicts a $\%R_o$ of about 1.7 % for the Barkley Canyon source rocks and a $\%R_o$ of about 1.3 % for the Green Canyon and Caspian Sea source rocks. Based on these values, it appears that oil generated from the Barkley Canyon source rocks is primarily gas condensate, while the Green Canyon and Caspian Sea samples are mature oils (James, 1983). Extensive exploration and oil production histories have established that mature oil is present in reservoirs of Green Canyon and the Caspian Sea. Until now, however, no liquid hydrocarbon from Barkley Canyon, specifically, and the Tofino Basin, in general, had been analyzed (See Section 4.5).

Mixing of ^{13}C-depleted microbial methane may explain why the measured $\delta^{13}C$ values of the hydrate methane are lower than that predicted by the natural gas plot model for pure thermogenic methane (Fig. 4). A simple isotope-mixing model, which assumes the microbial endmember stable carbon-isotope values listed in Table 2, was used to calculate the fraction of microbial methane in the hydrate bound methane. The microbial endmembers for Barkley Canyon and Green Canyon were determined from "pure" microbial gas samples collected within 100 km of the study sites, and the endmember value for the Caspian Sea was taken from the literature (Katz et al., 2002). The calculated microbial contribution at the three locations ranged from 25% to 41% of the

total methane. Contributions from microbial sources of methane were similar at Barkley

Canyon (25%) and Green Canyon (31%). Considering that 20% of the total

hydrocarbons are C_{2+} gases (Table 1), the total contribution of thermogenic gas to the

hydrate gas from Barkley Canyon is, on average, 80%.

4.5 Oil Composition

The partial gas chromatogram of a Barkley Canyon oil sample (Fig. 5) consisted

of low molecular weight branched and *n*-alkanes, the isoprenoids pristane and phytane

and small quantities of methyl-napthalenes. The low molecular weight of the

hydrocarbons (C_{11} to C_{20}) and the absence of a significant unresolved complex mixture

indicate this oil is primarily gas condensate (Hunt, 1996). This interpretation, which is

based on the actual oil composition, is consistent with the composition predicted by

stable carbon-isotope maturity indicators described above.

The ratio of pristane to phytane (Pr/Ph) was measured to provide additional

information on the origin of the source rock kerogen. Diagenesis under oxic conditions,

which is typical of riverine and deltaic environments (the origin of Type III humic

kerogen), imparts a Pr/Ph ratio that is usually > 2 (Powell and McKirdy, 1973; Didyk et

al., 1978). Anoxic diagenesis, typical of marine basins where Type II sapropelic kerogen

originates, usually results in Pr/Ph ratios < 1.2 (Chung et al., 1992). Our value of 3.2 for

the Barkley Canyon oil indicates the precursor organic matter for the source rock kerogen

was primarily humic material deposited in deltaic or fluvial environments. Humic

organic matter is the precursor of Type III kerogen.

4.6 D/H ratios (δD) of the hydrate gas

D/H ratios of marine organic matter are remarkably consistent because the δD of

marine water has not changed appreciably over geologic time (Lécuyer et al., 1998). On

the other hand, water in the terrestrial environment exhibits extreme temporal and

regional variations (Dansgaard, 1964), which is reflected in the δD of terrestrial organic

matter (Sauer et al., 2001). If post-depositional processes such as migration, maturation

and isotope exchange with formation waters did not erase the source signal, D/H ratios of

the C_1-C_4 hydrocarbons from the well described Green Canyon compared to similar data

from Barkley Canyon may allow us to further constrain the identity of the Barkley

Canyon source rock kerogen.

Similar comparisons have been made with crude oil and crude oil fractions from

terrestrial and marine sources (Li et al., 2001; Schimmelmann et al., 2004). Several

important conclusions were drawn from these studies, which are relevant to our analysis

of hydrate gas D/H data: 1) Terrestrial derived oils display considerably more variability

than marine derived oils; 2) migration of oil and gas between reservoirs does not cause

fractionation; 3) fractionation during hydrocarbon generation from source rock to oil

results in an increased δD in the product; 4) maturation of the source rock leads to a

progressive increase in the δD of the crude oil; 5) considerable hydrogen isotope

exchange with source waters occurs and is dependent upon the composition of the

organic matter, and; 6) δD values of n-alkanes increase with increasing carbon number.

D/H ratios of methane are also affected by the maturity of the source rock (Schoell, 1980)

and oxidation in the hydrate phase (Sassen et al., 1998), but are less affected by hydrogen

isotope exchange (Schimmelmann et al., 2004).

As expected, the δD of the alkanes becomes more enriched with D with increasing carbon number (Fig. 6; Table 3). On a compound specific basis, the δD of the hydrate methane from Barkley Canyon was enriched with D by 35‰ relative to Green Canyon hydrate methane. In contrast, the δD values of the C_2-C_4 hydrocarbons from each site were virtually identical. Since the isotopic composition of the gases is a function of the source rock kerogen isotope signature differences, maturity effects and/or numerous post-generation processes, constraining the effect of each of these factors requires careful evaluation of the data.

Schoell (1980) investigated the relationship between source rock maturity and the D/H ratios of gases from N.W. German coal beds and the Delaware-Val Verde basin. He found that the δD from the two gas groups became equally more positive with increasing maturity. Analogous to the KIE explanation employed to explain increased $^{13}C/^{12}C$ ratios with increased maturity, C-C bonds in CH_2D terminal groups of the source rock kerogen are stronger than C-C bonds in CH_3 terminal groups. As a result, they are less susceptible to cleavage and become D-enriched with increased source rock maturity. A similar effect has been noted with alkanes in crude oils (Li et al., 2001). Using the maturity indices calculated by the natural gas plot model (Barkley Canyon %R_o = 1.7% and Green Canyon %R_o = 1.3%) and the source rock maturity model developed by Schoell (1980), we found that maturity effects could only have accounted for a 4‰ enrichment in D for the Barkley Canyon hydrate methane (relative to the Green Canyon hydrate methane). Different source rock maturities do not explain the observed 35‰ difference between the Barkley Canyon and Green Canyon hydrate methane.

Microbial gas input and oxidation effects can also alter the δD of the methane (Whiticar, 1999; Sassen et al., 1998), but were also not likely significant factors in the differences observed between the Barkley Canyon and Green Canyon hydrate methane D/H ratios. We calculated similar microbial inputs for the Barkley Canyon (25%) and Green Canyon (31%) hydrate gas using the natural gas plot model (Sec 4.4). Assuming an input of microbial gas with a δD of -200‰, the average δD for microbial methane formed by carbonate reduction (Whiticar, 1999), microbial gas input would have decreased the δD of the Barkley Canyon hydrate methane by 9‰ relative to the Green Canyon methane. The decrease in the δD from microbial input offsets the 4‰ increase predicted by the maturity effect previously discussed. The net result of the calculated maturity effect and microbial gas input is a 5‰ decrease in the Barkley Canyon hydrate methane relative to the Green Canyon hydrate methane - a shift that opposes the observed difference of $+35$‰. This pattern suggests that a factor other than maturity or microbial input controls the differences in the δD signatures of the hydrate gases.

Studies by Sassen et al. (1998, 2003, 2004) suggest that microbial oxidation of methane in gas hydrates can lead to enrichment of D in the residual gas. In particular, the δD of altered hydrate methane from Bush Hill (another well studied site in Green Canyon) was, on average (n=6), -168‰, which was 10‰ more ^{13}C-enriched than unaltered vent gas (-178‰, n=4) (Sassen et al., 2004). Since we are evaluating two hydrate bound gases, which may have both been altered, the oxidation effect on this comparison would be expected to be less than the Sassen et al. (2004) comparison of hydrate methane and unaltered vent gas. Oxidation effects, therefore, are also not a likely explanation for the differences observed in the hydrate methane from the two study sites.

In summary, maturity effects, mixing of microbial gas and oxidation effects do not explain the observed differences in δD between the Barkley Canyon and Green Canyon gases. We, therefore, conclude that the major factor controlling the observed D ratios in the methane is a unique source rock signature. We cannot fully explain why a similar pattern was not observed in the C_2-C_4 hydrocarbons. The gas plot model indicated no microbial alteration of the C_2-C_4 hydrocarbons (Sec. 4.4) and microbial sources of C_2-C_4 are negligible. By process of elimination, we speculate that hydrogen isotope exchange, maturity effects or some other mechanism(s) may have overwhelmed a weaker initial source signature signal in the C_2-C_4 hydrocarbons.

Gases originating from sapropelic Type II kerogen and humic Type III kerogen plot in different zones of the C-D diagram (Fig. 7). C-D diagrams define the origin of methane based upon the distribution of δ^{13}C and δD signatures of methane from numerous, constrained methane sources (Schoell, 1980; Whiticar, 1986; Fig. 3 in Milkov, 2005 in this special issue). The comprehensive C-D diagram separates microbial, abiogenic, geothermal, hydrothermal and atmospheric methane (Whiticar, 1986). The values in Fig. 7 were corrected for microbial contributions using a simple two-source isotope-mixing model rearranged to solve for the isotopic composition of the thermogenic endmember:

$$\delta X_{thermo} = \frac{\delta X_{meas} - \left(f * \delta X_{micro} \right)}{1-f} \qquad \text{(Eq. 1)}$$

where δX_{thermo}, δX_{meas} and δX_{micro} represent the δD and δ^{13}C for the thermogenic endmember, measured value and microbial endmember, respectively. "f" is the fraction

of microbial gas, which was calculated using the natural gas plot model (see Table 2).

The microbial endmember $\delta^{13}C$ was the same value used in the natural gas plot model,

and the microbial endmember for dD was assumed to be –200‰ (Whiticar, 1999).

Type III kerogen derived methane falls into a restricted region of the C-D diagram

where methane is enriched in both D and ^{13}C (Fig. 7). All the corrected data from

Barkley Canyon hydrate gas fall into this zone, while the Green Canyon data fall into the

sapropelic Type II kerogen source zone (Whiticar, 1996). The scatter in the data from

Green Canyon, which was also observed by Sassen et al. (1998, 2004), is typical for oil-

prone Type II kerogen source rock, and the tight clustering of the Barkley Canyon data is

typical for gas-prone Type III kerogen source rock (Schoell, 1980).

5. Hydrological mechanism for fluid transport

Barkley Canyon is a headless canyon that may be the site of focused fluid flow

for a large portion of the northern Cascadia Margin accretionary complex. While most

submarine canyons form by erosional processes, headless canyons form when internal

forces resulting from excess pore pressure gradients overcome the cohesive and frictional

forces that stabilize slope sediments (Orange and Breen, 1992). These geologic features

are most prominent on the slopes of accretionary prisms where sediment compaction and

deformation generate steep pore pressure gradients. Once formed, vents in the canyon

wall focus and continue to discharge fluids accumulating from a large area of the

accretionary wedge. We hypothesize that Barkley Canyon and the shallow gas hydrates

found there originated by a similar process. Expulsion of gas-saturated fluids expelled

from a petroleum system deep within Tofino Basin triggered the formation of Barkley

Canyon and gas hydrate crystallized from gases that exsolved as the fluid depressurized during vertical migration. Hydrocarbon rich fluids from Tofino Basin source rocks and, possibly, from deeper subducted accretionary wedge sediments continue to concentrate in Barkley Canyon and support the existing seafloor gas hydrate field.

6. Conclusions

Massive gas hydrate accumulations, gas venting and oil seepage were observed on the seafloor of Barkley Canyon on the northern Cascadia Margin. Stable isotope ($^{13}C/^{12}C$ and D/H) and relative hydrocarbon abundance data from thermogenic hydrate gas and vent gas from Barkley Canyon compared to similar data from Green Canyon in the Gulf of Mexico indicate that the petroleum source rock is primarily Type III kerogen with a slight contribution from Type II kerogen. Oil collected at the seafloor was identified as gas condensate, a product of Type III kerogen pyrolysis. High pristine/phytane ratios and the isotopic data further suggest that the origin of the Type III kerogen from the northern Cascadia Margin is terrestrial humic organic matter. However, it is difficult to differentiate highly degraded marine clastic Type II kerogen from humic Type III kerogen. Detailed analysis of the source rock is required to make a conclusive distinction.

Our application of utilizing hydrate and vent gas collected at the seafloor to classify the source rock is a novel approach that is particularly valuable when evaluating areas like the northern Cascadia Margin where sedimentological or petrological investigations have been limited by logistical, technical or political factors. High-resolution multi-channel seismic studies and more extensive petrological studies must be conducted around Barkley Canyon to test our hypotheses and provide a more detailed

description of the relationship between Barkley Canyon and the deep northern Cascadia Margin petroleum system. The Integrated Ocean Drilling Program leg scheduled for drilling on the northern Cascadia Margin during late Summer/Fall 2005 is an excellent opportunity for exploring these questions.

References

Brooks, J.M., Kennicutt, M.C., Fay, R.R., McDonald, T.J., Sassen, R., 1984. Thermogenic gas hydrates in the Gulf of Mexico. Science 225, 409-411.

Brooks, J.M., Cox, H.B., Bryant, W.R., Kennicutt, M.C., Mann, R.G., McDonald, T.J., 1986. Association of gas hydrates and oil seepage in the Gulf of Mexico. Organic Geochemistry 10, 221-234.

Bustin, R.M., 1995. Organic maturation and petroleum source-rock potential of Tofino basin, southwestern British-Columbia. Bulletin of Canadian Petroleum Geology 43, 177-186.

Bustin, R.M. and Mastalerz, M., 1995. Organic petrology and geochemistry of organic-rich rocks of the late Triassic and early Jurassic Sandilands and Ghost Creek formations, Queen-Charlotte-Islands, British-Columbia. Marine and Petroleum Geology 12, 70-81.

Chapman, N.R., Pohlman, J.W., Coffin, R.B., Chanton, J.P., Lapham L., 2004. Thermogenic gas hydrates in the northern Cascadia Margin. EOS 85, 361,365.

Chung, H.M., Gormly, J.R., Squires, R.M., 1988. Origin of gaseous hydrocarbons in subsurface environments - theoretical considerations of carbon isotope distribution. Chemical Geology 71, 97-103.

Chung, H.M., Rooney, M.A., Toon, M.B., Claypool, G.E., 1992. Carbon isotope composition of marine crude oils. AAPG Bulletin-American Association of Petroleum Geologists 76, 1000-1007.

Chung, H.M., Claypool, G.E., Rooney, M.A., Squires, R.M., 1994. Source characteristics of marine oils as indicated by carbon isotopic-ratios of volatile hydrocarbons. AAPG Bulletin-American Association of Petroleum Geologists 78, 396-408.

Claypool, G.E., Threlkeld, C.N., Mankiewicz, P.N., Arthur, M.A., Anderson, T.F., 1985. Isotopic composition of interstitial fluids and origin of methane in slope sediment of the Middle America Trench, deep-sea drilling project Leg-84. Initial Reports of the Deep Sea Drilling Project 84, 683-691.

Dansgaard, W., 1964. Stable isotopes in precipitation. Tellus 16, 436-468.

Didyk, B.M., Simoneit, B.R.T., Brassell, S.C., Eglinton, G., 1978. Organic geochemical indicators of paleo-environmental conditions of sedimentation. Nature 272, 216-222.

George, S.C., Boreham, C.J., Minifie, S.A., Teerman, S.C., 2002. The effect of minor to moderate biodegradation on C-5 to C-9 hydrocarbons in crude oils. Organic Geochemistry 33, 1293-1317.

Ginsburg, G.D. and Soloviev, V.A., 1998. Submarine Gas Hydrates, VNII Okeangeologia, St Petersburg.

Hood, K.C., Wenger, L.M., Gross, O.P., Harrison, S.C., 2002. Hydrocarbon systems analysis of the northern Gulf of Mexico: delineation of hydrocarbon migration pathways using seeps and seismic imaging. In: Schumacher, D. and LeShack, L.A. (Eds.) Surface exploration case histories: Applications of geochemistry, magnetics, and remote sensing. pp. 25-40.

Hunt, J.M., 1996. Petroleum Geochemistry and Geology, 2nd Edition. Freeman, New York.

Hyndman, R.D., Yorath, C.J., Clowes, R.M., Davis, E.E., 1990. The Northern Cascadia Subduction Zone at Vancouver Island - seismic structure and tectonic history. Canadian Journal of Earth Sciences 27, 313-329.

James, A.T., 1983. Correlation of natural-gas by use of carbon isotopic distribution between hydrocarbon components. AAPG Bulletin-American Association of Petroleum Geologists 67, 1176-1191.

Katz, B.J., Narimanov, A., Huseinzadeh, R., 2002. Significance of microbial processes in gases of the South Caspian Basin. Marine and Petroleum Geology 19, 783-796.

Lécuyer, C., Gillet, P., Robert, F., 1998. The hydrogen isotope composition of seawater and the global water cycle. Chemical Geology 145, 249-261.

Li, M.W., Huang, Y.S., Obermajer, M., Jiang, C.Q., Snowdon, L.R., Fowler, M.G., 2001. Hydrogen isotopic compositions of individual alkanes as a new approach to petroleum correlation: Case studies from the Western Canada Sedimentary Basin. Organic Geochemistry 32, 1387-1399.

MacDonald, I.R., Guinasso, N.L., Reilly, J.F., Brooks, J.M., Callender, W.R., Gabrielle, S.G., 1990. Gulf-Of-Mexico hydrocarbon seep communities .6. Patterns in community structure and habitat. Geo-Marine Letters 10, 244-252.

McBride, B.C., Weimer, P., Rowan, M.G., 1998. The effect of allochthonous salt on the petroleum systems of northern Green Canyon and Ewing Bank (Offshore Louisiana), northern Gulf of Mexico. AAPG Bulletin 82, 1083-1112.

Milkov, A.V., Claypool, G.E., Lee, Y.-J, Sassen, R., 2005. Gas hydrate systems at Hydrate Ridge offshore Oregon inferred from molecular and isotopic properties of hydrate-bound gases. Geochimica et Cosmochimica Acta, in press.

Milkov, A.V., 2005. Organic geochemistry of hydrate-bound gases in the context of geological settings: Analysis of the global dataset. Organic Geochemistry 36, 681-702.

Orange, D.L. and Breen, N.A., 1992. The effects of fluid escape on accretionary wedges .2. seepage force, slope failure, headless submarine canyons, and vents. Journal of Geophysical Research-Solid Earth 97, 9277-9295.

Powell, T.G. and McKirdy, D.M., 1973. Relationship between ratios of pristane to phytane, crude-oil composition and geological environment in Australia. Nature-Physical Science 243, 37-39.

Rooney, M.A., Claypool, G.E., Chung, H.M., 1995. Modeling thermogenic gas generation using carbon isotope ratios of natural gas hydrocarbons. Chemical Geology 126, 219-232.

Sassen, R. and MacDonald, I.R., 1994. Evidence of Structure-H hydrate, Gulf of Mexico continental slope. Organic Geochemistry 22, 1029-1032.

Sassen, R., MacDonald, I.R., Requejo, A.G., Guinasso, N.L., Kennicutt, M.C., Sweet, S.T., Brooks, J.M., 1994. Organic geochemistry of sediments from chemosynthetic communities, Gulf-Of-Mexico slope. Geo-Marine Letters 14, 110-119.

Sassen, R., MacDonald, I.R., Guinasso, N.L., Joye, S., Requejo, A.G., Sweet, S.T., Alcala-Herrera, J., DeFreitas, D., Schink, D.R., 1998. Bacterial methane oxidation in sea-floor gas hydrate: significance to life in extreme environments. Geology 26, 851-854.

Sassen, R., Sweet, S.T., Milkov, A.V., DeFreitas, D.A., Salata, G.G., McDade, E.C., 1999a. Geology and geochemistry of gas hydrates, central Gulf of Mexico continental slope. Trans.Gulf Coast Assoc. Geol. Soc. 49, 462-468.

Sassen, R., Joye, S., Sweet, S.T., DeFreitas, D.A., Milkov, A.V., MacDonald, I.R., 1999b. Thermogenic gas hydrates and hydrocarbon gases in complex chemosynthetic communities, Gulf of Mexico continental slope. Organic Geochemistry 30, 485-497.

Sassen, R., Sweet, S.T., DeFreitas, D.A., Milkov, A.V., 2000. Exclusion of 2-methylbutane (isopentane) during crystallization of structure II gas hydrate in sea-floor sediment, Gulf of Mexico. Organic Geochemistry 31, 1257-1262.

Sassen, R., Losh, S.L., Cathles, L., Roberts, H.H., Whelan, J.K., Milkov, A.V., Sweet, S.T., DeFreitas, D.A., 2001a. Massive vein-filling gas hydrate: relation to ongoing gas migration from the deep subsurface in the Gulf of Mexico. Marine and Petroleum Geology 18, 551-560.

Sassen, R., Sweet, S.T., DeFreitas, D.A., Morelos, J.A., Milkov, A.V., 2001b. Gas hydrate and crude oil from the Mississippi Fan Foldbelt, downdip Gulf of Mexico Salt Basin: significance to petroleum system. Organic Geochemistry 32, 999-1008.

Sassen, R., Milkov, A.V., Ozgul, E., Roberts, H.H., Hunt, J.L., Beeunas, M.A., Chanton, J.P., DeFreitas, D.A., Sweet, S.T., 2003. Gas venting and subsurface charge in the

Green Canyon area, Gulf of Mexico continental slope: evidence of a deep bacterial methane source? Organic Geochemistry 34, 1455-1464.

Sassen, R., Roberts, H.H., Carney, R., Milkov, A.V., DeFreitas, D.A., Lanoil, B., Zhang, C.L., 2004. Free hydrocarbon gas, gas hydrate, and authigenic minerals in chemosynthetic communities of the northern Gulf of Mexico continental slope: relation to microbial processes. Chemical Geology 205, 195-217.

Sauer, P.E., Eglinton, T.I., Hayes, J.M., Schimmelmann, A., Sessions, A.L., 2001. Compound-specific D/H ratios of lipid biomarkers from sediments as a proxy for environmental and climatic conditions. Geochimica et Cosmochimica Acta 65, 213-222.

Schimmelmann, A., Sessions, A.L., Boreham, C.J., Edwards, D.S., Logan, G.A., Summons, R. E., 2004. D/H ratios in terrestrially sourced petroleum systems. Organic Geochemistry 35, 1169-1195.

Schoell, M., 1980. The hydrogen and carbon isotopic composition of methane from natural gases of various origins. Geochimica et Cosmochimica Acta 44, 649-661.

Sloan, E.D., 1998. Clathrate hydrates of natural gases, Marcel Dekker, New York.

Spence, G.D., Hyndman, R.D., Davis, E.E., Yorath, C.J., 1991. Seismic structure of the northern Cascadia accretionary prism: evidence from new multichannel seismic reflection data. Geodynamics 22, 257-363.

Spence, G.D. and Chapman, N.R., 2001. Fishing trawler nets massive "catch" of methane hydrates. EOS 82, 621,627.

Whiticar, M.J., Faber, E., Schoell, M., 1986. Biogenic methane formation in marine and fresh-water environments - CO_2 reduction vs acetate fermentation isotope evidence. Geochimica et Cosmochimica Acta 50, 693-709.

Whiticar, M.J., 1996. Stable isotope geochemistry of coals, humic kerogens and related natural gases. International Journal of Coal Geology 32, 191-215.

Whiticar, M.J., 1999. Carbon and hydrogen isotope systematics of bacterial formation and oxidation of methane. Chemical Geology 161, 291-314

Table 1
Stable carbon isotope and molecular composition of hydrate and vent gas

Sample Location	Dive / Core	Description	$\delta^{13}C\ C_1$ (‰)	C_1 (%)	$\delta^{13}C\ C_2$ (‰)	C_2 (%)	$\delta^{13}C\ C_3$ (‰)	C_3 (%)	$\delta^{13}C\ i\text{-}C_4$ (‰)	$i\text{-}C_4$ (%)	$\delta^{13}C\ n\text{-}C_4$ (‰)	$n\text{-}C_4$ (%)	C_5 (%)
Barkley Canyon, Northern Cascadia Margin													
	R694	Hydrate Gas	-43.4	85.1	-25.5	7.7	-23.5	3.3	-24.5	1.1	-22.5	1.7	1.1
	R694	Yellow Hydrate	-42.6	81.9	-24.8	10.4	-23.4	3.7	n.d.	1.2	-22.5	2.0	0.8
	R694	White Hydrate	-42.9	84.3	-24.8	9.1	-23.0	3.2	n.d.	1	-21.4	1.6	0.8
	R695	Hydrate Gas	-42.7	68.1	-25.7	10.8	-23.6	12.5	-24.8	4.2	-23.7	2.2	2.2
		Mean	-42.9	79.9	-25.2	9.5	-23.4	5.7	-24.7	1.9	-22.5	1.9	1.2
		s.d.	0.4	8.0	0.5	1.4	0.3	4.6	0.2	1.6	0.9	0.3	0.7
	R800	Vent Gas	-42.1	97.3	-25.3	1.2	-23.5	1.0	-24.3	0.3	-22.4	0.2	<0.1
Green Canyon (GC 234), Northern Gulf of Mexico													
	4215	GC 234 Hydrate	-50.0	66.1	-28.8	9.1	-25.4	17.2	-26.3	5.6	-24.0	1.4	0.6
	4216	GC 234 Hydrate	-48.8	68.3	-28.5	12.6	-25.8	12.2	-26.7	3.4	-23.3	2.1	1.4
	4220	GC 234 Hydrate	-49.5	62.3	-28.7	8.7	-25.7	19.4	-26.5	6.3	-24.8	1.4	1.9
		GC 234 Hydrate[a]	-47.5	74.2	-29.3	10.5	-26.1	11.2	-27.8	2.2	-25.4	1.6	0.3
		Mean[a]	-49.4	65.6	-28.7	10.1	-25.6	16.3	-26.5	5.1	-24.0	1.6	1.3
		s.d.	0.6	3.0	0.2	2.1	0.2	3.7	0.2	1.5	0.8	0.4	0.7
		GC 234 Vent Gas[a]	-48.5	93	-28.5	3.5	-26.2	2	-27.9	0.4	-25.3	0.6	0.5
South Caspian Sea Hydrates[c]													
	7s	Buzdag	-44.8	77.4	-25.8	18.3	-22.3	2.4	n.d.	0.4	-21.0	1.1	0.3
	1	Elm	-55.7	96.2	-25.7	0.6	-7.3	1.5	-29.4	1.7	n.a.	n.a.	0.01

[a] Sassen et al., 2004

[b] Does not include referenced data

[c] Ginsburg and Soloviev, 1998

n.a. = not available; n.d. = not determined

Table 2
Natural gas plot model inputs and results

Location	Site	Slope	Intercept	r^2	Modeled thermogenic $\delta^{13}C\text{-}CH_4$ (‰)	[a]Assumed microbial $\delta^{13}C\text{-}CH_4$ (‰)	Microbial Gas Source	Fraction Microbial
N. Cascadia Margin	Barkley Canyon	-10.7	-19.8	0.99	-30.6	-79.3	Bullseye Vent	0.25
N. Gulf of Mexico	Green Canyon	-18.5	-19.4	1.00	-37.9	-75.4	Keathley Canyon	0.31
S. Caspian Sea	Buzdag[b]	-19.5	-16	1.00	-35.5	-70	Katz et al. (2002)	0.41

[a]Selected values described in the text
[b]Ginsburg and Soloviev, 1998

Table 3
Deuterium isotope composition of gas hydrate samples

Sample Location	Dive / Core	Description	$\delta D\ C_1$ (‰)	$\delta D\ C_2$ (‰)	$\delta D\ C_3$ (‰)	$\delta D\ i\text{-}C_4$ (‰)	$\delta D\ n\text{-}C_4$ (‰)
Barkley Canyon Seafloor Hydrates							
	R694	Hydrate Gas	-143	-117	-96	-92	-89
	R694	Yellow Hydrate	-139	-116	-83	n.d.	n.d.
	R694	White Hydrate	-138	-115	-96	n.d.	n.d.
	R695	Hydrate Gas	-140	-122	-99	-88	-95
		Mean	-140.0	-117.5	-93.5	-90.0	-92.0
		s.d.	2.2	3.1	7.1	2.8	4.2
Northern Gulf of Mexico Hydrates							
	4215	GC-234	-153	-111	-98	n.d.	n.d.
	4216	GC-234	-179	-120	-94	n.d.	n.d.
	4220	GC-234	-192	-119	-99	-93	-90
		GC-234[a]	-185	n.a.	n.a.	n.a.	n.a.
		Mean[b]	-174.7	-116.7	-97.0	-93.0	-90.0
		s.d.	19.9	4.9	2.6		

[a]Sassen et al., 2004

[b]Does not include referenced data

n.a. = not available; n.d. = not determined
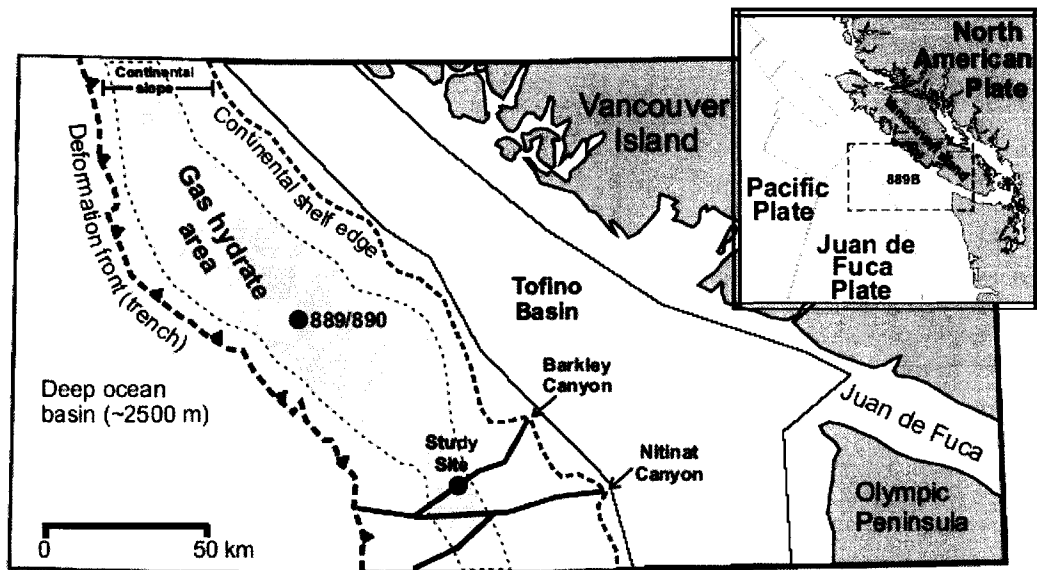
Figure 1. Location map showing the physiographic and geographical setting of Barkley Canyon. Thermogenic gas hydrates were collected at the study site, which is located on the continental slope in Barkley Canyon at about 850 m water depth. The presence of gas hydrates along the entire continental slope has been inferred from seismic reflections (Spence et al., 2000). Previously, hydrates containing microbial gas were collected at ODP drill sites 889/890 and a nearby seafloor vent. Figure modified from Spence et al. (2000).
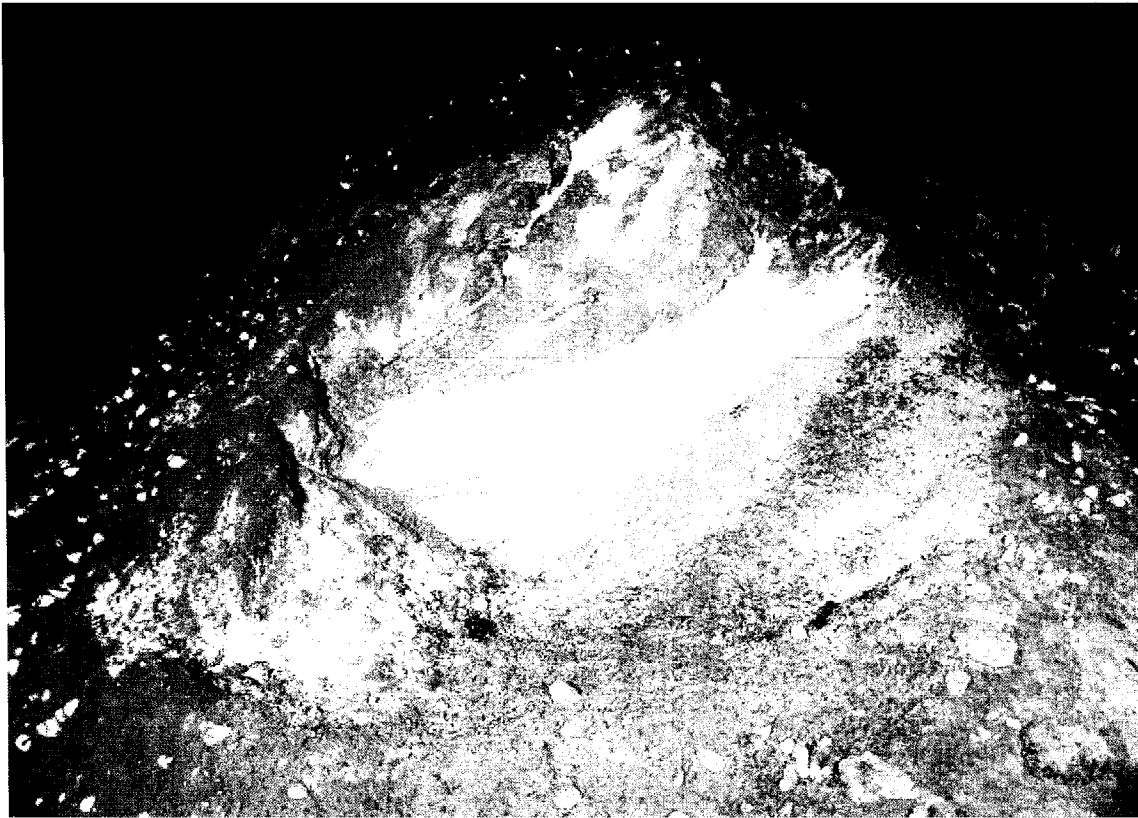
Figure 2. Gas hydrate mound "Pingo". The steep face of the mound is exposed hydrate. A thin layer of sediment with associated vesicomyid clams and white bacterial mats covers the top and base of the mound. The mound is approximately 2 m in height and 4 m wide.
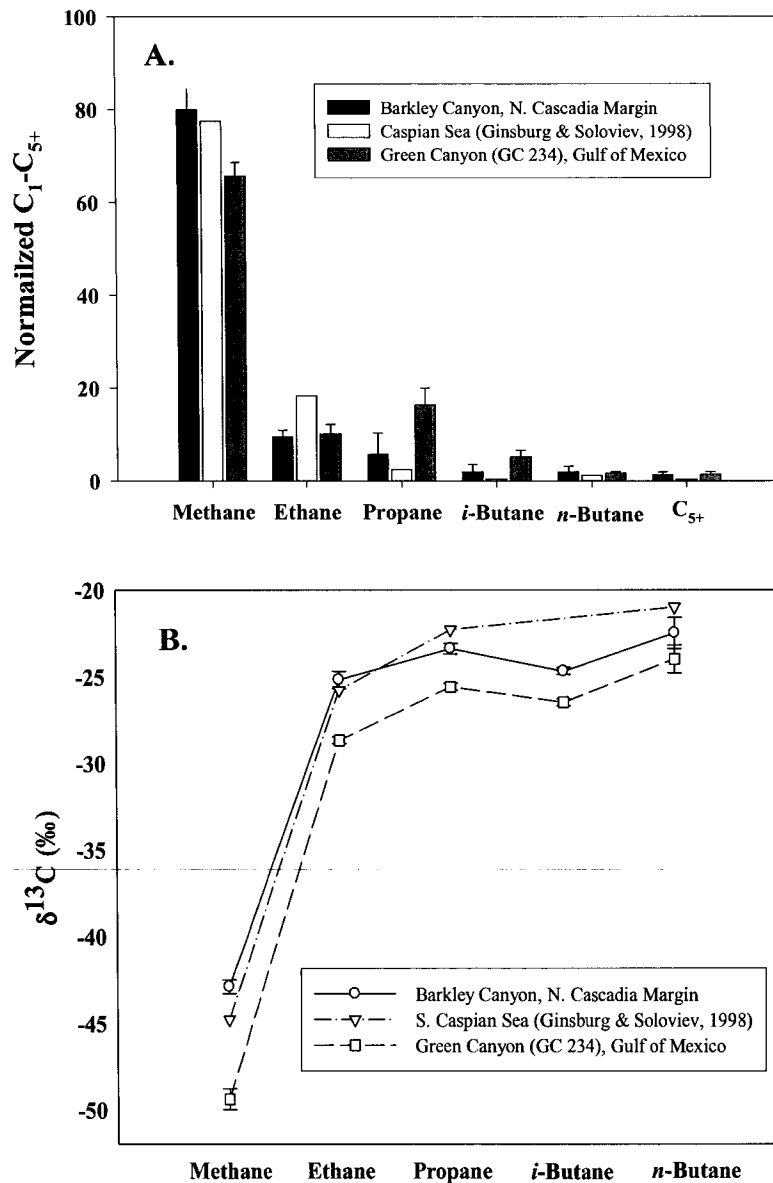
Figure 3. Normalized concentrations of C_1-C_{5+} hydrocarbons (A) and $\delta^{13}C$ values of C_1-C_4 hydrocarbons (B) from Barkley Canyon, Southern Caspian Sea and Northern Gulf of Mexico gas hydrates. Error bars (none for S. Caspian Sea data) represent the standard deviation of the mean and may not be visible if they are smaller than the symbol.
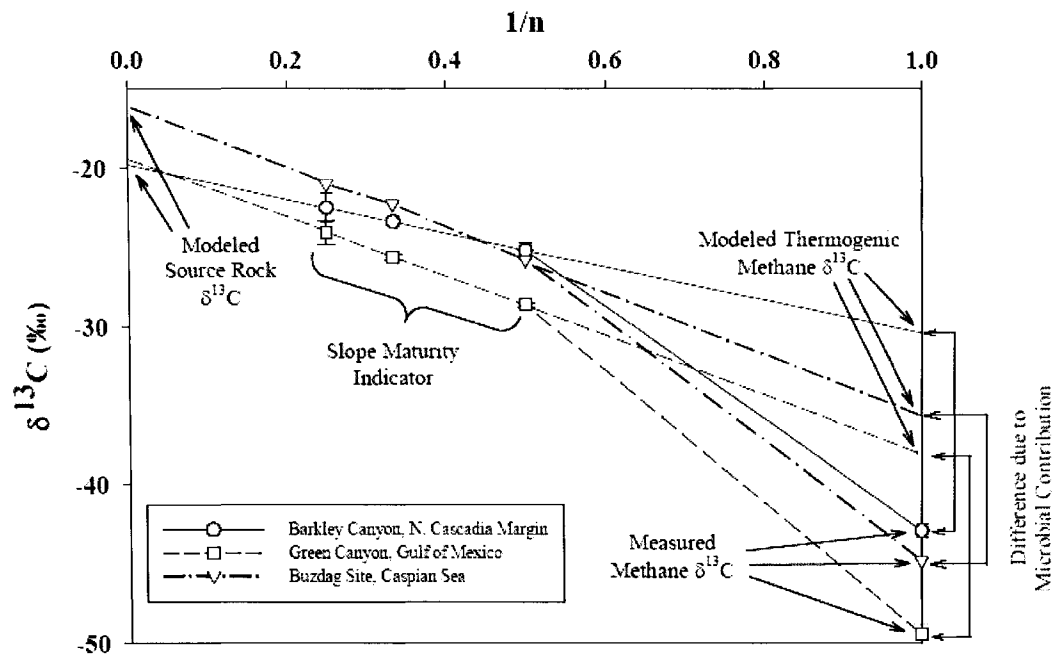
Figure 4. Gas plot model (Chung et al., 1988) using hydrate gas data from Barkley Canyon, Green Canyon and the Buzdag site. The hydrocarbons are plotted as the reciprocal of the carbon chain length (1/n) against the average $\delta^{13}C$ of the respective gas. The C_2-C_4 isotope data are extrapolated to the y-axis to predict the $\delta^{13}C$ of the source rock and to 1/n =1 to predict the $\delta^{13}C$ of the thermogenic methane endmember. The difference between the predicted $\delta^{13}C$ of thermogenic methane and measured $\delta^{13}C$ is due to microbial inputs.
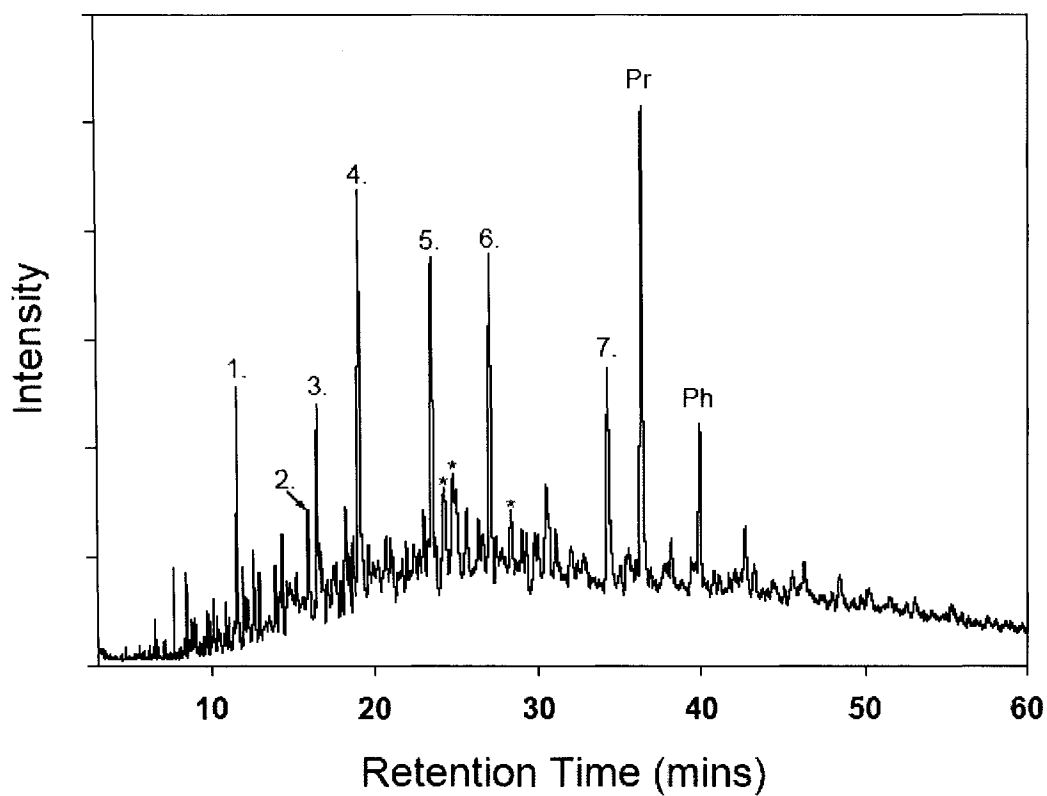
Figure 5. Partial gas chromatogram from a Barkley Canyon crude oil sample. Branched and n-alkanes include: 1) undecane, 2) dodecane, 3) 2,6-dimethylundecane, 4) 2,3,7-trimethyloctane, 5) 2,6,10-trimethyldodecane, 6) 2,3,7-trimethyldecane, 7) 2,6,10-trimethylpentadecane. Isoprenoids: pristane (Pr) and phytane (Ph). Asterisks (*) denote dimethyl- and trimethylnapthalenes.
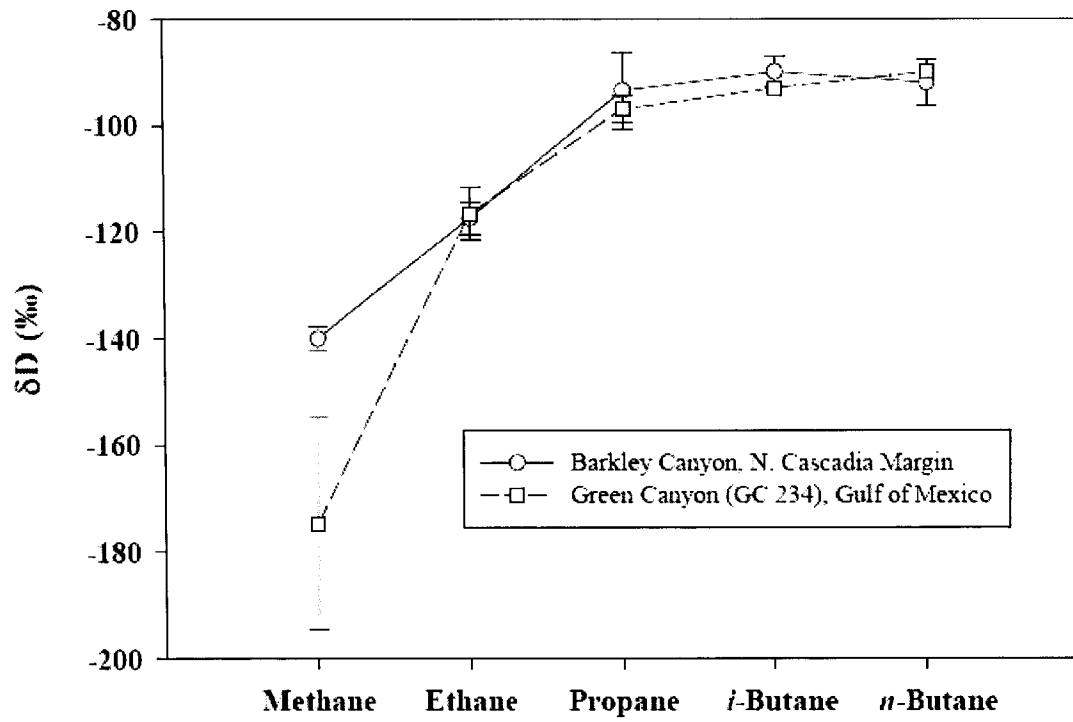
Figure 6. δD values of C₁-C₄ hydrocarbons from Barkley Canyon and Green Canyon gas hydrates. Error bars represent the standard deviation of the mean.
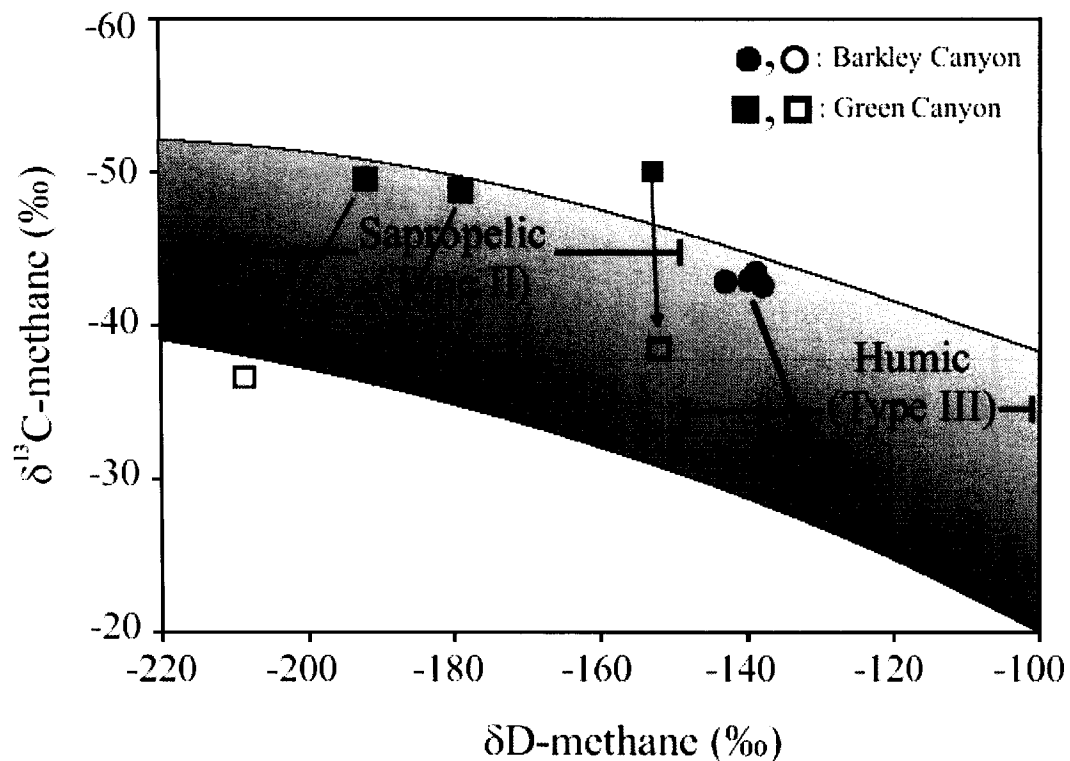
Figure 7. Natural gas region (shaded area) of the C-D diagram (modified from Whiticar, 1996) for classifying methane with $\delta^{13}C$ and δD data. The circles are data from Barkley Canyon on the northern Cascadia Margin, and the squares are data from Green Canyon in the Gulf of Mexico. The filled symbols are measured values, and the open symbols have been corrected to remove the influence of microbial inputs. See text for a description of the corrections. Arrows connect the measured values and corrected values (individually for Green Canyon data and collectively for Barkley Canyon data). The corrected Barkley Canyon data falls into a tight region defined as originating from humic Type III kerogen, while the corrected Green Canyon data fits within the sapropelic Type II kerogen region. The data range indicated for the kerogen types reflects ranges reported by Schoell (1980) and Whiticar (1996).

CHAPTER 4

PORE WATER BIOGEOCHEMISTRY AND FLUX REGIMES IN SEDIMENTS OF AN ACCRETIONARY MARGIN THERMOGENIC GAS HYDRATE SYSTEM (BARKLEY CANYON, NORTHERN CASCADIA MARGIN)

This chapter follows the format of Chemical Geology

Abstract

The Barkley Canyon gas hydrate system (~ 100 km offshore of Vancouver Island, Canada) is located along an active accretionary margin, yet the primary gas source supporting massive seafloor gas hydrate formations is a petrogenic system in the landward Tofino Basin. We investigated the pore water and sediment geochemistry from a variety of distinct seafloor sub-environments within Barkley Canyon to identify the fluid flux regimes and metabolic pathways that control the biogeochemical cycling of carbon in this complex system. Pore water profiles of sulfate and dissolved inorganic carbon (DIC) from underneath a thick bacterial mat, a dense clam community and bare sediment overlaying a gas hydrate mound indicated upward advecting, downward advecting, and diffusive flux regimes, respectively, with no evidence for substantial fluxes of methane to the water column from any of these sediment environments. Despite the lack of evidence from pore water profiles for sediment methane fluxes, methane concentrations in bottom waters (163-1724 nM) were elevated, indicating a sediment methane source. Pore water DIC ($\delta^{13}C$ = -25.0‰ ± 3.6) near the sulfate methane interface (SMI) was affected by the anaerobic oxidation of methane (AOM). Contributions of DIC from alternate sulfate reduction pathways utilizing sedimentary organic matter and/or gas condensate were also likely, but could not be delineated with the geochemical dataset. Methane accounted for up to 37% of the carbon present in carbonate nodules and up to 33% of the TIC, while the greatest contribution of methane carbon to the TOC was ~7%. Pore water $\delta^{13}CH_4$ values from -51.1 to -64.3‰ occurring at and immediately below the SMI were ^{13}C-depleted relative to the gas hydrate $\delta^{13}CH_4$ value of ~ -42‰. Localization of ^{13}C-depleted methane near the SMI suggests

that methanogenesis and sulfate reduction were coupled. Fatty acids associated with

sulfate reducing bacteria (SRB) and having $\delta^{13}C$ values as low as -67.6‰ further

implicate the role SRB in the AOM process in this gas hydrate system.

1. Introduction

Gas hydrate is concentrated in continental margin slope sediments (Kvenvolden et al., 1993) at water depths (~300-5,000 m) where the temperature and pressure regimes are suitable for gas hydrate crystallization (Sloan, 1998) and gas (primarily methane) concentrations are at saturation in sediment pore waters (Kvenvolden and Claypool, 1988; Harvey and Huang, 1995). Massive gas hydrate mounds were discovered at the seafloor along the upper continental slope of Barkley Canyon offshore of Vancouver Island, Canada (Chapman et al., 2004). Concentrations of C_2-C_{5+} alkanes in excess of 30% of the total hydrocarbon content, and stable carbon isotope signatures for methane from dissociated gas hydrate and vent gas samples were consistent with a predominantly thermogenic gas source (Pohlman et al., 2005). The Barkley Canyon system is the only location along a convergent margin where gas hydrate is supported by a predominant thermogenic gas source (Pohlman et al., 2005). The presence of thermogenic hydrocarbons in an accretionary system provides an opportunity to characterize the fluid dynamics and cycling of carbon in a tectonically driven hydrologic setting supported by diverse sources of reduced organic matter.

During seafloor observations of Barkley Canyon, thick orange and white bacterial mats and dense accumulations of vesicomyid clams were identified in close proximity to the gas hydrate mounds (Chapman et al., 2004). The bacterial mats and clams appear similar to *Beggiatoa* mats and *Calyptogena* clams from the Hydrate Ridge gas hydrate system (offshore Oregon, USA) (Sahling et al., 2002) that utilize sulfide to support their chemoautotrophic metabolism (Fisher, 1990). The source of sulfide at Hydrate Ridge is the anaerobic oxidation of methane (AOM) (Boetius et al., 2000) (Eq. 1):

$$CH_4 + SO_4^{-2} \rightarrow HCO_3^- + HS^- + H_2O \qquad (Eq.\ 1)$$

The anaerobic oxidation of methane (AOM) is mediated by ANaerobic MEthanotrophic (ANME) archaea and sulfate reducing bacteria (Hoehler et al., 1994; Boetius et al., 2000; Valentine and Reeburgh, 2000; Orphan et al., 2001). In sediments, AOM occurs within the sulfate methane interface (SMI), an interval of decreasing sulfate and increasing methane concentrations that occurs near the base of the sulfate reduction zone and upper methanogenic zone (Borowski et al., 1996). Utilization of ^{13}C-depleted methane within the SMI produces dissolved inorganic carbon (DIC) with a similar isotopic signature (Claypool and Kaplan, 1974). Thus, the depth of the δ^{13}C-DIC minimum indicates the region of greatest AOM activity.

AOM has been found to be the dominant pathway for sulfate reduction in some gas hydrate systems (Borowski et al., 1996; Niewohner et al., 1998; Boetius et al., 2000; Torres et al., 2003), while oxidation of sedimentary organic matter (Claypool et al., 2006) and hydrocarbons (Joye et al., 2004; Orcutt et al., 2005) are the predominant pathways in others. Understanding the environmental conditions that influence the expression of the different pathways and the activities of the unique microbial groups associated with each has been the subject of numerous recent studies (Orphan et al., 2004; Hallam et al., 2004; Elvert et al., 2005; Orcutt et al., 2005). In Barkley Canyon sediments, thermogenic hydrocarbons have the potential to support alternate sulfate reduction pathways, as has been observed in the northern Gulf of Mexico (Joye et al., 2004; Orcutt et al., 2005).

The biogeochemical complexity of AOM in cold seep systems is increased by sediment hydrologic regimes (e.g., diffusive and/or advective) that influence the availability of redox agents (Tryon et al., 1999; Tryon and Brown, 2001; Torres et al., 2002; Joye et al., 2005). The profiles of dissolved pore water constituents (e.g., sulfate, calcium and chloride) may be utilized to constrain the fluid regimes and mechanisms of solute transport in cold seep systems (Torres et al., 2002; Ruppel et al., 2005). Linear pore water profiles indicate diffusive solute transport (Borowski et al., 1997; Niewohner et al., 1998), whereas non-linear profiles suggest advective transport (Torres et al., 2002) or non-steady state conditions resulting from a recent change in the gas flux or a physical disruption (e.g., bioirrigation or mass deposition) (Hensen et al., 2003). In addition, distinct chemoautotrophic communities are frequently associated with specific fluid transport regimes (Tyron et al., 1999; Torres et al., 2002). For example, bacterial mat communities frequently occur in vertically-upward advective regimes, whereas bivalve communities occupy regions characterized by net in-flow of fluids and a reduced methane flux (Tsunogai et al., 2002; Torres et al., 2002; Treude et al., 2003; Orphan et al., 2004).

The present study investigated the fluid flux regimes and pore water biogeochemistry from different seafloor settings within the Barkley Canyon gas hydrate system. Analyses of pore water constituents (e.g., methane, DIC and sulfate), solid-phase sediments, and bottom waters were performed to infer flux regimes, evaluate the fate of methane and identify the fundamental biogeochemical pathways operating in this thermogenic gas hydrate system. Preliminary data for fatty acid concentrations and their

stable isotopic composition are further introduced to provide support for the role of sulfate reducing bacteria (SRB) in the oxidative cycling of methane.

2. Materials and Methods

2.1 Site Description

Barkley Canyon is a headless canyon on the northern Cascadia Margin that most likely formed when pore fluid pressures from sediment compaction overcame the cohesive forces that stabilized the slope sediments (Orange and Breen, 1992; Pohlman et al., 2005) (Fig. 1). Barkley Canyon (Pohlman et al., 2005), the northern Gulf of Mexico (Brooks et al., 1984) and the Caspian Sea (Ginsburg and Soloviev, 1998) are the only three known locations where thermogenic gas hydrate is exposed at the seafloor (Milkov, 2005). The gas hydrate (Fig. 2A) is located on an anticlinal ridge at ~850 m water depth and occurs as massive slabs (up to 7 m long) and mounds (up to 3 m high) (Chapman et al., 2004). Seepage of gas condensate, along with accumulations of bacterial mats and dense clusters of vesicomyid clams, occur within the approximate 0.5 km^2 gas hydrate field. The gas and gas condensate originates from low organic matter humic source rock (Type III kerogen) or possibly highly degraded Type II source rock kerogen in the landward Tofino Basin petroleum system (Pohlman et al., 2005).

2.2 Sample collection and seafloor observations

Sediment was collected using polycarbonate push cores (1' × 3" o.d., 1/8" wall thickness) using the mechanical arm of the research submersible ROPOS (Remotely Operated Platform for Ocean Science), which was operated from the CCGS John P.

Tully. The cores were recovered from five distinct seafloor settings in the Barkley

Canyon gas hydrate system (Table 1) on June 28 2003 (Dive R693) and June 30 2003

(Dive R696) to characterize the diverse sedimentary biogeochemical conditions. A low

flux site (R693-C3) was located at least 5 m from a gas hydrate mound. The seafloor was

smooth, had a low density of benthic fauna and no visible evidence of a chemosynthetic

biological community or authigenic carbonate rocks (Fig. 2B). The gas hydrate mound

(R696-C1) was cored on a thinly sedimented, sloped portion of the structure that was free

of dense clam or bacterial mat communities (Fig. 2C). The vesicomyid clam community

core (R696-C2) was taken from a bare spot ringed by living clams (Fig. 2D). Thin

bacterial mats were present nearby, but living clams and shell fragments were the most

prevalent seafloor feature. Epibenthic fauna (e.g., small galatheid crabs) were relatively

abundant in this area. The carbonate cemented core (R696-C3) was recovered several

meters from the closest observed gas hydrate mound. Exposure of carbonate debris

suggests the seafloor may have been eroded to expose authigenic carbonate cemented

sediment (Fig. 2E). The bacterial mat core (R696-C4) was taken from the top of an

elongated mound (Fig. 2F). The mat was ~1 cm thick and appeared as a continuous

blanket. There was no evidence of clams associated with this mat. Gas bubbles and gas

condensate were released from the sediment during core recovery from the thinly

sedimented gas hydrate mound (R696-C1), clam community (R696-C2) and bacterial mat

(R686-C4) cores, but continuous free gas or gas condensate discharge from the seafloor

was not observed at any time during this expedition. Recovered cores were placed in a

polycarbonate sleeve with a butyl stopper in the bottom to seal the push core; thus

minimizing disturbance of the cored material during the remainder of ROV operations and recovery.

2.3 Sample processing

In the shipboard laboratory, the sediment was extruded from the core liners under oxic conditions and sectioned at 3 cm intervals. Sample intervals reported in all tables represent the center of the sampled interval. Samples for gas concentration and stable carbon isotope analysis of methane were collected as 2 ml plugs from the top of each section using a 3 ml cut off plastic syringe, transferred into pre-weighed 20 ml serum vials (Hoehler et al., 2000) and sealed with 1 cm thick butyl rubber septa. For pore water collection, the sediment sections were packed into ~70 ml Reeburgh-style PVC press bodies and the pore water was extracted into 60 ml plastic syringes by applying a headspace pressure of ~80 psi to a latex sheet separating the sample from the headspace gas (Reeburgh, 1967). The pore water samples were filtered through 0.2 μm Acrodisc PES syringe filters (Pall Corporation) into clean pre-combusted (450 °C) scintillation vials and dispensed into containers appropriate to the post-cruise analyses. Extracted sediments were removed from the press bodies, wrapped in pre-combusted (450 °C) aluminum foil and placed in plastic bags. All aqueous and solid phase samples were stored at -20 °C until analysis on shore.

Water column samples were collected between 1 and 15 m above the seafloor with 5-L Niskin™ bottles mounted to the ROPOS instrument platform. 40 ml water volumes were collected in 60 ml plastic syringes using 1/8" i.d. silicone bubble tubing (Cole-Parmer) connected to the Niskin™ bottle. The syringe and tubing were rinsed and

flushed with sample water several times to remove air bubbles. Nitrogen was added to the syringe to obtain a 2:1 headspace ratio of water to gas. Dissolved gases were extracted using the headspace equilibration method (McAuliffe, 1971) by vigorously shaking the syringes for 2 minutes. Headspace methane was analyzed shipboard as described below.

2.4 Chemical and isotopic analyses of pore waters and bottom waters

Methane gas concentrations in the headspace of serum vials containing sediment plugs, and syringes containing bottom water, were analyzed on-board with a Shimadzu 14-A gas chromatograph (GC) equipped with a flame ionization detector (FID). Methane was separated isothermally (50 °C) from the other gases with a Poraplot-Q stainless steel column (8 ft, 1/8" o.d.) packed with 60/80 mesh and was quantified against certified methane standards (Scott Gas, Plumbsteadville PA). Sample vial headspace concentrations were converted to dissolved concentrations according the method described by Hoehler et al. (2000), which includes a porosity factor.

Porosity was calculated as percent water (v/v) (Eq. 2):

$$Porosity(\phi) = \frac{ml_{pw}}{\left(ml_{pw} + ml_{sed}\right)} \qquad \text{Eq. 2}$$

where the volume of pore water (ml_{pw}) was calculated from the mass loss after drying and an using an assumed seawater density of 1.03 g ml^{-1}. The volume of sediment (ml_{sed}) was calculated from the dry sediment mass and using an assumed sediment density of 2.5 g

ml^{-1} (data not shown). Obtaining accurate porosity measurements was complicated by the presence of carbonate nodules in the sediment cores, which altered the sediment density and made it difficult to fill the syringe with sediment. To minimize the effect of outlier values, porosities that varied from the mean by more than 2-standard deviations were removed from the dataset. An exponential equation fit to the modified porosity profile from all cores (Eq. 3) was used to estimate porosity values as a function of depth (z):

$$\phi(z) = 0.41^{(-0.45 \times \text{depth (cmbsf)})} + 0.63 \qquad \text{(Eq. 3)}$$

Methane from the headspace of the serum vials was analyzed for stable carbon isotope composition using a Thermo Electron Trace GC modified with a dual-cryogenic focusing inlet and a Finnigan Delta Plus XP isotope ratio mass spectrometer (IRMS) with high resistivity amplifiers to maximize instrument sensitivity (Plummer et al., 2005; Pohlman, 2006b). The $^{13}C/^{12}C$ ratios are expressed in the δ notation by standardization with tank CO_2 referenced to the NIST RM 8560 natural gas standard. The analytical precision for $\delta^{13}C\text{-}CH_4$ was better than 0.5‰.

Pore water DIC concentrations were determined with a model 5011 UIC coulometer and quantified relative to a seawater certified reference material (University of California, San Diego, CA) with an analytical precision of ±1%. One ml of 10% phosphoric acid saturated with copper sulfate was added to the vials containing 3 ml of sample to convert the DIC to carbon dioxide and precipitate dissolved sulfides (Boehme et al., 1996) which may interfere with coulometric detection of CO_2. Carbon dioxide

extracted from the samples was transferred to the coulometer using a purified helium carrier gas. Laboratory tests confirmed that the addition of the $CuSO_4/H_3PO_4$ solution did not cause any analytical artifacts.

The stable carbon isotope composition (^{13}C /^{12}C) of the pore water DIC was measured using a Thermo Finnigan Delta S IRMS. 200 µl of 85% phosphoric acid saturated with $CuSO_4$ was added to a 3-ml sample vial with a headspace of less than 500 µl. The samples were shaken vigorously at least once every 15 minutes for 1 hour to allow the DIC to transfer into the headspace as CO_2. Headspace gas from the sample vial was injected into a Thermo Finnigan Trace GC, where the CO_2 was separated isothermally (50 °C) on a Poraplot-Q capillary column (30 m, 0.32 mm i.d.). Values are reported relative to the VPBD standard in the standard δ notation. The analytical precision for $\delta^{13}C$-DIC was ±1‰, as determined from triplicate analysis of every tenth sample.

Sulfate and chloride concentrations were determined with a Dionex DX-120 ion chromatograph (IC) equipped with a 4-mm AS-9HC column and an AS-40 autosampler using the method described by Paull et al. (2005) except that our samples were diluted 1:50 (not 1:100) with Milli-Q water. Peak areas for sulfate and chloride from the diluted samples were quantified against equivalently diluted standard seawater (International Association for the Physical Sciences of the Oceans, IAPSO) analyzed at the beginning of each run and after every fifth sample. The analytical precision for dissolved sulfate and chloride was ±1% of the IAPSO standard values.

2.5 Solid phase sediment analyses

The stable carbon isotope composition (^{13}C/^{12}C) and concentrations (wt%) of the total organic carbon (TOC) and total inorganic carbon (TIC) were determined using a Thermo Finnigan Delta Plus XP IRMS for samples from cores R696-C1 and R696-C2. These cores were targeted for solid phase sediment analysis because they had substantial methane fluxes (see Results) and therefore were most likely to show evidence of alterations by AOM. The TOC samples were weighed with a microbalance into silver cups, acidified with 10% HCl to dissolve particulate carbonates, dried at 50 °C for 24 hours and then combusted on-line with a Fisons EA-1100 Elemental Analyzer (EA) interfaced to the IRMS. The total peak area from masses 44 and 45, normalized to an acetanilide standard, were used to calculate the TOC concentration. Total carbon (TC) and total nitrogen (TN) concentrations were determined in a similar manner with the exception that they were not acidified. TIC concentration was calculated as the difference between the TC and TOC. TIC concentrations are expressed as wt% $CaCO_3$, which is equivalent to the TIC concentration multiplied by 8.33 (Pimmel and Claypool, 2001). TN (used to calculate C:N mass ratios) was calculated from the acetanilide normalized total peak area from masses 28 and 29. Samples for δ^{13}C-TIC were prepared by injecting 200-μl of 85% phosphoric acid saturated with $CuSO_4$ into 2 ml serum vials containing approximately 0.2 g sediment. After heating the vials at 50 °C for 24 hours, headspace gas from the vials was injected into a Thermo Finnigan Trace gas chromatograph (GC) where gases were separated isothermally (50 °C) on a Poraplot-Q capillary column (30 m, 0.32 mm ID). The ^{13}C/^{12}C ratio is expressed in conventional δ notation relative to the VPDB standard. The average standard deviation from triplicate analyses of each sample is presented in Table 3.

2.6 Fatty acid analysis

Lipids were extracted from sediment samples with a modified Bligh Dyer method

(1959) using accelerated solvent extraction (ASE). The lipid extract was saponified

using 1N KOH and then extracted under acidic conditions to yield the acid fraction

(Canuel and Martens, 1993). The acid fraction was methylated with 3% BF_3-CH_3OH to

produce fatty-acid methyl esters (FAME). The FAME were quantified using a Hewlett

Packard 5890 GC equipped with a 30 m apolar DB-5 capillary column, a cool on-column

injector and a flame ionization detector (FID). Carbon isotope composition of the FAME

was determined by GC-C-IRMS using a TRACE GC ULTRA with a 50 m HP5-MS

column, a GC/C-III combustion unit and a Finnigan DELTA Plus XP IRMS. The

measured values have not been corrected for the addition of carbon during derivatization.

The isotope effect for adding carbon from the methylation will differ for each compound

in proportion to the number of carbon atoms in the FAME (Abrajano et al., 1994; Canuel

et al., 1997). With the exception of *i*15:0 and *ai*15:0, which were identified based on the

retention times of standard materials, the compounds were identified by their relative

retention times and retention patterns published by Elvert et al. (2003). The compound

identifications are, at this time, tentative and further work is required to unequivocally

determine double bond positions (as dimethyl disulfide - DMDS - adducts) and the

presence of cyclopropyl rings (as 4,4-dimethyloxazoline - DMOX - derivatives).

Concentrations of the fatty acids are calculated as ng gdws^{-1}, where gdws is "grams dry

weight sediment".

3. Results

3.1 Low flux site (R693-C3) pore water distributions

Concentration profiles of all pore water constituents from R693-C3 were largely

invariant with depth (Table 2; Fig. 3). Methane concentrations increased from 10 μM at

4.5 centimeters below the seafloor (cmbsf) to 80 μM at 13.5 cmbsf. Sulfate

concentrations were similar to seawater (~29 mM) in the shallowest section and

decreased slightly to 26.7 mM at the depth of the methane maxima. Near-surface DIC

concentrations were also similar to seawater (~2.2 mM) and increased to 3.9 mM at the

depth of the methane maxima. Dissolved chloride concentrations ranged between 537 to

556 mM and showed no trend with depth (Table 2). The relative standard deviation of

the chloride concentrations for this core was ±1.3%, which is similar to the ±1%

analytical variation. Similar chloride concentrations were obtained for all subsequent

cores analyzed (Table 2).

Throughout the core, the pore water $\delta^{13}CH_4$ values were similar to the gas hydrate

signature (-42.9‰ ± 0.4; Pohlman et al., 2005) (Fig. 3B). The δ^{13}C-DIC values

decreased with depth from a maximum of -5.3‰ at 1.5 cmbsf to a minimum of -15.8‰ at

10.5 cmbsf. The SMI was not captured with this core.

3.2 Gas hydrate mound (R696-C1) pore water and solid-phase distributions

In contrast to R693-C3, core R696-C1 captured the SMI at ~ 8 cmbsf and both

concentration and isotopic profiles displayed significant depth-dependent variability

(Table 2; Fig. 4A). Methane concentrations increased from 60 μM near the sediment

surface to 9.1 mM at 13.5 cmbsf, while sulfate concentrations decreased linearly from

near-seawater concentrations at the seafloor to 0.5 mM at 10.5 cmbsf. Below 10.5 cmbsf,

sulfate concentrations were uniformly low (i.e., < 2 mM). DIC concentrations increased

linearly from 4.4 mM near the seafloor to 27.4 mM at 10.5 cmbsf and were constant (27.2

to 27.5 mM) below 10.5 cmbsf. With the exception of the near-surface value, all

methane $\delta^{13}C$ values were substantially lower than the gas hydrate methane signature

(Fig. 4B). The $\delta^{13}C$-DIC value at the SMI was -26.3‰. The $\delta^{13}C$ values of both

methane and DIC progressively increased with increasing vertical distance from near the

SMI (both upcore and downcore).

The wt% of TOC for R696-C1 was invariant with depth (1.25 ± 0.07; Table 3,

Fig. 4C). The lowest $\delta^{13}C$-TOC value (-26.3‰) coincided with the SMI. C:N ratios

ranged from 7.8 to 9.9 with the highest value occurring at the bottom of the core (Table

3). The wt% of $CaCO_3$ was highest at the SMI (16.7 wt%), somewhat elevated

immediately above the SMI (6.4 %), and low (≤0.6) at other depths (Fig. 4D). Where

the wt% $CaCO_3$ was elevated, the $\delta^{13}C$-TIC values were lowest (-18‰ to -19.2‰).

3.3 Clam bed (R696-C2) pore water and solid-phase distributions

From the sediment surface to the SMI (10.5 cmbsf) in core R696-C2, methane

concentrations increased from 0.01 mM to 0.23 mM and DIC concentrations increased

from 2.6 mM to 13.5 mM, while sulfate concentrations decreased from 29.2 mM to 16.3

mM (Table 2; Fig. 5A). Relative to the concentration gradients from the seafloor to the

SMI, the concentration change for methane ($\Delta = 5.66$ mM), DIC ($\Delta = 11.8$ mM) and

sulfate ($\Delta = 15.9$ mM) in the 3 cm interval immediately below the SMI was greater. This

pattern of increasing concentration change with depth resulted in concave (i.e., non-

linear) profiles for each of the dissolved constituents. A methane $\delta^{13}C$ value in this same

core (-64.3‰) was the lowest measured in this study (Fig. 5B) and all methane $\delta^{13}C$

values from R696-C2 were lower than the gas hydrate methane $\delta^{13}C$ signature. $\delta^{13}C$-DIC

values decreased from the top (-7.7‰) and bottom (-9.2‰) of the core to a minimum

value of -24.8‰ at the SMI.

Compared to core R696-C1 from the gas hydrate mound site (Fig. 4C; Table 3),

the wt% of TOC values from R696-C2 were higher (Fig. 5C; Table 3). The highest

values (2.9 to 3.1 %) occurred above the SMI, while samples from greater depths were

slightly lower (~2.7 %). The $\delta^{13}C$-TOC profile was similar in shape to the wt% TOC

profile, and the deeper sections had lower values (-24.4 to -24.9‰) than those from

shallower depths (-23.4 to -23.6‰). C:N ratios ranged between 8.6 and 11.0 (Table 3).

The wt% $CaCO_3$ was 0.5% at the surface and increased gradually with depth to 5.7% at

the bottom of the core (Fig. 5D). The lowest $\delta^{13}C$-TIC values occurred at the SMI (-

15.9‰) and the bottom of the core (-15.8‰). Measurements of the $\delta^{13}C$ values of bulk

carbonate from discrete carbonate nodules removed from the top and bottom of the core

liner had lower $\delta^{13}C$ values (-20.3‰ and -21.5‰) than all TIC samples analyzed in this

study.

3.4 Carbonate field (R696-C3) pore water distributions

Methane concentrations from core R696-C3 were between 0.0 to 0.1 mM from

the surface to the SMI at 13.5 cmbsf (the deepest of all cores) and increased to 0.37 mM

at the bottom of the core (Table 2, Fig. 6A). Sulfate concentrations gradually decreased

to 8.9 mM at the bottom of the core, and DIC concentrations gradually increased to15.6

mM near the bottom of the core. With the exception of the low flux core (R693-C3), the methane, sulfate and DIC values from this core displayed the smallest downcore concentration changes. The depth of the $\delta^{13}CH_4$ (-53.3‰) and $\delta^{13}DIC$ (-20.3‰) minima also coincided with the depth of the SMI.

3.5 Bacterial mat (R696-C4) pore water distributions

The near-surface (0.6 mM) and maximum (12.0 mM) methane concentrations from core R696-C4 were the highest among all ROPOS push cores (Table 2, Fig. 7A). The sulfate concentrations decreased and the DIC concentrations increased with depth, as observed in the previous cores. However, the concavity of the sulfate and DIC profiles was opposite that observed for cores R696-C2 (Fig. 5A) and R696-C3 (Fig. 6A). Sulfate concentrations were elevated (31.1 mM) relative to seawater in the near-surface sample, decreasing to ~4 mM below the 4.5 cmbsf SMI. The minimum $\delta^{13}CH_4$ values (-60.1‰) occurred at the SMI (Fig. 7B), and all $\delta^{13}CH_4$ values were lower than the gas hydrate methane. The $\delta^{13}C$-DIC minima (-28.8‰) at the relatively shallow SMI (4.5 cmbsf) was the lowest DIC value measured in this study.

3.6 Bottom water methane concentrations

The average bottom water methane concentrations ranged from 14 nM (Dive 693) to 209 nM (Dive 694) (Table 4). Samples collected near large gas hydrate mounds were generally higher (33 to 209 nM) than the samples collected from other seafloor settings (14 to 45 nM). A 15 m concentration profile from above a seafloor gas hydrate mound

during Dive 694 displayed a rapid concentration decrease with distance from the exposed

gas hydrate structure (Table 4).

3.7. Fatty Acid distributions and $\delta^{13}C$ *signatures*

Core R696-C1 from the gas hydrate mound was selected for detailed fatty acid

analysis because the pore water system was characterized by strong diffusive methane

flux with a constrained pattern of post-depositional alterations by sulfate reduction

(including AOM) at the SMI (Fig. 4). The fatty acids reported represent greater than

90% of the total fatty acid content. The highest abundances of individual compounds -

monounsaturated 16:1 (e.g., 16:1ω7c, 16:1ω5c), 18:1 and a saturated 16:0 - occurred near

the sediment-water interface and ranged from 2.4 to 8.2 μg (g dws)$^{-1}$ (Table 5).

Concentrations of 16:0, 18:0 and the long-chained fatty acids (i.e. C_{22}-C_{30}; LCFA) did not

show substantial concentration changes with depth (except the peak surface

concentrations noted above). Peak concentrations of all other fatty acids typically

occurred at the SMI (~7.5 cmbsf; Table 5).

The $\delta^{13}C$ values of the LCFA ranged from -27.9 to -32.1‰ and did not

systematically vary with depth (Table 6; Fig 8). Similarly, the $\delta^{13}C$ values for the

unsaturated 16:0 and 18:0 fatty acids were within the range of -24.9 to -36.0‰ and did

not show an obvious vertical profile trend. In contrast, the other fatty acids (branched

fatty acids (BrFA) and monounsaturated compounds) had a wide range of $\delta^{13}C$ values (-

28.0 to -67.6‰), with the lowest $\delta^{13}C$ values clearly associated with the SMI (Fig. 8).

4. Discussion

4.1 Controls on fluid and pore water solute fluxes

Vertical profiles of pore water sulfate and DIC were utilized to identify variations in the flux regimes of Barkley Canyon sediments. Concave (or non-linear) profiles of pore water constituents in cold seeps indicate an advective fluid regime, while linear profiles indicate a diffusive regime (Borowski et al., 1997; Torres et al., 2002). Establishing whether or not the fluid flux regime is advective or diffusive is important for constraining the fluxes of reactants in reduction-oxidation reactions (e.g., sulfate and methane) and for interpreting how they are cycled within the sedimentary system. For example, modeled profiles of dissolved calcium from a bacterial mat site on Hydrate Ridge required upward advective fluid velocities between 50 and 100 cm yr^{-1} (Torres et al., 2002). A subsequent model study of Hydrate Ridge showed that the effect of diffusion was only significant when the upward advective velocity was less than 15 cm yr^{-1} (Luff and Wallmann, 2003). Clearly the flux and, therefore, the potential turnover of reactive pore water components (e.g., methane and sulfate) are much greater under advective conditions. Thus, interpreting of the flux regime based on the shapes of pore water profiles is important for evaluating the sedimentary biogeochemical cycles in cold seep systems. Furthermore, at Barkley Canyon and other seep sites, methane distributions are useful for evaluating the potential methane flux across the sediment-seawater interface under different flux regimes, and hence its potential as a source of fossil carbon and organic matter to the oceanic water column (Pohlman, Chapter 2).

The potential for gas hydrate dissociation to release water and gas must be evaluated when interpreting pore water profiles in gas hydrate bearing sediments. Hydrate water dilutes the solute concentrations in the vicinity of the gas hydrate (Ussler

and Paull, 1995), while gas ebullition will enrich the methane concentrations and may lead to vertical homogenization of both pore waters and solid phase materials. The concentration of dissolved chloride (a biogeochemically conservative tracer) was utilized to determine if dilution effects due to hydrate dissociation occurred. Chloride is excluded from the matrix during gas hydrate formation, and initially becomes concentrated in the surrounding pore fluids (Ussler and Paull, 1995). With time, the excess chloride diffuses and equilibrates with the bulk pore water so that when the gas hydrate dissociates, the surrounding pore fluid is diluted, thus resulting in chloride values below ambient. Evidence of dissociated gas hydrate is inferred from low-chloride anomalies in recovered cores (Ussler and Paull, 1995). Pore water chloride concentrations from all cores (544 mM ± 7 mM; Table 2) were indistinguishable from ambient seawater for this region (Suess et al., 1999). The uniform seawater chloride signature from the Barkley Canyon push cores (Table 2) indicates that none of them contained gas hydrate. .

Given the evidence that gas hydrate dissociation did not influence the chemical composition of the pore fluids, the profiles should reflect the *in situ* conditions, within the limits of the sampling protocol. For the low flux core (R693-C3; Fig. 3A), concentrations of pore water constituents were similar to seawater. Although such profiles may result from seawater in-flow or bioirrigation, there was no visible or other evidence for either of these processes; thus suggesting a nominal fluid and chemical flux regime. The concentration gradients in the carbonate debris site profiles (R696-C3; Fig. 6) were greater than the low flux site, but were less than the other sites investigated in this study. The production of authigenic carbonate rocks typically occurs at the SMI in high flux settings. Thus, the occurrence of authigenic carbonate rocks on the seafloor

suggests the seafloor has been eroded, and the nominal pore water gradients suggest a

reduction in the flux of methane and at this site. In contrast, steep linear sulfate and DIC

profiles from the thinly sedimented gas hydrate mound (R696-C1; Fig. 4A) indicate

active diffusive fluid and chemical fluxes (Borowski et al., 1997; Niewohner et al., 1998)

and near-complete consumption of methane within these sediments.

The concavity in the sulfate and DIC profiles from the clam site (R696-C2; Fig.

5A) and bacterial mat site (R696-C4; Fig. 7A) suggest advective flux regimes or cycling

of these constituents between the sediment water interface and the SMI (Torres et al.,

2002). Concavity similar to that observed at clam site (R696-C2) has been attributed to

downward fluid advection resulting from active clam bioirrigation (Torres et al., 2002;

Orphan et al., 2004). The biological fluid pumping rate of fluid into sediment by clam

communities can be as high 100 L m^{-2} d^{-1} (Suess et al., 1998), which equates to a sulfate

flux of about 2,900 mmols m^{-2} d^{-1}; an influx that vastly exceeds maximum measured rates

of sulfate consumption (140 to 244 mmols m^{-2} d^{-1}) from cold seeps at Hydrate Ridge

(Boetius et al., 2000) and the northern Gulf of Mexico (Joye et al., 2004; Orcutt et al.,

2005). Excess sulfate availability at the Barkley Canyon clam site appears to have

supported rates of AOM sufficient to reduce the methane concentration to <80 μM and

minimize the potential for methane to escaping from seafloor of sites colonized by clams.

Furthermore, it has been shown that the flux of material in advective systems overwhelms

reactive effects occurring between the seafloor and the SMI (Torres et al., 2002). Thus,

the profile curvature we observed likely due to advective mixing between the seawater

and SMI endmembers, not reactive effects occurring between them.

The concave pore water sulfate and DIC profiles at the bacterial mat site (R696-C4; Fig. 7A) indicated upward advective fluid flow, consumption of sulfate between the sediment water interface and the SMI, or both (Torres et al., 2002). The combination of upward fluid advection and high methane concentrations near the seafloor make the bacterial mat site the most likely to support a flux of methane to the overlying water column. To evaluate this potential, we calculated methane flux under the assumption of advective fluid flow. The advective flux velocity we utilized (75 cm yr^{-1}) was the average velocity from the Hydrate Ridge site (Torres et al., 2002) that had a sulfate profile similar to R696-C4. Conservative transport of 0.62 mM methane from 1.5 cmbsf (Table 2) at an advective velocity of 75 cm yr^{-1} through sediment with a porosity of 0.75 yields a potential water column methane flux of 0.9 mmol m^{-2} d^{-1}, which is negligible when compared to methane fluxes of 30 and 90 mmol m^{-2} d^{-1} measured at Hydrate Ridge by Torres et al. (2002). Evidence for the complete oxidation of methane has been found by numerical modeling of methane turnover in sediments overlying gas hydrate at Hydrate Ridge (Luff and Wallmann, 2003) at fluid advection velocities below 100 cm yr^{-1}. This finding is consistent with the methane fluxes we calculate here for Barkley Canyon, but not those reported by Torres et al. (2002) at Hydrate Ridge. Obtaining accurate methane concentrations is difficult because the *in situ* levels frequently exceed saturation at atmospheric pressure (~1.8 mM; Yamamoto, 1976). Hence, significant methane may be lost during core recovery and sample processing, leading to an underestimate using the approach we employed. However, the surface porewater samples were undersaturated with methane, so rapid loss of methane from those samples is not expected. Alternatively, the discrepancy between our calculation and those of

Torres et al. (2002) may indicate spatial and temporal heterogeneities, sampling artifacts or a more active AOM consortium in Barkley Canyon.

4.2 Pore water methane sources and alterations

The range of $\delta^{13}C$ values of methane extracted from Barkley Canyon sediment pore waters (-34.6‰ to -64.3‰; Table 2) contrasts with the uniform gas hydrate bound $\delta^{13}CH_4$ signatures (-42.7‰ ± 0.5, n=5; Pohlman et al., 2005). The $\delta^{13}C$ value of the gas hydrate methane represents the deep source signature; whereas the $\delta^{13}C$ values of the pore water methane also reflects contributions from methanogenesis and alterations from methane oxidation. During methane oxidation, $^{12}CH_4$ is preferentially consumed, which leaves the residual methane pool ^{13}C-enriched (Claypool and Kaplan, 1974). A trend of decreasing concentration and $\delta^{13}C$ for methane profiles from the SMI to the sediment water interface (Figs. 4-7, panels A and B; Table 2) is consistent with oxidation of methane in that interval. In contrast, the $\delta^{13}CH_4$ values at and below the SMI were as low as -68‰ and were always less than the hydrate-bound methane (Figs. 4-7, panel B). These values are between the typical range of microbial methane (-70 to -90‰; Whiticar, 1999) and the thermogenic gas source (-42.7‰ ± 0.5, n=5; Pohlman et al., 2005), which indicates methane in this interval is likely a mixture of microbial methane and the thermogenic endmember.

Although the northern Cascadia margin accretionary system contains a large deep reservoir of microbial methane (Hyndman and Davis, 1992) with numerous occurrences of gas hydrate near the seafloor (Milkov et al., 2005; Riedel et al., 2006; Pohlman, Chapter 5), it is unlikely that migration of deep microbial gas accounts for the microbial

contributions near the SMI. A more plausible explanation is *in situ* production of

microbial methane near the SMI, which is consistent with similar isotopic evidence

(Borowski et al., 1997; Pohlman, Chapter 6), rate measurements (Hoehler et al., 1994;

Orcutt et al., 2005) and molecular ecological evidence (Hallam et al., 2004) indicating

methanogenesis is coupled to sulfate reduction and/or AOM near the SMI. In marine

systems, the primary methanogenic pathway is carbonate reduction (Whiticar, 1999).

Thus, the $\delta^{13}CH_4$ values near the SMI are likely a mixture of thermogenic methane that

has migrated from greater depth and microbial methane generated by carbonate reduction

near the SMI.

4.3 Evidence for anaerobic methane oxidation and alternate substrates for sulfate

reduction

Consumption of methane and sulfate, and production of DIC in cores R696-C1 to

C4 (Figs. 4-7, panel A) are consistent with AOM (Eq. 1). However, without direct AOM

rate measurements (Treude et al., 2003; Joye et al., 2004) or $\delta^{13}C$-DIC values being less

than the $\delta^{13}C$ of the alternate carbon sources, proof of AOM is considered equivocal

(Claypool and Kaplan, 1974; Suess and Whiticar, 1989; Claypool et al., 2006). Making

this distinction in Barkley Canyon is confounded by the presence of numerous alternate

reduced carbon substrates (e.g., TOC and gas condensate) and a $\delta^{13}CH_4$ thermogenic gas

signature less distinct than microbial methane from the alternate carbon sources.

To evaluate the significance of AOM in this system, the DIC concentration and

$\delta^{13}C$-DIC data from the ROPOS push cores were compared to 2-source mixing models of

seawater DIC (2.3 mM, 0.5‰; Ortiz et al., 1997) and all other potential sources of DIC in

this system (Fig. 9). The δ^{13}C-DIC values for samples in the concentration range of 2-12 mM DIC require a methane contribution, thus indicating that contributions of DIC from AOM within that interval. The shift toward lower δ^{13}C-DIC values at greater concentrations (Fig. 9) implies an increased contribution from the non-methane carbon sources according to the mixing model. However, the shift toward greater δ^{13}C-DIC values may also be explained by ^{13}C-enrichment of the DIC pool by *in situ* methanogenesis - a process that likely occurred (see above), but one that is not considered in the mixing models. During the carbonate reduction methanogenic pathway (Eq. 4), ^{12}C-DIC is preferentially assimilated (Claypool and Kaplan, 1974).

$$4H_2 + HCO_3^- + H^+ \rightarrow CH_4 + 3H_2O \qquad \text{(Eq. 4)}$$
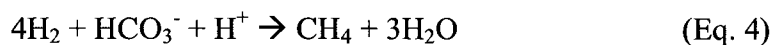
As a result, the residual DIC pool becomes ^{13}C-enriched; thus yielding greater δ^{13}C-DIC values. Consequently, the δ^{13}C-DIC values in the methanogenic zone do not reflect simple endmember mixing. Thus, although AOM was likely an active process, given the large number of potential DIC sources, the isotopic similarity among many of them and the potential effect of methanogenesis on the DIC signatures, it was not possible to apportion relative contributions from the individual sources.

In other methane-rich systems, complex hydrocarbons (Joye et al., 2004; Orcutt et al., 2005) and TOC (Claypool et al., 2006) have been shown to dominate sulfate reduction while still quantitatively consuming methane by AOM. Given the abundance of gas condensate in the Barkley Canyon sediments and the relatively high wt % of TOC in the ROPOS push cores (Table 3), it is possible that reduced organic compounds also

supported sulfate reduction, further complicating the relationships and interpretation of Figure 9. To fully constrain the sulfate reduction pathways and the effect of methanogenesis, simultaneous studies targeting the specific processes and biomarkers indicative of specific microbes must be conducted. The present study nonetheless demonstrates that AOM was an active process and illustrates the limitation of evaluating the source of DIC in cold seep systems with simple isotope mixing models.

4.4 Sources and alterations of sedimentary carbon (TOC and TIC)

Relative to biogenic carbonate, which has a $\delta^{13}C$ ranging from ~ -2 to +2 ‰ (Suess and Whiticar, 1989), the TIC from this study (-9.9‰ ± 6.4; Table 3) was lower and indicates an authigenic carbonate contribution (Aloisi et al., 2002). AOM, an active process in the cores we investigated, generates alkalinity as HCO_3^- (Eq. 1), which supports the production of authigenic carbonates according to Eq. 5 (Berner, 1980):

$$Ca^{+2} + 2HCO_3^- \rightarrow CaCO_3(s) + CO_2 + H_2O \qquad (Eq.~5)$$
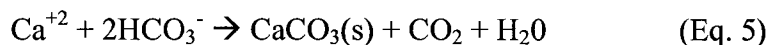
Because AOM is focused at the SMI, authigenic carbonate production is predicted to be most prevalent at the SMI in cold seep systems (Wallmann et al., 2006). In the diffusive core R696-C1 (Fig. 4D), the lowest $\delta^{13}C$-TIC values (-18.0‰ to -19.2‰) and highest wt% $CaCO_3$ (6.7 to 16.7%) were found at the SMI (Fig. 4D; Table 3) - a pattern consistent with *in situ* production of authigenic carbonate at the SMI. The potential contribution of methane carbon to the bulk TIC at the SMI in R696-C1 was determined by a simple isotope mass balance approach (Eq. 6):

$$f_{methane} = \frac{\delta^{13}C_{TIC} - \delta^{13}C_{methane}}{\delta^{13}C_{Biogenic} - \delta^{13}C_{methane}} \qquad \text{(Eq. 6)}$$

where $f_{methane}$ is the fractional contribution of methane, $\delta^{13}C_{TIC}$ is the measured $\delta^{13}C$

values of the TIC (-18.0‰ and -19.2‰; Table 3), $\delta^{13}C_{methane}$ is the $\delta^{13}C$ of methane at the

SMI (-58.2‰; Table 2), and $\delta^{13}C_{biogenic}$ is the $\delta^{13}C$ of biogenic carbonate for this oceanic

region (0‰; Ortiz et al, 1997). The results of this model indicate methane carbon was as

much as ~31 to 33% of the total carbon in the TIC, assuming no other sulfate reduction

pathways contributed. In contrast, TIC below the SMI displayed a decreasing

contribution from authigenic carbonate with greater depth (Fig. 4D). The wt% CaCO₃

was uniformly low (below detection to 0.6%) and the $\delta^{13}C$ increased from -5.1‰

immediately below the SMI to -0.9‰ at the bottom of the core (Table 3). The $\delta^{13}C$-TIC

of the deepest sample (-0.9‰) was within the expected range of pure biogenic carbonate

(Ortiz et al., 1997). The absence of substantial alterations in TIC near the bottom of this

core suggests the methane flux at this site may have increased since the sediment was

deposited.

If the TIC below the SMI of diffusive core R696-C1 was unaltered by a post

depositional process (e.g., AOM), the $\delta^{13}C$ of the TOC values from that interval (~ -24‰;

Fig. 4C, Table 3), may represent the depositional source signature of the TOC (a.k.a,

particulate organic carbon, or POC). Assuming this source signature remained constant

during the time when the material was deposited, the $\delta^{13}C$ of the TOC from that interval

may be utilized as an endmember to identify potential contributions of methane carbon to

the TOC (e.g., as microbial biomass) at other depths and other locations. A mass balance approach similar to that performed above that used the methane $\delta^{13}C$ value at the SMI (-58.2‰; Table 2) and the unaltered TOC value discussed above (-24‰; Table 3) as endmembers for the measured TOC at the SMI (-26.3‰; Table 3) indicates methane contributed as much as ~7% of the carbon in the TOC sample from SMI if no other sulfate reduction pathways contributed to the TOC.

The $\delta^{13}C$ values of the TIC from the clam core R696-C2 (-3.2‰ to 15.9‰) were also altered by post-depositional authigenic carbonate production (Fig. 5D), but the greatest alterations were not from material in the sulfate reduction zone as they were in the diffusive core R696-C1. For example, authigenic carbonate nodules from the above and below the SMI had $\delta^{13}C$ values of -20.3‰ and -21.5‰, respectively. Using the methane $\delta^{13}C$ value from the SMI (-58.1‰) and the biogenic carbonate $\delta^{13}C$ signature for this region (0‰; Ortiz et al, 1997), the mass balance estimate for the contribution of methane carbon to the authigenic nodules was as much as ~35 to 37%. In contrast, it was not possible to identify potential contributions of methane in the TOC because the TOC $\delta^{13}C$ values (-23.4‰ to -24.9‰; Table 3) were similar to the inferred TOC source material (-24.0‰).

4.5 Role of sulfate reducing bacteria (SRB) in AOM

The $\delta^{13}C$ values and concentrations of the fatty acids discussed in this section are tentative because the $\delta^{13}C$ values have not been corrected for the addition of a methyl carbon added during derivatization, and the compounds have not been unambiguously identified (see Methods). Despite those limitations, we believe the reported $\delta^{13}C$ values

and compound identification are representative of the actual values and compounds, and, thus, are useful for a preliminary discussion. There were four primary types of fatty acids identified (Volkman, 1998 and references therein): 1) those ubiquitous to plants, bacteria and zooplankton (16:0 and 18:0); 2) long-chained fatty acids (LCFA) derived from waxes of terrigenous plants (22:0 to 30:0); 3) monounsaturated fatty acids (e.g., 16:1ω7c); and 4) -iso and -anteiso branched fatty acids (BrFA) (e.g., ai-15:0). The SRB biomarkers, which are of greatest interest to this study, are the monounsaturated and branched fatty acids (Hinrichs et al., 2000; Elvert et al., 2003). The $\delta^{13}C$ values of the terrigenous plant LCFAs and ubiquitous unsaturated 16:0 and 18:0 fatty acids did not change with depth and had $\delta^{13}C$ values (-24.9‰ to -36.0‰) that were considerably more enriched than the monounsaturated, -iso and -anteiso branched fatty acids (-28.3‰ to -67.6‰) (Fig. 8, Table 6). The ^{13}C-depletion of the monounsaturated fatty acids and branched fatty acids indicative of SRBs was greatest at the SMI (Fig. 8), which provides strong evidence that methane carbon was assimilated into the SRB membrane lipids (Hinrichs et al., 2000; Elvert et al., 2003). Furthermore, the ~30‰ range of $\delta^{13}C$ values among these compounds indicates alternate reduced organic compounds were also utilized as carbon sources, or detrital sources contributed to the isotopic signatures.

The tentatively identified compounds have been associated with the Desulfosarcina/Desulfococcus (DSS) group of SRBs, which are members of the consortium of ANMEs and SRBs that mediate AOM (Hinrichs et al., 1999; Boetius et al., 2000; Orphan et al., 2001; Elvert et al., 2003; Orphan et al., 2004; Elvert et al., 2005). The most ^{13}C-depleted fatty acids from Barkley Canyon were the i-15:0 and ai-15:0 BrFA (Fig. 8; Table 6). Recent evidence has shown these lipids occur in DSS groups that

associate with the ANME-1 type cluster (Blumenberg et al., 2004). In the northern Gulf of Mexico, ai-15:0 was the most abundant fatty acid present and was among the most ^{13}C-depleted from a gas hydrate associated sample (Zhang et al., 2002). In contrast, at Hydrate Ridge, ai-15:0 was not particularly abundant and was not among the most ^{13}C-depleted fatty acids. Confirmation of the additional diverse FAs from Barkley Canyon will provide information about the specific organisms that facilitate AOM at Barkley Canyon and will be useful for comparing Barkley Canyon to other cold seep systems.

4.6 Bottom water methane and potential sources

Bottom water methane concentrations (14-209 nM; Table 4) from ~0.5 meters above the seafloor at Barkley Canyon were 1-2 orders of magnitude greater than background deep ocean concentrations of ~ 1 nM (Scranton and Brewer, 1978), but are less than values as high as 4400 nM from "several tens of meters" above the seafloor at Hydrate Ridge (Heeschen et al., 2005). Potential mechanisms for transferring methane to the water column include diffusive flux, advective fluid flux (Linke et al., 1994; Torres et al., 2002), gas (bubble ebullition) discharge (Torres et al., 2002), and dissolution of the gas hydrate mounds in direct contact with seawater (Haeckel et al., 2004). Among these possibilities, we have shown a negligible flux of methane from diffusive and advective sedimentary settings (see Sec. 4.1), and we observed no evidence of gas discharge at any time during this expedition. In contrast, bubble discharge from the seafloor (Torres et al., 2002; Tryon et al., 2002) and evidence for bubbles in the water column (Heeschen et al., 2003) are a persistent features of Hydrate Ridge, where elevated water column concentrations have been measured (Heeshen et al., 2005). Bottom water currents of 0.9

cm s^{-1} over a vent (< 0.5 km^2) at Hydrate Ridge can completely replace the bottom water on timescales between 0.5 and 2 hrs (Heeschen et al., 2005). Thus, unless gas is actively discharging from the seafloor, the local bottom water methane concentrations are not likely to be substantially affected by this source.

Higher methane concentrations from samples collected near the gas hydrate mounds and decreasing concentrations with increasing distance from the mounds (Table 6) suggest that a likely source of methane in bottom waters at Barkley Canyon was from seawater exposed gas hydrate (see Fig. 2A). Although the seafloor is within the gas hydrate stability zone, gas hydrate in direct contact with seawater undergoes constant dissociation because of the dramatic concentration gradient between gas hydrate and seawater (Haeckel et al., 2004). Alternatively, unidentified venting of gas-rich fluids that support the massive gas hydrate accumulations might also have contributed. Differentiating the specific source (dissociation or fluid venting) requires a more focused sampling technique or high resolution geochemical and thermal profiles of the fluids near the gas hydrate mounds (e.g., Joye et al., 2005). Also, the contribution from bubble discharge (when active) should be investigated since subsequent observations at Barkley Canyon have identified this process (Pohlman et al., 2005).

5. Synthesis and Conclusions

Barkley Canyon contains the first known cold seep with gas hydrate at the seafloor that is both located along an active accretionary margin and sustained by a primary thermogenic gas source. This study was designed to investigate the relationship between seafloor settings and the fluid flux regimes and to establish a basic geochemical

model of carbon cycling for this seep system. Fluid flux regimes were inferred from pore water concentration profiles of methane, sulfate and DIC collected from distinct seafloor settings (e.g., bacterial mats and clam colonies). Advective and diffusive fluid flux regimes were identified in the various sub-environments, and, in all cases, the surface sediments (12-18 cm) were an efficient bioreactor for methane consumption; thus limiting the flux of methane across the sediment-water interface (Fig. 10). However, the water column concentrations of methane were several orders of magnitude greater than background seawater. Because there were no observations of active gas discharge from the seafloor at any time during this expedition, we suggest that dissolution of gas hydrate exposed directly to seawater or unidentified active fluid seeps may be the source of the water column methane.

Stable carbon isotope data from dissolved methane, DIC, gas condensate, TOC, TIC and authigenic carbonates were utilized to construct a biogeochemical model for the Barkley Canyon seep system (Fig. 11). Although the primary source of methane was thermogenic, we identified a microbial contribution near the SMI suggestive of coupled AOM and methanogenesis. δ^{13}C-DIC values were less than what is possible by contributions from all other sources of carbon except methane, confirming AOM was an active process at this site. However, other reduced organic compounds (e.g., gas condensate and POC) may have also contributed to the net consumption of sulfate and production of DIC. Methane contributed as much as ~37% of the carbon present in carbonate nodules and ~33% of the TIC, while the greatest contribution of methane carbon to the TOC was ~7%.

This geochemical description of the Barkley Canyon gas hydrate system should provide a foundation for studies targeting specific pathways and processes that have been evaluated at the more extensively studied Hydrate Ridge and the northern Gulf of Mexico cold seeps. For example, rate measurements of specific processes can more definitively establish the relative importance of each pathway to the net carbon and sulfur cycles, while combined biomarker and phylogenetic studies can help identify the organisms that mediate the processes and define their roles in this complex ecosystem. Ultimately, a more comprehensive understanding of this system will improve our understanding of all cold seep systems, which play a critical role in controlling the flux of materials to the hydrosphere and atmosphere.

References

Abrajano, T. A.; Murphy, D. E.; Fang, J.; Comet, P.; Brooks, J. M. $^{13}C/^{12}C$ ratios in individual fatty-acids of marine mytilids with and without bacterial symbionts. Org. Geochem. 21: 611-617; 1994.

Aloisi, G.; Pierre, C.; Rouchy, J. M.; Faugeres, J. C. Isotopic evidence of methane-related diagenesis in the mud volcanic sediments of the Barbados Accretionary Prism. Continental Shelf Research. 22: 2355-2372; 2002.

Berner, R. A. Early Diagenesis: A Theoretical Approach. Princeton, NJ: Princeton University Press; 1980.

Bligh, E. G.; Dyer, W. J. A rapid method of total lipid extraction and purification. Canadian Journal of Biochemistry and Physiology. 37: 911-917; 1959.

Blumenberg, M.; Seifert, R.; Reitner, J.; Pape, T.; Michaelis, W. Membrane lipid patterns typify distinct anaerobic methanotrophic consortia. Proceedings of the National Academy of Sciences of the United States of America. 101: 11111-11116; 2004.

Boehme, S. E.; Blair, N. E.; Chanton, J. P.; Martens, C. S. A mass balance of ^{13}C and ^{12}C in an organic-rich methane-producing marine sediment. Geochim. Cosmochim. Acta. 60: 3835-3848; 1996.

Boetius, A.; Ravenschlag, K.; Schubert, C. J.; Rickert, D.; Widdel, F.; Gieseke, A.; Amann, R.; Jorgensen, B. B.; Witte, U.; Pfannkuche, O. A marine microbial consortium apparently mediating anaerobic oxidation of methane. Nature. 407: 623-626; 2000.

Borowski, W. S.; Paull, C. K.; Ussler, W. Marine pore-water sulfate profiles indicate in situ methane flux from underlying gas hydrate. Geology. 24: 655-658; 1996.

Borowski, W. S.; Paull, C. K.; Ussler, W. Carbon cycling within the upper methanogenic zone of continental rise sediments: An example from the methane-rich sediments overlying the Blake Ridge gas hydrate deposits. Mar. Chem. 57: 299-311; 1997.

Brooks, J. M.; Kennicutt, M. C. I.; Fay, R. R.; McDonald, T. J.; Sassen, R. Thermogenic gas hydrates in the Gulf of Mexico. Science. 225: 409-411; 1984.

Bustin, R. M. Organic maturation and petroleum source-rock potential of Tofino Basin, Southwestern British-Columbia. Bulletin of Canadian Petroleum Geology. 43: 177-186; 1995.

Canuel, E. A.; Martens, C. S. Seasonal-variations in the sources and alteration of organic-matter associated with recently-deposited sediments. Org. Geochem. 20: 563-577; 1993.

Canuel, E. A.; Freeman, K. H.; Wakeham, S. G. Isotopic compositions of lipid biomarker compounds in estuarine plants and surface sediments. Limnol. Oceanogr. 42: 1570-1583; 1997.

Chapman, N. R.; Pohlman, J. W.; Coffin, R. B.; Chanton, J. P.; Lapham L. Thermogenic gas hydrates in the northern Cascadia Margin. EOS. 85: 361-365; 2004.

Claypool, G. E.; Kaplan, I. R. The origin and distribution of methane in marine sediments. In: Kaplan, I. R., ed. Natural Gases in Marine Sediments: Plenum Press. 99-139; 1974.

Claypool, G. E.; Milkov, A. V.; Lee, Y.-J.; Torres, M. E.; Borowski, W.; Tomaru, H. Microbial methane generation and gas transport in shallow sediments of accretionary complex, southern Hydrate ridge (ODP Leg 204), offshore Oregon, USA. Proc. ODP Sci. Results, 204; 2006.

Elvert, M.; Boetius, A.; Knittel, K.; Jorgensen, B. B. Characterization of specific membrane fatty acids as chemotaxonomic markers for sulfate-reducing bacteria involved in anaerobic oxidation of methane. Geomicrobiology Journal. 20: 403-419; 2003.

Elvert, M.; Hopmans, E. C.; Treude, T.; Boetius, A.; Suess, E. Spatial variations of methanotrophic consortia at cold methane seeps: implications from a high-resolution molecular and isotopic approach. Geobiology. 3: 195-209; 2005.

Fisher, C. R. Chemoautotrophic and methanotrophic symbioses in marine-invertebrates. Reviews in Aquatic Sciences. 2: 399-436; 1990.

Ginsburg, G. D.; Soloviev, V. A. Submarine Gas Hydrates. St Petersburg: VNII Okeangeologia; 1998.

Haeckel, M.; Suess, E.; Wallmann, K.; Rickert, D. Rising methane gas bubbles form massive hydrate layers at the seafloor. Geochimica et Cosmochimica Acta. 68: 4335-4345; 2004.

Hallam, S. J.; Putnam, N.; Preston, C. M.; Detter, J. C.; Rokhsar, D.; Richardson, P. M.; Delong, E. F. Reverse methanogenesis: Testing the hypothesis with environmental genomics. Science. 305: 1457-1462; 2004.

Harvey, L. D. D.; Huang, Z. Evaluation of the potential impact of methane clathrate destabilization on future global warming. Journal of Geophysical Research-Atmospheres. 100: 2905-2926; 1995.

Heeschen, K. U.; Collier, R. W.; de Angelis, M. A.; Suess, E.; Rehder, G.; Linke, P.; Klinkhammer, G. P. Methane sources, distributions, and fluxes from cold vent sites at Hydrate Ridge, Cascadia Margin. Global Biogeochemical Cycles. 19: 2005.

Heeschen, K. U.; Trehu, A. M.; Collier, R. W.; Suess, E.; Rehder, G. Distribution and height of methane bubble plumes on the Cascadia Margin characterized by acoustic imaging. Geophysical Research Letters. 30: doi:10.1029/2003GL016974; 2003.

Hensen, C.; Zabel, M.; Pfeifer, K.; Schwenk, T.; Kasten, S.; Riedinger, N.; Schulz, H. D.; Boettius, A. Control of sulfate pore-water profiles by sedimentary events and the significance of anaerobic oxidation of methane for the burial of sulfur in marine sediments. Geochim. Cosmochim. Acta. 67: 2631-2647; 2003.

Hinrichs, K. U.; Hayes, J. M.; Sylva, S. P.; Brewer, P. G.; Delong, E. F. Methane-consuming archaebacteria in marine sediments. Nature. 398: 802-805; 1999.

Hinrichs, K. U.; Summons, R. E.; Orphan, V.; Sylva, S. P.; Hayes, J. M. Molecular and isotopic analysis of anaerobic methane-oxidizing communities in marine sediments. Org. Geochem. 31: 1685-1701; 2000.

Hoehler, T. M.; Alperin, M. J.; Albert, D. B.; Martens, C. S. Field and laboratory studies of methane oxidation in an anoxic marine sediment - evidence for a methanogen-sulfate reducer consortium. Glob. Biogeochem. Cycle. 8: 451-463; 1994.

Hoehler, T. M.; Borowski, W. S.; Alperin, M. J.; Rodriguez, N. M.; Paull, C. K. Model, Stable isotope,and radiocarbon characterization of anaerobic methane oxidation in gas hydrate-bearing sediments of the Blake Ridge. Proceedings of the Ocean Drilling Program, Scientific Results: Ocean Drilling Program. 79-85; 2000.

Hyndman, R. D.; Davis, E. E. A mechanism for the formation of methane hydrate and sea-floor bottom-simulating reflectors by vertical fluid expulsion. J. Geophys. Res. -Solid Earth. 97: 7025-7041; 1992.

Joye, S. B.; Boetius, A.; Orcutt, B. N.; Montoya, J. P.; Schulz, H. N.; Erickson, M. J.; Lugo, S. K. The anaerobic oxidation of methane and sulfate reduction in sediments from Gulf of Mexico cold seeps. Chem. Geol. 205: 219-238; 2004.

Joye, S. B.; MacDonald, I. R.; Montoya, J. P.; Peccini, M. Geophysical and geochemical signatures of Gulf of Mexico seafloor brines. Biogeosciences. 2: 295-309; 2005.

Kvenvolden K.A.; Claypool, G. E. Gas Hydrates in Oceanic Sediment. Denver, CO: U.S. Geologic Survey; 1988.

Kvenvolden, K. A.; Ginsburg, G. D.; Soloviev, V. A. Worldwide distribution of subaquatic gas hydrates. Geo-Marine Letters. 13: 32-40; 1993.

Linke, P.; Suess, E.; Torres, M.; Martens, V.; Rugh, W. D.; Ziebis, W.; Kulm, L. D. In-situ measurement of fluid-flow from cold seeps at active continental margins. Deep-Sea Research Part I-Oceanographic Research Papers. 41: 721-739; 1994.

Luff, R.; Wallmann, K. Fluid flow, methane fluxes, carbonate precipitation and biogeochemical turnover in gas hydrate-bearing sediments at Hydrate Ridge, Cascadia Margin: Numerical modeling and mass balances. Geochim. Cosmochim. Acta. 67: 3403-3421; 2003.

McAuliffe, C. Gas chromatographic determination of solutes by multiple pahse equilibrium. Limnol. Oceanogr. 45: 1546-1557; 1971.

Milkov, A. V. Molecular and stable isotope compositions of natural gas hydrates: A revised global dataset and basic interpretations in the context of geological settings. Org. Geochem. 36: 681-702; 2005.

Milkov, A. V.; Claypool, G. E.; Lee, Y. J.; Sassen, R. Gas hydrate systems at Hydrate Ridge offshore Oregon inferred from molecular and isotopic properties of hydrate-bound and void gases. Geochimica et Cosmochimica Acta. 69: 1007-1026; 2005.

Niewohner, C.; Hensen, C.; Kasten, S.; Zabel, M.; Schulz, H. D. Deep sulfate reduction completely mediated by anaerobic methane oxidation in sediments of the upwelling area off Namibia. Geochim. Cosmochim. Acta. 62: 455-464; 1998.

Orange, D. L.; Breen, N. A. The effects of fluid escape on accretionary wedges .2. Seepage force, slope failure, headless submarine canyons, and vents. Journal of Geophysical Research-Solid Earth. 97: 9277-9295; 1992.

Orcutt, B.; Boetius, A.; Elvert, M.; Samarkin, V.; Joye, S. B. Molecular biogeochemistry of sulfate reduction, methanogenesis and the anaerobic oxidation of methane at Gulf of Mexico cold seeps. Geochimica et Cosmochimica Acta. 69: 5633-5633; 2005.

Orphan, V. J.; House, C. H.; Hinrichs, K. U.; McKeegan, K. D.; Delong, E. F. Methane-consuming archaea revealed by directly coupled isotopic and phylogenetic analysis. Science. 293: 484-487; 2001.

Orphan, V. J.; Ussler, W.; Naehr, T. H.; House, C. H.; Hinrichs, K. U.; Paull, C. K. Geological, geochemical, and microbiological heterogeneity of the seafloor around methane vents in the Eel River Basin, offshore California. Chem. Geol. 205: 265-289; 2004.

Ortiz, J.; Mix, A.; Hostetler, S.; Kashgarian, M. The California current of the last glacial maximum: Reconstruction at 42 degrees N based on multiple proxies. Paleoceanography. 12: 191-205; 1997.

Paull, C. K.; Ussler, W.; Lorenson, T.; Winters, W.; Dougherty, J. Geochemical constraints on the distribution of gas hydrates in the Gulf of Mexico. Geo-Marine Letters. 25: 273-280; 2005.

Pimmel, A.; Claypool, G. Introduction to shipboard organic geochemistry on the JOIDES Resolution. ODP Tech. Note, 30 (online); 2001.

Plummer, R. E.; Pohlman, J. W.; Coffin, R. B. Compound specific stable carbon isotope analysis of low-concentration complex hydrocarbon mixtures from natural gas hydrate systems. American Geophysical Union, Dec 5-9, San Francisco CA.; 2005.

Pohlman, J. W.; Canuel, E. A.; Chapman, N. R.; Spence, G. D.; Whiticar, M. J.; Coffin, R. B. The origin of thermogenic gas hydrates on the northern Cascadia Margin as inferred from isotopic ($^{13}C/^{12}C$ and D/H) and molecular composition of hydrate and vent gas. Org. Geochem. 36: 703-716; 2005.

Reeburgh, W. S. An improved interstitial water sampler. Limnology and Oceanography. 12: 163-165; 1967.

Riedel, M.; Collett, T.; Malone, M.; Akiba, F.; Blanc-Valleron, M.; Ellis, M.; Guerin, G.; Hashimoto, Y.; Heuer, V.; Higashi, Y.; Holland, M.; Jackson, P.; Kaneko, M.; Kastner, M.; Kim, J.-H.; Katijama, H.; Long, P.; Malinvero, A.; Myers, G.; Palekar, L.; Pohlman, J.; Schultheiss, P.; Teichert, B.; Torres, M.; Trehu, A.; Wang, J.; Wortmann, U.; Yoshhioka, H. Gas hydrate transect across northern Cascadia margin. EOS. 87: 325, 330, 332; 2006.

Riedel, M.; Novosel, I.; Spence, G. D.; Hyndman, R. D.; Chapman, R. N.; Solem, R. C.; Lewis, T. Geophysical and geochemical signatures associated with gas hydrate-related venting in the northern Cascadia margin. Geological Society of America Bulletin. 118: 23-38; 2006.

Ruppel, C.; Dickens, G. R.; Castellini, D. G.; Gilhooly, W.; Lizarralde, D. Heat and salt inhibition of gas hydrate formation in the northern Gulf of Mexico. Geophysical Research Letters. 32: doi:10.1029/2004GL021909; 2005.

Sahling, H.; Rickert, D.; Lee, R. W.; Linke, P.; Suess, E. Macrofaunal community structure and sulfide flux at gas hydrate deposits from the Cascadia convergent margin, NE Pacific. Marine Ecology-Progress Series. 231: 121-138; 2002.

Scranton, M. I.; Brewer, P. G. Consumption of dissolved methane in deep ocean. Limnology and Oceanography. 23: 1207-1213; 1978.

Sloan, E. D. Clathrate Hydrates of Natural Gases. New York: Marcel Deker; 1998.

Spence, G. D.; Hyndman, R. D.; Chapman, N. R.; Walia, R.; Gettrust, J.; Edwards, R. N. North Cascadia deep sea gas hydrates. Ann. NY Acad. Sci. 912: 65-75; 2000.

Suess, E.; Bohrmann, G.; von Huene, R.; Linke, P.; Wallmann, K.; Lammers, S.; Sahling, H.; Winckler, G.; Lutz, R. A.; Orange, D. Fluid venting in the eastern Aleutian subduction zone. Journal of Geophysical Research-Solid Earth. 103: 2597-2614; 1998.

Suess, E.; Torres, M. E.; Bohrmann, G.; Collier, R. W.; Greinert, J.; Linke, P.; Rehder, G.; Trehu, A.; Wallmann, K.; Winckler, G.; Zuleger, E. Gas hydrate destabilization: enhanced dewatering, benthic material turnover and large methane plumes at the Cascadia convergent margin. Earth and Planetary Science Letters. 170: 1-15; 1999.

Suess, E.; Whiticar, M. J. Methane-Derived CO_2 in Pore Fluids Expelled from the Oregon Subduction Zone. Palaeogeography Palaeoclimatology Palaeoecology. 71: 119-136; 1989.

Torres, M. E.; McManus, J.; Hammond, D. E.; de Angelis, M. A.; Heeschen, K. U.; Colbert, S. L.; Tryon, M. D.; Brown, K. M.; Suess, E. Fluid and chemical fluxes in and out of sediments hosting methane hydrate deposits on Hydrate Ridge, OR, I: Hydrological provinces. Earth and Planetary Science Letters. 201: 525-540; 2002.

Torres, M. E.; Mix, A. C.; Kinports, K.; Haley, B.; Klinkhammer, G. P.; McManus, J.; de Angelis, M. A. Is methane venting at the seafloor recorded by $\delta^{13}C$ of benthic foraminifera shells? Paleoceanography. 18: doi:1029/2002PA000824; 2003.

Treude, T.; Boetius, A.; Knittel, K.; Nauhaus, K.; Elvert, M.; Kruger, M.; Losekann, T.; Wallmann, K.; Jorgensen, B. B.; Widdel, F.; Amman, R. Anaerobic oxidation of methane at Hydrate Ridge (OR). Geochimica et Cosmochimica Acta. 67: A491-A491; 2003.

Tryon, M. D.; Brown, K. M. Complex flow patterns through Hydrate Ridge and their impact on seep biota. Geophys. Res. Lett. 28: 2863-2866; 2001.

Tryon, M. D.; Brown, K. M.; Torres, M. E. Fluid and chemical flux in and out of sediments hosting methane hydrate deposits on Hydrate Ridge, OR, II: Hydrological processes. Earth and Planetary Science Letters. 201: 541-557; 2002.

Tryon, M. D.; Brown, K. M.; Torres, M. E.; Trehu, A. M.; McManus, J.; Collier, R. W. Measurements of transience and downward fluid flow near episodic methane gas vents, Hydrate Ridge, Cascadia. Geology. 27: 1075-1078; 1999.

Tsunogai, U.; Yoshida, N.; Gamo, T. Carbon isotopic evidence of methane oxidation through sulfate reduction in sediment beneath cold seep vents on the seafloor at Nankai Trough. Marine Geology. 187: 145-160; 2002.

Ussler, W.; Paull, C. K. Effects of ion-exclusion and isotopic fractionation on pore-water geochemistry during gas hydrate formation and decomposition. Geo-Marine Letters. 15: 37-44; 1995.

Valentine, D. L.; Reeburgh, W. S. New perspectives on anaerobic methane oxidation. Environmental Microbiology. 2: 477-484; 2000.

Volkman, J. K.; Barrett, S. M.; Blackburn, S. I.; Mansour, M. P.; Sikes, E. L.; Gelin, F. Microalgal biomarkers: A review of recent research developments. Org. Geochem. 29: 1163-1179; 1998.

Wallmann; Aloisi, G.; Haeckel, M.; Obzhirov, A.; Pavlova, G.; Tishchenko P. Kinetics of organic matter degradation, microbial methane generation, and gas hydrate formation in anoxic marine sediments. Geochimica et Cosmochimica Acta. 70: 3905-3927; 2006.

Whiticar, M. J. Carbon and hydrogen isotope systematics of bacterial formation and oxidation of methane. Chem. Geol. 161: 291-314; 1999.

Yamamoto, S.; Alcauskas, J. B.; Crozier, T. E. Solubility of methane in distilled water and seawater. Journal of Chemical and Engineering Data. 21: 78-80; 1976.

Zhang, C. L. L.; Li, Y. L.; Wall, J. D.; Larsen, L.; Sassen, R.; Huang, Y. S.; Wang, Y.; Peacock, A.; White, D. C.; Horita, J.; Cole, D. R. Lipid and carbon isotopic evidence of methane-oxidizing and sulfate-reducing bacteria in association with gas hydrates from the Gulf of Mexico. Geology. 30: 239-242; 2002

.

Table 1. Barkley Canyon push core information

Dive/Core	Core	Latitude (N)	Longitude (W)	Water Depth (m)	Core Length (cm)	Description
R693-C3	3	48° 18.686'	126° 3.907'	856	17	Control site
R696-C1	1	48° 18.680'	126° 3.957'	867	18	Gas hydrate mound
R696-C2	2	48° 18.677'	126° 3.931'	859	18	Clam bed
R696-C3	3	48° 18.696'	126° 3.938'	859	18	Carbonate debris
R696-C4	4	48° 18.686'	126° 3.922'	856	12	Bacterial mat

Table 2. Barkley Canyon pore water data

Dive	Core	Depth (cmbsf)	Methane mM	Methane $\delta^{13}C$	DIC mM	DIC $\delta^{13}C$	Sulfate mM	Chloride mM
R693	3	1.5	b.d.	-42.7	2.5	-5.3	28.6	536
		4.5	0.01	-39.9	2.5	-9.5	28.0	557
		7.5	0.02	-44.9	2.8	-9.5	28.9	541
		10.5	0.06	-43.7	3.9	-15.8	27.1	538
		13.5	0.08	-42.4	3.9	-15.5	26.7	547
		16	0.01	-37.2	3.2	-10.6	28.4	544
R696	1	1.5	0.06	-34.6	4.4	-16.6	25.3	551
		4.5	0.29	-49.4	11.6	-24.7	16.9	547
		7.5	1.25	-58.2	20.0	-26.3	8.4	542
		10.5	6.52	-60.8	27.4	-18.5	0.5	535
		13.5	9.13	-57.2	27.5	-12.0	0.9	552
		16.5	2.70	-54.5	27.2	-7.4	1.9	546
R696	2	1.5	0.01	-48.9	2.6	-7.7	29.2	534
		4.5	0.04	-47.9	5.0	-18.3	24.4	550
		7.5	0.08	-50.8	n.a.	n.a.	n.a.	n.a.
		10.5	0.23	-58.1	13.5	-24.8	16.3	539
		13.5	5.89	-64.3	25.3	-22.1	3.4	537
		16.5	4.86	-58.0	25.5	-9.2	4.3	536
R696	3	1.5	0.00	-50.8	2.7	-9.5	31.1	554
		4.5	0.01	-48.0	3.2	-13.1	28.1	539
		7.5	0.02	-44.0	6.4	-18.2	n.a.	537
		10.5	0.09	-48.3	12.8	-19.9	20.9	551
		13.5	0.10	-53.3	15.6	-20.3	14.2	548
		16.5	0.37	-51.1	n.a.	-16.0	8.9	559
R696	4	1.5	0.62	-47.7	9.1	-25.2	19.4	551
		4.5	2.19	-60.1	19.7	-28.8	8.1	540
		7.5	8.20	-55.5	20.7	-23.3	4.3	532
		10.5	12.04	-51.7	21.6	-19.3	3.8	551

b.d.: below detection

n.a.: not available

Table 3. Barkley Canyon solid phase total organic carbon (TOC) and total inorganic carbon (TIC) data

Dive/Cruise	Core	Depth (cmbsf)	Total organic carbon			Total inorganic carbon	
			$\delta^{13}C$	wt%	C:N	$\delta^{13}C$	wt% CaCO$_3$
R696	1	1.5	-24.5 ± 0.1	1.23 ± 0.04	8.0 ± 0.04	-13.7 ± 0.4	0.6 ± 0.1
		4.5	-25.3 ± 0.1	1.19 ± 0.01	8.0 ± 0.01	-19.2 ± 0.2	6.4 ± 0.2
		7.5	-26.3 ± 0.3	1.18 ± 0.01	7.8 ± 0.01	-18.0 ± 0.2	16.7 ± 0.2
		10.5	-24.0 ± 0.1	1.23 ± 0.01	6.5 ± 0.01	-5.1 ± 0.5	b.d.
		13.5	-24.1 ± 0.03	1.28 ± 0.01	6.7 ± 0.01	-3.3 ± 0.1	0.6 ± 0.3
		16.5	-24.0 ± 0.1	1.37 ± 0.04	9.9 ± 0.04	-0.9 ± 0.3	b.d.
R696	2	1.5	-23.6 ± 0.2	2.90 ± 0.04	8.6 ± 0.04	-8.3 ± 0.1	b.d.
		4.5	-23.4 ± n.a.	3.03 ± 0.03	9.0 ± 0.03	-8.7 ± 0.8	b.d.
		7.5	-23.5 ± 0.1	3.08 ± 0.03	8.8 ± 0.03	-3.2 ± 0.2	1.7 ± 0.1
		10.5	-24.4 ± 0.1	2.75 ± 0.03	8.7 ± 0.03	-15.9 ± 0.1	2.2 ± 0.1
		13.5	-24.4 ± 0.1	2.77 ± 0.07	9.7 ± 0.07	-6.4 ± 0	3.9 ± 0.2
		16.5	-24.9 ± 0.02	2.75 ± 0.04	11.0 ± 0.04	-15.8 ± 0.2	5.7 ± 0.1

b.d.: below detection

Table 4. Water column methane concentrations

Dive	Bottle	Water Depth (m)	Distance from seafloor (m)	Conc (nM)	Description
692	1	857.3	1	130 ± 1	Hydrate Mound
	3	853.9	1	18	Clam Colony
693	1	860.5	1	14 ± 1	Clam Colony
	3	855.4	1	45	Clam/Mat Site
	4	868.6	1	33	Hydrate Mound
694	1	867.8	1	209 ± 2	Hydrate Mound Profile Site
	2	860.7	7.6	38 ± 5	"
	3	853.3	15	22 ± 5	"
696	1	867.0	1	34	Hydrate Mound
	3	856.0	1	19 ± 0.05	Clam Colony
	4	856.0	1	38	[3]Carbonate Mound

[3]Sediment disturbed prior to collecting sample

Table 5. Major fatty acid concentrations from R696 Core 1.

Depth (cmbsf)	Concentration (ng/g dw sediment)														
	$C_{14:0}$	i-$C_{15:0}$	ai-$C_{15:0}$	$C_{16:1\omega7c}$	$C_{16:1\omega?}$	$C_{16:1\omega5c}$	$C_{16:0}$	ai-$C_{17:0}$	$C_{18:1\omega7}$	$C_{18:0}$	$C_{22:0}$	$C_{24:0}$	$C_{26:0}$	$C_{28:0}$	$C_{30:0}$
0-3	1220	441	1356	8210	982	2405	5151	430	4214	1544	601	1148	1227	1056	627
3-6	566	216	1173	1488	b.d.	788	1794	167	876	669	501	988	1137	941	530
6-9	596	298	1088	1291	b.d.	822	1868	205	1215	751	525	1029	1171	946	532
9-12	329	129	397	305	b.d.	319	1070	b.d.	276	515	317	647	851	877	576
12-15	642	177	547	309	b.d.	305	2070	b.d.	251	991	522	1049	1333	1197	678
15-18	589	156	569	280	b.d.	233	1690	b.d.	164	752	421	856	1070	919	516

b.d. below detection

Table 6. Major fatty acid stable carbon isotope composition R696, Core 1.

Depth (cmbsf)	Fatty Acid ($\delta^{13}C$)														
	$C_{14:0}$	$i\text{-}C_{15:0}$	$ai\text{-}C_{15:0}$	$C_{16:1\omega7c}$	$C_{16:1\omega7t}$	$C_{16:1\omega5c}$	$C_{16:0}$	$ai\text{-}C_{17:0}$	$C_{18:1\omega7t}$	$C_{18:0}$	$C_{22:0}$	$C_{24:0}$	$C_{26:0}$	$C_{28:0}$	$C_{30:0}$
0-3	-36.2	-42.4	-43.4	-37.7		-49.0	-31.1	-37.0	-36.3	-25.9	-29.8	-29.5	-29.4	-31.3	-31.2
3-6	-37.1	-52.6	-62.0	-48.8	-55.3	-57.0	-36.0	-66.5	-54.4	-32.1	-32.1	-30.4	-30.6	-30.2	-30.1
6-9	-42.0	-59.7	-67.6	-50.7	-61.5	-68.4	-33.2	-65.0	-55.3	-27.9	-29.8	-28.7	-29.4	-30.7	-31.3
9-12	-35.1	-53.1	-57.9	-47.1		-49.6	-29.1	-51.7		-25.9	-32.1		-29.9	-30.5	-30.1
12-15	-30.2		-35.0				-27.7			-24.9	-30.2	-29.3	-27.9	-28.4	-29.8
15-18	-28.0		-28.3				-27.1			-27.6	-29.8	-28.4	-28.3	-28.4	-29.8
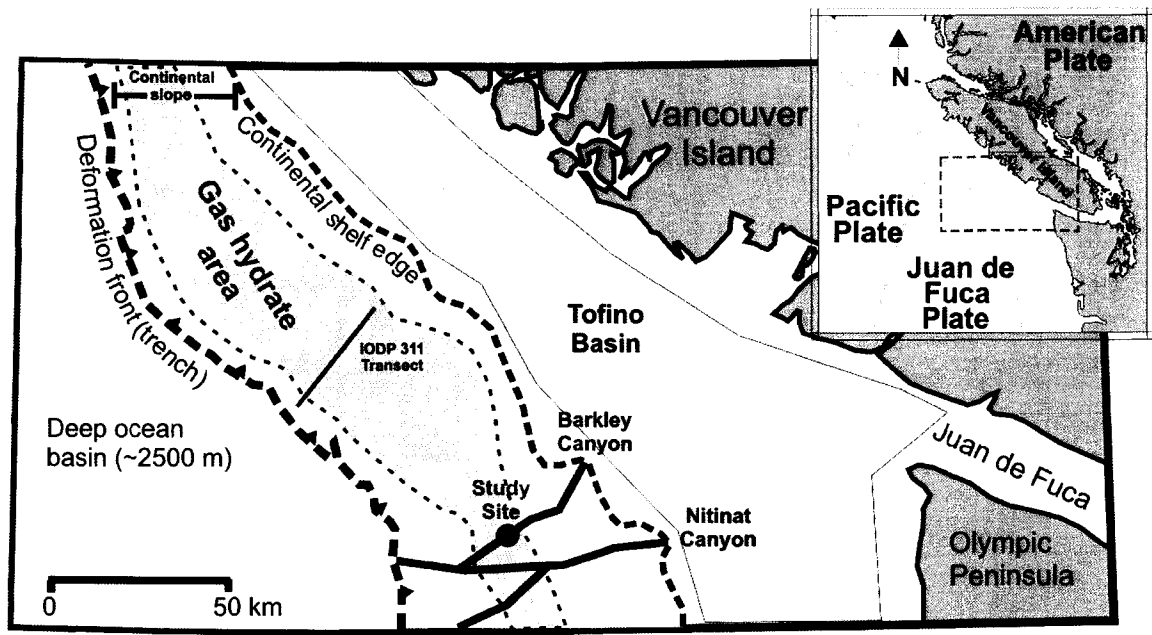
Figure 1. Geographical setting of Barkley Canyon. The study site is located at ~850 m water depth on the slope of the northern Cascadia margin. The presence of gas hydrate along the entire continental slope has been inferred from seismic reflections (Spence et al., 2000), but Barkley Canyon is the only location where thermogenic gas hydrate has been recovered (Pohlman et al., 2005). The Tofino Basin hydrocarbon province underlies about 7500 km^2 of the continental margin (Bustin, 1995)
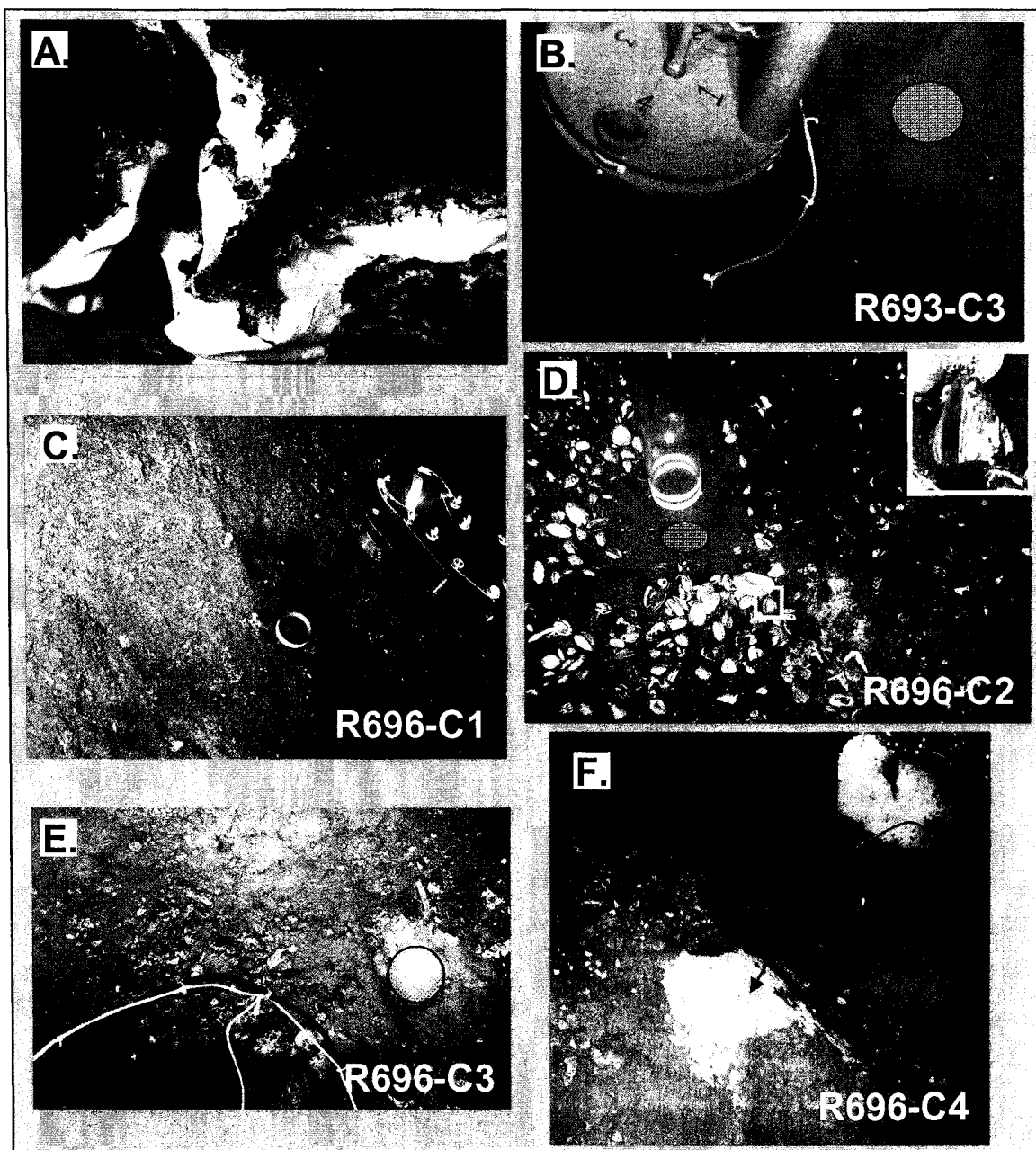
Figure 2. Photographs of seafloor settings and coring locations in Barkley Canyon. (A) Example of gas hydrate exposed to seawater. (B) Low flux site. Core R693-C3 was collected adjacent an in-situ pressure pore water sampler (L. Lapham, UNC) (core location indicated by circle; see Fig. 3 for chemical data). (C) Sedimented sloping gas hydrate mound where core R696-C1 was collected (see Fig. 4 for chemical profiles). (D) Clam colony site R696-C2. The core location is indicated by the circle below the core (see Fig. 5 for chemical profiles). The inset figure displays close up of a living clam. (E) Carbonate site after recovery of core R696-C3 (core location indicated by circle; see Fig. 6 for chemical profiles). Exposure of carbonate debris indicates the seafloor has been eroded. (F) Bacterial mat where core R696-C4 was collected (see Fig. 7 for chemical profiles). The arrow indicates the exact coring location (see inset).

R693-C3: Low Flux

Figure 3. Geochemical profiles for core R693-C3. (A) Methane, sulfate and DIC concentrations. (B) Methane and DIC $\delta^{13}C$ values. The red line is the gas hydrate methane $\delta^{13}C$ value, which is also indicated in subsequent figures. The range of $\delta^{13}C$ values are approximately the width of the line (Pohlman et al., 2005). The SMI was not encountered with this core.

R696-C1: Gas Hydrate Mound Site
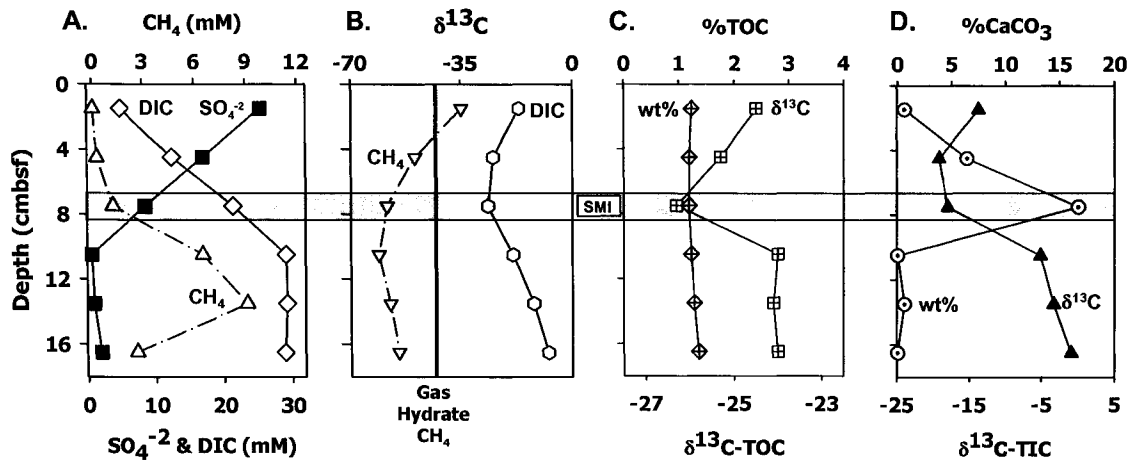
Figure 4. Geochemical profiles for core R696-C1. The grey box indicates the SMI depth, which is also indicated in subsequent figures. (A) Methane, sulfate and DIC concentrations. (B) Methane and DIC δ^{13}C values. (C) wt% and δ^{13}C for TOC. (D) wt% CaCO$_3$ and δ^{13}C for TIC.

R696-C2: Clam Bed Site
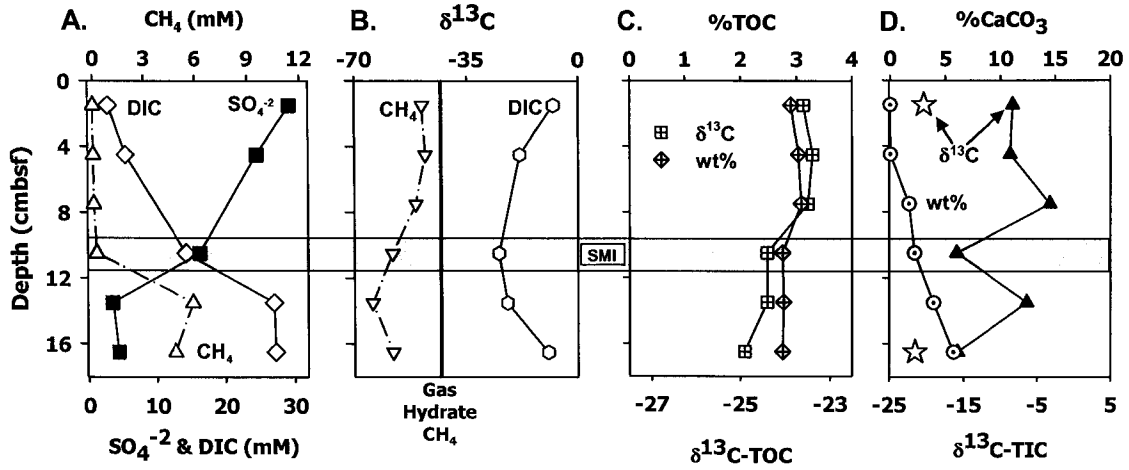
Figure 5. Geochemical profiles for core R696-C2. (A) Methane, sulfate and DIC concentrations. (B) Methane and DIC $\delta^{13}C$ values. (C) wt% and $\delta^{13}C$ for TOC. (D) wt% $CaCO_3$ and $\delta^{13}C$ for TIC (triangles) and authigenic carbonate nodules (stars).

R696-C3: Carbonate Debris Site
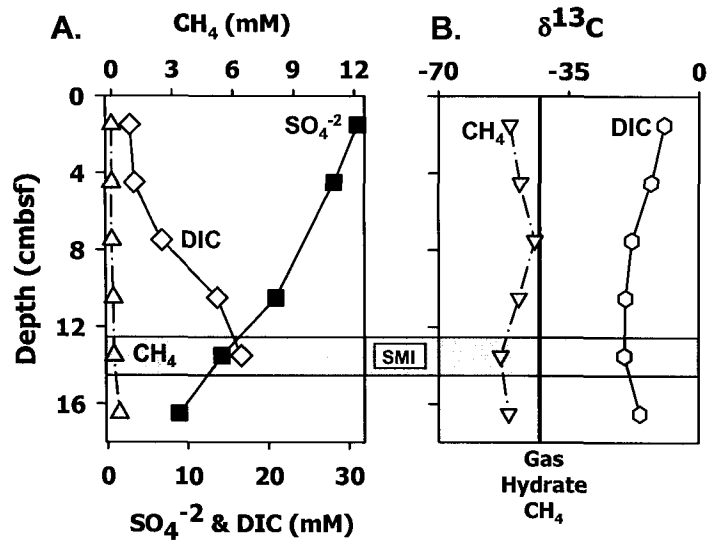
Figure 6. Geochemical profiles for core R696-C3. (A) Methane, sulfate and DIC concentrations. (B) Methane and DIC $\delta^{13}C$ values.
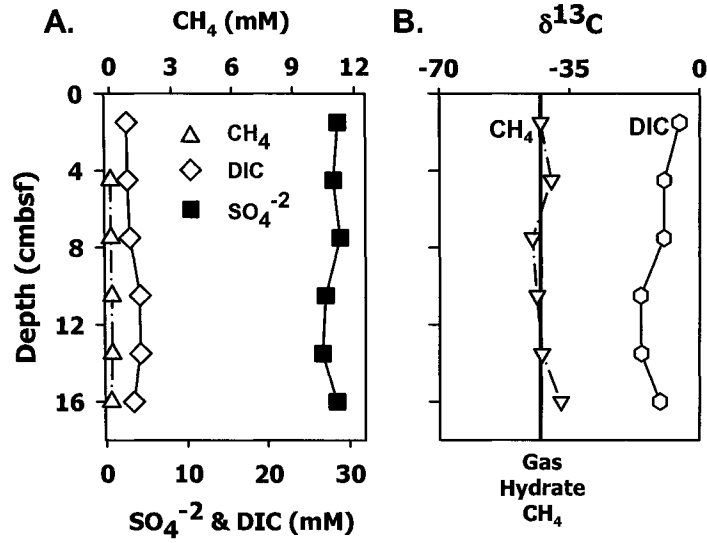
R696-C4: Bacterial Mat Site
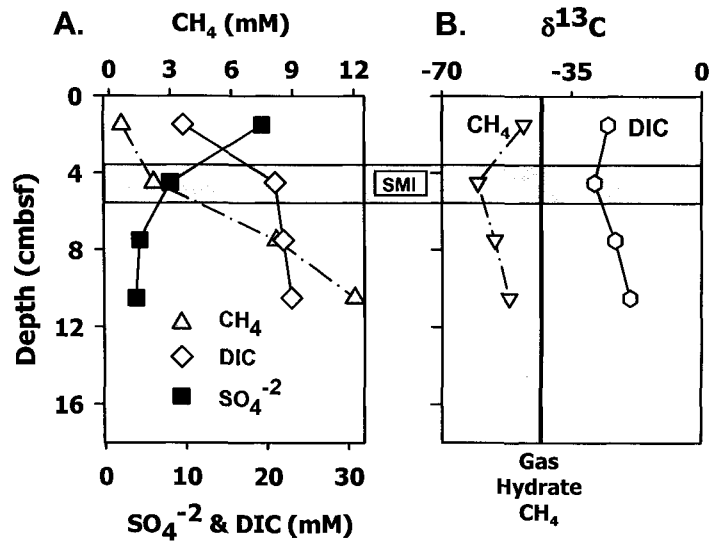
Figure 7. Geochemical profiles for core R696-C4. (A) Methane, sulfate and DIC concentrations. (B) Methane and DIC $\delta^{13}C$ values.
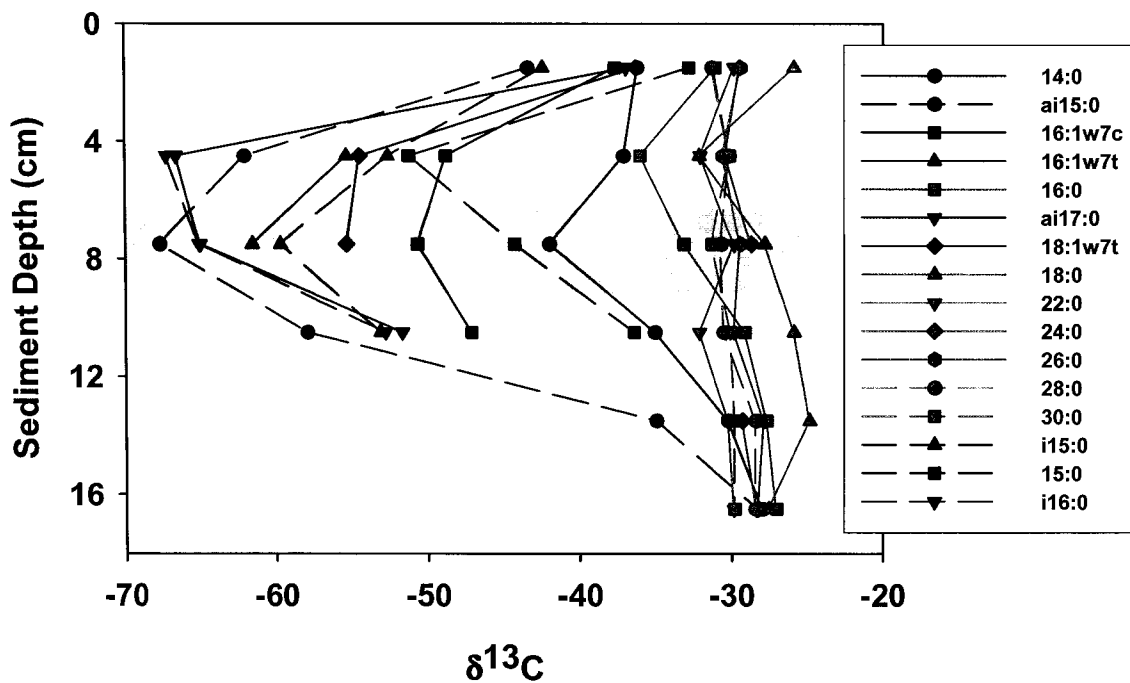
Figure 8. Fatty acid δ^{13}C composition from core R696-C1. The shaded area represents the sulfate methane interface (SMI) inferred from the geochemical data in Fig. 4. Blue symbols are those that displayed ^{13}C-depleted values indicative of assimilation of methane carbon by AOM and are compounds that have been previously associated with AOM (Hinrichs et al., 2000; Elvert et al., 2003; Zhang et al., 2002; Orcutt et al., 2005). The green symbols showed no evidence of methane carbon assimilation and are compounds known to occur in terrestrial plant waxes or are ubiquitous in plants, bacteria and zooplankton (Volkman et al., 1998).

DIC (mM)

0   5   10   15   20   25   30

+0.5‰   +2‰
0   Biogenic Calcite   -2‰

δ¹³C-DIC

-10   TOC and
           gas condensate

-20

-30

Methane

-61‰   -42‰

R693-C3
R696-C1
R696-C2
R696-C3
R696-C4

-22.4 to -25.3‰
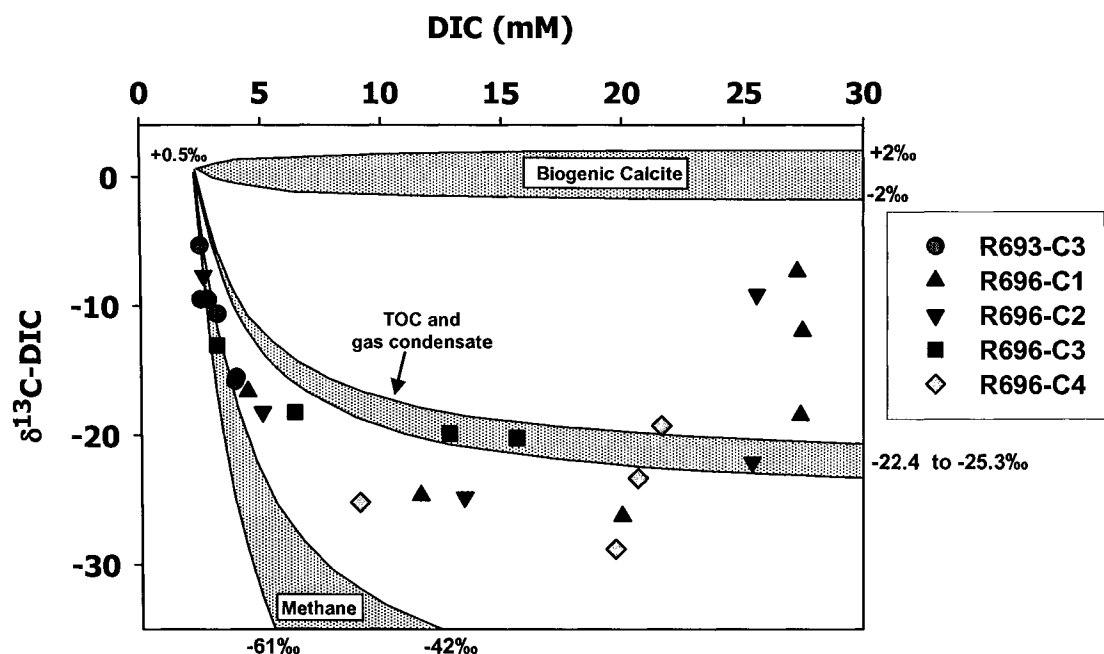
Figure 9. Barkley Canyon pore water DIC concentration versus δ^{13}DIC. The shaded areas are 2-source DIC mixing models of seawater (+0.5‰; Ortiz et al., 1998) and the other potential DIC sources: biogenic calcite, TOC, gas condensate and methane. The dissolution of biogenic calcite is not expected to influence the δ^{13}C of the DIC (Suess and Whiticar, 1989). The methane δ^{13}C value endmember range is the minimum value measured in this study and the gas hydrate methane value (Pohlman et al., 2005). The TOC endmember values (-23.4 to -24.4‰) are the δ^{13}C -TOC values from R696-C2; a core with no indication of AOM, which can alter δ^{13}C -TOC values (Joye et al., 2004). The gas condensate δ^{13}C value (-24.1‰, Pohlman et al., 2005) overlapped, and, thus, is encompassed within the TOC value range. The proximity of the data to the model regions indicates relative contributions of the endmembers to the pore water DIC values. Pore water DIC values at low and intermediate concentrations (~2-12 mM) indicate a contribution of DIC from AOM. At greater concentrations (~10-28 mM) corresponding to depths below the SMI (see Figs 4-6), the δ^{13}C-DIC values likely increased because of preferential assimilation of ^{12}DIC during methanogenesis (Claypool and Kaplan, 1974); not contributions from oxidation of the alternate carbon substrates, as the mixing models imply.
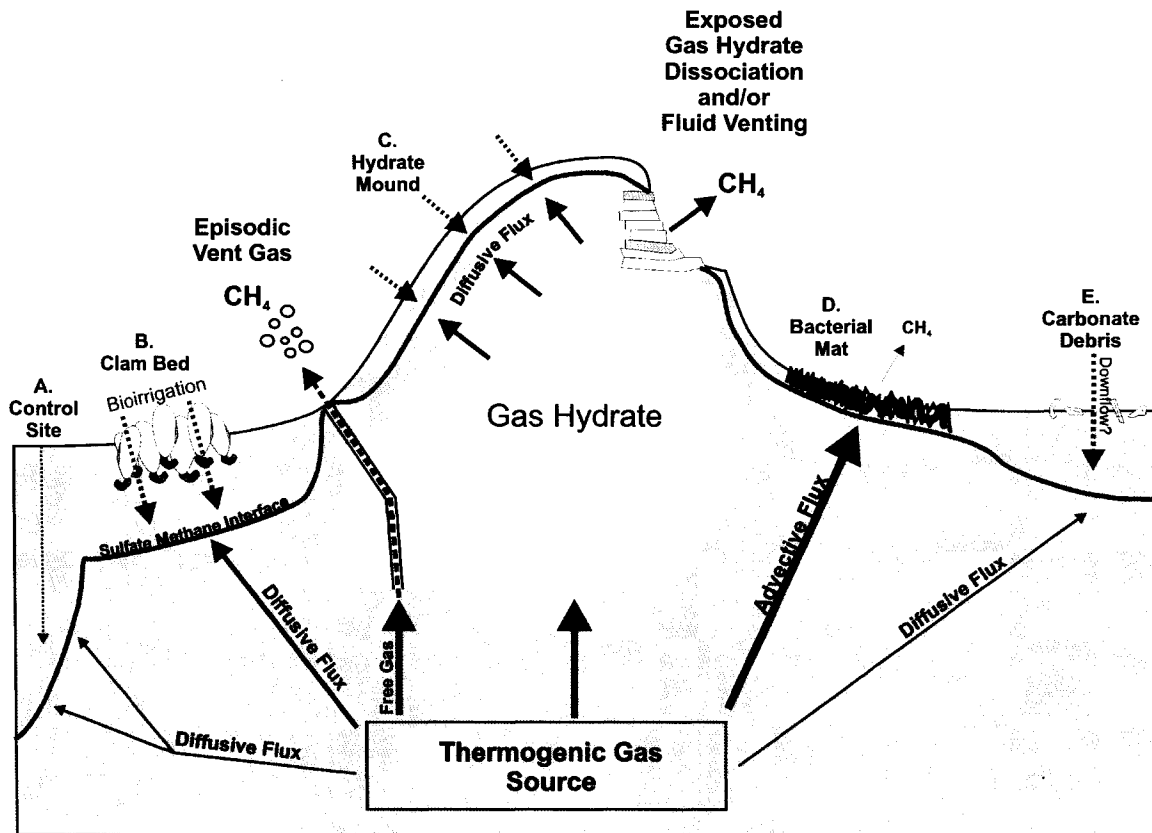
Figure 10. A summary of the geochemically inferred fluid and gas flux regimes at Barkley Canyon. The black arrows originating from the thermogenic gas source indicate the type and intensity of the fluid and gas fluxes. The relative depth of the sulfate methane interface (SMI) is represented by the red line. Each of the seafloor settings investigated was characterized by a distinct flux regime: A) the low flux site was supplied by a weak diffusive flux and deep sulfate penetration (blue dotted line); B) clam bioirrigation enhances the delivery of sulfate and produces sharp geochemical gradients at the SMI; C) the gas hydrate mound forms a physical barrier to fluid advection and, thus, is characterized by steep diffusive gradients near the seafloor; D) the bacterial mat site is underlain by an upward advective flux and elevated methane concentrations near the seafloor supporting a nominal water column flux; E) indication of seawater downflow suggests a physically driven fluid advection process at the carbonate debris site. Intermittent free gas flow at discrete vent sites, fluid venting and continuous dissociation of exposed gas hydrate are potential sources of bottom water methane.
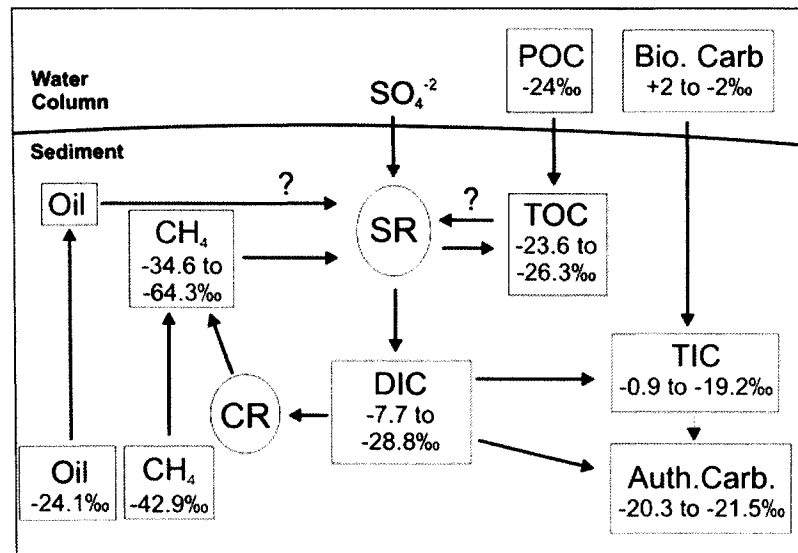
Figure 11. Carbon pools (rectangles) and biogeochemical processes (circles) that control the cycling of carbon in shallow sediments of the Barkley Canyon cold seep. Sulfate reduction (SR) is the primary oxidative pathway for converting reduced organic compounds (CH_4: methane; TOC: total organic carbon and oil) to dissolved inorganic carbon (DIC). The anaerobic oxidation of methane (AOM) is the only pathway capable of generating the most depleted $\delta^{13}C$-DIC values. DIC carbon enters the TIC and authigenic carbonate pools and some portion is recycled back to methane by the methanogenic carbonate reduction (CR) pathway. The sediment $\delta^{13}C$ values represent the range of values obtained in this study. The particulate organic carbon (POC) value was obtained from a TOC sample determined to have no input from AOM/SR and the biogenic carbonate range is from Suess and Whiticar (1989).

CHAPTER 5

METHANE CARBON FLUX AND CYCLING AT A GAS HYDRATE-BEARING
COLD SEEP (BULLSEYE VENT, NORTHERN CASCADIA MARGIN)

This chapter follows the format of Geochimica et Cosmochimica Acta

138

Abstract

Methane from fluids expelled by tectonic compression of the northern Cascadia margin accretionary system sustains massive accumulations of gas hydrate at the Bullseye vent cold seep. A transect of seven piston cores collected along a deep-towed acoustics/geophysics system (DTAGS) seismic line that crossed the cold seep site was conducted to investigate the flux and cycling of methane within and around this seep site. The seep was characterized by an advective fluid regime and prominent seismic blanking related to methane gas fluxing upward to the seafloor. Outside the active seep area, methane fluxes calculated using a sulfate gradient model diminished with distance from the seep. The occurrence and intensity of vertical seismic blanking columns was related to the intensity of the calculated methane fluxes. Subsurface horizontal sulfate gradients on the margins of the seep suggested an additional sulfate source for supporting anaerobic oxidation of methane (AOM) in ascending seep fluids.

In the non-seep cores, methane $\delta^{13}C$ values as low as -112‰ at the sulfate methane interface (SMI) suggest AOM and methanogenesis were coupled. The ^{13}C-depleted $\delta^{13}CH_4$ methane values resulted from isotopic fractionation of microbial methane carbon as it was cycled through the DIC pool (min $\delta^{13}C$ = -47.5‰) and was reduced back to methane. Downward diffusion of AOM-derived DIC from the SMI into the upper methanogenic zone was identified by isotope separation factors ($\epsilon_c = \delta^{13}C_{DIC} - \delta^{13}C_{CH4}$) that violated the Rayleigh distillation-based methane-carbon dioxide partition model. The lowest ϵ_c (~40) occurred immediately below SMI where the contribution from AOM-derived DIC in the methanogenic region of the cores was greatest. With greater depth, ϵ_c values increased as the contribution of DIC derived from AOM

139

decreased. A simple source-diffusion model supported the suggestion that downward

diffusion of AOM derived DIC accounted for the observed ε_c values. Discrepancies

between the model results and measured values were attributed to a downward advective

component not included in the model. This study provides the first detailed geochemical

description of the flux and cycling of methane at the Bullseye vent, a location

investigated during the recent IODP Expedition 311 (Site U1328), and provides insight

into processes that influence the distribution of pore water constituents and carbon

cycling in cold seep systems.

140

1. Introduction

A two-fold increase in atmospheric methane concentrations has been observed since the onset of the industrial revolution and has been linked to contemporary global warming (Intergovernmental Panel on Climate Change, 2001). Although the growing atmospheric methane burden is primarily the result of escalating anthropogenic inputs (Lelieveld et al., 1998), the geologic record contains numerous signals indicating massive methane releases from natural oceanic sources (e.g., gas hydrate) that may have stimulated or exacerbated rapid climate change (Dickens et al., 1995; Hesselbo et al., 2000). Under current conditions, the combined contribution from the oceans and gas hydrate is only ~3% of the annual 600 Tg yr^{-1} (1 Tg = 10^{12} g) flux of methane to the atmosphere (Lelieveld et al., 1998). However, continued ocean warming could increase these contributions by destabilizing the massive marine gas hydrate reservoir (Kennett et al., 2002). Near-seafloor gas hydrate stability, particularly at shallower ocean depths (i.e., 400-1000 m), is predicted to respond most rapidly to ocean temperature change and, consequently, has been the subject of considerable investigation (Suess et al., 1999; Wood et al., 2002; MacDonald et al., 2005).

The anaerobic oxidation of methane (AOM) in continental shelf and slope sediments is thought to be a major factor moderating the flux of methane from marine sediments. With the exception of seabed seeps where methane is discharged directly into the ocean (Judd, 2004), AOM removes greater than 99% of methane generated in continental margin sediments (Alperin and Reeburgh, 1984). A recent estimate of the global consumption of methane by AOM in marine sediment (300 Tg yr^{-1}) is

approximately half the estimated current annual emission to the atmosphere (Hinrichs and Boetius, 2002).

AOM is mediated by a syntrophic consortium of methane-oxidizing archaea and sulfate reducing bacteria (Eq. 1) (Hoehler et al., 1994; Hinrichs et al., 1999; Boetius et al., 2000) as:

$$SO_4^{-2} + CH_4 \rightarrow HCO_3^- + HS^- + H_2O \qquad \text{(Eq. 1)}$$
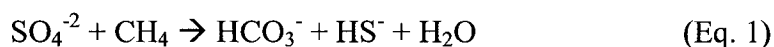
In marine sediments, AOM occurs at the sulfate-methane interface (SMI) where downward diffusing seawater sulfate encounters dissolved methane diffusing or advecting upward (Borowski et al., 1999). Immediately below the SMI, methane concentrations increase due to methanogenesis and migration of methane from deeper microbial or thermogenic sources. Production of DIC at the SMI that is more ^{13}C-depleted than organic matter in the system is considered to be a reliable indication of the occurrence of AOM (Claypool and Kaplan, 1974; Blair and Aller, 1995).

Recent biogeochemical and microbiological studies have identified phylogenetic and chemotaxonomic relationships among organisms involved with AOM; advancing our basic understanding of how methane carbon and related elements are cycled (see review by Hinrichs and Boetius 2002 and literature cited therein). However, it is uncertain to what extent, and over what timescales, AOM can respond to increased methane flux and modulate the transfer of methane from the seabed to the hydrosphere if the warming of ocean waters stimulates rates of methanogenesis and gas hydrate dissociation in near-surface marine sediments (Kennett et al., 2002). Our understanding of how microbial

processes operate within sediments containing shallow gas hydrate and a range of

methane fluxes may thus benefit from a detailed investigation of sediment pore water

chemistry and its relationship to AOM.

To that end, the fluxes of methane and associated pore water constituents were

investigated in piston cores collected along a transect across a gas hydrate-bearing cold

seep (Bullseye vent) on the northern Cascadia Margin accretionary prism (Fig. 1).

Recent evidence that the greatest concentrations of gas hydrate occur in accretionary

systems suggests that these systems may be the most significant reservoirs for long-term

energy development potential (Dallimore and Collett, 2005) and climate change driven

by methane releases to the atmosphere. Scientific drilling during the Integrated Ocean

Drilling Program (IODP) Expedition 311 at Bullseye Vent (Site U1328) was designed to

describe the deep gas hydrate and fluid system supporting the seep (Riedel et al., 2006a).

This study is complementary to the IODP effort in that it focuses on high resolution

lateral (~1 km) and vertical (~35 cm) variations in surficial sediments traversing the cold

seep system.

2. Regional geology, site description and geochemistry

The northern Cascadia continental margin offshore of Vancouver Island is an

accretionary prism formed by subduction (~45 mm yr^{-1}) of the Juan de Fuca plate beneath

the North American plate (Riddihough, 1984) (Fig. 1A). Sediment scraping and

consolidation form a series of anticlinal ridges underlain by thrust faults (Davis and

Hyndman, 1989). These deeply penetrating subvertical faults serve as conduits for

methane enriched fluid migration that support gas hydrate formation (Hyndman and

Davis, 1992). A wide (20-30 km) band containing some gas hydrate at depths between 50 and 250 meters below the seafloor has been inferred to occur because of the existence of a bottom simulating reflector (BSR) along most of the continental slope offshore Vancouver Island (Spence et al., 2000).

Bullseye vent was detected as a ~ 400 m circular region of incoherent reflections seen in seismic reflection profiles as "blanking" zones (Riedel et al., 2002) that result from subsurface gas (Wood et al., 2002) or gas related features (e.g., gas hydrate) (Riedel et al., 2002). The Bullseye vent cold seep is expressed as a mound extending ~ 6 m above the surrounding seafloor (Riedel et al., 2002). Gas hydrate has been collected by piston coring the upper 10 mbsf of the cold seep (Riedel et al., 2002; Pohlman, Chapter 2; Riedel et al., 2006b). Bullseye vent occurs within a ~3-km wide mini-basin filled with modern laminated sediments that is bound by ~200 m-high anticlinal ridges formed by thrust faulting and folding within the accretionary prism (Riedel et al., 2002). Numerous seismic blanking zones in addition to Bullseye vent are present along an uplifted sediment block on the inner portion of the basin (Riedel et al., 2006b). Several scientific drill site locations (ODP Leg 146 Site 889B and IODP Expedition 311 Sites U1327 and U1328) are located near Bullseye vent.

Previous geochemical studies at Bullseye Vent characterized the origins of the gas supporting near-surface gas hydrate accumulations (Riedel et al., 2006b; Pohlman, Chapter 2) and utilized low magnetic susceptibilities resulting from AOM-induced reduction of ferromagnetic minerals as a record of AOM activity (Novosel et al., 2005). The stable carbon isotope signature of gas hydrate-bound methane (-65.4‰ to -70.4‰) suggests a microbial gas source supports the near-surface gas hydrate accumulations

(Chapter 2; Riedel et al., 2006b), although slight contributions from a thermogenic source were also identified. The methane flux modeled from sulfate gradients ranged from 32-60 mmol m^{-2} yr^{-1} (Riedel et al., 2006b). Bullseye vent gas hydrate contains near-fossil (i.e., highly depleted in ^{14}C) methane carbon, indicating that the primary source of organic matter supporting methanogenesis was at least 50 ka old and suggesting that fluids that transport methane to the near-surface sediments have migrated upward from greater depth (Pohlman, Chapter 2). Despite these efforts and numerous geophysical studies that have described the geology and gas hydrate system for this region (Spence et al., 2000; Riedel et al., 2002; Wood et al., 2002), a detailed geochemical study related to the cycling and fate of methane carbon at Bullseye vent has been lacking.

3. Materials and Methods

3.1 Sample collection and processing

In October 2002 (Cruise PGC0208) seven piston cores were collected along an 850 meter section of the deep towed acoustic/geophysics system (DTAGS) seismic line 9 from the *CCGS John P. Tully* across the Bullseye Vent (Fig. 1; Table 1). A receiver deployed with DTAGS or attached to the wire of the piston corer was used to monitor their locations within a seafloor acoustic transponder net. As a result, the locations of the piston cores relative to the DTAGS line are accurate to ~4 m. Two of the cores (C3 and C5) were collected from within the cold seep where gas hydrate occurs below the seafloor (Fig. 1). Hence, these cores are hereafter referred to as "seep site" cores and the others, "non-seep site" cores.

A total of 123 sediment sections (each 10 cm in thickness) were cut from polycarbonate core liners at a vertical resolution of 30-35 cm with a pipe cutter. Samples for gas concentration and isotopic analysis were collected as 2-ml plugs from the top of each section and transferred into pre-weighed 20-ml serum vials (Hoehler et al., 2000). The sediment sections were capped and immediately transported to the shipboard laboratory for pore water extraction. To avoid contamination by seawater, the exposed surface of the sediment was scraped off and the sample was removed from the center of the core section. Sediment was packed into pressure filtration squeezers and pore water was extracted into air-tight 60-ml plastic syringes by applying a nitrogen headspace pressure of ~5 bar to a latex sheet separating the sample from the headspace gas (Reeburgh, 1967). The pore water samples were filtered through 0.2-μm Acrodisc PES syringe filters (Pall Corporation) into scintillation vials baked at 450 °C for 4 hours and were subsequently dispensed into storage containers for post cruise analyses. Extracted sediments were removed from the housings, wrapped in precombusted (450 °C) aluminum foil and placed in plastic bags. All samples were stored at –20 °C until analysis on shore.

3.2 Methane concentration and $\delta^{13}CH_4$ measurements

The headspace gas concentrations of methane in the serum vials were analyzed using a Shimadzu 14-A gas chromatograph (GC) equipped with a flame ionization detector (FID). Methane was separated isothermally (50 °C) from the other gases with Poraplot-Q stainless steel column (8 ft, 1/8" OD) packed with 60/80 mesh and was quantified against certified methane standards (Scott Gas, Plumbsteadville PA). Vial

headspace concentrations were converted to aqueous concentrations according to the method described by Hoehler et al. (2000). Porosities were determined for each sample by weighing the pre-weighed vials before and after sediments were completely dried at 50 °C (2-3 days), yielding values from 0.78 to 0.63.

Methane from the headspace of the serum vials was analyzed for stable carbon isotope composition using a Thermo Electron Trace gas chromatograph (GC) modified with a dual-cryogenic focusing inlet and a Finnigan Delta Plus XP isotope ratio mass spectrometer (IRMS) with high resistivity amplifiers (Plummer et al., 2005). Variable volume (0.02- to 15.0 ml) gas samples containing at least 10 ng of methane carbon were injected into an 8 ml min^{-1} He carrier stream. Following initial cryofocusing onto a ¼" ss Poraplot-Q loop immersed in liquid nitrogen (LN$_2$), the methane was refocused with LN$_2$ at the head of the column in a small section of fused silica capillary packed with 80/100 mesh Poraplot-Q. Dual focusing was required for the larger volume injections (>5 ml) to reduce the transfer of atmospheric nitrogen to the GC column. After reducing the He carrier flow to 1.6 ml min^{-1}, methane was rapidly desorbed (100°C) and separated at -10 °C on a Poraplot-Q column (25 m, 0.32 mm id), oxidized to CO$_2$ with a GCC-III interface (Thermo-Electron) and analyzed by IRMS. Sub-ambient cooling was necessary to separate the methane from residual nitrogen. The ^{13}C/^{12}C ratios are expressed in the standard δ-notation using tank CO$_2$ referenced to the NIST RM 8560 natural gas standard. The analytical precision (obtained by triplicate analyses of every tenth sample) was less than 0.5‰.

3.3 Pore water analyses

Pore water sulfate was determined using a Dionex DX-120 ion chromatograph (IC) equipped with a 4-mm AS-9HC column and an AS-40 autosampler using the method described by Paull et al. (2005), with the exception that our samples were diluted 1:50. Peak areas for sulfate from the diluted samples were quantified against equivalently diluted International Association for the Physical Sciences of the Oceans (IAPSO) standard seawater analyzed at the beginning of the run and after every fifth sample. The analytical precision for dissolved sulfate was ±1% of the IAPSO standard value (28.9 mM).

Total dissolved sulfides were determined spectrophotometrically (670 nm) using a modification of the Cline method (Cline, 1969). A 0.12 M solution of Cline reagent was prepared less than one week before the cruise. Separate standard curves were prepared for low (0-2 mM) and high (2-25 mM) concentration samples. Low concentration samples were diluted 1:2 with the Cline reagent, and high concentration samples were diluted 1:10 to make sure the reagent was present in excess quantity. The entire low concentration sample mix (2 ml) and 20% of the high concentration sample mix (10 ml) were diluted to 50 ml with deionized water before spectrophotometric determination. The analytical precision for dissolved sulfide was ±5% of the mean.

Pore water DIC concentrations were determined with a model 5011 UIC coulometer and quantified relative to a seawater certified reference material (CRM) (University of California, San Diego, CA). One ml of 10% phosphoric acid saturated with copper sulfate was added to the vials containing 3-ml of sample to convert the DIC to carbon dioxide and precipitate dissolved sulfides as CuS. The carbon dioxide was

transferred to the coulometer with a purified helium carrier gas and was measured with an analytical precision of ±1% of the CRM (~2.2 mM).

The stable carbon isotope composition (^{13}C /^{12}C) of the pore water DIC was measured with a Thermo Finnigan Delta S IRMS. 200-μl of 85% phosphoric acid were added to a 3-ml sample vial having less than 500 μl of headspace. The samples were shaken vigorously at least once every 15 minutes for 1 hour to transfer the DIC into the headspace as CO_2. Headspace gas from the sample vial was injected into a Thermo Finnigan Trace GC, where the CO_2 was separated isothermally (50 °C) on a Poraplot-Q capillary column (25 m, 0.32 mm ID). The $^{13}C/^{12}C$ ratios are reported in the standard δ-notation relative to VPDB with an analytical precision of ± 0.5‰, determined from replicate injections of at least every tenth sample.

3.4 Flux calculations

The diffusive flux of sulfate in sediments was calculated according to Fick's first law (Berner, 1980) as:

$$J = -\phi \cdot D_s \cdot \frac{dC}{dz}$$

(Eq. 2)

where J is the diffusive flux (mmol m^{-2} yr^{-1}), ϕ is the average sediment porosity above the SMI, D_s is the sediment diffusion coefficient (1.01×10^{-2} m^2 yr^{-1}) corrected for temperature and porosity effects (Iversen and Jorgensen, 1993), C is the pore water concentration of sulfate (mmol L^{-1}), and z is sediment depth (mbsf). The effect of sediment burial rates on the net sulfate flux, a factor important in areas with rapid

sediment deposition (i.e., ~1 cm yr^{-1}; Blair and Aller, 1995), was not included. Assuming the fate of sulfate in this shallow-SMI, high flux region was entirely due to AOM (Niewohner et al., 1998), methane consumption, DIC production and sulfide production may be inferred from the sulfate flux since each of these compounds are either consumed (methane and sulfate) or produced (DIC and sulfide) at 1:1 stoichiometric ratios (Eq. 1).

4. Results

4.1 Pore water Solute Distributions

The SMI is defined as the depth interval where sulfate concentrations were > 0.1 mM and methane concentrations were greater than background levels (~20 µM). The depth of the SMI generally increased with distance away from the cold seep sites C3 and C5 (Fig. 2A-G). At the non-seep sites (Fig. 2A,B,E, F and G), sulfate decreased from seawater concentration values (~29 mM) near the seafloor to <0.1 mM below the SMI with the exception of four samples (0.1 to 0.9 mM) from C4 (Fig. 2E), which may have been contaminated with traces of seawater. At the cold seep site, C5 (Fig. 2C), sulfate averaged 2.6 ± 0.8 mM (n=9) throughout the extent of the core.

In most near-surface samples above the SMI, methane concentrations ranged from ~ 0.002 to 0.02 mM (Fig. 2A-G). However, methane was present at a concentration of 1.6 mM near the sediment-water interface (10 cmbsf) in C5 (Fig. 2C). Below the SMI, peak methane concentrations ranged between 3.1 and 9.7 mM (Fig. 2A-G), but these values likely underestimate the in-situ concentrations because of losses during core recovery and handling. The solubility of methane at 1 bar and 4°C is ~ 1.8 mM

(Yamamoto et al., 1976); therefore, concentrations at and above this value likely experienced considerable methane loss during sampling.

DIC concentrations increased from the sediment water interface (~2.2 mM) to the SMI where concentrations ranged between 16.4 and 23 mM (Fig. 2A-G). However, because the SMI was located near the sediment water interface in C5 (Fig. 2C), the concentration increase between the sediment surface and the SMI was not observable at our sampling resolution. Below the SMI, DIC concentrations at the non seep sites (Fig. 2A,B,E,F and G) increased gradually with greater depth.

Sulfide was present near the SMI in the non-seep cores, but the maximum concentrations in cores C6, C4 and C1 (23 to 35 μM; Fig. 2A,E and F) were at least 2 orders of magnitude lower than those from C2 and C7 (2.3 mM; Fig. 2B and G). In contrast, sulfide concentrations were high and persistent throughout the vent site cores (C3 and C5; Fig 2C and D), where total dissolved sulfide concentrations were as high as 29 mM.

4.2 Stable carbon isotope distributions

Minimum δ^{13}C-DIC values (-43.3‰ to -47.5‰) occurred at the SMI (Figs. 2H-N), and minimum δ^{13}CH$_4$ values (-72.6‰ to -112.0‰) generally corresponded with or occurred at a depth slightly below the δ^{13}C-DIC minimum (Fig. 2H-N). The minimum δ^{13}CH$_4$ values from cores outside the cold seep (Fig. 2H,I,L,M and N) were considerably more ^{13}C-depleted (-103.5‰ to -112.0‰) than those from within the cold seep (-72.6‰ to -80.6‰; Fig. 2J and K). The δ^{13}C values of both methane and DIC progressively

increased with increasing vertical distance from the SMI (both upcore and downcore) in all cores, within and outside the seep area.

5. Discussion

5.1 Relationship between seismic blanking and gas flux

The DTAGS seismic survey Line 9 contained four zones of seismic blanking (Fig. 3). To determine if the extent of seismic blanking in the deeper subsurface (i.e. > 10 mbsf) and the methane flux at the seafloor were related, the sulfate and DIC pore water profiles along the DTAGS survey line were evaluated to infer methane fluxes. Linear sulfate profiles between the seafloor and the SMI, as was observed at the non-seep sites (Fig. 2A,B,E,F and G) and the seep site, C3 (Fig. 2D) (see Table 2 for r^2 values of the linear regression), suggest solute transport at those locations was diffusively controlled. Previous studies suggest sulfate reduction in other methane-charged, diffusive sediment systems is driven primarily by AOM (Borowski et al., 1996; Niewohner et al., 1998). Since AOM consumes equivalent quantities of sulfate and methane (Eq. 1), the downward diffusive fluxes of sulfate calculated by the sulfate gradient diffusion model for each core site (Eq. 4; Table 2) are a proxy for the upward diffusive flux of dissolved methane (Niewohner et al., 1998). In contrast, the non-linearity of the sulfate profile from the cold seep core C5 (Fig. 2C) does not indicate molecular diffusion as the major form of solute flux. Instead, the near-vertical DIC profile from C5 (Fig. 2C), which ranged from 16.6 to 21.5 mM, is consistent with upward fluid advection (Torres et al., 2002) that results in a greater net flux of methane than by diffusion alone (Luff and Wallmann, 2003).

The most prominent blanking columns occurred beneath the cold seep cores C3 and C5 (Fig. 3) where upward fluid advection and the greatest inferred diffusive methane flux occurred (264 mmol m^{-2} yr^{-1}; Table 2). Blanking columns were also present SW of the cold seep and beneath cores C6 and C2 (Fig. 3). The calculated flux rates for those cores (53 to 63 mmol m^{-2} a^{-1}) were greater than the non-vent cores NE of the cold seep and beneath cores C4, C1 and C7 where a single, narrow blanking column was observed (31 to 52 mmol m^{-2} a^{-1}) (Table 2). Furthermore, with increasing distance from the cold seep and its associated seismic blanking, the modeled methane flux rates in the northeasterly direction decreased from 52 mmol m^{-2} yr^{-1} at C4 to 31 mmol m^{-2} yr^{-1} at C7. These results suggest a coupling between the extent of seismic blanking in the deeper sediments and upward flux of methane at the seafloor above the seismic blanking zones at the Bullseye vent site.

5.2 Subsurface lateral sulfate gradients: Potential for enhanced AOM in advective seeps

Sulfate and sulfide were present throughout C5 (Fig. 2D); a pattern that contrasts with the complete consumption of sulfate in the upper 60 cmbsf in the core collected from the other seep location (Fig. 2C). Deep penetration of sulfate into the region where methane occurs is only possible if the influx of sulfate exceeds the consumption rate and should be accompanied by a decreasing sulfate concentration profile. The vertical sulfate concentration profile from C5 does not support such an influx by downward diffusion of sulfate from overlying seawater. Potential explanations for the uniform sulfate and sulfide profiles include: 1) upward advection of sulfate from deep high-salinity brines (Mitterer et al., 2001), 2) oxidation of dissolved sulfide during sample handling and

processing, 3) dissociation of methane-hydrogen sulfide gas hydrate (Kastner et al., 1998), or 4) lateral advection of sulfate from adjacent sediments with a deeper (i.e. > 2.5 mbsf) SMI. There is no evidence of deep brines along the northern Cascadia margin, thus allowing us to discount their role here. While sulfide oxidation is a possible source of the sulfate, the presence of sulfide throughout the core requires that sulfate was present before the core was recovered, unless the source of the sulfide was from dissociation of methane-hydrogen sulfide gas hydrate. However, within the time frame the core was processed (~1 hr) it is not likely that sulfide would have transitioned from the gas hydrate phase to the uniformly high dissolved concentrations (~29 mM) we measured.

An alternative explanation for the vertical sulfate profile from C5 (Fig. 2C) and horizontal sulfate gradients at the margins of the cold seep (Fig. 4) is a lateral flux from the non-seep region. Horizontal fluid fluxes occur in hydrothermal vent systems where fluids expelled from the seafloor are replaced by seawater penetration at the flanks of the ridge crests (Anderson and Langseth, 1977) and in sedimentary basins where dissolution of salt diapirs causes density inversions in the pore fluids (Hanor, 1987). Ruppel et al. (2005) discussed convective upwelling and downwelling based on observational data in the GOM. However, to our knowledge, similar circulation patterns have never been reported for an accretionary margin cold seep. There is no evidence of thermal anomalies driving convective fluid flow at Bullseye vent (Riedel et al., 2006b), but recent studies suggest that seafloor relief (Wilson and Ruppel, 2005) and fluid overpressure due to sediment compaction (Dugan and Flemings, 2000) can generate flow rates as high as of several millimeters per year. This type of circulation in a cold seep would cause an

increase in the volume of sediment where AOM is occurring, and would be predicted to

increase the consumption of methane in seep systems with this type of fluid circulation.

5.3 ^{13}C-depletion and isotope separation (ε_c) of DIC and methane in diffusive cores

The minimum δ^{13}C values for methane (-103‰ to -112‰) and DIC (-43.3‰ to -

46.8‰) in the non-seep cores occurred at the SMI (Fig. 2H,I,L,M and N). Such a pattern

suggests AOM and methanogenesis were coupled at the SMI (Borowski et al., 1997;

Paull et al., 2000). AOM (Eq. 1) produces DIC with a δ^{13}C similar to the source methane

(Claypool and Kaplan, 1974), and because ^{12}C-DIC is preferentially reduced during

carbonate reduction (Eq. 3),

$$4H_2 + HCO_3^- + H^+ \rightarrow CH_4 + 3H_2O \qquad \text{(Eq. 3)}$$
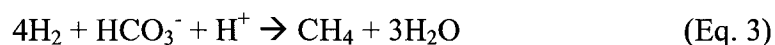
the subsequent reduction of DIC to methane is accompanied by a downward isotopic shift

of 50-90‰ (Whiticar, 1999); thus yielding the observed δ^{13}C methane values.

The extremely low δ^{13}C values (e.g., < 100‰) were only observed in the non-

seep cores (Fig. 2H,I,L,M and N) where diffusion was the dominant flux process (see

discussion above). In contrast, the seep cores, C3 and C5, did not display similarly low

δ^{13}C methane values (Fig. 2J and K). Advection was the dominant fluid transport process

at C5, and although a diffusive flux was calculated for C3, the sampling resolution was

insufficient for determining whether the net flux was diffusive, advective or some

combination of both. However, given that C3 was located within the cold seep and

contained gas hydrate, advection was likely an important component of the fluid

dynamics. A $\delta^{13}CH_4$ value of -103‰ has been reported from a diffusive system at Blake Ridge on the Carolina Rise (Borowski et al., 1997), suggesting diffusive conditions may be required for producing methane with such depleted $\delta^{13}C$ values.

To better understand the factors controlling the isotopic composition of methane and DIC in the diffusive cores, the methane-carbon dioxide partition model developed by Whiticar and Faber (1986) was applied to the non-seep (i.e., diffusive) core data set (Fig. 5). The methane-carbon dioxide partition model is useful for differentiating regions of methane oxidation and production, and for calculating the extent of carbon isotope fractionation in marine sediments. Isotopic fractionation between pore water DIC and methane is expressed as the isotope separation factor (ε_c), the difference between the $\delta^{13}C$ composition of DIC and methane (Eq. 4):

$$\varepsilon_c \approx \delta^{13}C_{DIC} - \delta^{13}C_{CH4} \qquad \text{(Eq. 4)}$$

The ε_c during methanogenesis ranges from 49 to more than 100 (Whiticar, 1999). In shallow sediment systems (e.g., < 10 mbsf) the ε_c is reported to be constant (Whiticar, 1999). A trend of constant ε_c (75 to 82) to a depth of 330 mbsf was demonstrated during ODP Leg 146 at a site (889A) near Bullseye vent (Whiticar and Hovland, 1995; Whiticar et al., 1995). However, in other deep sediment systems (e.g., >100 mbsf) the ε_c has been shown to decrease with greater depth due to a decreasing efficiency of carbonate reduction to by methanogens (Paull et al., 2000). During methane oxidation, the magnitude of carbon isotope fractionation is lower; ε_c ranges from 4-27 and decreases as the pool of methane is depleted (Whiticar, 1999).

The effects of methane production and oxidation on the methane and DIC $\delta^{13}C$

signatures are clearly differentiated when $\delta^{13}C$ values from paired methane and DIC

samples from the five non-seep cores are plotted relative to one another (Fig. 5).

Samples with the most depleted $\delta^{13}CH_4$ values occur at the isotope reversal point, which

represents the SMI depth where AOM and methanogenesis are coupled. The methane

oxidation trend in Fig. 5, which includes anaerobic and aerobic oxidation, follows the

depth interval from the isotope reversal point to the sediment water interface and displays

gradual ^{13}C-enrichment of the residual methane. With the exception of the region

representing the shallowest sample depths where DIC concentrations approach that of

seawater (~2.2 mM), $\delta^{13}DIC$ values were constant because the concentration of the DIC

pool was high enough that the addition of DIC produced by methane oxidation did not

perceptibly influence the overall $\delta^{13}C$ signature (Alperin and Reeburgh, 1984). The

methane production trend in Fig. 5 followed the depth interval from the isotope reversal

point to the base of the cores and displays progressive ^{13}C-enrichment of DIC and

methane with greater depth. Preferential removal of ^{12}C-DIC during methanogenesis

directly enriches the DIC with ^{13}C. In turn, methane is also ^{13}C-enriched since methane

is synthesized from the ^{13}C-enriched DIC. Progressive enrichment occurs along the

methane production/depth trend because fluids at greater depth have been buried for a

greater length of time and, therefore, are more extensively fractionated (Whiticar, 1999).

The oxidation and production trends affecting the $\delta^{13}C$ signatures of the methane

and DIC from the Bullseye vent dataset described above are in accordance with the

Rayleigh distillation model, the basis for the methane-carbon dioxide partition model

(Whiticar, 1999). However, the model predictions did not fit the data in the following

respects: 1) $\delta^{13}C$ values of the DIC and methane were outside the methane production and oxidation fields (shaded areas in Fig. 5) defined by Whiticar and Faber (1986); 2) the production trend does not follow the lines of constant isotopic fractionation (dashed lines in Fig. 5), which are expected to be constant for a particular location (Whiticar, 1999). Among all cores, the ε_c ranged between ~60 and 50 at the isotope reversal point (Fig. 5). Below that depth (following the methane production/depth trend in Fig. 5) the ε_c abruptly shifted to ~40 and then gradually returned to ~60 near the base of the core.

Coupling between AOM and methanogenesis at the SMI (Borowski et al., 1997) appears to be a plausible, and mechanistically realistic, explanation for reconciling the discrepancy between the data from the non-seep sites and the fields defined by Whiticar and Faber (1986) (i.e., shaded areas in Fig. 5). The shift to lower ε_c values at the top of the methanogenic zone may be related to the diffusive nature of the cores. Specifically, downward diffusion of ^{13}C-depleted DIC from the SMI would lower the ε_c, provided the deeper methane pool was not similarly affected by downward diffusion of ^{13}C-depleted methane. At the SMI, the concentration of DIC (16.4 to 23.0 mM) was between 2-3 orders of magnitude greater than the concentration of methane (0.02 to 0.2 mM) (Fig. 2A,B,E, F and G). Thus, the amount of DIC diffusing away from the SMI would be expected to be greater than that for methane. Given that DIC from the SMI is ^{13}C-depleted relative the deeper DIC pool, the effect of downward DIC diffusion would be more ^{13}C-depleted DIC values at depth, which would lower the ε_c values since methane is unaffected by diffusion of DIC.

5.4 Dissolved inorganic carbon (DIC) source-diffusion model

To test the mechanistic description provided above, a simple source-diffusion model was developed to determine if diffusion of DIC produced at the SMI could mix with seawater and deep source endmembers to reproduce the measured DIC concentration profiles. The model concentrations will be subsequently used in a stable carbon isotope mass balance model to determine whether modeled concentrations produce a $\delta^{13}C$ profile similar to the measured profile.

The methane-carbon dioxide partition model, as described by Whiticar (1999), is based on the closed-system Rayleigh distillation model. In other words, the only processes affecting the isotopic composition of the DIC at each depth interval are those occurring within that interval. In contrast, the mechanism we have described for explaining the discrepancies between the Bullseye vent data and the closed system model assumes that solutes (in particular, DIC) diffuse between depth intervals. To determine if downward diffusion of DIC from the SMI to the methanogenic zone could account for the isotopic separation (ϵ_c) pattern observed in the non-seep cores, a simple one-dimensional steady-state source-diffusion model was developed to calculate DIC concentration profiles in a system where DIC produced at the SMI was allowed to distribute itself via diffusion. In turn, the relative contributions and stable carbon isotope signatures of DIC from seawater burial, AOM and the bottom of the cores (6-8 mbsf) were utilized in a stable carbon isotope mass balance model to calculate $\delta^{13}DIC$ profiles.

The partial differential equation utilized to describe DIC concentrations at steady state contains a diffusion term, a source term and a sink term:

$$D_{s,DIC} \frac{\partial^2 C_{DIC}}{\partial z^2} + S_{DIC} - Q_{DIC} = 0 \qquad \text{(Eq. 5)}$$

where $D_{s,DIC}$ is the sediment diffusion coefficient for DIC (6.32×10^{-6} cm^2 s^{-1}) estimated

from the tracer diffusion coefficient for HCO$_3^-$ (Li and Gregory, 1974) and corrected for

in situ temperature (4°C) by the Stokes-Einstein Equation (Li and Gregory, 1974) and

porosity (Iversen and Jorgensen, 1993). The C_{DIC} term is the concentration of DIC, z is

depth (positive downward) and S_{DIC} is the source term for DIC calculated from the

sulfate flux (mmol cm^{-2} s^{-1}; Table 2) and the assumed thickness of the SMI (20 cm) for

all cores, and Q_{DIC} (the sink term) is an empirically determined fraction of S_{DIC} (25%, as

discussed below) assumed to be lost from the system by authigenic carbonate formation

to balance the model output and measured DIC concentrations.

Utilizing the sulfate flux as a proxy for the DIC source term (S_{DIC}) is based on the

assumption that AOM is the only process that consumes sulfate, and that sulfate

consumption and DIC production occur at a 1:1 ratio (Eq. 1). Previous studies support

the assumption that AOM is the predominant sulfate sink in methane-charged marine

sediments with diffusive flux regimes (Borowski et al., 1997; Niewohner et al., 1998;

Boetius et al., 2000). Because AOM occurs at the SMI, DIC produced by the source term

(S_{DIC}) is limited to the model component (region II) representing the SMI (Fig. 6A). The

model further assumes linear DIC gradients in regions I and III (i.e., $\partial^2 C_{DIC}/\partial z^2 = 0$,

meaning there are no source or sink terms) (Fig. 6A), which is supported by the

observation of near-linear DIC gradients above and below the SMI in the non-seep cores

(Figs. 2A,B,E,F and G).

In the simple case where $Q_{DIC} = 0$ (i.e., no carbonate precipitation) in region II,

the total concentration of DIC (C_T) at any depth (z) is the sum of three components (Eq.

6; Fig. 6A)

$$C_T = C_{SW} + C_D + C_S \qquad\qquad \text{(Eq. 6)}$$

where C_{SW} is the contribution from buried seawater, C_D is the contribution by diffusion

from the deep source and C_S is the contribution by diffusion from AOM. The steady

state solution to the partial differential equation was determined with the following

boundary conditions: 1) The concentration of seawater (C_{SW}) at the sediment water

interface (z_0) was assumed to be 2.2 mM (Ortiz et al., 1997); 2) The concentration from

the deep source (C_3) was the measured concentration at the bottom of each core (z_3); and

3) The boundaries between adjacent regions are continuous, both in concentration and

gradient (dC/dz). According to the solution to Eq. 5, C_{SW} is constant with depth, C_D

increases linearly with depth, and C_S has linear slopes in regions I and II, but quadratic

curvature within region II (the SMI). Specific model output values based on the general

solution, shown in Fig. 6A, depend on the values of the input parameters C_{SW}, C_3, Z_1, Z_2,

Z_3, S_{DIC} and $D_{S,DIC}$ (Table 3).

The situation is more complicated when the sink term Q_{DIC} is non-zero in region

II (Fig. 6B). In that case, the concentration C_T is reduced by a quantity C_Q to C_T^*. In this

process, the concentrations of C_{SW}, C_D and C_S are reduced to a fraction (f) of their values

in the absence of any sink (Eqs. 7-9):

$$C_{SW}^* = f \times C_{SW} \qquad\qquad \text{(Eq. 7)}$$

$$C_D^* = f \times C_D \qquad\qquad \text{(Eq. 8)}$$

$$C_S^* = f \times C_S \qquad\qquad \text{(Eq. 9)}$$

where

$$f = 1 - \frac{C_Q}{C_{SW} + C_D + C_S}$$

The removal term (f), only applies in region II where the sink process occurs, and was used to determine the concentrations of endmembers for each component (C_1 and C_2) at Z_1 and Z_2 (Fig. 6B). Limiting the sink process to region II (which represents the SMI) is based on the assumption that authigenic carbonate production occurs only at the SMI; where alkalinity, as DIC, is generated (Luff and Wallmann, 2003). Concentrations for all components in region I were determined by linear interpolation between the endmembers C_0 and C_1 at Z_1 and Z_2, respectively (Fig. 6B). Similarly, the concentrations for all components in region III were determined by linear interpolation between endmembers C_2 and C_3 at Z_2 and Z_3, respectively (Fig. 6B). Concentrations based on these interpolations are represented by C' (Fig. 6B).

The best fit between the model results and the measured values (Figs. 7A-E) was obtained with an "f" value of 0.75. An "f" value of 0.75 is equivalent to removing 25% of the total DIC generated. The presumed fate of the lost DIC is authigenic carbonate precipitation (Eq. 11) induced by alkalinity generated at the SMI by AOM (Eq. 1) (Paull et al., 1992; Kulm and Suess, 1990; Wallmann et al., 2006).

$$HCO_3^- + (Ca, Mg)^{+2} + \rightarrow (Ca, Mg)CO_3 + H^+ \qquad (Eq.11)$$
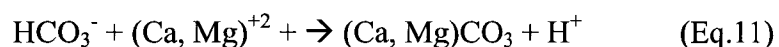
Authigenic carbonate observed near the SMI at ODP Leg 164 Sites 994, 995 and 997 was associated with sharp concentration decreases of calcium and magnesium associated with precipitation of calcite ($CaCO_3$) and dolomite ($CaMg(CO_3)_2$) (Eq. 11)

(Rodriguez et al., 2000). To determine if the 25% removal term was realistic, we calculated the potential flux of calcium from seawater (~10 mM) into the sediments to determine if the previously calculated carbonate production rates we calculated could be sustained with an f of 0.75. If authigenic carbonate formation is the primary sink for DIC, the carbonate production rate must be balanced by an equivalent flux of calcium and magnesium. Using Fick's First Law (Eq. 4) with a temperature- and porosity-corrected sediment diffusion coefficient ($D_S = 2.00 \times 10^{-6}$ cm^2 s^{-1}; Li and Gregory, 1974; Iversen and Jorgensen, 1993), a concentration gradient assuming complete consumption of calcium from seawater (~10 mM) to the SMI and measured porosities for each core (Table 2), we calculated the average potential flux of calcium to be 26% ($\pm$ 3%, n=5) of the DIC production. Thus, the potential calcium flux alone is sufficient to balance the assumed 25% removal term. However, complete consumption of calcium is not an absolute requirement since dolomite ($CaMg(CO_3)_2$) precipitation would reduce the amount of calcium consumed during authigenic carbonate precipitation. A removal term of 25% is in line with other studies that have shown that about one third of the alkalinity generated by AOM is removed by authigenic carbonate precipitation (Luff and Wallman, 2003; Wallman et al., 2006).

5.5 Stable carbon isotope mass balance model

The source-sink-diffusion model concentrations (C^* in region II and C' in regions I and III, hereafter collectively referred to as C^m) were used in an isotope mass balance model (Eq. 12) to determine if the assumptions of the concentration-based model were also applicable to describing the δ^{13}C-DIC values.

$$\delta_T C_T{}^m = \delta_{SW} C_{SW}{}^m + \delta_D C_D{}^m + \delta_S C_S{}^m \qquad\qquad \text{(Eq. 12)}$$

where

$\delta_{T,} C_T{}^m$ = modeled $\delta^{13}C$ and total DIC concentration ($C_T{}^m$).

$\delta_{SW,} C_{SW}{}^m = \delta^{13}C$ of seawater (0‰; Ortiz et al., 1997) and modeled contribution

$\quad$ ($C_{SW}{}^m$) from seawater DIC endmember.

$\delta_{D,} C_D{}^m = \delta^{13}C$ and modeled contribution ($C_D{}^m$) from the deep sourced DIC

$\quad$ endmember. The δ_D was determined from the $\delta^{13}CH_4$ at the bottom of each

$\quad$ core, plus a methanogenic fractionation factor (ε_c) of 60 (Whiticar, 1999).

$\delta_{S,} C_S{}^m = \delta^{13}C$ and modeled contribution ($C_S{}^m$) of DIC from AOM. The δ_S was

$\quad$ determined from the $\delta^{13}CH_4$ slightly below the SMI of each core where

$\quad$ concentrations still exceeded 1mM, plus a fractionation factor (ε_c) of -4 to

$\quad$ account for oxidation effects (Whiticar, 1999). The $\delta^{13}CH_4$ values slightly

$\quad$ below the SMI are assumed to represent the source CH_4 that supports the

$\quad$ production of DIC during AOM. Methane with low $\delta^{13}C$ values produced

$\quad$ from recycled DIC was present at low concentration and, thus, is not

$\quad$ considered a major source for the AOM derived DIC component.

The modeled $\delta^{13}C$ profiles of DIC displayed a pattern similar to the measured

values, however, offsets (both positive and negative) in the modeled vs. observed profiles

were observed in all cases in at least part of each profile (Figs. 7F-J). The modeled $\delta^{13}C$-

DIC results from cores C6, C2 and C4, which were located adjacent to the cold seep and

had the highest methane fluxes (as inferred from the SMI depths), were consistently

lower than the measured values, particularly at the depths above the SMI. In contrast,

modeled δ^{13}C-DIC results from cores C1 and C7, which had lower SMI depth-inferred

methane fluxes, were slightly greater than the measured values, particularly in the deeper

regions of the profiles. The discrepancy between the modeled and measured values may

reflect the absence of an advective model component. Profiles from cores with lower

modeled δ^{13}C values (C6 and C4; Fig. 7F and H) have slight curvature that suggest some

downward advection of seawater. Upon closer inspection, similar slight curvature was

also present in the sulfate profiles (Figs. 2A and E). The addition of seawater DIC (δ^{13}C

~ 0‰; Ortiz et al., 1997) by advection would cause an enrichment in the δ^{13}C of the DIC

relative to that predicted for a purely diffusive system and is consistent with the observed

offsets between the modeled and observed values. Additional model and data

discrepancies (e.g., C1 and C7) might be related to the incorrect model assumptions in

the fractionation factors selected (ε_c = 60 for methanogenesis and ε_c = -4 for oxidation),

effects from recycling of DIC at the SMI, and biogeochemical processes that occurred in

regions I and III, which were assumed to be non-reactive.

The purpose of this model, however, was not to fully integrate the diffusive,

advective and biogeochemical complexities of this system, but to demonstrate the relative

importance of AOM and diffusion in controlling the concentration and isotope

composition of the DIC. Based on the model, we infer that ^{13}C-depleted DIC generated

at the SMI likely diffuses into the upper methanogenic zone where it reduces the isotope

separation factor (ε_c) between DIC and methane relative to the closed-system Rayleigh

distillation-based methane-carbon dioxide partition model (Whiticar, 1999). In cases

where the carbon isotope mass balance model and the measured profiles deviated, slight

advective downwelling of seawater at non-seep sites adjacent to the cold seep is

suggested – a conclusion not obvious from evaluating the shapes of the concentration

profiles. Furthermore, the choice of identical fractionation factors (ε_c) for all cores may

not fully represent the complexities of methane oxidation and methanogenesis in this

system.

6. Conclusions

A systematic study of the diffusive and advective regions of an accretionary

margin cold seep system was conducted to evaluate processes that controlled the flux and

cycling of methane carbon within the pore water fluids. High vertical resolution

geochemical data were obtained from a seven core transect that encompassed the active

cold seep and adjacent non-seep areas. A clear relationship was observed between the

extent of seismic blanking and geochemically inferred methane fluxes. Furthermore,

subsurface lateral sulfate gradients along the margins of the advective cold seep

suggested a mechanism for supplying ascending seep fluids with sulfate that supported

AOM throughout the upper 250 cmbsf of the cold seep.

Diffusion of AOM derived DIC into the upper methanogenic region was proposed

as a mechanism for supporting production of methane with $\delta^{13}C$ values as depleted as -

112‰ and isotope separation factors (ε_c) between methane and DIC that were

inconsistent with the methane-DIC partition model. A simple source-diffusion model

developed to simulate production of DIC generated at the SMI, mixing with seawater and

deep source endmembers and loss of DIC by authigenic carbonate precipitation at the

SMI was coupled to a stable carbon isotope mass balance model. The models produced concentration and $\delta^{13}C$-DIC profiles similar to the measured values. Where the model and measured values did not agree, downward advection of seawater was suggested.

References

Alperin, M. J.; Reeburgh, W. S. Geochemical observations supporting anaerobic methane oxidation. In: Crawford, R.; Hanson, R., ed. Microbial Growth on C-1 Compounds: American Society for Microbiology. 282-289; 1984.

Anderson, R. N.; Langseth, M. G. Mechanisms of heat-transfer through the floor of the Indian Ocean. Journal of Geophysical Research. 82: 3391-3409; 1977.

Berner, R. A. Early Diagenesis: A Theoretical Approach. Princeton, NJ: Princeton University Press; 1980.

Blair, N. E.; Aller, R. C. Anaerobic methane oxidation on the Amazon shelf. Geochim. Cosmochim. Acta. 59: 3707-3715; 1995.

Boetius, A.; Ravenschlag, K.; Schubert, C. J.; Rickert, D.; Widdel, F.; Gieseke, A.; Amann, R.; Jorgensen, B. B.; Witte, U.; Pfannkuche, O. A marine microbial consortium apparently mediating anaerobic oxidation of methane. Nature. 407: 623-626; 2000.

Borowski, W. S.; Paull, C. K.; Ussler, W. Marine pore-water sulfate profiles indicate in situ methane flux from underlying gas hydrate. Geology. 24: 655-658; 1996.

Borowski, W. S.; Paull, C. K.; Ussler, W. Carbon cycling within the upper methanogenic zone of continental rise sediments: An example from the methane-rich sediments overlying the Blake Ridge gas hydrate deposits. Mar. Chem. 57: 299-311; 1997.

Borowski, W. S.; Paull, C. K.; Ussler, W. Global and local variations of interstitial sulfate gradients in deep-water, continental margin sediments: Sensitivity to underlying methane and gas hydrates. Mar. Geol. 159: 131-154; 1999.

Claypool, G. E.; Kaplan, I. R. The origin and distribution of methane in marine sediments. In: Kaplan, I. R., ed. Natural Gases in Marine Sediments: Plenum Press. 99-139; 1974.

Cline, J. D. Spectrophotometric determination of hydrogen sulfide in natural waters. Limnology and Oceanography. 14: 454-458; 1969.

Dallimore, S. R.; Collett, T. S. Scientific Results From the Mallik 2002 Gas Hydrate Production Research Well Program, Mackenzie Delta, Northwest Territories, Canada. Bull. Geol. Surv. Canada; 2005.

Davis, E. E.; Hyndman, R. D. Accretion and recent deformation of sediments along the northern Cascadia subduction zone. Geol. Soc. Am. Bull. 101: 1465-1480; 1989.

Dickens, G. R.; Oneil, J. R.; Rea, D. K.; Owen, R. M. Dissociation of oceanic methane hydrate as a cause of the carbon-isotope excursion at the end of the Paleocene. Paleoceanography. 10: 965-971; 1995.

Dugan, B.; Flemings, P. B. Overpressure and fluid flow in the New Jersey continental slope: Implications for slope failure and cold seeps. Science. 289: 288-291; 2000.

Hanor, J. S. Kilometer-scale thermohaline overturn of pore waters in the Louisiana Gulf-Coast. Nature. 327: 501-503; 1987.

Hesselbo, S. P.; Grocke, D. R.; Jenkyns, H. C.; Bjerrum, C. J.; Farrimond, P.; Bell, H. S. M.; Green, O. R. Massive dissociation of gas hydrate during a Jurassic oceanic anoxic event. Nature. 406: 392-395; 2000.

Hinrichs, K. U.; Boetius, A. The anaerobic oxidation of methane: new insights in microbial ecology and biogeochemistry. In: Wefer, G.; Billett, D.; Jorgensen, B. B.; Schluter, M.; van Weering, T., ed. Ocean Margin Systems: Springer. 457-477; 2002.

Hinrichs, K. U.; Hayes, J. M.; Sylva, S. P.; Brewer, P. G.; Delong, E. F. Methane-consuming archaebacteria in marine sediments. Nature. 398: 802-805; 1999.

Hoehler, T. M.; Alperin, M. J.; Albert, D. B.; Martens, C. S. Field and laboratory studies of methane oxidation in an anoxic marine sediment - evidence for a methanogen-sulfate reducer consortium. Glob. Biogeochem. Cycle. 8: 451-463; 1994.

Hoehler, T. M.; Borowski, W. S.; Alperin, M. J.; Rodriguez, N. M.; Paull, C. K. Model, stable isotope,and radiocarbon characterization of anaerobic methane oxidation in gas hydrate-bearing sediments of the Blake Ridge. Proceeedings of the Ocean Drilling Program, Scientific Results: Ocean Drilling Program. 79-85; 2000.

Hyndman, R. D.; Davis, E. E. A mechanism for the formation of methane hydrate and sea-floor bottom-simulating reflectors by vertical fluid expulsion. J. Geophys. Res. -Solid Earth. 97: 7025-7041; 1992.

Intergovernmental Panel on Climate Change Climate Change 2001 - The Scientific Basis. Cambridge, UK: Cambridge University Press; 2001.

Iversen, N.; Jorgensen, B. B. Diffusion-coefficients of sulfate and methane in marine-sediments - Influence of porosity. Geochimica et Cosmochimica Acta. 57: 571-578; 1993.

Judd, A. G. Natural seabed gas seeps as sources of atmospheric methane. Environmental Geology. 46: 988-996; 2004.

Kastner, M.; Kvenvolden, K. A.; Lorenson, T. D. Chemistry, isotopic composition, and origin of a methane- hydrogen sulfide hydrate at the Cascadia subduction zone. Earth Planet. Sci. Lett. 156: 173-183; 1998.

Kennett, J. P.; Cannariato, K. G.; Hendy, I. L.; Behl, R. J. Methane Hydrates in Quaternary Climate Change. Washington D.C.: American Geophysical Union; 2002.

Kulm, L. D.; Suess, E. Relationship between carbonate deposits and fluid venting - Oregon accretionary prism. Journal of Geophysical Research-Solid Earth and Planets. 95: 8899-8915; 1990.

Lelieveld, J.; Crutzen, P. J.; Dentener, F. J. Changing concentration, lifetime and climate forcing of atmospheric methane. Tellus Series B-Chemical and Physical Meteorology. 50: 128-150; 1998.

Li, Y. H.; Gregory, S. Diffusion of ions in sea-water and in deep-sea sediments. Geochimica et Cosmochimica Acta. 38: 703-714; 1974.

Luff, R.; Wallmann, K. Fluid flow, methane fluxes, carbonate precipitation and biogeochemical turnover in gas hydrate-bearing sediments at Hydrate Ridge, Cascadia Margin: Numerical modeling and mass balances. Geochim. Cosmochim. Acta. 67: 3403-3421; 2003.

MacDonald, I. R.; Bender, L. C.; Vardaro, M.; Bernard, B.; Brooks, J. M. Thermal and visual time-series at a seafloor gas hydrate deposit on the Gulf of Mexico slope. Earth and Planetary Science Letters. 233: 45-59; 2005.

Mitterer, R. M.; Malone, M. J.; Goodfriend, G. A.; Swart, P. K.; Wortmann, U. G.; Logan, G. A.; Feary, D. A.; Hine, A. C. Co-generation of hydrogen sulfide and methane in marine carbonate sediments. Geophysical Research Letters. 28: 3931-3934; 2001.

Niewohner, C.; Hensen, C.; Kasten, S.; Zabel, M.; Schulz, H. D. Deep sulfate reduction completely mediated by anaerobic methane oxidation in sediments of the upwelling area off Namibia. Geochim. Cosmochim. Acta. 62: 455-464; 1998.

Novosel, I.; Spence, G. D.; Hyndman, R. D. Reduced magnetization produced by increased methane flux at a gas hydrate vent. Marine Geology. 216: 265-274; 2005.

Ortiz, J.; Mix, A.; Hostetler, S.; Kashgarian, M. The California current of the last glacial maximum: Reconstruction at 42 degrees N based on multiple proxies. Paleoceanography. 12: 191-205; 1997.

Paull, C. K.; Chanton, J. P.; Neumann, A. C.; Coston, J. A.; Martens, C. S.; Showers, W. Indicators of methane-derived carbonates and chemosynthetic organic carbon deposits; examples from the Florida Escarpment. PALAIOS. 7: 361-375; 1992.

Paull, C. K.; Lorenson, T. D.; Borowski, W. S.; Ussler, W.; Olsen, K.; Rodriguez, N. M. Isotopic composition of CH_4, CO_2 species, and sedimentary organic matter within samples from the Blake Ridge: Gas source implications. In: Paull, C.;

Matsumoto, R.; Wallace, P. J.; Dillon, W. P., ed. Proceedings of the Ocean Drilling Program, Scientific Results, Vol. 164. 67-78; 2000.

Paull, C. K.; Ussler, W.; Lorenson, T.; Winters, W.; Dougherty, J. Geochemical constraints on the distribution of gas hydrates in the Gulf of Mexico. Geo-Marine Letters. 25: 273-280; 2005.

Plummer, R. E.; Pohlman, J. W.; Coffin, R. B. Compound specific stable carbon isotope analysis of low-concentration complex hydrocarbon mixtures from natural gas hydrate systems. American Geophysical Union, Dec 5-9, San Francisco CA.; 2005.

Reeburgh, W. S. An improved interstitial water sampler. Limnology and Oceanography. 12: 163-165; 1967.

Riddihough, R. Recent movements of the Juan-De-Fuca Plate system. Journal of Geophysical Research. 89: 6980-6994; 1984.

Riedel, M.; Collett, T.; Malone, M.; Akiba, F.; Blanc-Valleron, M.; Ellis, M.; Guerin, G.; Hashimoto, Y.; Heuer, V.; Higashi, Y.; Holland, M.; Jackson, P.; Kaneko, M.; Kastner, M.; Kim, J.-H.; Katijama, H.; Long, P.; Malinvero, A.; Myers, G.; Palekar, L.; Pohlman, J.; Schultheiss, P.; Teichert, B.; Torres, M.; Trehu, A.; Wang, J.; Wortmann, U.; Yoshhioka, H. Gas hydrate transect across northern Cascadia margin. EOS. 87: 325, 330, 332; 2006a.

Riedel, M.; Novosel, I.; Spence, G. D.; Hyndman, R. D.; Chapman, R. N.; Solem, R. C.; Lewis, T. Geophysical and geochemical signatures associated with gas hydrate-related venting in the northern Cascadia margin. Geological Society of America Bulletin. 118: 23-38; 2006b.

Riedel, M.; Spence, G. D.; Chapman, N. R.; Hyndman, R. D. Seismic investigations of a vent field associated with gas hydrates, offshore Vancouver Island. Journal of Geophysical Research-Solid Earth. 107: doi:10.1029/2001JB000269; 2002.

Rodriguez, N. M.; Paull, C. K.; Borowski, W. S. Zonation of authigenic carbonates within gas hydrate-bearing sedimentary sections on the Blake Ridge: Offshore southeastern North America. In: Paull, C. K.; Matstumoto, R.; Wallace, P. J.; Dillon, W. P., ed. Proceedings of the Ocean Drilling Program, Scientific Results, Vol. 164. 301-312; 2000.

Spence, G. D.; Wood, W. T.; Coffin, R. B. DTAGS2: Deep Towed Seismics and Piston Coring for Gas Hydrates Offshore Vancouver Island: Cruise PGC02-08 Cruise Report. Victoria, BC: University of Victoria; 2003.

Spence, G. D.; Hyndman, R. D.; Chapman, N. R.; Walia, R.; Gettrust, J.; Edwards, R. N. North Cascadia deep sea gas hydrates. Ann. NY Acad. Sci. 912: 65-75; 2000.

Suess, E.; Torres, M. E.; Bohrmann, G.; Collier, R. W.; Greinert, J.; Linke, P.; Rehder, G.; Trehu, A.; Wallmann, K.; Winckler, G.; Zuleger, E. Gas hydrate destabilization: enhanced dewatering, benthic material turnover and large methane plumes at the Cascadia convergent margin. Earth and Planetary Science Letters. 170: 1-15; 1999.

Wallmann; Aloisi, G.; Haeckel, M.; Obzhirov, A.; Pavlova, G.; Tishchenko P. Kinetics of organic matter degradation, microbial methane generation, and gas hydrate formation in anoxic marine sediments. Geochimica et Cosmochimica Acta. 70: 3905-3927; 2006.

Whiticar, M. J. Carbon and hydrogen isotope systematics of bacterial formation and oxidation of methane. Chem. Geol. 161: 291-314; 1999.

Whiticar, M. J.; Hovland, M.; Kastner, M.; Sample, J. C. Organic geochemistry of gases, fluids, and hydrates at the Cascadia accretionary margin. In: Carson, B.; Westbrook, G. K.; Musgrave, R. J.; Suess, E., ed. Proceedings of the Ocean Drilling Program, Scientific Results. 385-397; 1995.

Whiticar, M. J.; Hovland, M. Molecular and stable isotope analysis of sorbed and free hydrocarbon gases of Leg 146, Cascadia and Oregon margins. In: Carson, B.; Westbrook, G. K.; Musgrave, R. J.; Suess, E., ed. Proceedings of the Ocean Drilling Program, Scientific Results. 439-450; 1995.

Whiticar, M. J.; Faber, E. Methane oxidation in sediment and water column environments - Isotope evidence. Org. Geochem. 10: 759-768; 1986.

Wilson, A.; Ruppel, C. Impact of shallow convection on the gas hydrate reservoir in the Gulf of Mexico salt tectonics province. EOS Tranactions. 86: Abstract OS41-06; 2005.

Wood, W. T.; Gettrust, J. F.; Chapman, N. R.; Spence, G. D.; Hyndman, R. D. Decreased stability of methane hydrates in marine sediments owing to phase-boundary roughness. Nature. 420: 656-660; 2002.

Yamamoto, S.; Alcauskas, J. B.; Crozier, T. E. Solubility of Methane in Distilled Water and Seawater. Journal of Chemical and Engineering Data. 21: 78-80; 1976.

Table 1. Information for piston cores recovered from Bullseye Vent, including core abbreviations used throughout text

Station	Latitude (N)	Longitude (W)	Water Depth (m)	Core Length (m)	Distance from Cold Seep (m)[1]
PGC0208-01 (C1)	48° 40.2530'	126° 50.8650'	1274	7.33	313
PGC0208-02 (C2)	48° 40.0146'	126° 51.0389'	1282	7.95	125
PGC0208-03 (C3)	48° 40.0983'	126° 50.9898'	1276	7.25	seep site
PGC0208-04 (C4)	48° 40.1829'	126° 50.9317'	1274	8.58	167
PGC0208-05 (C5)	48° 40.0744'	126° 50.9961'	1282	7.77	seep site
PGC0208-06 (C6)	48° 39.9388'	126° 51.0953'	1284	6.44	275
PGC0208-07 (C7)	48° 40.3125'	126° 50.8405'	1268	8.51	423

[1] Distance calculated relative to nearest seep site (PGC0208-03 or PGC0208-05)

Table 2. Sulfate diffusive flux input parameters and calculated rates for the non-seep cores and seep site C3

Station	D_s of sulfate (cm^2s^{-1})	Porosity (ϕ)	Sulfate gradient $(mM\ cm^{-1})$	r^2	[a]Diffusive flux rate of sulfate/methane $(mmol\ m^{-2}a^{-1})$
PGC0208-01 (C1)	3.07×10^{-6}	0.72	-0.06	0.995	41
PGC0208-02 (C2)	2.91×10^{-6}	0.69	-0.08	0.996	53
PGC0208-03 (C3)	2.82×10^{-6}	0.67	-0.44	0.935	264
PGC0208-04 (C4)	2.99×10^{-6}	0.71	-0.08	0.987	52
PGC0208-06 (C6)	2.95×10^{-6}	0.70	-0.10	0.984	63
PGC0208-07 (C7)	2.98×10^{-6}	0.71	-0.05	0.986	31

[a]Assumes sulfate and methane are consumed in a 1:1 stoichiometric ratio (Eq. 1). See text for discussion.

Table 3. Input parameters for source-sink-diffusion model

Input parameter	Description	PGC0208				
		C1	C2	C4	C6	C7
C_{SW}	Seawater concentration (mM)	2.2	2.2	2.2	2.2	2.2
C_3	Concentration at the bottom of core (mM)	21.1	21.1	20.2	19.9	21.1
Z_1	Top of SMI (cmbsf)	463	315	371	235	553
Z_2	Bottom of SMI (cmbsf)	483	335	391	255	573
Z_3	Bottom of core (cmbsf)	683	762	817	606	818
S_{DIC}[1]	DIC source term (mol cm^{-3} s^{-1})	6.54×10^{-15}	8.40×10^{-15}	8.25×10^{-15}	9.98×10^{-15}	4.93×10^{-15}
$D_{S,DIC}$	DIC diffusion coefficient (cm^2 s^{-1})	3.32×10^{-6}	3.27×10^{-6}	3.22×10^{-6}	3.27×10^{-6}	3.12×10^{-6}

[1]Assumes an SMI interval depth of 20 cm
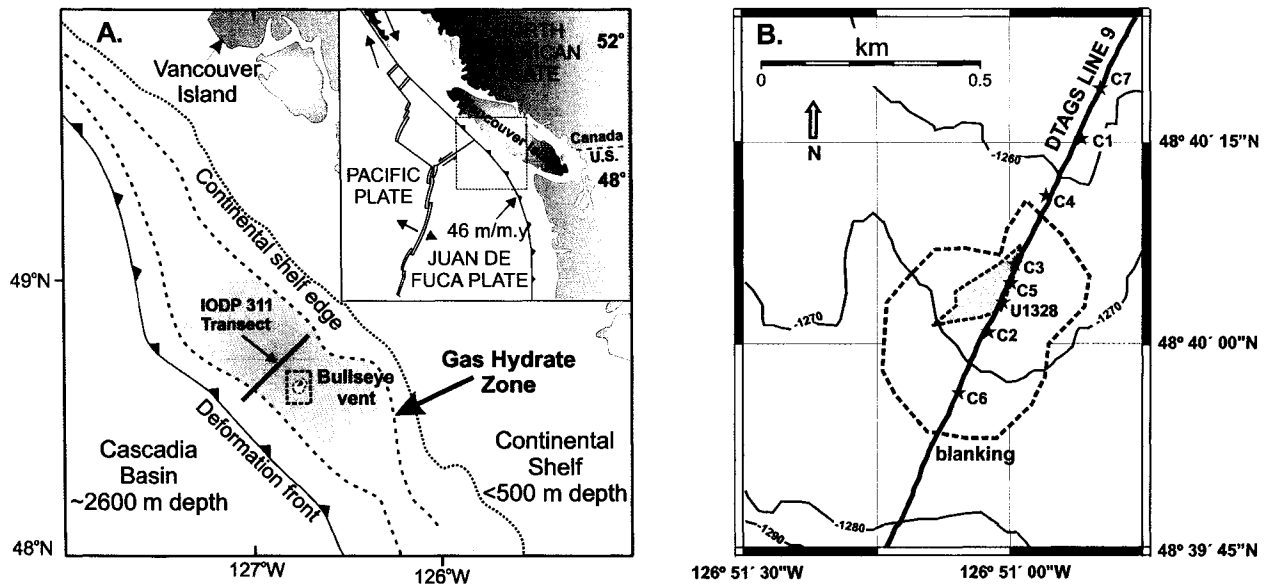
Figure 1. A. Geographic setting of Bullseye vent and the location of IODP Expedition 311 (x311) drilling transect on the northern Cascadia margin. The gas hydrate zone (shaded area) is inferred from a bottom simulating reflector (BSR) that covers ~50% of the mid-continental slope (Spence et al., 2000). B. The coring locations (red stars) and IODP x311 off-transect Site U1328 (green star) were along DTAGS seismic line 9 (blue line). The transect crossed an area with enhanced seismic blanking (yellow) and near-surface gas hydrate (aqua) (modified from Spence et al., 2003).
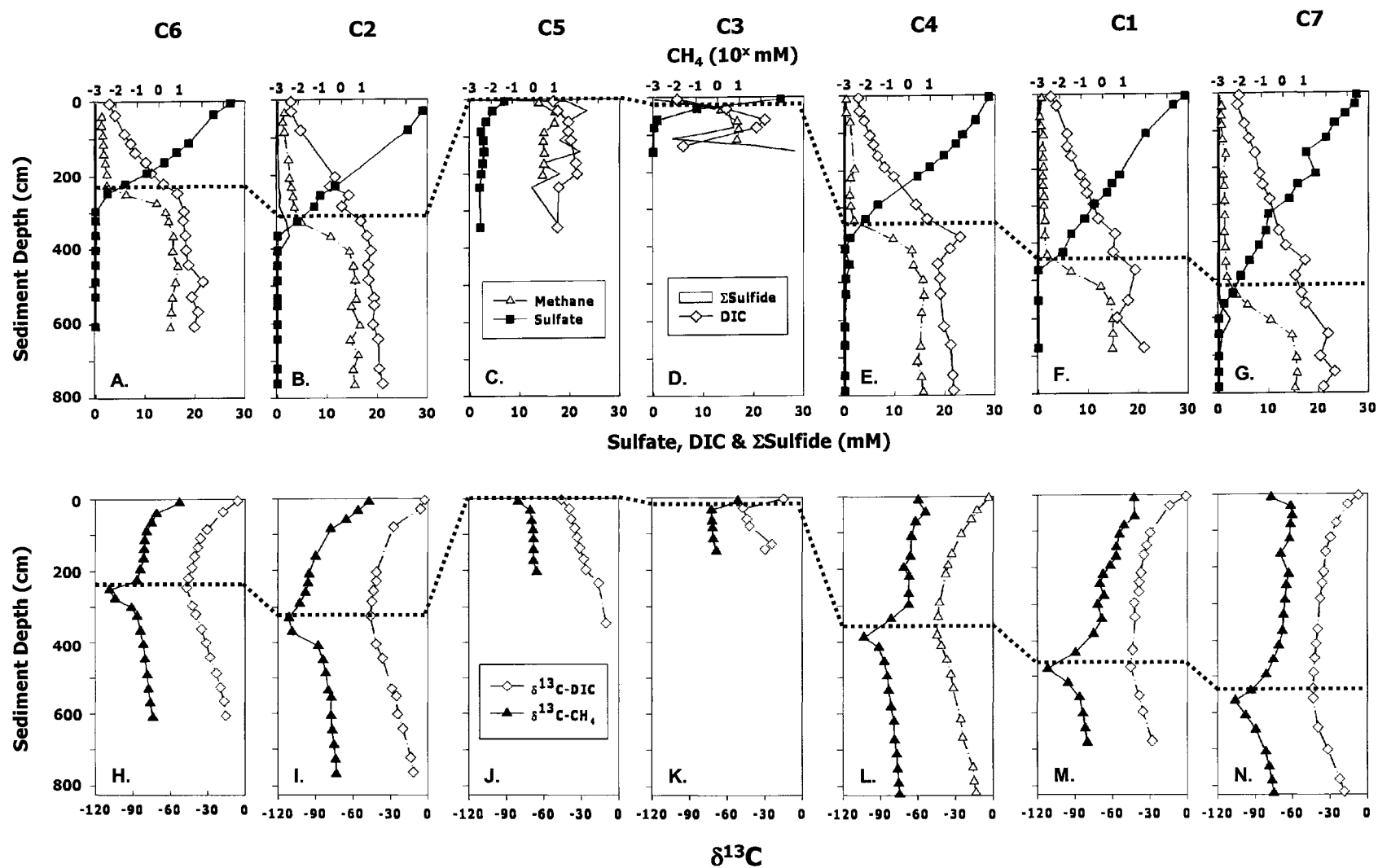
Figure 2. Vertical profiles of dissolved pore water constituents from the piston core transect across the Bullseye vent site. Top row (A-G): Concentration profiles of methane, sulfate, sulfide and dissolved inorganic carbon (DIC). Bottom row: Stable carbon isotope profiles of methane and DIC. The cores are arranged in their relative locations along the SW to NE trending transect across Bullseye vent, as indicated in Fig. 1. The dashed horizontal line represents the sulfate-methane interface (SMI).
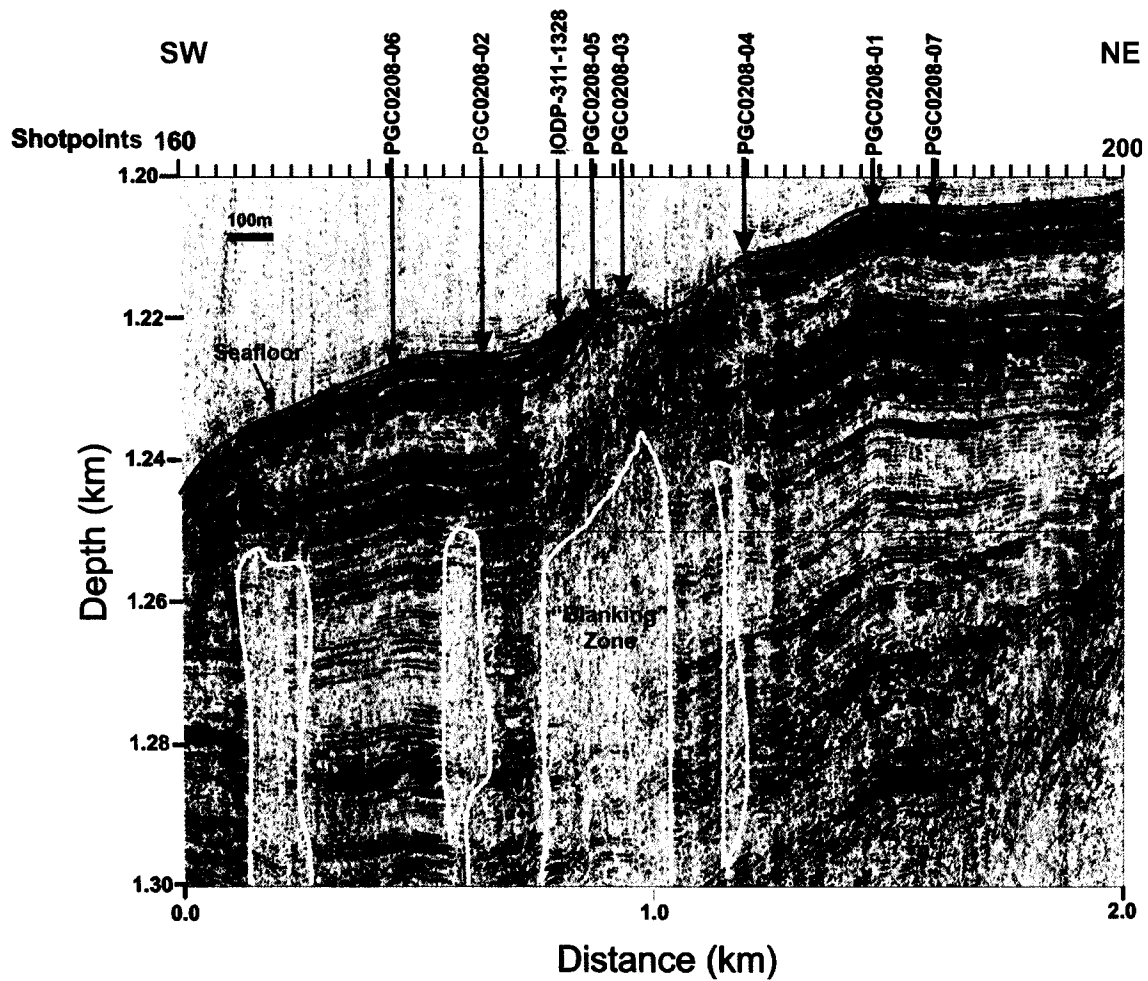
Figure 3. DTAGS (Line 9) high resolution seismic image of the Bullseye vent area. The coring locations from this study and approximate location of IODP Expedition 311 Site 1328 are indicated where arrows contact the seafloor. Seismic blanking zones (regions of anomalously weak reflectivity that appear as vertical bands of muted colors and are bound by yellow lines) are commonly interpreted as being associated with gas related features. Depth is the distance below the air-water interface.
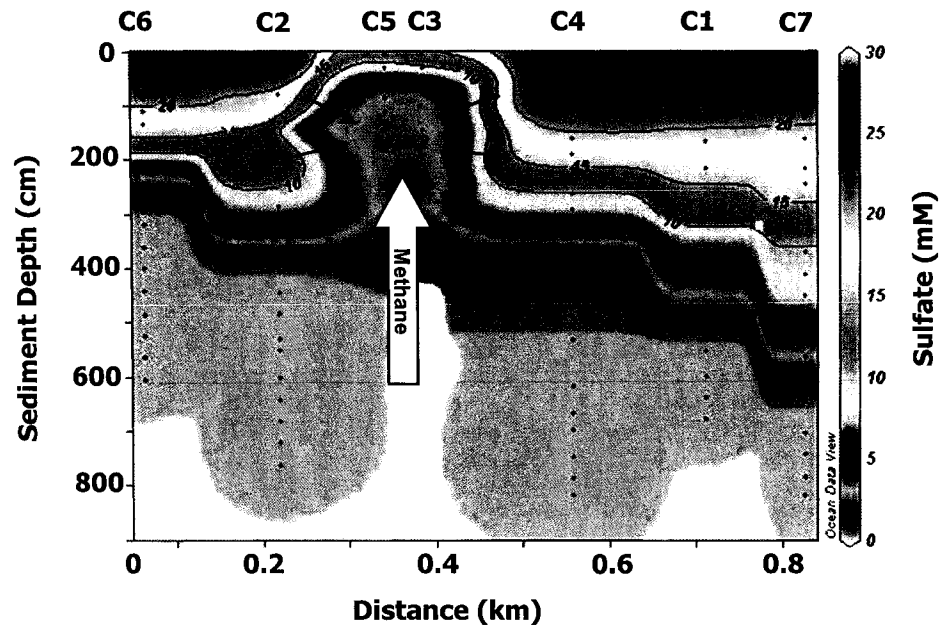
Figure 4. Color contour plot of pore water sulfate for the piston coring transect. Individual samples are indicated as black dots at each core location. The cold seep (core locations C5 and C3) is bound by subsurface lateral sulfate gradients which might support AOM along the margins of the cold seep.

Figure 5. Methane-DIC $\delta^{13}C$ property-property plot for the non-seep cores from the Bullseye vent site. The dashed, diagonal lines indicate iso-fractionation ($\Delta\varepsilon_c = 0$) lines between DIC and methane (Eq. 2). The arrows and shaded areas indicate the carbon isotope sep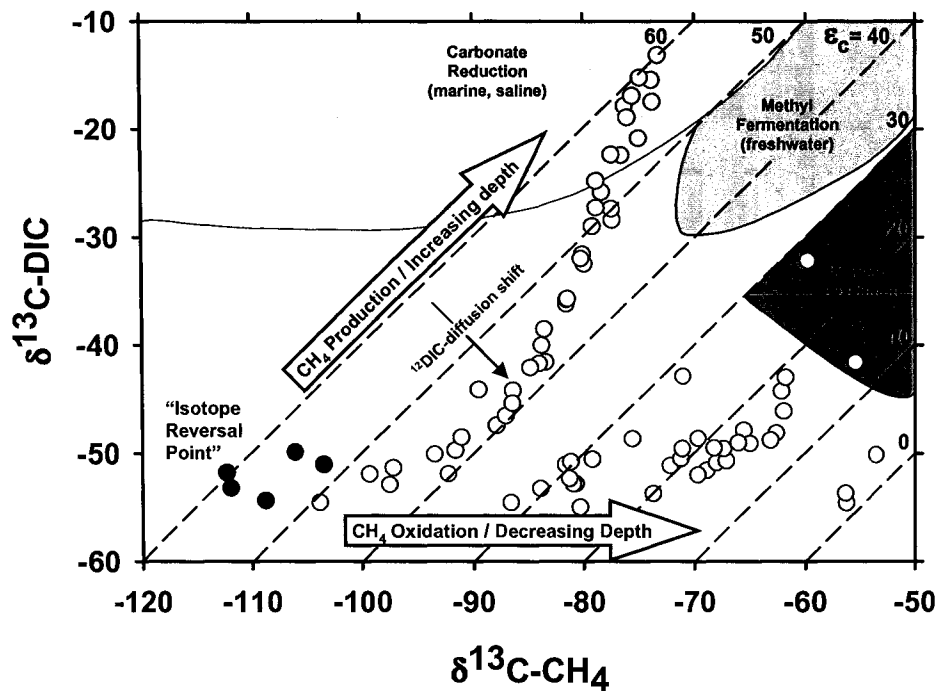aration (ε_c) trajectories and distribution fields, respectively, expected for methane production and oxidation (Whiticar and Faber, 1986). The deeper methanogenic region of the Bullseye vent cores is indicated by open circles and the shallow oxidative region is indicated by shaded (grey) circles. The filled circles (black) are the isotope reversal points from each core; the region where DIC from AOM is recycled back to methane in the upper methanogenic region. Notable discrepancies between the Bullseye vent data and the patterns described by Whiticar and Faber (1986) are that the $\delta^{13}C$ values of methane and DIC are more ^{13}C-depleted, and the methane production trend does not follow the iso-fractionation trajectory with increasing depth from the isotope reversal point. These discrepancies are attributed to diffusion of ^{13}C-depleted DIC, which was generated by AOM, into the methanogenic region. The methane oxidation trajectory is similar to that described by Whiticar and Faber (1986). To highlight the oxidation and production effects, the values plotted in this figure were mass balance corrected to remove the seawater DIC component contributed during sediment burial.
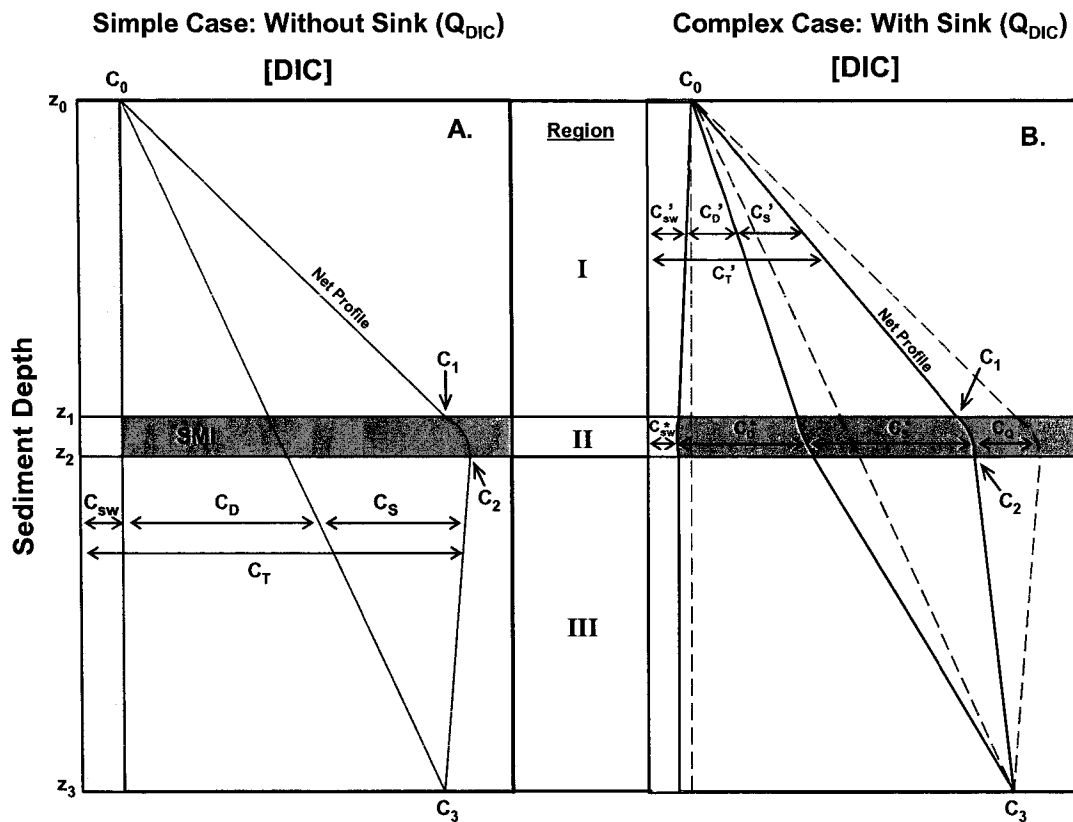
Figure 6. Conceptual diagrams for the DIC source-sink-diffusion model (Eq. 5). (A) Simple case: assumes no DIC sink term (Q_{DIC}), (B) Complex case: includes the DIC sink term. For the simple case (A), the net DIC profile (C_T) is the sum of the seawater burial contribution (C_0, diagonal lines), diffusion from the deep source (C_D, no shading) and DIC generated at the SMI (C_S, shaded area). All DIC production is assumed to occur within region I, the SMI. For the complex case (B), losses from the DIC sink term (C_Q) are partitioned among each of the constituent pools. The losses are represented by the concentration difference between the dashed (no sink) and solid lines (with sink). The other terms are described in the text.
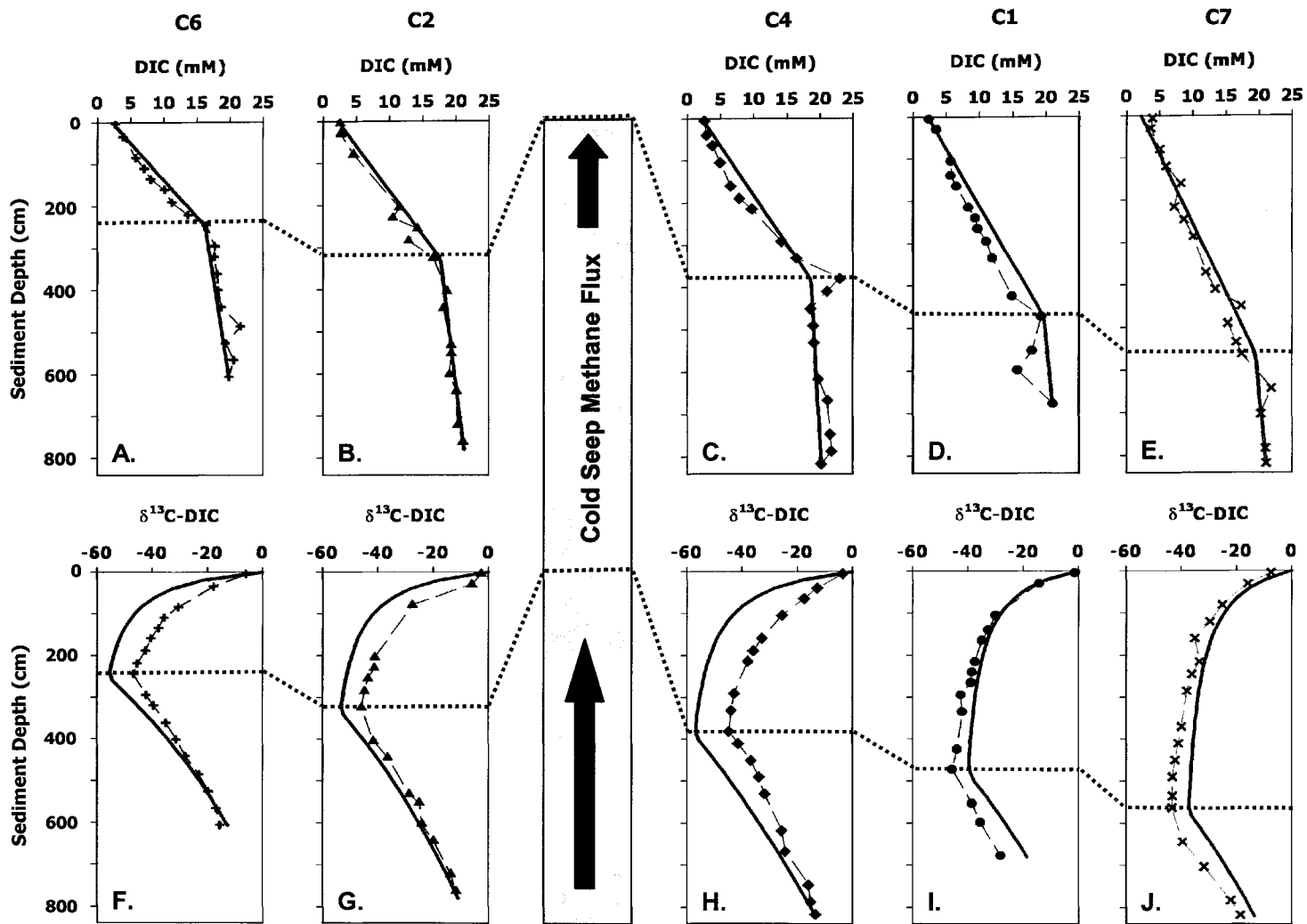
Figure 7. DIC source-sink-diffusion model results. Top row (A-E): Modeled DIC concentration profiles (solid lines) compared to data (symbols). Bottom row (F-J): Modeled δ^{13}C-DIC profiles (solid lines) compared to data (symbols). The cores are arranged in their relative locations along the SW to NE trending transect that crosses the cold seep, as indicated in Fig. 1. The dashed horizontal line crossing the plots represents the sulfate-methane interface (SMI), and shaded area represents the location of the cold seep.

CHAPTER 6

SEDIMENTARY ORIGINS AND DEPOSITIONAL HISTORY OF A GAS
HYDRATE-BEARING COLD SEEP (BULLSEYE VENT, NORTHERN CASCADIA
MARGIN) SINCE THE LAST GLACIAL MAXIMUM

This chapter follows the format of Marine Geology

Abstract

In sedimentary cold seep systems, conversion of methane into other forms of carbon by the anaerobic oxidation of methane (AOM) is frequently identified by ^{13}C-depleted stable carbon isotope values. However, because the transfer of ^{13}C-depleted methane carbon into dissolved and solid phase sedimentary pools by the anaerobic oxidation of methane (AOM) overprints the primary source origins of the pools into which it is subsequently assimilated, the origins and depositional history of the sedimentary system from stable carbon isotope signatures alone may be challenging to establish. In an attempt to circumvent this problem, stable carbon isotope and radiocarbon measurements from solid and dissolved phase carbon pools from Bullseye vent on the northern Cascadia margin were used to infer the sedimentary carbon sources and identify assimilation of methane into these carbon pools. While the total organic carbon (TOC) was apparently unaltered and primarily terrigenous in origin, planktonic foraminifera and the total inorganic carbon (TIC) displayed evidence of methane overprinting in authigenic carbonate resulting from AOM. Mass balance models were therefore applied to calculate the extent of methane overprinting by authigenic carbonate and the radiocarbon ages of the biogenic foraminiferal component. The calibrated foraminiferal ages between sediment depths of 70 and 573 cm were from 14.9 to 15.9 kyrs BP; similar to the timing of the termination of the last glacial maximum (LGM). In addition, the interpretation of the isotopic signatures of TOC and TIC suggested seafloor erosion and nominal sediment accumulation since the LGM. This interpretation was corroborated by seismic data, suggesting an uplift event isolated the vent site on a plateau within a minibasin, which may have starved it from subsequent sediment deposition and

exposed the seafloor to erosive bottom currents. The age similarity between the surface

sedimentary material and the termination of glaciation suggests the uplift event may have

been coupled with tectonic activity triggered by isostatic rebound of Vancouver Island as

the ice load diminished.

1. Introduction

Gas hydrate-bearing cold seep systems occur along active and passive continental margins where methane migrates along structural features (e.g., faults and fractures) to the seafloor (Milkov et al., 2005; Whelan et al., 2005). Although some of the methane may be temporarily stored as gas hydrate (Dickens, 2003) or released to the water column (Judd, 2004; Kvenvolden and Rogers, 2005), most is oxidized at the sulfate methane interface (SMI) by microbially mediated anaerobic oxidation of methane (AOM) where ascending methane and downward diffusing seawater sulfate co-occur (Reeburgh et al., 1993) according to the following equation:

$$CH_4 + SO_4^{-2} \rightarrow HCO_3^- + HS^- + H_2O \qquad\qquad Eq. 1$$
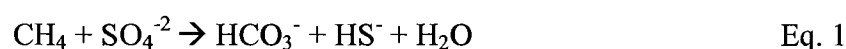
Methane carbon is characterized by stable isotope signatures distinct from other marine and terrestrial carbon sources (Suess and Whiticar, 1989; Whiticar, 1999). Thus, assimilation of methane carbon into the sedimentary system may be identified by stable carbon isotope analysis of the carbon reservoirs. Methane-derived carbon has been observed in dissolved inorganic carbon (DIC) (Claypool and Kaplan, 1974; Suess and Whiticar, 1989; Borowski et al., 2000; Pohlman, Chapters 3&5), microbial biomarkers (Hinrichs et al., 1999; Elvert et al., 2003), macrobiota (Childress et al., 1986; Paull et al., 1989; MacAvoy et al., 2002), bulk total organic carbon (TOC) (Paull et al., 1989; Pohlman, Chapter 4), authigenic carbonates (Paull et al., 1992), volatile fatty acids (Heuer et al., 2006) and as authigenic carbonate on planktonic and benthic foraminiferal tests (Torres et al., 2003) in cold seep systems. While methane-derived DIC and authigenic carbonate are direct products of methane oxidation, assimilation of methane

carbon into the other pools (e.g., biomass and TOC) involves chemoautotrophic pathways.

Alteration of the depositional signatures in sedimentary systems by incorporation of methane limits the utility of geochemical proxies to reconstruct the depositional history of continental margin settings (Jasper and Gagosian, 1989; Keigwin and Jones, 1994; Ohkouchi et al., 2002). In the absence of such alterations, stable carbon isotope signatures of the sediment organic matter have been shown to record glacial-interglacial climatic oscillations (Jasper and Gagosian, 1989). During glacial periods (i.e., during sea level low stands), more ^{13}C-depleted terrestrial material (δ^{13}C $\sim$ -27‰) accumulates on the slope, whereas during interglacials (i.e., during sea level high stands) terrestrial organic matter is preferentially trapped on the shelf, and marine inputs (δ^{13}C $\sim$ -21‰) dominate slope sites. The presence of methane-derived carbon in the sedimentary carbon pools, however, may "overprint" the primary source signatures such that these climatically influenced signals are no longer evident. This effect might be expected to be greater in cold seep systems where large quantities of isotopically distinct methane exist (Paull et al., 1989).

The complications associated with overprinting by methane-derived carbon also affect radiocarbon signatures. Methane in gas hydrate-dominated cold seeps is at least 99% fossil (^{14}C-depleted) (Pohlman, Chapter 2). As such, obtaining radiocarbon ages reflecting the biogenic origins of sedimentary material affected by methane-related diagenesis requires knowledge of the relative contribution and isotopic signatures of the methane carbon. Thus, few studies have attempted to characterize the sources of the sedimentary material or the depositional history of cold seeps.

In this study, we used stable carbon and radiocarbon isotope data from different sedimentary fractions of carbon (e.g., TOC, total inorganic carbon (TIC) and foraminifera) to infer the carbon sources and evaluate the dynamics of sediment deposition at a gas hydrate-bearing cold seep, Bullseye vent (Fig. 1). Sources of carbon were apportioned based on the stable carbon isotope signatures, and the chronology of sediment deposition was constrained through radiocarbon dating of planktonic foraminifera obtained from piston cores taken in and around the cold seep. Post-depositional contributions from authigenic carbonate on the tests of the foraminifera were quantified and corrected by mass balance to estimate the unaltered radiocarbon ages of the material. Finally, patterns of sediment accumulation based on the radiocarbon and geochemical data were interpreted within the context of seismic reflection profile data from the region.

2. Site Description

Bullseye vent, a location of recent scientific drilling (Site U1328) during the Integrated Ocean Drilling Program (IODP) Expedition 311 (Riedel et al., 2006a), occurs in the saddle of a minibasin between topographic highs formed by thrust faulting within the accretionary prism (Fig. 2A). The basin is filled with bedded sediments that gradually thin into the footwall side of the uplifted thrust faults (Fig. 2B) (Riedel et al., 2002). The vent occurs above vertical columns of incoherent reflections described as "blanking" zones in seismic reflection profiles. Several vertical blanking zones, or "chimneys" are present along the inner margin of the landward thrust fault (Riedel et al., 2006b). Seismic blanking producing the observed chimney structures results from

acoustic scattering associated with free gas, shallow carbonates or gas hydrate accumulations (Wood et al., 2002; Riedel et al., 2006b).

Recent investigations at the Bullseye vent site have recovered gas hydrate and studied the flux and biogeochemical cycling of sedimentary methane in shallow sediments (Riedel et al., 2006b; Pohlman, Chapter 5). Methane $\delta^{13}C$ values of ~80‰ sampled from sediment from > 4 mbsf and below the sulfate reduction zone indicate a predominant microbial source for the methane at Bullseye vent. $\delta^{13}C$-DIC values as low as -47.5‰ at the SMI further indicate AOM was a source of DIC (Pohlman, Chapter 5). The methane flux was greatest in the immediate vicinity of the cold seep where seismic blanking extended to the sediment water interface (Pohlman, Chapter 5). Advection of methane-charged fluids and migration of free gas supports the near-seafloor gas hydrate accumulations and flux of methane into the water column (Wood et al., 2002; Riedel et al., 2006b; Pohlman, Chapter 5). Beyond the immediate active cold seep, the methane flux decreased with distance from the seep, and methane was completely consumed within the sediments.

3. Methods

3.1 Sample collection and processing

The sediment samples for this study were obtained in October 2002 from four piston cores collected along an 850 m transect across the Bullseye vent site during cruise PGC0208 on board the CCGS John P. Tully (Table 1). A detailed description of the pore water processing and geochemistry of the vent site was described previously (Pohlman, Chapter 5). Samples for radiocarbon analysis of the DIC were collected in pre-

combusted (450 °C) 20-ml glass serum vials (Wheaton), sealed with Teflon-lined septa and frozen at -20 °C until analysis. Sediment samples for radiocarbon analysis were collected from distinct samples adjacent to those processed for pore water analysis. Higher resolution solid phase elemental and stable carbon isotope vertical profiles (25-40 cm intervals) were obtained from sediment processed for pore water extraction. Sediment samples were freeze dried and split into fractions for isolation of foraminifera and analysis of TOC and TIC. The sediment samples for foraminiferal separation were disaggregated by sonication for 1 hour in a dilute Calgon© solution and the >125 μm size fraction was rinsed and separated by wet sieving. After drying for 24 hours at 50°C, 7-10 mg of mixed planktonic foraminiferal species (primarily *Neogloboquadrina spp.* and *Globigerinoides spp.*, the dominant species in the study area for the past 50 ka (Kennett and Ingram, 1995)), were picked by hand. Samples for TOC and TIC analysis were ground with mortar and pestle and stored in glass vials.

3.2 Radiocarbon sample preparation and analysis

The foraminifera and TIC were converted to CO_2 in an evacuated quartz carbonate digester by adding a solution of 85% H_3PO_4 saturated with $CuSO_4$ to dissolve the carbonate and precipitate sulfides evolved during the digestion/extraction process (Boehme et al., 1996). DIC was extracted as CO_2 from the pore water by adding 1 ml of the $H_3PO_4/CuSO_4$ solution into the serum vials and stripping the solution with He for 15 minutes. Sediment for TOC analysis was acidified with a 10% solution of HCl to remove inorganic carbon, rinsed thoroughly with distilled water, freeze dried and then placed in ¼" Vycor© tubes with ~200 mg copper oxide (oxidant) and a grain of silver (sulfur trap).

The tubes were evacuated and placed in a 900 °C muffle furnace for 6 hours to convert the organic matter to CO_2 (Pohlman et al., 2000).

The CO_2 from the TIC, foraminifera, DIC and TOC was purified cryogenically by a series of vacuum distillations with the radiocarbon sample distillation and graphite preparation system at the Naval Research Lab (NRL), as described by Pohlman et al. (2000). Approximately 1 mg of sample carbon, as purified CO_2, was transferred into graphite production reactors. The remaining CO_2 from the foraminifera, TIC and TOC samples were collected in Vycor© tubes for archiving and $\delta^{13}C$ analysis at Texas A&M University. The $\delta^{13}C$ of the DIC was determined from discrete samples by continuous flow gas chromatography – isotope ratio mass spectrometry (cf-GC-IRMS) as described by Pohlman (Chapter 5). The CO_2 for radiocarbon analysis was catalytically reduced to graphite with hydrogen and 3 mg of iron by heating the reactor at 600 °C for 6 hrs (Vogel et al., 1984; Pohlman et al., 2000).

The graphite was analyzed for radiocarbon at the NRL accelerator mass spectrometry (AMS) facility. The NRL AMS is 3 MV Pelletron tandem accelerator with an MC-SNICS ion source (Grabowski et al., 2000). Results are reported as the conventional radiocarbon age (^{14}C yr) and the $D^{14}C$ notation according to Stuiver and Pollach (1977). The radiocarbon age and $D^{14}C$ notation are interchangeable because they are both reported relative to the age of the absolute international radiocarbon standard (Stuiver and Polach, 1977). The reported error for each sample represents the fully propagated internal errors from the sample, standards and blanks (Tumey et al., 2004). Radiocarbon years for the planktonic foraminifera were converted to calendar years using the CALIB 5.0 program (Stuiver and Reimer, 1993) with the Marine04 calibration dataset

(Hughen et al., 2004) and a reservoir correction of 1,100 ±200 yrs (Kienast and McKay,

2001).

3.3 Bulk sediment analysis

The stable carbon isotope composition ($\delta^{13}C$) and concentrations (wt%) of the

TOC and TIC were determined with a Thermo Finnigan Delta Plus XP IRMS. TOC

samples were weighed in silver cups with a microbalance, acidified with 10% HCl to

remove carbonate, dried at 50 °C for 24 hours and then combusted on-line with a Fisons

EA-1100 Elemental Analyzer (EA) interfaced to the IRMS. The $^{13}C/^{12}C$ ratio is

expressed in conventional δ-notation relative to the VPDB standard (Peterson and Fry,

1987). The total peak area from masses 44 and 45, normalized to an acetanilide standard,

was used to calculate the TOC concentration. Total carbon (TC) and total nitrogen (TN)

concentrations were determined in a similar manner, except that samples for these

analyses were not acidified. TN (used to calculate C:N mass ratios) was calculated from

the acetanilide normalized total peak area from masses 28 and 29. TIC concentration was

calculated as the difference between the TC and TOC. TIC concentrations are expressed

as %CaCO$_3$, which is equivalent to the TIC concentration multiplied by 8.33 (Pimmel

and Claypool, 2001).

Samples for $\delta^{13}C$-TIC were prepared by injecting 200 μL of 85% phosphoric acid

saturated with cupric sulfate into 2 mL serum vials containing approximately 0.2 g

sediment. After heating the vials at 50 °C for 24 hours, headspace gas was injected into a

Thermo Finnigan Trace gas chromatograph (GC). Gases were separated isothermally

(50°C) on a Poraplot-Q capillary column (30 m, 0.32 mm ID) and analyzed for $\delta^{13}C$ with

the IRMS. The average standard deviation of the mean (n=3) was calculated for each sample.

4. Results

4.1 Radiocarbon age and $\delta^{13}C$ of planktonic foraminifera, TOC, TIC and DIC

The ^{14}C ages of the planktonic foraminifera, TOC and TIC were 14,850 to 16,100, 13,950 to 20,550 and 19,600 to 30,500 ^{14}C yr BP, respectively (Table 2; Fig. 3). The sediment profiles did not display any obvious age relationships with depth. However, the age differences among the sediment fractions were distinct. In general, the radiocarbon age of the planktonic foraminifera was the youngest, the age of TOC was intermediate and the age of TIC was the oldest (Fig. 3). In contrast to the solid phases, the ^{14}C ages of the DIC profiles increased with sediment depth (Table 3; Fig. 4). The ^{14}C ages of the DIC ranged from a minimum of 6,320 ^{14}C yr BP at 55 centimeters below the seafloor (cmbsf) from PGC0208-07 to a maximum of 23,850 ^{14}C yr BP at 697 cmbsf from PGC0208-04. DIC ^{14}C ages from the shallow, active seep site (PGC0208-05) were greater than those from the non-seep sites.

Average δ^{13}C values for the planktonic foraminifera, TOC, TIC and DIC samples analyzed for radiocarbon were -3.3 ± 1.4 ‰, -24.8 ± 0.5‰, -8.1 ± 5.6‰ and -31.0 ± 9.2‰, respectively (Tables 2 and 3). Several of the foraminiferal samples for δ^{13}C analysis were lost during shipping to TAMU. As a result, values for the missing samples were estimated by regression analysis of paired foraminifera and TIC samples from which data were available (r^2 = 0.97; P < 0.001; n=6). The propagated errors for the estimated values are included in Table 2.

4.2 Organic matter profiles

The composition ($\delta^{13}C$ and wt%) of the TOC was fairly uniform (Table 4; Fig. 5A). All but three of the 74 samples analyzed for $\delta^{13}C$–TOC ranged from -23.0% to -26.4% and averaged -24.5‰ ± 0.5. The three outlier values (all from the cold seep core PGC0208-05) ranged from -28.1‰ to -32.3‰. The wt% TOC ranged from 0.22% to 0.67% and averaged 0.36 ± 0.10 wt% (Table 4). C:N ratios (by mass) ranged from 5.7 to 9.6 with an average value of 7.5 ± 1.1 (Table 4).

4.3 Total inorganic carbon (carbonate) profiles

The TIC data displayed greater variation than the TOC data in both the $\delta^{13}C$-TIC and wt% TIC (Table 4, Fig. 5B). The $\delta^{13}C$-TIC values ranged from +2.5‰ to -27.0‰ with an average value of -6.0 ± 5.8‰. The TIC concentration (expressed throughout as wt% $CaCO_3$) ranged from 1.4 to 9.1 and averaged 4.0 ± 1.6 (Table 4, Fig. 5B).

5. Discussion

5.1 Origins and post-depositional alterations of sedimentary carbon

Establishing the origins and depositional history of sedimentary material in methane-charged systems on the basis of the carbon isotope compositions (^{13}C and ^{14}C) is complicated by the numerous biogeochemical transformations associated with AOM. For example, methane carbon may be assimilated directly into microbial biomass (Paull et al., 1989) or converted to DIC by AOM (Eq. 1). Authigenic carbonate formation is induced by alkalinity generated by the addition of HCO_3^- (Eq. 1) during AOM (Paull et

al., 1992), yet the total porewater DIC pool from which the carbonate precipitates is a product of AOM, diagenesis of organic matter and seawater burial (Suess and Whiticar, 1989; Blair and Aller, 1995). The isotopic signature of carbonate precipitating from the total DIC reflects the relative contributions of those endmembers. Evaluating how these post-depositional alterations influenced the depositional signal of the solid phase constituents requires a thorough consideration of the stable carbon and radiocarbon isotopic composition of the methane, TOC, TIC (includes carbonate), foraminifera and total porewater DIC.

The radiocarbon ages of the three sediment fractions analyzed (Fig. 3 & Table 2) exhibited considerable variability, which indicates the components were either different ages when deposited or that substantial diagenetic assimilation of fossil methane-derived carbon occurred. Production of ^{13}C-depleted authigenic carbonate has been shown to overprint the primary biogenic signal of living and dead foraminiferal tests at Hydrate Ridge (Torres et al., 2003; Hill et al., 2004). Foraminifera from Bullseye vent with δ^{13}C values as low as -5.2‰ (Table 2) indicate that a similar process may have occurred. Furthermore, because the radiocarbon age of the DIC was greater than the foraminifera (Fig. 4), it likely that post-depositional overprinting shifted the radiocarbon ages of the foraminifera in proportion to the amount and age of the DIC that precipitated as authigenic carbonate. More extreme ^{13}C-depletion in the TIC (Table 2) relative to the foraminifera suggests the TIC contained an even larger contribution from fossil methane and explains why the TIC fraction exhibited the "oldest" radiocarbon ages among the solid phase pools (Fig. 3).

In contrast, the TOC did not contain evidence for extensive incorporation of methane-derived carbon. With the exception of the three samples from PGC0208-05 which had $\delta^{13}C$-TOC values less than -28‰, the $\delta^{13}C$ values of the TOC were similar (-24.5‰ ± 0.5) at all depths in all cores and were within the range of the terrigenous (-27‰) and marine phytoplankton (-21‰) endmembers along the Vancouver Island continental margin (McKay et al., 2004) (Fig. 5A). Alterations related to AOM would have skewed the $\delta^{13}C$ toward more ^{13}C-depleted values, as was observed in the TIC (Fig. 5B). The relatively uniform $\delta^{13}C$ values for the non-seep site TOC suggests a consistent source of organic matter unaltered by incorporation of methane-derived carbon. The calculated contribution of terrigenous organic matter using marine and terrigenous endmember values of -27‰ and -21‰, respectively, was 63 ± 9%. Given such a large predicted terrigenous contribution, the measured radiocarbon ages of the TOC (Fig. 3) were likely influenced by contributions from pre-aged terrestrial organic matter (Ohkouchi et al., 2002) such as the aged POM discharged to ocean margins by present-day rivers (Raymond and Bauer, 2001; Masiello and Druffel, 2001; Blair et al., 2003), rather than post-depositional alterations.

5.2 Mass balance-corrected radiocarbon dates

As a result of the deduced post-depositional alterations and burial of pre-aged terrestrial material, the uncorrected radiocarbon ages provided in Table 1 do not accurately represent the chronology of sediment deposition. To obtain a better sediment chronology from the planktonic foraminifera radiocarbon measurements, corrections for

overprinting by authigenic carbonate (AC) were made using a series of isotope mass balance equations based on a simple two-component mixing model (Eq 2).

$$X_{foram} = (X_{DIC} * f_{AC}) + (X_{biogenic} * (1 - f_{AC}))$$ Eq. 2

where X is the $\delta^{13}C$ or $D^{14}C$ of the foraminifera (X_{foram}), porewater DIC (X_{DIC}) or biogenic calcite ($X_{biogenic}$). The porewater DIC component represents the isotopic signature of the AC, and the pure biogenic calcite component represents the isotopic signature of foraminifera unaltered by AC.

The fraction of authigenic carbonate (f_{AC}) present in the foraminifera was calculated by rearranging Eq. 2 and inserting appropriate $\delta^{13}C$ values (Eq. 3) as:

$$f_{AC} = \frac{(\delta^{13}C_{foram} - \delta^{13}C_{biogenic})}{(\delta^{13}C_{DIC} - \delta^{13}C_{biogenic})}$$ Eq. 3

where $\delta^{13}C_{foram}$ is the measured $\delta^{13}C$ value of the foraminifera, $\delta^{13}C_{biogenic}$ is the $\delta^{13}C$ for biogenic calcite, which was assumed to be 0.0 ± 0.5‰ (Ortiz et al., 1996), and $\delta^{13}C_{DIC}$ is the measured porewater $\delta^{13}C$-DIC value at the SMI of the respective core (Pohlman, Chapter 5). The model assumes there were no contributions from diagenetically altered carbonate rock from Vancouver Island, which could potentially cause 2-3‰ variation in the $\delta^{13}C$ of the TIC (Balsam and Williams, 1993). The model results (Table 5) based on the measured and estimated $\delta^{13}C$ values for the foraminifera (Table 2) indicate that post-depositional accumulation of authigenic carbonate accounted for ~3-12% of the

carbonate in the foraminifera tests. These findings are similar to those from Hydrate

Ridge which were comprised of 3-20% authigenic carbonate (Torres et al., 2003).

The biogenic $D^{14}C$ value ($D^{14}C_{biogenic}$) for the foraminifera was calculated by

rearranging Eq. 2 and inserting appropriate $D^{14}C$ values (Eq. 4).

$$D^{14}C_{biogenic} = \frac{D^{14}C_{foram} - (D^{14}C_{DIC} * f_{AC})}{(1 - f_{AC})}$$
Eq. 4

where f_{AC} was the fraction of authigenic contribution calculated using Eq. 3 (Table 4),

$D^{14}C$ of DIC ($D^{14}C_{DIC}$) was the $D^{14}C$ value of porewater DIC nearest the SMI from each

core (Table 3) and the $D^{14}C$ of the foraminifera ($D^{14}C_{foram}$) was the value measured from

each sample (Table 4). Selecting a porewater $D^{14}C_{DIC}$ value for the cold seep site

(PGC0208-05) was difficult because the SMI (the region of overlapping elevated sulfate

and methane concentrations) extended from the seafloor to ~ 300 cmbsf (Pohlman,

Chapter 5). The $D^{14}C_{DIC}$ value selected was that in closest proximity to shallowest

sediment depth from where the foraminifera data were obtained (120 cmbsf). The

proximity of the DIC sample and the foraminifera sample suggests that $D^{14}C_{DIC}$ value

may be the best representative of DIC that precipitated on the foraminifera tests. The

corrected $D^{14}C$ values were then converted to corrected ^{14}C ages (Stuiver and Polach,

1977) as:

$$^{14}C_{Age} = -8033 \times \ln(1 + \frac{D^{14}C_{biogenic}}{1000})$$
Eq. 5

The corrected ^{14}C ages for the foraminifera (Table 5) were 50 to 400 yrs younger than the measured values. The 1σ age error for these corrected values represents the combined propagated errors from the ^{14}C analysis, the δ^{13}C calculation (where applied), the ^{13}C and ^{14}C mass balance corrections, the Marine04 calibration curve (Hughen et al., 2004), and the reservoir correction (Kienast and McKay, 2001).

Although the ^{14}C age corrections were minor, the corrected age-depth profiles (Fig. 7) display a trend of increasing age with depth for core PGC0208-C6 not observed with the uncorrected ^{14}C ages (Fig. 3), . Without these corrections, the depositional record at the cold seep age profile would falsely imply instantaneous deposition of uniform aged material or physical mixing of the sediment column.

5.3 Sediment deposition patterns at Bullseye vent since the last glacial maximum (LGM)

Coverage of the northern Cascadia margin by the Cordilleran ice sheet peaked around 15 to 16 ^{14}C kyr BP (Blaise et al., 1990). During its subsequent retreat, ice rafting and turbidity currents released at the ice edge supported rapid sediment accumulation along the continental slope (Clague and James, 2002). Previous studies in the region report sedimentation rates of 160 cm kyr^{-1} (PAR85-01: Blaise et al., 1990) and ~47 cm kyr^{-1} (JT96-09: McKay et al., 2004) during early deglaciation (see Fig. 1 for the coring locations for those studies). During that same time period, the average calculated sedimentation rate at the Bullseye Vent site (as interpolated from the age-depth profile from core PGC0208-06) was ~175 cm kyr^{-1} (Fig 7). Thus, the Bullseye vent site and the surrounding region were areas of net sediment accumulation during the late glacial period

with the sediment accumulation rate at the Bullseye vent site approximately three times that of site JT96-09 (located approximately 20 km to the northwest; Fig. 1).

Since the late glacial period, however, the dynamics of sediment deposition in this region have changed. Foraminifera from the nearest seafloor samples of PGC0208-05 (70 cmbsf) and PGC0208-06 (120 cmbsf) had radiocarbon ages of the 16.0 ^{14}C kyr BP and 14.9 ^{14}C kyr BP (Table 5). Meanwhile, planktonic foraminifera from JT96-09 with a similar radiocarbon age (14.1 ^{14}C kyr BP) occurred at a greater depth of 350 cmbsf, and planktonic foraminifera from the depth interval 35-36 cmbsf had a radiocarbon age of 9.8 ^{14}C kyr BP. The absence of material "younger" than 14.5 ^{14}C kyr BP at Bullseye vent, the greater depth of similarly aged material at JT96-09 and the presence of material with an overall younger age at JT96-09 suggests a relative reduction in the rate of sediment accumulation at the Bullseye vent site since the late glacial period (when accumulation rates at the Bullseye vent site were greater), or, perhaps, non-depositional conditions.

Evidence for non-deposition at Bullseye vent was obtained by comparing the records of terrigenous and marine organic mater contributions to sediments at Bullseye vent and JT96-09 (Fig. 1) (McKay et al., 2004). During glacial and deglacial periods, enhanced offshore transport increases the contribution of ^{13}C-depleted terrigenous organic matter to the slope (Jasper and Gagosian, 1989; McKay et al., 2004). Thus, the δ^{13}C of the TOC is proxy for the climatic condition (e.g., glacial or interglacial). Using a stable carbon mass balance approach, McKay et al. (2004) calculated that TOC deposited at site JT96-09 during the late glacial-deglacial period (~13.5 to 16.0 calendar kyr BP) was between 50 – 70% terrigenous in origin. The terrigenous contribution to the TOC at the Bullseye vent site (63 ±9%; see above) was similar.

Following the termination of glaciation, the contribution of terrigenous organic matter at JT96-09 decreased as sea level dropped and terrigenous material was trapped within the coastal fjords. This transition was recorded in the sediment record where accumulation of marine organic matter has dominated since the onset of the Holocene (~10 calendar kyr BP) (McKay et al., 2004). There was no evidence of a similar transition in any of the Bullseye vent cores. Marine dominated TOC was completely absent from all three of the Bullseye vent cores, which is consistent with the radiocarbon based evidence that Bullseye vent site became an area of non-deposition. The δ^{13}C-TOC data are perhaps more conclusive than the radiocarbon data because δ^{13}C-TOC dataset is laterally and vertically more extensive.

The stable and radiocarbon isotope signatures of the TIC offer additional insight into the sedimentary dynamics at Bullseye vent by suggesting erosion may have contributed to the observed pattern of non-deposition. The δ^{13}C values of the TIC are consistent with a contribution from methane-derived DIC. Relative to marine biogenic carbonate from this region (0 ± 0.5 ‰, Ortiz et al., 1996), most of the TIC all the Bullseye vent cores was depleted in ^{13}C (Fig. 6E-H, Table 4). The lowest measured δ^{13}C value was -22.4‰ from PGC0208-05. Potential sources of ^{13}C-depleted TIC include methane (from AOM) and organic matter (from sulfate reduction); although the latter scenario is unlikely since the DIC pool would have been almost entirely derived from organic matter. Furthermore, multiple lines of evidence from the sediment organic matter from the Bullseye vent system suggest it is not suitable for supporting diagenetic carbonate production: (1) the TOC concentrations were uniformly low in all the cores (wt% = 0.36 ± 0.10). Assuming steady state accumulation, diagenesis of organic matter

results in TOC profiles that decrease gradually with age/depth (Middelburg, 1989), (2)

terrigenous organic matter (the dominant source of organic matter present at Bullseye

vent) is likely extensively degraded during transport, making it relatively resistant to

further degradation (Hedges and Keil, 1995), and (3) the low TOC may simply be a result

of dilution by large quantities of fine grained glacial material released from the retreating

ice edge (Blaise et al., 1990); not a consequence of degradation. Thus, the most likely

origin of ^{13}C-depleted TIC is ^{13}C-depleted authigenic carbonate resulting from AOM at

the SMI (Paull et al., 1992; Luff and Wallman, 2003).

The mere presence of authigenic carbonate in the TIC, however, does not directly

indicate erosion. Rather, evidence for erosion was inferred from the distribution of the

authigenic TIC component. Among the non-seep cores (PGC0208-04, PGC0208-06 and

PGC0208-07), the most ^{13}C-depleted TIC typically occurred above the SMI (Figs. 6E,G

and H) where methane concentrations (generally less than 20 μM; Pohlman, Chapter 5)

are not likely to support AOM (Hoehler et al., 1994). The presence of TIC in an

environment lacking sufficient methane substrate for AOM indicates the biogeochemical

conditions have changed (i.e., methane has been consumed). Sediment erosion or a

reduction in the methane flux could have depleted methane at the shallow depths where

^{13}C-depleted TIC and low methane concentrations co-occur. Evidence from IODP

Expedition 311 indicates gas hydrate is still actively forming in the near-surface

sediments within the cold seep (Riedel et al., 2006a), which suggests the methane flux

has not decreased. The more likely scenario for the observed separation of the SMI and

^{13}C-depleted TIC is sediment erosion, which could have isolated methane derived

authigenic carbonate in sediment where methane is absent. The depth of the SMI is

primarily controlled by the magnitude of the methane flux (Borowski et al., 1999). As

material is eroded from the seafloor, the location of the SMI should adjust downward by

a distance equivalent to the depth eroded in order to maintain the SMI at a constant depth

below the seafloor (Hensen et al., 2003). Any methane derived authigenic carbonate

formed at the former location of the SMI would have become spatially separated from the

deeper sources of methane.

5.4 Seismic evidence for tectonic uplift

Thrust faulting from compression of the accretionary prism is a common feature

of the northern Cascadia margin that has led to the expression of numerous uplift features

at the seafloor (Riedel et al., 2002). Bathymetry and multichannel seismic (MCS) images

from the Bullseye vent region provide compelling evidence that uplift has altered the

local geology. Bathymetric evidence of a prominent thrust fault extends along the

upslope side of the minibasin (Fig. 2A). A characteristic sequence resulting from

constructive interference of at least two positive polarity reflectors (e.g., turbidite

deposits) is present in all of the subsurface seismic images (Fig. 2B-C). The sequence

was once likely a continuous stratigraphic unit that was vertically offset during uplift (M.

Riedel, pers. comm.). The dramatic seafloor relief (~225 m) of the prominent eastward-

facing fault scarp (Fig. 2B) most likely developed during the uplift of the mini-basin.

Additional faulting has led to uplift of ~60 m and rotation of a sediment block that

contains Bullseye vent (Fig. 2C and D). Isolation of the Bullseye vent site atop the

uplifted block may have starved it from sediment deposition or exposed it to erosive

bottom currents; processes that were independently inferred from the radiocarbon and geochemical data.

Agreement between the age of the shallow (0-5 mbsf) sediments in the minibasin and the termination of the LGM (~13.5 kyr BP) suggests that the faulting and uplift may have been synchronous with the termination of the LGM. As the ice load from the Cordilleran ice sheet diminished, the west coast of Vancouver Island isostatically rebounded by as much as 120 m in about 1,000 yrs (James et al., 2000; Clague and James, 2002). Rapid crustal rebound during and after glacier melting has been shown to coincide with tectonic activity (Sigvaldason, 2002). One possible explanation is that the faulting which led to the uplift of the minibasin sediment block where the Bullseye vent site is located was influenced by crustal movement resulting from unloading the Cordilleran ice sheet from the Vancouver Island continental margin.

6. Summary

Geochemical tools frequently applied to evaluate the sources and cycling of methane carbon in cold seeps were combined with radiocarbon measurements of organic (TOC) and inorganic (TIC, DIC and planktonic foraminifera) carbon pools to elucidate the geologic history of a cold seep site. Alterations to the radiocarbon ages of the carbon pools resulting from AOM were, in most cases, related to the extent of methane carbon assimilation. A mass balance approach was applied to correct the measured foraminiferal ages and obtain an accurate history of sediment deposition at the Bullseye vent site. These data, in combination with seismic data and stable carbon isotope records of TOC

and TIC indicate the minibasin where the Bullseye vent occurs may have been uplifted and undergone surface sediment erosion since the LGM.

References

Balsam, W. L.; Williams, D. Transport of Carbonate Sediment in the Western North-Atlantic - Evidence from Oxygen and Carbon Isotopes. Marine Geology. 112: 23-34; 1993.

Blair, N. E.; Aller, R. C. Anaerobic methane oxidation on the Amazon shelf. Geochim. Cosmochim. Acta. 59: 3707-3715; 1995.

Blair, N. E.; Leithold, E. L.; Ford, S. T.; Peeler, K. A.; Holmes, J. C.; Perkey, D. W. The persistence of memory: The fate of ancient sedimentary organic carbon in a modern sedimentary system. Geochim. Cosmochim. Acta. 67: 63-73; 2003.

Blaise, B.; Clague, J. J.; Mathewes, R. W. Time of maximum Late Wisconsin glaciation, west-coast of Canada. Quaternary Research. 34: 282-295; 1990.

Boehme, S. E.; Blair, N. E.; Chanton, J. P.; Martens, C. S. A mass balance of C-13 and C-12 in an organic-rich methane-producing marine sediment. Geochim. Cosmochim. Acta. 60: 3835-3848; 1996.

Borowski, W. S.; Hoehler, T. M.; Alperin, M. J.; Rodriguez, N. M.; Paull, C. K. Significance of anaerobic methane oxidation in methane-rich sediments overlying the Blake Ridge gas hydrates. In: Paull, C. K.; Matsumoto, R.; Wallace, P. J.; Dillon, W. P., ed. Proceeding of the Ocean Drilling Program, Scientific Results: Ocean Drilling Program; 2000; 87-99.

Borowski, W. S.; Paull, C. K.; Ussler, W. Global and local variations of interstitial sulfate gradients in deep-water, continental margin sediments: Sensitivity to underlying methane and gas hydrates. Mar. Geol. 159: 131-154; 1999.

Childress, J. J.; Fisher, C. R.; Brooks, J. M.; Kennicutt, M. C.; Bidigare, R.; Anderson, A. E. A Methanotrophic Marine Molluscan (Bivalvia, Mytilidae) Symbiosis - Mussels Fueled by Gas. Science. 233: 1306-1308; 1986.

Clague, J. J.; James, T. S. History and isostatic effects of the last ice sheet in southern British Columbia. Quaternary Science Reviews. 21: 71-87; 2002.

Claypool, G. E.; Kaplan, I. R. The origin and distribution of methane in marine sediments. In: Kaplan, I. R., ed. Natural Gases in Marine Sediments: Plenum Press; 1974; 99-139.

Dickens, G. R. Rethinking the global carbon cycle with a large, dynamic and microbially mediated gas hydrate capacitor. Earth and Planetary Science Letters. 213: 169-183; 2003.

Elvert, M.; Boetius, A.; Knittel, K.; Jorgensen, B. B. Characterization of specific membrane fatty acids as chemotaxonomic markers for sulfate-reducing bacteria involved in anaerobic oxidation of methane. Geomicrobiology Journal. 20: 403-419; 2003.

Grabowski, K. S.; Knies, D. L.; DeTurck, T. M.; Treacy, D. J.; Pohlman, J. W.; Coffin, R. B.; Hubler, G. K. A report on the Naval Research Laboratory AMS facility. Nucl. Instrum. Methods Phys. Res. Sect. B-Beam Interact. Mater. Atoms. 172: 34-39; 2000.

Hedges, J. I.; Keil, R. G. Sedimentary organic-matter preservation - An assessment and speculative synthesis. Marine Chemistry. 49: 81-115; 1995.

Hensen, C.; Zabel, M.; Pfeifer, K.; Schwenk, T.; Kasten, S.; Riedinger, N.; Schulz, H. D.; Boettius, A. Control of sulfate pore-water profiles by sedimentary events and the significance of anaerobic oxidation of methane for the burial of sulfur in marine sediments. Geochim. Cosmochim. Acta. 67: 2631-2647; 2003.

Heuer, V.; Elvert, M.; Tille, S.; Krummen, M.; Mollar, X. P.; Hmelo, L. R.; Hinrichs, K. U. Online $\delta^{13}C$ analysis of volatile fatty acids in sediment/porewater systems by liquid chromatography-isotope ratio-mass spectrometry. Limnology and Oceanography: Methods. In Press: 2006.

Hill, T. M.; Kennett, J. P.; Valentine, D. L. Isotopic evidence for the incorporation of methane-derived carbon into foraminifera from modern methane seeps, Hydrate Ridge, Northeast Pacific. Geochim. Cosmochim. Acta. 68: 4619-4627; 2004.

Hinrichs, K. U.; Hayes, J. M.; Sylva, S. P.; Brewer, P. G.; Delong, E. F. Methane-consuming archaebacteria in marine sediments. Nature. 398: 802-805; 1999.

Hoehler, T. M.; Alperin, M. J.; Albert, D. B.; Martens, C. S. Field and laboratory studies of methane oxidation in an anoxic marine sediment - evidence for a methanogen-sulfate reducer consortium. Glob. Biogeochem. Cycle. 8: 451-463; 1994.

Hughen, K. A.; Baillie, M. G. L.; Bard, E.; Beck, J. W.; Bertrand, C. J. H.; Blackwell, P. G.; Buck, C. E.; Burr, G. S.; Cutler, K. B.; Damon, P. E.; Edwards, R. L.; Fairbanks, R. G.; Friedrich, M.; Guilderson, T. P.; Kromer, B.; McCormac, G.; Manning, S.; Ramsey, C. B.; Reimer, P. J.; Reimer, R. W.; Remmele, S.; Southon, J. R.; Stuiver, M.; Talamo, S.; Taylor, F. W.; Van der Plicht, J.; Weyhenmeyer, C. E. Marine04 marine radiocarbon age calibration, 0-26 cal kyr BP. Radiocarbon. 46: 1059-1086; 2004.

James, T. S.; Clague, J. J.; Wang, K. L.; Hutchinson, I. Postglacial rebound at the northern Cascadia subduction zone. Quaternary Science Reviews. 19: 1527-1541; 2000.

Jasper, J. P.; Gagosian, R. B. Glacial interglacial climatically forced $\delta^{13}C$ variations in sedimentary organic-matter. Nature. 342: 60-62; 1989.

Judd, A. G. Natural seabed gas seeps as sources of atmospheric methane. Environmental Geology. 46: 988-996; 2004.

Keigwin, L. D.; Jones, G. A. Western North-Atlantic evidence for millennial-scale changes in ocean circulation and climate. Journal of Geophysical Research-Oceans. 99: 12397-12410; 1994.

Kennett, J. P.; Ingram, B. L. A 20,000 year record of ocean circulation and climate-change from the Santa-Barbara basin. Nature. 377: 510-514; 1995.

Kienast, S. S.; McKay, J. L. Sea surface temperatures in the subarctic Northeast Pacific reflect millennial-scale climate oscillations during the last 16 kyrs. Geophysical Research Letters. 28: 1563-1566; 2001.

Kvenvolden, K. A.; Rogers, B. W. Gaia's breath - global methane exhalations. Marine and Petroleum Geology. 22: 579-590; 2005.

Luff, R.; Wallmann, K. Fluid flow, methane fluxes, carbonate precipitation and biogeochemical turnover in gas hydrate-bearing sediments at Hydrate Ridge, Cascadia Margin: Numerical modeling and mass balances. Geochim. Cosmochim. Acta. 67: 3403-3421; 2003.

MacAvoy, S. E.; Carney, R. S.; Fisher, C. R.; Macko, S. A. Use of chemosynthetic biomass by large, mobile, benthic predators in the Gulf of Mexico. Marine Ecology-Progress Series. 225: 65-78; 2002.

Masiello, C. A.; Druffel, E. R. M. Carbon isotope geochemistry of the Santa Clara River. Global Biogeochemical Cycles. 15: 407-416; 2001.

McKay, J. L.; Pedersen, T. F.; Kienast, S. S. Organic carbon accumulation over the last 16 kyr off Vancouver Island, Canada: evidence for increased marine productivity during the deglacial. Quaternary Science Reviews. 23: 261-281; 2004.

Middelburg, J. J. A simple rate model for organic-matter decomposition in marine-sediments. Geochim. Cosmochim. Acta. 53: 1577-1581; 1989.

Milkov, A. V.; Claypool, G. E.; Lee, Y. J.; Sassen, R. Gas hydrate systems at Hydrate Ridge offshore Oregon inferred from molecular and isotopic properties of hydrate-bound and void gases. Geochimica et Cosmochimica Acta. 69: 1007-1026; 2005.

Ohkouchi, N.; Eglinton, T. I.; Keigwin, L. D.; Hayes, J. M. Spatial and temporal offsets between proxy records in a sediment drift. Science. 298: 1224-1227; 2002.

Ortiz, J. D.; Mix, A. C.; Rugh, W.; Watkins, J. M.; Collier, R. W. Deep-dwelling planktonic foraminifera of the northeastern Pacific Ocean reveal environmental control of oxygen and carbon isotopic disequilibria. Geochimica et Cosmochimica Acta. 60: 4509-4523; 1996.

Paull, C. K.; Martens, C. S.; Chanton, J. P.; Neumann, A. C.; Coston, J.; Jull, A. J. T.; Toolin, L. J. Old carbon in living organisms and young $CaCO_3$ cements from abyssal brine seeps. Nature. 342: 166-168; 1989.

Paull, C. K.; Chanton, J. P.; Neumann, A. C.; Coston, J. A.; Martens, C. S.; Showers, W. Indicators of methane-derived carbonates and chemosynthetic organic carbon deposits; examples from the Florida Escarpment. PALAIOS. 7: 361-375; 1992.

Peterson, B. J.; Fry, B. Stable isotopes in ecosystem studies. Annual Review of Ecology and Systematics. 18: 293-320; 1987.

Pimmel, A.; Claypool, G. Introduction to shipboard organic geochemistry on the JOIDES Resolution. ODP Tech. Note, 30 (online); 2001.

Pohlman, J. W.; Knies, D. L.; Grabowski, K. S.; DeTurck, T. M.; Treacy, D. J.; Coffin, R. B. Sample distillation/graphitization system for carbon pool analysis by accelerator mass spectrometry (AMS). Nucl. Instrum. Methods Phys. Res. Sect. B-Beam Interact. Mater. Atoms. 172: 428-433; 2000.

Raymond, P. A.; Bauer, J. E. Riverine export of aged terrestrial organic matter to the North Atlantic Ocean. Nature. 409: 497-500; 2001.

Reeburgh, W. S.; Whalen, K. A.; Alperin, M. J. The role of methylotrophy in the global methane budget. In: Murrell, J. C.; Kelley, D. P., ed. Microbial Growth on C-1 Compounds: Interceprt Ltd; 1993.

Riedel, M.; Collett, T.; Malone, M.; Akiba, F.; Blanc-Valleron, M.; Ellis, M.; Guerin, G.; Hashimoto, Y.; Heuer, V.; Higashi, Y.; Holland, M.; Jackson, P.; Kaneko, M.; Kastner, M.; Kim, J.-H.; Katijama, H.; Long, P.; Malinvero, A.; Myers, G.; Palekar, L.; Pohlman, J.; Schultheiss, P.; Teichert, B.; Torres, M.; Trehu, A.; Wang, J.; Wortmann, U.; Yoshhioka, H. Gas hydrate transect across northern Cascadia margin. EOS. 87: 325, 330, 332; 2006a.

Riedel, M.; Novosel, I.; Spence, G. D.; Hyndman, R. D.; Chapman, R. N.; Solem, R. C.; Lewis, T. Geophysical and geochemical signatures associated with gas hydrate-related venting in the northern Cascadia margin. Geological Society of America Bulletin. 118: 23-38; 2006b.

Riedel, M.; Spence, G. D.; Chapman, N. R.; Hyndman, R. D. Seismic investigations of a vent field associated with gas hydrates, offshore Vancouver Island. Journal of Geophysical Research-Solid Earth. 107: doi:10.1029/2001JB000269; 2002.

Spence, G. D.; Hyndman, R. D.; Davis, E. E.; Yorath, C. J. Seismic structure of the northern Cascadia accretionary prism: evidence from new multichannel seismic reflection data. Geodynamics. 22: 257-363; 1991.

Stuiver, M.; Polach, H. A. Discussion: Reporting ^{14}C data. Radiocarbon. 19: 355-363; 1977.

Stuiver, M.; Reimer, P. J. Extended C-14 Data-Base and Revised Calib 3.0 C-14 Age Calibration Program. Radiocarbon. 35: 215-230; 1993.

Suess, E.; Whiticar, M. J. Methane-derived CO_2 in pore fluids expelled from the Oregon Subduction Zone. Palaeogeography Palaeoclimatology Palaeoecology. 71: 119-136; 1989.

Sigvaldason, G. E. Volcanic and tectonic processes coinciding with glaciation and crustal rebound: an early Holocene rhyolitic eruption in the Dyngjufjoll volcanic centre and the formation of the Askja caldera, north Iceland. Bulletin of Volcanology. 64: 192-205; 2002.

Torres, M. E.; Mix, A. C.; Kinports, K.; Haley, B.; Klinkhammer, G. P.; McManus, J.; de Angelis, M. A. Is methane venting at the seafloor recorded by delta C-13 of benthic foraminifera shells? Paleoceanography. 18: doi:1029/2002PA000804; 2003.

Tumey, S. J.; Grabowski, K. S.; Knies, D. L.; Mignerey, A. C. Radiocarbon data collection, filtering and analysis at the NRL TEAMS facility. Nuclear Instruments & Methods in Physics Research Section B-Beam Interactions with Materials and Atoms. 223-24: 216-220; 2004.

Vogel, J. S.; Southon, J. R.; Nelson, D. E.; Brown, T. A. Performance of catalytically condensed carbon for use in accelerator mass-spectrometry. Nuclear Instruments & Methods in Physics Research Section B- Beam Interactions with Materials and Atoms. 233: 289-293; 1984.

Whelan, J.; Eglinton, L.; Cathles, L.; Losh, S.; Roberts, H. Surface and subsurface manifestations of gas movement through a N-S transect of the Gulf of Mexico. Marine and Petroleum Geology. 22: 479-497; 2005.

Whiticar, M. J. Carbon and hydrogen isotope systematics of bacterial formation and oxidation of methane. Chem. Geol. 161: 291-314; 1999.

Wood, W. T.; Gettrust, J. F.; Chapman, N. R.; Spence, G. D.; Hyndman, R. D. Decreased stability of methane hydrates in marine sediments owing to phase-boundary roughness. Nature. 420: 656-660; 2002.

Table 1. Information for piston cores from Bullseye Vent investigated in this study.

Station	Latitude (N)	Longitude (W)	Water Depth (m)	Core Length (m)
PGC0208-04	48° 40.1829'	126° 50.9317'	1274	8.58
PGC0208-05	48° 40.0744'	126° 50.9961'	1282	7.77
PGC0208-06	48° 39.9388'	126° 51.0953'	1284	6.44
PGC0208-07	48° 40.3125'	126° 50.8405'	1268	8.51

Table 2. Radiocarbon (^{14}C) age and δ^{13}C of planktic forams, TOC and TIC.

Core	Depth (cmbsf)	Planktic Forams			Total organic carbon (TOC)			Total inorganic carbon (TIC)		
		^{14}C Age (yrs)	δ^{13}C (‰)	AMS ID	^{14}C Age (yrs)	δ^{13}C (‰)	AMS ID	^{14}C Age (yrs)	δ^{13}C (‰)	AMS ID
PGCO208-C5	70	15950 ± 150	2.8 ± 0.6*	NRL-651	20550 ± 310	-24.9	NRL-332	28200 ± 800	-6.9	NRL-814
	95	16050 ± 250	-4.9	NRL-788	19850 ± 290	-25.0	NRL-333	25800 ± 350	-14.7	NRL-815
	130	16100 ± 240	-3.4	NRL-780	18750 ± 480	-25.0	NRL-337	28100 ± 400	-10.3	NRL-818
	210	16100 ± 260	-4.4	NRL-795	20300 ± 570	-25.6	NRL-338	30500 ± 650	-12.0	NRL-819
PGCO208-C6	120	14850 ± 240	-3.8	NRL-789	17750 ± 300	-24.5	NRL-3	23000 ± 650	-9.6	NRL-798
	200	15300 ± 370	-5.2	NRL-790	17950 ± 210	-25.0	NRL-25	26700 ± 900	-15.2	NRL-799
	330	15050 ± 130	-1.6 ± 0.5*	NRL-649	13950 ± 160	-25.0	NRL-26	27100 ± 650	-1.4	NRL-800
	370	15500 ± 160	-1.8 ± 0.5*	NRL-710	18200 ± 180	-24.2	NRL-7	27600 ± 350	-2.3	NRL-809
	496	16000 ± 140	-1.4 ± 0.5*	NRL-647	17600 ± 180	-23.9	NRL-8	21100 ± 300	-0.5	NRL-803
PGCO208-C7	573	15000 ± 300	-1.0	NRL-782	19750 ± 300	-24.4	NRL-5	19600 ± 500	-2.7	NRL-905

*Values extrapolated by regression of δ^{13}C data from paired foram and TIC samples (see text for details). Values include the propagated error.

Table 3. Radiocarbon (^{14}C) age, D^{14}C and δ^{13}C of DIC

Core	Depth (cmbsf)	Dissolved Inorganic Carbon (DIC)			
		^{14}C Age (yrs)	D^{14}C	δ^{13}C (‰)	AMS ID
PCG0208-04	180	12300 ± 330	-783 ± 9	-36 ± 0.1	NRL-1233
z_{SMI} = 376	261	15750 ± 220	-860 ± 4	-40 ± 0.3	NRL-1263
	431	20600 ± 220	-923 ± 2	-37 ± 0.1	NRL-1234
	627	21200 ± 260	-929 ± 2	-26 ± 0.1	NRL-1235
	697	23850 ± 450	-949 ± 3	-20 ± 0.3	NRL-1256
	797	22450 ± 270	-939 ± 2	-15 ± 0.1	NRL-1236
PCG0208-05	45	14900 ± 170	-844 ± 3	-38 ± 0.3	NRL-1246
z_{SMI} = 0-300	120[a]	19800 ± 250	-915 ± 3	-31 ± 0.3	NRL-1247
	180	18700 ± 230	-902 ± 3	-28 ± 0.3	NRL-1248
PCG0208-06	60	7780 ± 140	-620 ± 7	-26 ± 0.3	NRL-1273
z_{SMI} = 240	270[a]	19850 ± 260	-916 ± 3	-44 ± 0.3	NRL-1262
	421	21000 ± 230	-927 ± 2	-28 ± 0.1	NRL-1228
	546	22000 ± 290	-935 ± 2	-17 ± 0.1	NRL-1232
PCG0208-07	55	6320 ± 200	-545 ± 11	-21 ± 0.3	NRL-1274
z_{SMI} = 558	238	9100 ± 140	-678 ± 6	-36 ± 0.3	NRL-1243
	325	15350 ± 250	-852 ± 5	-39 ± 0.3	NRL-1265
	588[a]	18600 ± 300	-901 ± 4	-43 ± 0.3	NRL-1244
	603	20450 ± 380	-922 ± 4	-41 ± 0.3	NRL-1257
	768	21450 ± 270	-931 ± 2	-22 ± 0.3	NRL-1245

z_{SMI}: approximate depth (cmbsf) of the sulfate methane interface (Pohlman 2006, Ch.3).

[a]depth (cmbsf) selected to represent the DIC endmember in Eq. 4

Table 4. Solid phase total organic carbon (TOC) and total inorganic carbon data from PGC0208

Core	Depth (cmbsf)	Total organic carbon (TOC)			Total inorganic carbon (TIC)	
		$\delta^{13}C$	wt%	C:N	$\delta^{13}C$	wt% CaCO$_3$
PGC0208-04	5	-23.9 ± 0.02	0.41 ± 0.01	8.0 ± 0.4	-1.0 ± 0.5	2.6 ± 0.5
	40	-24.3 ± 0.08	0.42 ± 0.01	8.4 ± 0.4	-1.5 ± 0.9	1.5 ± 0.2
	65	-24.3 ± 0.2	0.47 ± 0.01	9.0 ± 0.4	-3.2 ± 0.1	1.8 ± 0.07
	105	-24.2 ± 0.06	0.51 ± 0.02	8.7 ± 0.4	-8.2 ± 0.3	3.9 ± 0.3
	130	-24.0 ± 0.07	0.37 ± 0.01	7.0 ± 0.3	-7.8 ± 0.5	5.1 ± 0.6
	160	-25.2 ± 0.1	0.26 ± 0.01	5.7 ± 0.4	-13.3 ± 0.1	6.9 ± 0.5
	190	-24.4 ± 0.08	0.26 ± 0.01	6.3 ± 0.4	-7.2 ± 0.1	3.9 ± 0.5
	215	-24.3 ± 0.08	0.49 ± 0.01	8.8 ± 0.2	-11.3 ± 0.3	4.7 ± 0.6
	261	-25.1 ± 0.1	0.42 ± 0.01	8.5 ± 0.3	-8.9 ± 0.4	2.4 ± 0.09
	291	-25.2 ± 0.05	0.35 ± 0.01	6.3 ± 1.5	-12.1 ± 0.1	1.9 ± 0.3
	331	-25.2 ± 0.5	0.42 ± 0.01	8.4 ± 0.3	-15.3 ± 0.3	2.5 ± 0.1
	361	-26.4 ± 0.4	0.35 ± 0.01	7.1 ± 0.4	-3.9 ± 0.3	3.2 ± 0.05
	411	-25.0 ± 0.03	0.38 ± 0.01	8.0 ± 0.3	-3.8 ± n.a.	2.1 ± 0.1
	451	-24.6 ± 0.3	0.39 ± 0.08	9.2 ± 1.9	-3.2 ± n.a.	3.4 ± 0.7
	491	-25.0 ± 0.06	0.23 ± 0.01	5.9 ± 0.3	-2.2 ± n.a.	3.6 ± 0.08
	531	-24.4 ± 0.1	0.55 ± 0.01	9.1 ± 0.2	-2.7 ± n.a.	3.3 ± 0.1
	617	-25.0 ± 0.09	0.24 ± 0.01	6.6 ± 0.3	-4.2 ± n.a.	3.6 ± 0.2
	667	-25.0 ± 0.1	0.29 ± 0.01	7.0 ± 0.3	-4.2 ± n.a.	3.9 ± 0.1
	697	-25.2 ± 0.08	0.24 ± 0.01	7.3 ± 1.7	2.3 ± 0.3	3.9 ± 0.03
	747	-23.7 ± 0.04	0.67 ± 0.02	9.5 ± 0.2	-2.3 ± n.a.	6.8 ± 0.5
	787	-25.3 ± 0.1	0.27 ± 0.01	6.4 ± 0.3	-11.8 ± 0.7	5.2 ± 0.1
	817	-25.1 ± 0.08	0.24 ± 0.01	7.2 ± 1.4	-3.9 ± n.a.	3.7 ± 0.2
PGC0208-C5	5	-32.3 ± 0.3	0.50 ± 0.02	7.0 ± 0.3	-16.0 ± 0.4	3.5 ± 0.2
	30	-28.1 ± 0.5	0.32 ± 0.01	6.3 ± 0.1	-27.0 ± 0.9	7.2 ± 0.6
	60	-25.2 ± 0.05	0.38 ± 0.02	7.0 ± 0.4	-12.8 ± 0.3	4.0 ± 0.3
	85	-25.2 ± 0.2	0.35 ± 0.01	6.5 ± 0.2	-16.0 ± 0.2	6.0 ± 0.3
	110	-26.2 ± 0.1	0.31 ± 0.01	8.7 ± 0.7	-22.4 ± 0.01	6.0 ± 0.7
	140	-25.1 ± 0.1	0.32 ± 0.01	8.3 ± 0.2	-8.3 ± 0.4	5.1 ± 0.1
	170	-24.9 ± 0.02	0.32 ± 0.01	8.2 ± 0.3	-9.1 ± 0.6	5.3 ± 0.2
	200	-27.5 ± 0.5	0.34 ± 0.01	8.2 ± 0.2	-21.8 ± 0.3	7.9 ± n.a.
	346	-25.6 ± 0.03	0.34 ± 0.01	6.5 ± 0.2	-11.6 ± 0.3	6.0 ± 0.1
	236	-25.3 ± 0.2	0.34 ± 0.01	6.6 ± 0.3	-10.9 ± 0.5	5.0 ± 0.1
PGC0208-C6	5	-23.0 ± 0.1	0.56 ± 0.03	8.0 ± 0.4	-0.7 ± 0.5	2.2 ± 0.3
	35	-24.8 ± 0.03	0.22 ± 0.01	5.7 ± 0.2	-1.3 ± 0.1	3.5 ± 0.06
	60	-24.5 ± 0.06	0.26 ± 0.01	6.3 ± 0.7	-6.5 ± 0.5	3.6 ± 0.6
	85	-24.1 ± 0.1	0.42 ± 0.03	7.5 ± 0.6	-0.2 ± 0.6	9.0 ± 0.6
	110	-24.9 ± 0.05	0.41 ± 0.03	7.5 ± 0.5	-14.4 ± 0.7	6.2 ± 0.2
	135	-25.2 ± 0.2	0.39 ± 0.01	7.8 ± 0.2	1.3 ± 0.6	3.4 ± 0.09
	160	-25.2 ± 0.04	0.37 ± 0.02	7.5 ± 0.4	-3.3 ± 1	2.3 ± 0.1
	190	-25.7 ± 0.5	0.40 ± 0.06	8.1 ± 1.4	2.5 ± 1.1	3.2 ± 0.6
	220	-25.0 ± 0.2	0.38 ± 0.01	7.3 ± 0.2	-6.1 ± 0.1	2.6 ± 0.2
	245	-24.8 ± 0.04	0.30 ± 0.01	6.5 ± 0.1	-7.3 ± 0.3	3.8 ± 0.07
	270	-24.9 ± 0.1	0.40 ± 0.02	8.1 ± 0.4	-4.6 ± 0.1	1.9 ± 0.2
	285	-24.7 ± 0.06	0.33 ± 0.01	7.3 ± 0.2	-3.2 ± 1.3	4.3 ± 0.06
	320	-24.7 ± 0.06	0.40 ± 0.01	8.0 ± 0.4	-2 ± 0.5	2.7 ± 0.1
	361	-24.8 ± 0.09	0.35 ± 0.02	7.2 ± 0.4	-0.1 ± 0.09	3.1 ± 0.2

Table 4. (cont.)

Core	Depth (cmbsf)	Total organic carbon (TOC)			Total inorganic carbon (TIC)	
		$\delta^{13}C$	wt%	C:N	$\delta^{13}C$	wt%
PGC0208-C6	401	-24.3 ± 0.02	0.39 ± 0.01	7.8 ± 0.3	-1.5 ± 0.9	4.3 ± 0.1
	441	-25.4 ± 0.3	0.28 ± 0.01	6.5 ± 0.2	1.6 ± 0.2	4.4 ± 0.06
	486	-24.2 ± 0.04	0.42 ± 0.02	8.1 ± 0.5	-0.6 ± 1	4.7 ± 0.2
	526	-24.7 ± 0.08	0.26 ± 0.01	6.2 ± 0.2	-1.3 ± n.a.	4.1 ± 0.2
	566	-24.9 ± 0.04	0.23 ± 0.01	6.0 ± 0.2	-2.8 ± 0.2	3.7 ± 0.07
	606	-24.0 ± 0.01	0.59 ± 0.01	9.2 ± 0.2	-1.3 ± 0.6	5.0 ± 0.1
PGC0208-C7	5	-24.9 ± 0.02	0.41 ± 0.01	9.4 ± 0.3	-3.7 ± 0.4	1.4 ± 0.06
	30	-24.4 ± 0.07	0.54 ± 0.01	9.6 ± 0.1	-9.5 ± 0.4	3.3 ± 0.1
	55	-24.1 ± 0.04	0.51 ± 0.01	8.6 ± 0.2	-6.6 ± 0.4	6.2 ± 0.6
	80	-25.1 ± 0.07	0.22 ± 0.01	5.9 ± 0.2	-4.0 ± 0.6	3.9 ± 0.1
	120	-24.9 ± 0.01	0.27 ± 0.01	6.5 ± 0.2	-11.1 ± 0.3	4.5 ± 0.2
	160	-25.2 ± 0.06	0.37 ± 0.01	8.4 ± 0.3	-7.5 ± 0.3	1.7 ± 0.03
	215	-24.7 ± 0.09	0.34 ± 0.01	7.3 ± 0.3	1.8 ± 0.06	3.4 ± 0.2
	245	-24.8 ± 0.2	0.22 ± 0.01	5.9 ± 0.2	-3.0 ± 0.4	3.9 ± 0.03
	285	-25.0 ± 0.07	0.36 ± 0.01	8.1 ± 0.4	-8.8 ± 0.6	2.0 ± 0.07
	325	-24.8 ± 0.04	0.39 ± 0.01	8.5 ± 0.1	-8.7 ± 0.6	2.3 ± 0.06
	370	-25.1 ± 0.1	0.39 ± 0.01	8.3 ± 0.1	-4.0 ± 0.4	1.9 ± 0.06
	410	-24.9 ± 0.04	0.37 ± 0.01	7.9 ± 0.3	-5.8 ± 0.5	2.0 ± 0.05
	450	-25.0 ± 0.04	0.34 ± 0.01	7.5 ± 0.1	-4.9 ± 0.2	4.9 ± 0.06
	490	-25.0 ± 0.08	0.26 ± 0.01	6.3 ± 0.2	-2.6 ± 0.1	4.0 ± 0.04
	535	-24.8 ± 0.02	0.38 ± 0.02	7.8 ± 0.6	-6.0 ± 0.6	3.6 ± 0.2
	563	-24.5 ± 0.3	0.39 ± 0.02	7.3 ± 0.5	-3.8 ± 0.6	4.8 ± 0.3
	603	-24.8 ± 0.09	0.26 ± 0.01	6.1 ± 0.2	-4.4 ± 0.5	4.2 ± 0.02
	643	-24.7 ± 0.05	0.25 ± 0.01	6.1 ± 0.1	-3.0 ± 0.2	4.5 ± 0.04
	703	-24.6 ± 0.06	0.32 ± 0.01	7.4 ± 0.3	-3.3 ± 0.7	4.8 ± 0.1
	743	-25.0 ± 0.2	0.25 ± 0.01	6.0 ± 0.2	-4 ± 0.03	4.1 ± 0.05
	783	-25.1 ± 0.2	0.24 ± 0.01	6.0 ± 0.3	-3.1 ± 0.6	3.8 ± 0.05
	818	-24.0 ± 0.06	0.41 ± 0.01	8.0 ± 0.3	-2.2 ± 0.2	4.1 ± 0.2

n.a.: not available

Table 5. Planktic foram mass balance radiocarbon (^{14}C) correction inputs and outputs.

Core	Depth (cmbsf)	[a]Percent Authigenic Carbonate	[b]Measured D^{14}C (‰)	[c]Corrected D^{14}C (‰)	[d]Corrected ^{14}C Age (yr BP)	[e]Δ^{14}C Age	[f]Calendar Age (kyr BP±1σ)
PGC0208-05	70	7.2 ± 1.0	-863 ± 3	-860 ± 3	15800 ± 160	150	17.78 ± 0.66
	95	11.6 ± 1.3	-864 ± 4	-858 ± 5	15650 ± 260	400	17.57 ± 0.91
	130	8.4 ± 1.1	-865 ± 4	-861 ± 4	15850 ± 250	300	17.90 ± 0.71
	210	10.5 ± 1.2	-865 ± 4	-860 ± 5	15750 ± 270	350	17.73 ± 0.95
PGC0208-06	120	9.2 ± 1.1	-842 ± 5	-836 ± 5	14550 ± 250	300	15.94 ± 0.75
	200	12.0 ± 1.3	-852 ± 7	-844 ± 7	14950 ± 380	350	16.49 ± 1.13
	330	4.4 ± 0.9	-846 ± 2	-845 ± 3	15000 ± 140	50	16.54 ± 0.51
	370	4.8 ± 0.9	-855 ± 3	-853 ± 3	15400 ± 170	100	17.17 ± 0.67
	496	4.0 ± 0.8	-863 ± 2	-863 ± 3	15950 ± 150	50	18.13 ± 0.57
PGC0208-07	573	3.4 ± 0.9	-845 ± 6	-843 ± 6	14900 ± 310	100	16.46 ± 0.90

[a]calcuated by Eq. 3 (includes propagated error)

[b]calculated according to Stuiver and Polach (1977)

[c]calculated according to Eq. 4

[d]calculated according to Eq. 5 using the corrected D^{14}C value (includes propagated error)

[e]calculated as the difference between the corrected ^{14}C age and the measured ^{14}C age

[f]calibrated calendar age using the corrected ^{14}C age, the CALIB 5.0 program (Stuiver and Reimer, 1993) and the Marine04 calibration data (Hughen et al, 2004)
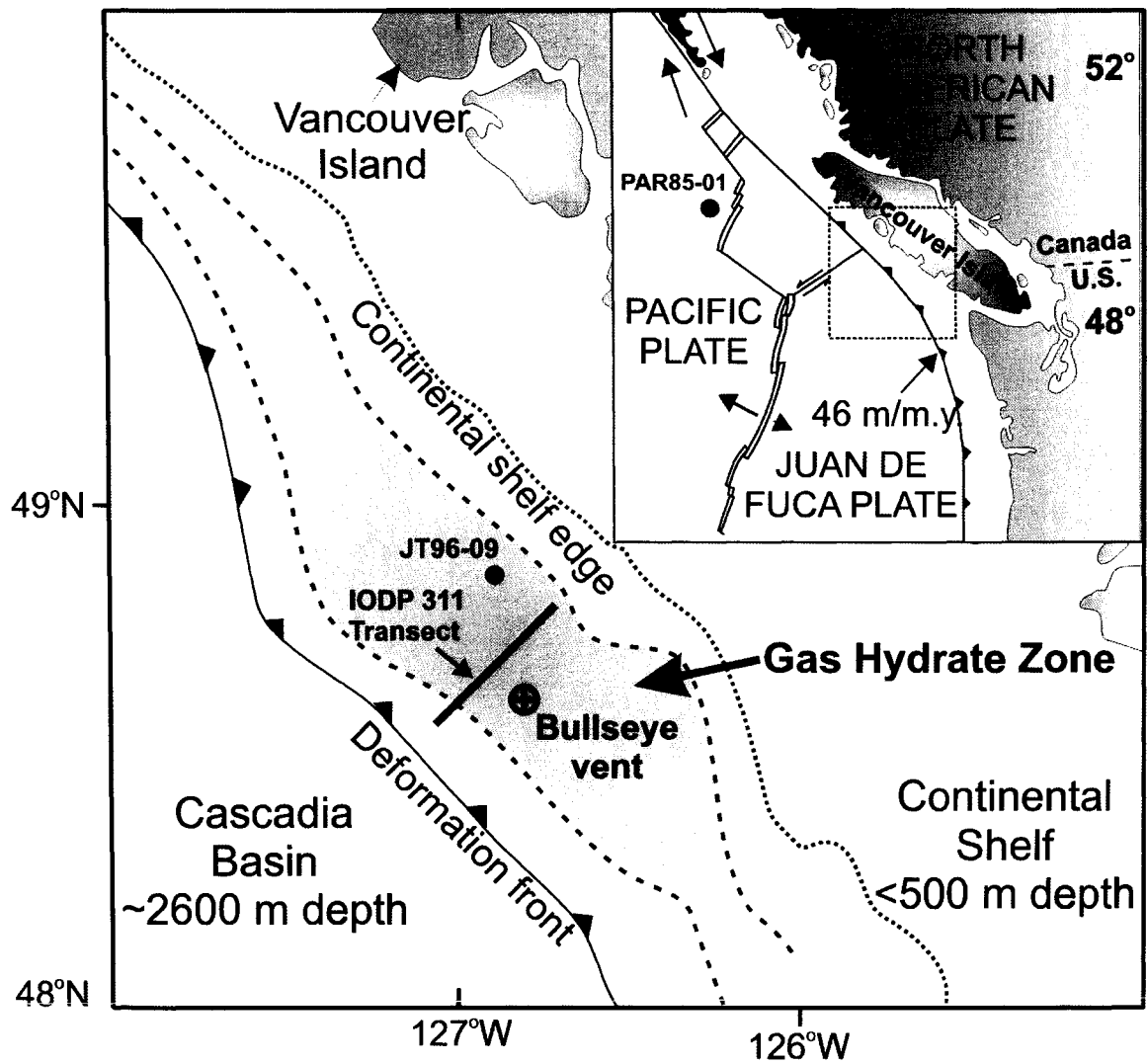
Figure 1. Geographic setting of the northern Cascadia margin. Bullseye vent is located ~2 km off the IODP Expedition 311 transect and was the drilling location for the off transect Site 1328. Gas hydrate has been inferred from bottom simulation reflectors (BSR) in the shaded area of the continental slope (Spence et al, 1991). Additional coring locations discussed in the text (JT96-09, McKay et al., 2004; PAR85-01, Blaise et al., 1990) are included for reference.
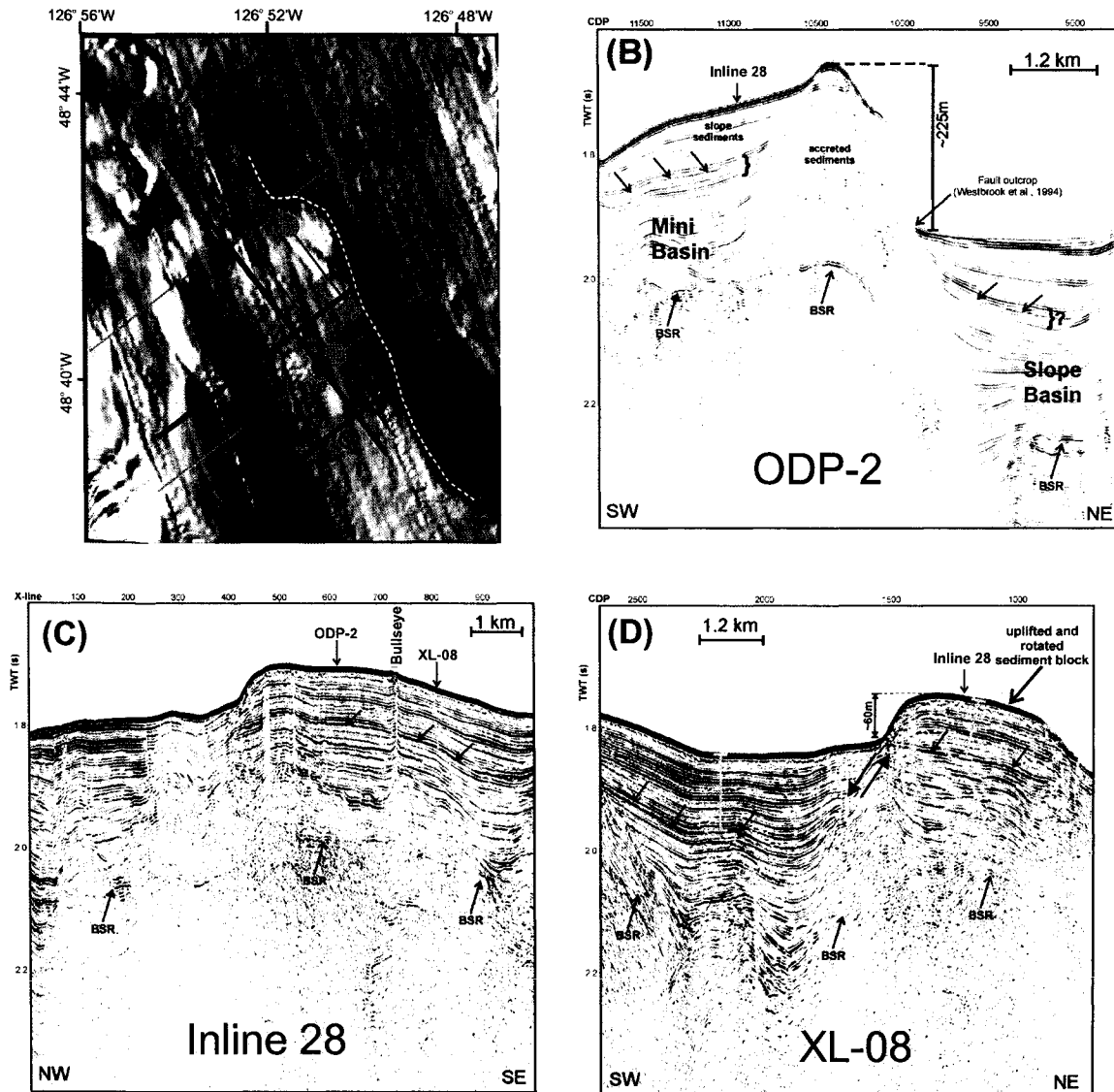
Figure 2. (A) Seafloor relief and seismic lines from the study area. Shaded regions represent the shadow of elevated bathymetric features. Bullseye vent lies within the saddle of a minibasin separated from the broad slope basin to the northeast by a steep escarpment (indicated by dashed yellow line). (B) ODP-2: Strong continuous reflections from bedded sediments in the minibasin and slope basin contrast with the incoherent reflections in the accreted sediments. The eastward facing fault scarp vertically separates the slope basin from the minibasin by ~225 m. The unlabelled arrows, which appear in all of the seismic images, indicate a broad seismic reflection of common stratigraphic origin. The vertical offset reflects uplift due to deformation and faulting within the accretionary complex. (C) Inline 28: Bullseye vent is located on an uplifted sediment block within the minibasin. (D) XL-08: the sediment block is uplifted relative to the adjacent area by ~ 60 m. The bottom simulation reflector (BSR), an indication of free gas near the base of the gas hydrate stability zone, is present in all seismic lines. Figures courtesy of Dr. Michael Riedel (McGill University).
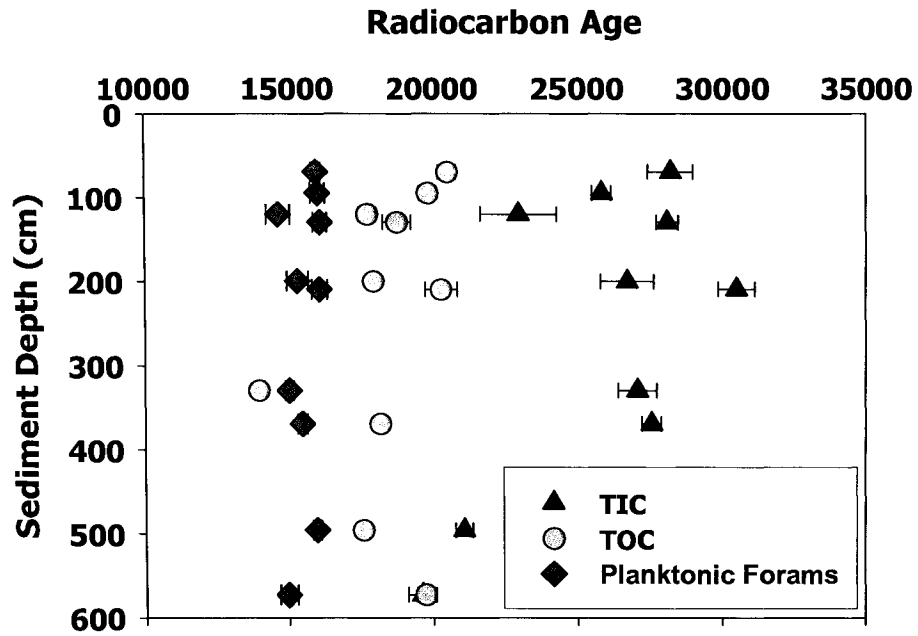
Figure 3. Radiocarbon (^{14}C) age comparison of total inorganic carbon (TIC), total organic carbon (TOC) and planktonic foraminifera from paired samples collected at the Bullseye vent site (see Table 2 for data). The horizontal bars indicate the propagated analytical errors. In many cases, the error was less than the size of the symbol.
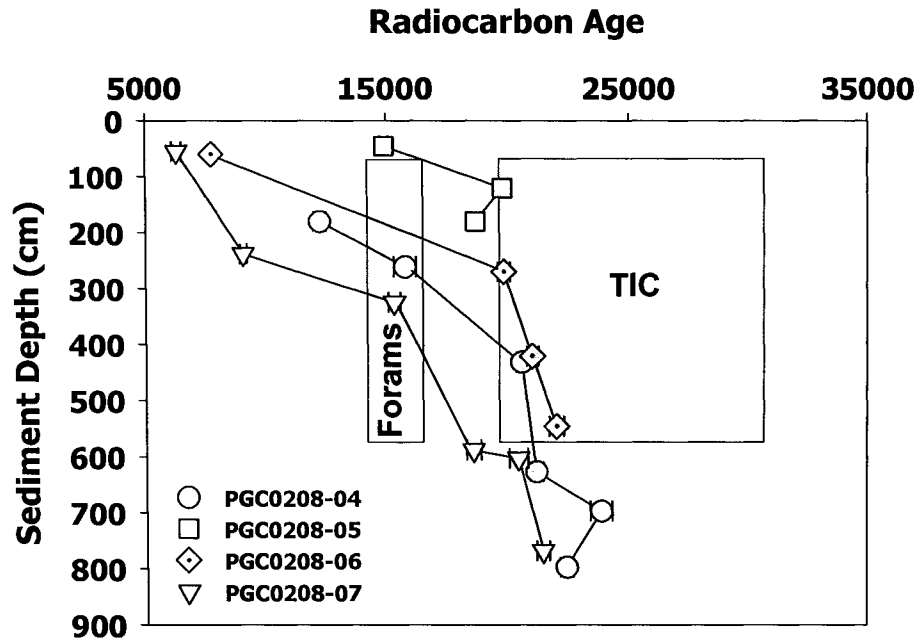
Radiocarbon Age

Figure 4. DIC radiocarbon (^{14}C) age profiles compared to the planktonic foraminifera and TIC data set (Fig. 3). DIC samples collected above the SMI (white symbols) are of similar or lesser age than the foraminifera. DIC samples from near and below the SMI (grey symbols) are of greater age than the foraminifera. The ^{14}C age of DIC near the SMI determines the signature of authigenic carbonate induced by AOM. The horizontal bars for each symbol (where visible) indicate the propagated analytical errors.
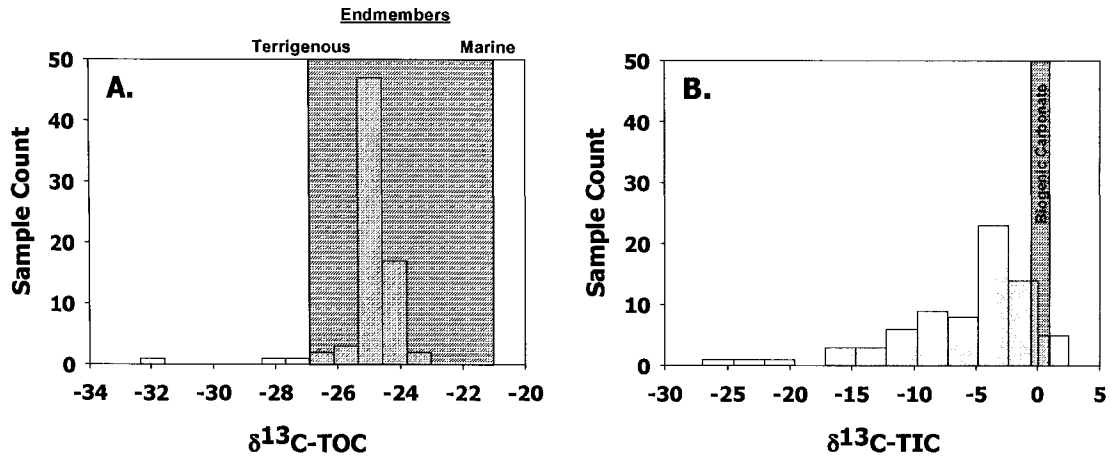
Figure 5. Frequency histograms of δ^{13}C-TOC (**A.**) and δ^{13}C -TIC (**B.**) data from all cores. The shaded areas represent the regional ranges for depositional sources of TOC (McKay et al., 2004) and TIC (Ortiz et al., 1996).
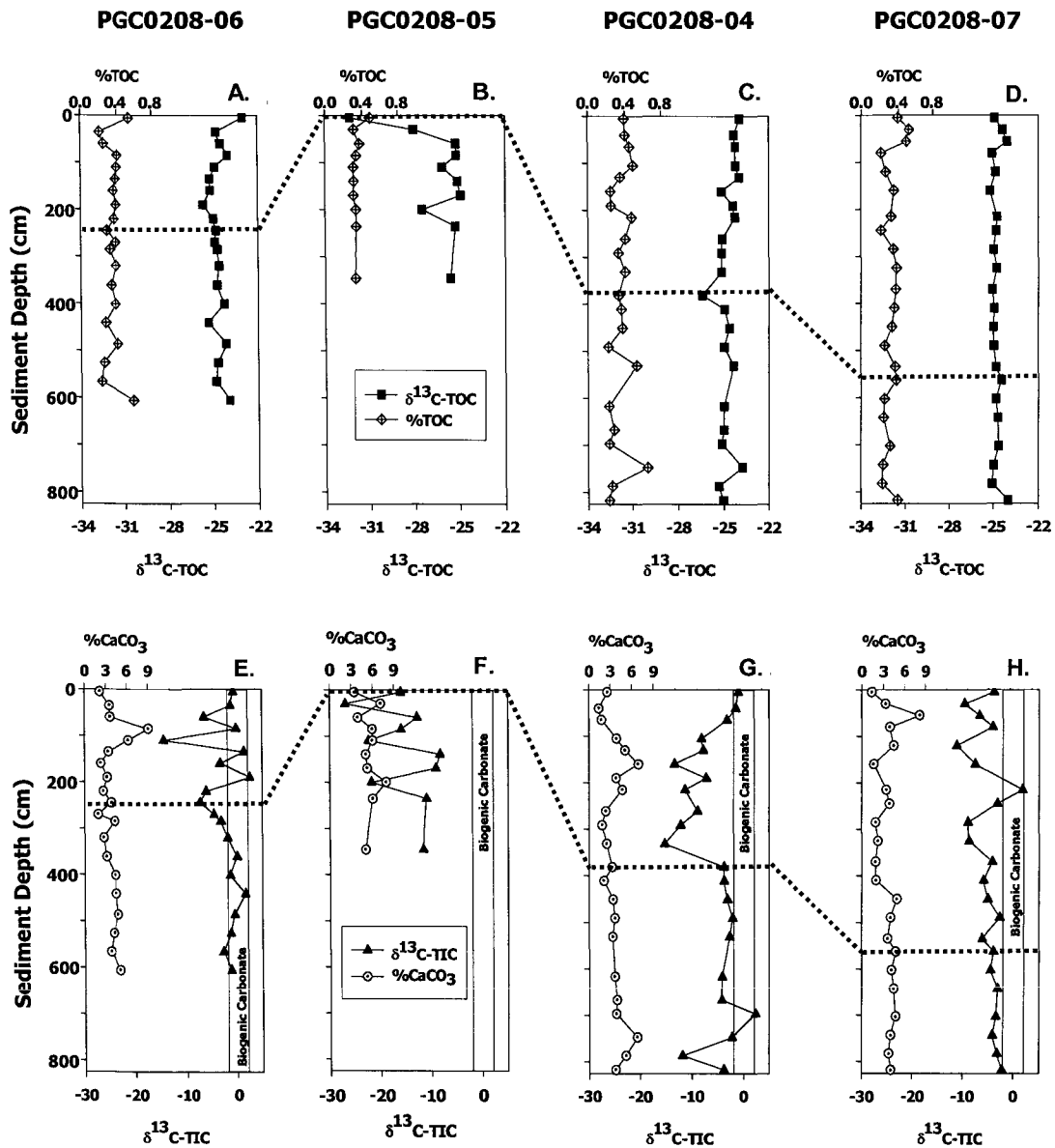
Figure 6. Vertical profiles of solid phase constituents from the piston core transect across the Bullseye vent site. The cores are arranged in their relative locations along the SW to NE trending transect. PGC0208-05 is located within the active cold seep. Top row (A-D): TOC wt% and δ^{13}C profiles. Bottom row (E-H): TIC wt% (expressed as wt% $CaCO_3$) and δ^{13}C profiles. The shaded area represents the expected δ^{13}C range for biogenic carbonate. Negative offsets from the biogenic carbonate values indicate authigenic carbonate contributions. The dashed horizontal line crossing the plots represents the SMI. Note that the greatest offsets occurred above the depth of the SMI, where no methane was present.
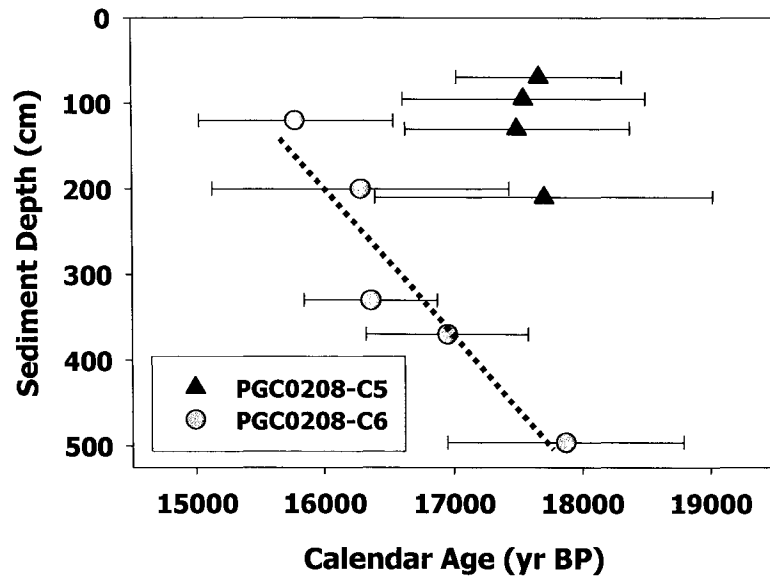
Figure 7. Planktonic foraminifera based age-depth profiles ($\pm1\sigma$) for the calendar age model based on mass-balance age corrections described in the text. A sedimentation rate of 175 cm kyr^{-1} was interpolated from the PGC0208-06 profile. The error bars represent the propagated error from all analytical, calibration and mass balance correction uncertainties.

CHAPTER 7

SUMMARY

224

Previously, it was assumed that the only significant source of methane available for gas hydrate formation in the northern Cascadia margin was microbial (Hyndman and Davis, 1992). The discovery of thermogenic gas hydrate at Barkley Canyon (Chapman et al., 2004) and a gas-source rock correlation that ties the source of the gas to the landward Tofino Basin (Pohlman, Chapter 3) suggest the fluid expulsion model describing how methane charged fluids support gas hydrate formation near the seafloor (Hyndman and Davis, 1992) may be incomplete and should also include contributions from the continental shelf system. The presence of a microbial gas hydrate-bearing cold seep (Bullseye vent) and a thermogenic gas hydrate-bearing cold seep (Barkley Canyon) separated by less than 75 km within a continuous region of gas hydrate occurrence along the northern Cascadia margin (Spence et al., 1991) is fascinating because: 1) it expands the potential source area for gas supporting gas hydrate into the 7,500 km^2 Tofino Basin hydrocarbon province, 2) it presents an opportunity for constraining how the addition of an alternate carbon source (petroleum hydrocarbons) affects the biogeochemical cycles of otherwise similar cold seep sites, and 3) challenges our conception of the geological and geochemical factors that control the occurrence of gas hydrate in accretionary margins.

The chapters in this dissertation examined the sources of gas that sustain the gas hydrate accumulations and the biogeochemical cycling of methane within the study systems. Prior to initiating this study, five hypotheses were proposed:

1. Microbial and thermogenic hydrate gas from the Northern Cascadia Margin (NCM) are formed from a "deep" fossil (>50,000 year B.P.) carbon source.

2. The source of gas for the thermogenic gas hydrate in Barkley Canyon is the Tofino Basin hydrocarbon province located adjacent to Barkley Canyon.

3. The flux and anaerobic oxidation of methane from the deep-water microbial gas hydrate site and the thermogenic gas hydrate site will be greatest close to the near-surface and surface gas hydrate expressions and will decrease with distance from the gas hydrate.

4. "Fossil" methane derived carbon constitutes a significant fraction of carbon in the SOC, DIC, DOC and authigenic carbonate pools of gas hydrate-bearing cold seep systems.

5. Sulfate-reducing bacterial fatty acid composition, concentration and $\delta^{13}C$ will be related to the predominant source (i.e., microbial vs. thermogenic) and flux of the methane.

By analyzing the radiocarbon composition from gas hydrate bound and core gas methane samples collected from 6 distinct high gas flux (HGF) continental margin settings (Chapter 2), the widely accepted, but largely unsupported, assumption that methane from gas hydrate systems is almost entirely fossil was validated (see Hypothesis 1). Radiocarbon composition of the methane indicated gas hydrate and core gas samples were derived from 99.5% (n=15) and 99% (n=8) fossil (devoid of ^{14}C) sources, respectively. Since methane and metabolic products derived from methane have been identified in the water column, it was suggested that definitive recognition of the enormous, dynamic and reactive gas hydrate reservoir as fossil may alter our understanding of how methane from gas hydrate systems influences the radiocarbon ages of other ocean carbon reservoirs (i.e., DOC and DIC). Furthermore, the uniform fossil

signature of methane was later used as an endmember value for tracking methane carbon into other sediment carbon pools (Chapter 6; see Hypothesis 4).

A detailed analysis of the isotopic (δ^{13}C and δD) and hydrocarbon composition of hydrate-bound and vent gas collected from the seafloor of Barkley Canyon supported visual observations of petroleum leaking from the seafloor that suggested a connection to the landward Tofino Basin petroleum system (Chapter 3; see Hypothesis 2). The hydrate gas contained methane having δ^{13}C values of -43.4 to -42.6‰, δD values of -143 to -138‰ and a large percentage (14.9 to 31.9%) of C_2 to C_{5+} hydrocarbons; values consistent with a thermogenic gas source. Barkley Canyon is currently the only known thermogenic gas hydrate system that occurs within an accretionary margin system. The presence of a petroleum system along the Canadian coastline has implications for recent considerations to reassess the British Columbia coastal margin petroleum potential. However, analysis of gas and oil samples collected from the seafloor indicated they were generated from Type III kerogen; a source rock with low hydrocarbon potential. The use of gas hydrate and vent gas collected at the seafloor to classify the source rock is a novel approach for evaluating the resource potential of areas like the northern Cascadia Margin where more detailed sedimentological or petrological investigations are lacking.

The seafloor setting of Barkley Canyon is unique among areas where gas hydrate occurs at the seafloor (e.g., Hydrate Ridge and the northern Gulf of Mexico). The fluid flux regimes might be similar to those from Hydrate Ridge, which is also located on an accretionary margin, but the presence of thermogenic gases (C_{2+}) and gas condensate present the possibility that alternate sulfate reduction pathways may have also been operating, as has been observed at seeps in the Gulf of Mexico. The pore water and

sediment geochemistry from a variety of distinct seafloor sub-environments within

Barkley Canyon were investigated to identify the fluid flux regimes and metabolic

pathways that control the biogeochemical cycling of carbon in this complex system

(Chapter 4). The samples analyzed during this study were obtained from push cores

recovered by the ROPOS ROV. Pore water profiles of sulfate and dissolved inorganic

carbon (DIC) from a thick bacterial mat, a dense clam community and bare sediment

believed to overlay a gas hydrate mound indicated active and distinct flux regimes. In

contrast, a site located greater than 5 m from an exposed gas hydrate mound showed no

evidence of a substantial methane flux (see Hypothesis 3). Pore water δ^{13}C-DIC values (-

25.0‰ $\pm$ 3.6) near the sulfate methane interface (SMI) were affected by anaerobic

oxidation of methane (AOM), but contributions from alternate sulfate reduction pathways

based on the δ^{13}C of the DIC were not evident. Furthermore, comparison of the DIC

concentration and δ^{13}C data to 2-source mixing models of the other potential DIC sources

did not provide conclusive evidence for a greater contribution of AOM derived DIC in

the high flux settings when compared to the low flux settings (see Hypothesis 3),

although near quantitative consumption of methane and sulfate in the high flux cores

suggested otherwise. The 2-source mixing model approach may underestimate the AOM

contribution because it ignores fractionation effects resulting from coupled AOM and

methanogenesis. Pore water δ^{13}CH$_4$ values of -51.1 to -64.3‰ at and immediately below

the SMI were substantially less than the gas hydrate δ^{13}CH$_4$ value of -42.9‰ $\pm$ 0.4

suggesting that AOM and methanogenesis were, indeed, coupled. An additional

interesting observation was that there was no evidence for substantial fluxes of methane

to the water column from any of these sediment environments. However, elevated

methane concentrations in bottom waters (163-1724 nM) indicated a sediment methane source, possibly related to the direct exposure of gas hydrate to seawater.

The pore water data from the Bullseye vent were extracted from long (up to 8 m) piston cores. As such, the focus of this study was somewhat different than that of the Barkley Canyon study where short push cores were collected from specific, visually selected seafloor settings within the active cold seep. In contrast, only two of the seven piston cores from Bullseye vent were from within the cold seep. While it is true (and somewhat miraculous) that both coring techniques captured the same processes (a relevant comparison), the broader implications of the site specific studies were somewhat different. At Barkley Canyon, it was demonstrated that seafloor settings within the cold seep had distinct flux regimes, but the processes occurring within cores with an SMI (i.e., "high" flux cores) were similar (AOM and methanogenesis) and yielded the same net result – complete consumption of the methane by the "AOM reactor" within a thin veneer of sediment blanketing the gas system. At Bullseye vent, less attention was paid to the processes occurring within the seep. Instead, a greater emphasis was placed on how the flux varied with relation to the cold seep. The implications of the Bullseye vent study were that: 1) the flux diminished with distance from the cold seep, 2) there was a relationship between the extent of seismic blanking from deeper (> 10 mbsf) gas related features and the modeled methane flux to the overlying seafloor, and 3) that subsurface lateral gradients of sulfate on the margins of the cold seep suggest the AOM reactor may also operate along the flanks adjacent to the cold seep. The overall conclusion regarding the capacity of AOM to limit the transfer of methane carbon from the gas hydrate

reservoir to the water column and atmosphere is that the AOM reactor is remarkably efficient and operates on a 3-dimensional scale.

The minimum $\delta^{13}C$ values for methane from near the SMI of Bullseye vent (-112‰) are the lowest from a natural setting that I have encountered or observed in the scientific literature. Such values indicate a coupling between AOM and methanogenesis whereby ^{13}C-depleted DIC generated during AOM is recycled to methane and subjected to additional fractionation. This process was briefly described by Borowski et al (1997) from a diffusive flux regime on the Blake Ridge diapir. The occurrence of "extreme" ^{13}C-depletion of methane from Bullseye vent cores with a diffusive flux regime suggests the relationship between diffusion and the low $\delta^{13}CH_4$ values was more than causal. I approached the observation of an unreported pattern of isotope separation factors among the non-seep (or diffusive) cores with a diffusive mechanism as a potential explanation. The isotope separation factors (ε_c) between DIC and methane did not follow patterns predicted by the methane - carbon dioxide partition model developed by Whiticar and Faber (1986). The ε_c is simply the $\delta^{13}C$ difference between DIC and methane ($\varepsilon_c = \delta^{13}C_{DIC} - \delta^{13}CH_4$). According to the methane - carbon dioxide partition model the isotope separation (ε_c) should be constant within a diagenetic setting. The observation was that the ε_c decreased sharply from 60 at the SMI to 40 at the top of the methanogenic zone and with greater depth increased back to 60 (Chapter 5). A mechanistic description of this pattern is that ^{13}C-depleted DIC produced by AOM diffused from the SMI into the upper methanogenic zone, thus increasing the ε_c. Gradually, with greater depth, the influence from DIC produced at the SMI diminished and values returned to 60, the same value from the SMI. A simple source diffusion model was developed and coupled with a

stable isotope mass balance model to evaluate the mechanism described above. The model results and measured values were surprisingly similar considering the simplicity of the model (e.g., advection was ignored entirely and the reactive component was limited to the SMI), which supported the mechanistic description. The findings from the pore water data described above are an extension of the simple and somewhat obvious Hypothesis 3.

The proposition that the fossil methane signature may be an effective methane carbon tracer (see Hypothesis 4) proved far more difficult than imagined, but not for reasons anticipated. Indeed, the fossil signature of methane is valuable not only because the resolving power for radiocarbon ($\Delta^{14}C$ range ~ 1000‰) is greater than stable carbon isotopes ($\delta^{13}C$ range ~ 100‰), but also because fossil carbon contains no ^{14}C and, therefore, cannot be fractionated. The challenge, and ultimately the limitation, of the proposed approach was constraining the radiocarbon content of the of target pools (i.e., TOC and TIC). It was proposed that the age of buried planktonic foraminifera would serve as a proxy for the depositional age (and by extension the endmember signature) of the target pools. For TOC, however, this assumption was inherently flawed because the age/signature of particulate organic carbon (POC) did not necessarily indicate the "time since deposition" (Ohkouchi et al., 2002), as proposed. Contributions of "pre-aged" terrigenous organic matter may influence the age of POC transported to ocean sediments (Raymond and Bauer, 2001). This effect was recognized in the Bullseye vent TOC, which was comprised of ~60% terrigenous organic matter. Furthermore, diagenetic alterations induced by AOM that convey methane carbon into other sedimentary carbon pools had a measurable influence on the radiocarbon signature of the foraminifera. I was able to calculate and correct for the diagenetic contribution and age alteration in the

foraminifera data, but the process was expensive, laborious and subject to considerable error propagation. I conclude stable carbon isotopes were a superior proxy for identifying the sources and fate of carbon in this AOM dominated system.

The radiocarbon data did, however, provide unexpected insight into the depositional history of the Bullseye vent site. The corrected and calibrated foraminiferal ages between sediment depths of 70 and 573 cm were from 14.9 to 15.9 kyr BP; similar to the timing of the termination of the last glacial maximum (LGM). Furthermore, the strong terrigenous signature of the TOC (the primary source of organic matter during the LGM) suggested the near-surface sediments were comprised almost entirely of glacial aged material. The suggestion of non-deposition since the LGM at the Bullseye vent site contrasted with data reported from a site located ~26 km from Bullseye vent, which contained several meters of Holocene aged material (McKay et al., 2004). These observations, in combination with complementary geochemical and seismic data, suggest the Bullseye vent has experienced net erosion since the LGM. Seismic reflection profiles of the slope basin and minibasin that contains Bullseye vent also suggest that the minibasin has been uplifted by as much as 60 m since the termination of the LGM; thus isolating it from turbidite deposition.

The final objective of this dissertation was to utilize lipid biomarkers (specifically fatty acids from sulfate reducing bacteria, SRB) as chemotaxonomic markers to contrast the SRB community composition and determine whether alternate sulfate reduction pathways were supported by contributions from higher molecular weight hydrocarbons at Barkley Canyon (Hypothesis 5). Unfortunately, the timeframe for this dissertation was insufficient for fully exploring that exciting opportunity. Fully characterizing the

biogeochemical system was more complicated and involved than anticipated.

Nevertheless, preliminary data on the fatty acids compositions, concentrations and $\delta^{13}C$

values are noteworthy. The $\delta^{13}C$ values of terrigenous plant LCFAs and ubiquitous

unsaturated 16:0 and 18:0 fatty acids did not change with depth and had $\delta^{13}C$ values (-

24.9‰ to -36.0‰) that were considerably greater than the monounsaturated, -iso and –

anteiso branched fatty acids (BrFA) (-28.3‰ to -67.6‰) indicative of SRB. The ^{13}C-

depletion of the monounsaturated fatty acids and branched fatty acids was pronounced at

the SMI, which provides strong evidence that methane carbon was assimilated into the

SRB membrane lipids (Hinrichs et al., 2000; Elvert et al., 2003). Furthermore, the ~30‰

range of $\delta^{13}C$ values among these compounds indicates alternate reduced organic

compounds were also utilized as carbon sources. The most ^{13}C-depleted fatty acids from

Barkley Canyon were the i-15:0 and ai-15:0 BrFA. In the northern Gulf of Mexico, ai-

15:0 was the most abundant fatty acid present and was among the most ^{13}C-depleted from

a gas hydrate associated sample (Zhang et al., 2002). In contrast, at Hydrate Ridge, ai-

15:0 was not particularly abundant and was not among the most ^{13}C-depleted fatty acids.

These data tentatively suggest the community composition may be closely related to the

availability of the thermogenic hydrocarbons, rather than other site specific factors since

Hydrate Ridge is located on the same continental margin.

Although much was learned from this dissertation research project, a number of

new questions arose in the course of the project that remain unresolved. Below I offer a

list of potential future research topics for further characterizing the sources and forms of

organic matter supporting gas production in gas hydrate bearing cold seep systems and

investigate the biogeochemical processes that control the sedimentary cycling of methane there.

Top 10 suggestions for future research

1. Expand the global database of methane radiocarbon values from gas hydrate bound and core gas methane. Slight contributions of modern methane (up to 2.2 pmC) in core gas samples from Bullseye vent suggested limited production of modern methane in the near-surface. Additional data from similar settings will substantiate or refute the hypothesis of a fossil origin for methane from gas hydrate cold seep systems.

2. Determine if the fossil gas hydrate methane reservoir influences other globally relevant ocean carbon pools (e.g., oceanic DOC, and its associated great ages). We are currently analyzing water column and pore water DOC samples from Bullseye vent and Barkley Canyon to determine if a localized effect is present.

3. Characterize source rocks from the Tofino Basin and the accretionary prism to directly characterize the source rock kerogen type and confirm that the source of the thermogenic gas is indeed Tofino Basin.

4. Conduct a margin-wide deep-drilling transect to constrain the extent that thermogenic gas occurs in the accretionary system. This was a specific objective of the Integrated Ocean Drilling Program (IODP) Expedition 311, which took place on the northern Cascadia margin from Sept-Oct 2005. I had the fortunate opportunity to participate in this program and am currently analyzing samples to test this hypothesis.

5. Determine whether the fluid flux regimes associated with the distinct seafloor settings at Barkley Canyon were controlled by the subsurface geology or the biological community inhabiting the seafloor. Long term observation of the seafloor will be possible once the NEPTUNE cabled seafloor observatory is emplaced. A suggested study for that program would be to monitor the recruitment and succession of biological communities to determine whether benthic communities and associated fluid flux regimes evolve with time.

6. Measure directly the rates of AOM and sulfate reduction in sediment cores from Barkley Canyon to determine whether alternate sulfate reduction pathways (other than AOM) are operating. These studies should be coupled with molecular biological studies and lipid biomarker studies to characterize the microbial consortium and trace the carbon sources into the biomarkers. Radiocarbon and deuterium analysis of the lipid biomarkers may prove particular useful for differentiating contributions from fossil methane, other hydrocarbons and TOC.

7. Measure directly the flux of methane from the Barkley Canyon sediments and exposed gas hydrate to constrain the source of methane measured in the water column.

8. Measure sedimentary DIC and methane concentrations and $\delta^{13}C$ values at other cold seep systems to test the hypotheses that: 1) "extremely" ^{13}C-depleted methane $\delta^{13}C$ values and diffusive flux conditions have a causal relationship, and 2) diffusion of ^{13}C-depleted DIC produced at the SMI alters the isotope separation values (ε_c) in the upper methanogenic region.

9. Improve the source-diffusion model by integrating advective and reactive components to provide a more thorough description of the factors controlling the isotopic composition of DIC and methane in AOM dominated systems. Also, utilize measured AOM and sulfate reduction rates to constrain the source terms in the model.

10. Conduct a more rigorous seismic evaluation of the structure of the slope basin and mini basin along the northern Cascadia margin to test the hypothesis that rapid and recent uplift of the slope sediments has occurred since the termination of the LGM. Investigate the glacial history in the immediate vicinity of the coastal margin of Vancouver Island and construct a geophysical model to determine how rapid unloading of the Cordilleran ice sheet from the continental slope may have influenced plate subduction and deformations within the accretionary prism. Couple that model to one that predicts how the gas hydrate system might have responded to a reduced pressure regime and structural deformations within the minibasin.

References

Borowski, W. S.; Paull, C. K.; Ussler, W. Carbon cycling within the upper methanogenic zone of continental rise sediments: An example from the methane-rich sediments overlying the Blake Ridge gas hydrate deposits. Mar. Chem. 57: 299-311; 1997.

Chapman, N. R.; Pohlman, J. W.; Coffin, R. B.; Chanton, J. P.; Lapham L. Thermogenic gas hydrates in the northern Cascadia Margin. EOS. 85: 361-365; 2004.

Elvert, M.; Boetius, A.; Knittel, K.; Jorgensen, B. B. Characterization of specific membrane fatty acids as chemotaxonomic markers for sulfate-reducing bacteria involved in anaerobic oxidation of methane. Geomicrobiology Journal. 20: 403-419; 2003.

Hinrichs, K. U.; Summons, R. E.; Orphan, V.; Sylva, S. P.; Hayes, J. M. Molecular and isotopic analysis of anaerobic methane-oxidizing communities in marine sediments. Org. Geochem. 31: 1685-1701; 2000.

Hyndman, R. D.; Davis, E. E. A mechanism for the formation of methane hydrate and sea-floor bottom-simulating reflectors by vertical fluid expulsion. J. Geophys. Res. -Solid Earth. 97: 7025-7041; 1992.

Kvenvolden, K. A.; Ginsburg, G. D.; Soloviev, V. A. Worldwide Distribution of Subaquatic Gas Hydrates. Geo-Marine Letters. 13: 32-40; 1993.

McKay, J. L.; Pedersen, T. F.; Kienast, S. S. Organic carbon accumulation over the last 16 kyr off Vancouver Island, Canada: evidence for increased marine productivity during the deglacial. Quaternary Science Reviews. 23: 261-281; 2004.

Ohkouchi, N.; Eglinton, T. I.; Keigwin, L. D.; Hayes, J. M. Spatial and temporal offsets between proxy records in a sediment drift. Science. 298: 1224-1227; 2002.

Raymond, P. A.; Bauer, J. E. Riverine export of aged terrestrial organic matter to the North Atlantic Ocean. Nature. 409: 497-500; 2001.

Sassen, R.; Sweet, S. T.; Milkov, A. V.; DeFreitas, D. A.; Salata, G. G.; McDade, E. C. Geology and geochemistry of gas hydrates, central Gulf of Mexico continental slope. Trans. Gulf Coast Assoc. Geol. Soc. 49: 462-468; 1999.

Spence, G. D.; Hyndman, R. D.; Davis, E. E.; Yorath, C. J. Seismic structure of the northern Cascadia accretionary prism: evidence from new multichannel seismic reflection data. Geodynamics. 22: 257-363; 1991.

Whiticar, M. J.; Faber, E. Methane oxidation in sediment and water column environments - Isotope evidence. Org. Geochem. 10: 759-768; 1986.

Zhang, C. L. L.; Li, Y. L.; Wall, J. D.; Larsen, L.; Sassen, R.; Huang, Y. S.; Wang, Y.; Peacock, A.; White, D. C.; Horita, J.; Cole, D. R. Lipid and carbon isotopic evidence of methane-oxidizing and sulfate-reducing bacteria in association with gas hydrates from the Gulf of Mexico. Geology. 30: 239-242; 2002.

VITA

Born in Monroe, Louisiana, USA, June 23, 1970. Studied Chemistry at Rockhurst

College in Kansas City MO, USA (1988-89) and graduated with a B.S. in Zoology

(Magna Cum Laude) from Louisiana Tech University (Ruston LA, USA) in 1992.

Attended Texas A&M University in College Station TX, USA and graduated with an

M.S. in Bological Oceanography in 1995. Worked as a research associate at the Naval

Research Lab (NRL) in Washington D.C. from 1996 until present. Supervised the Gas

Hydrate Research Group for Geo-Centers/SAIC from 2002 until present and entered the

PhD program in the Physical Sciences Department at the School of Marine Science,

College of William and Mary in 2001.